Predicting acoustic emission attenuation in solids using ray-tracing within a 3D solid model

Mohamed Nabil El-Shaib

Submitted for the degree of Doctor of Philosophy on completion of research in the School of Engineering and Physical Sciences
Heriot-Watt University

November 2012

ABSTRACT

Acoustic Emission (AE), is a non-destructive testing and monitoring technique that can be applied to a wide range of situations for condition monitoring and fault diagnosis in mechanical systems and components. Acoustic emission technology involves the propagation of elastic (stress) waves generated by such events as particle impingement, cracking or fluid flow. These waves are recorded at one or more surface-mounted sensor placed at some distance from the generating site(s) and it is necessary to have a means of coping with the implications of the propagation path. It is generally not practicable to solve the wave equation for all possible modes of AE propagation in a solid and this project is based on simulating such propagation using ray tracing applied within a computer-generated solid model representing the structure being monitored.

As the attenuation of AE waves is affected not only by the material properties but also by the geometry of the object and the type of surrounding media, knowledge of attenuation is essential to ensure that sensors can be placed appropriately on large or complex structures. The aim of the current work was to establish the capability of predicting the attenuation of AE using a computer-graphical ray tracing technique incorporated in a 3D solid model.

The investigative approach involved simulating AE propagation in a range of simple objects of various shapes and sizes and also measuring propagation in these objects using a point source. By comparing simulated and measured attenuation, it was possible to determine appropriate values for the parameters of the simulation, such as the reflection coefficients and the degree of internal friction as well as the proportion of energy carried in surface and bulk waves, respectively.

It is concluded that the ray tracing technique has the capability to predict AE attenuation in different shapes and with different environments and materials using a simple division of wave modes into bulk and surface waves. Refinements are suggested in the further work for cases where a more precise representation of the propagation modes is needed.

DEDICATION

Lovingly dedicated this work to my Parents

ACKNOWLEDGMENTS

Above all, I thank Almighty God for helping me to complete this work. This thesis appears in its current form due to assistance of several people who encouraged and inspired me during my study. Therefore, I owe a sincere debt of gratitude to all of them.

Firstly, I would like to offer my profound gratitude to Prof. Robert Reuben, I will stay all my life grateful for his generous scientific and technical support, advice and encouragement over the entire period of my research, and for his most useful and valuable comments on my thesis writing. I could not have imagined that this opportunity would be as rewarding.

I would like also to express my sincere gratitude to Dr. Theo Lim for providing inspiration and suggestions for improvement my thesis.

I shall always remain highly obliged to Dr. M. Shehadeh and to all the members of the department of Mechanical Engineering at Heriot-Watt University for their time, feedback and assistance they have provided.

I would like to take this opportunity to express my appreciation to all my friends, who made these years very memorable and extremely enjoyable, especially to Ghazi, Wael, Fiona, Sneha, Estelle, Katerina, Kaiye, Anais, Laura, Afroditi, Aymeric, Gabin, Quico, Flor, Louise, Samer and Enaba. Also, to my warden team and international committee.

Research Thesis Submission

Name:	Mohamed Nabil Ahmed Amin El-Shaib		
School/PGI:	School of Engineering and Physical Sciences, Mechanical Engineering		
Version:	Final	Degree Sought	PhD

Declaration

In accordance with the appropriate regulations, I hereby submit my thesis and I declare that:

1) The thesis embodies the results of my own work and has been composed by myself
2) Where appropriate, I have made acknowledgement of the work of others and have made reference to work carried out in collaboration with other persons
3) The thesis is the correct version of the thesis for submission and is the same version as any electronic versions submitted*.
4) My thesis for the award referred to, deposited in the Heriot-Watt University Library, should be made available for loan or photocopying and be available via the Institutional Repository, subject to such conditions as the Librarian may require
5) I understand that as a student of the University I am required to abide by the Regulations of the University and to conform to its discipline.

* *Please note that it is the responsibility of the candidate to ensure that the correct version of the thesis is submitted.*

Signature of Candidate:		Date:	

Submission

Submitted By:	
Signature of Individual Submitting:	
Date Submitted:	

For Completion in Academic Registry

Received in the Academic Registry by:			
Method of Submission *(Handed in to Academic Registry; posted through internal/external mail)*:			
Signature:		Date:	

LIST OF CONTENTS

LIST OF TABLES

LIST OF FIGURES

NOMENCLATURE

E_y	Young's modulus of elasticity for the material (Pa or N/m^2)
ρ	Density of the material (kg/m3)
ν	Poisson's Ratio for the material
f	Wave frequency (Hz)
λ	Wave length (mm)
c	Wave speed, $c = \lambda \times f$, (m/s)
ω	Angular frequency, $\omega = 2\pi f$, (rad/s)
k_v	Wave vector or wave number, $k_v = 2\pi/\lambda$, (rad/sec)
ϕ	Phase offset, $\phi = k \times x$
t	Propagation wave time (sec)
x, r	Wave propagation distance from the source (m)
c_1	Longitudinal wave speed (m/s)
c_2	Shear wave speed (m/s)
c_r	Rayleigh wave speed (m/s)
c_e	Extensional wave speed (m/s)
c_f	Flexural wave speed (m/s)
h	Plate thickness (mm)
E_t	Transmitted Energy (V^2.s)
E_r	Reflected Energy (V^2.s)
E_x	AE energy at distance *x* from the source (V^2.s)
E_o	AE energy of the source (V^2.s)
Z	Acoustic impedance ($\mathrm{kg/m^2 s}$)
θ, β, γ	Angles (degs)
V_1, V_2, V_3	Various wave velocities (m/s)
A	Wave amplitude (V)
A_1	Measured amplitude at a receiver sensor at distance, x from the source (V)
A_o	Reference amplitude is the maximum signal amplitude (V) at the source position
D	Distance between two sensors (m)

k	Measured attenuation factor (m^{-1})
$\bar{k}$	Weighted mean for different attenuation measures, (m^{-1})
k'	Simulated attenuation factor (m^{-1})
I	Unit vectors representing the incident ray direction
N	Unit vectors representing the surface normal
R^2	Correlation factor
N_f	Number or rays fired
N_h	Number or rays hitting the sensor
n	No of reflected rays
x_r	Ray distance
α	Internal material frication
R_U	Upper reflection coefficient
R_L	Lower reflection coefficient
$\alpha_U{}'$	Upper pseudo-internal friction coefficients,
$\alpha_L{}'$	Lower pseudo-internal friction coefficients,

ABBREVIATIONS

NDT	Non-destructive testing
AE	Acoustic Emission
ADC	Analogue to Digital Converter
PAC	Physical Acoustic Corporation
DAQ	Data Acquisition System
NI	National Instruments
PZT	Lead Zirconate Titanate
SCU	Signal Conditioning Unit
GUI	Graphical User Interface

CHAPTER 1: INTRODUCTION

"Acoustic emission" is a term commonly used to describe the stress waves generated in a material or structure when they are subjected to a localised disturbance. The waves are caused by the rapid release of energy within a material due to events such as the unloading resulting from a unit of crack extension and even the deceleration of dislocations after a unit of plastic deformation. AE is manifest as transient elastic waves which (usually) are detected by suitable transducers [1] placed on the surface of the object. Used in this way, AE can provide early information on degradation of materials, structures, machines and processes. In the last 50 years, AE has been shown to be an important non-destructive testing technique [2] and has been developed for a number of condition monitoring applications.

1.1 Background

AE is a passive listening technique, and, as such, is distinct from other non-destructive test techniques like ultrasonic or radiographic testing, which use more-or-less structured waves to probe an object for defects. To use AE, there needs to be some activity in the material and, although it is possible in principle to detect movements on the atomic scale, the sensitivity decreases with distance between the source and the transducer [3]. In most practical applications, the source is extended in time and space, which means that any detected AE is a complex mixture of modes, phases, intensities and frequencies.

Unlike other NDT techniques, AE monitoring allows damage processes to be observed over a period of time, for example in a mechanical test where emissions can be detected during the entire loading history without any disturbance to the specimen. Thus, the AE method can detect the dynamic processes associated with the degradation of structure integrity [4]. Also, the energy that is detected in AE is released from within the test object rather than being supplied by the test method, as in radiographic or ultrasonic

testing [2, 5]. The fact that AE propagates in all directions for a source means that a transducer located anywhere in the vicinity can detect the resulting AE and, further, that multiple sensors recording the same event can be used to locate the source.

In spite of the great number of studies on AE wave propagation, the technological field of AE monitoring has several limitations, which need to be overcome to get more use out of practical results [2, 5, 6]. One of the major problems is to reconstruct the source of an AE signal which has been recorded at one or more sensors at unknown distances from it. A significant part of this can be answered if it is known how much the AE signal is attenuated in the material or structure. AE attenuation in solids is a difficult parameter to specify in absolute terms as AE waves are affected not only by the material properties but also by the geometry of the object and the surrounding media [5, 6]. Another problem with AE is background noise, which can have a major impact on Acoustic Emission testing and may even drown out signals of interest and so prevent a test from being performed [2, 6]. Again, a knowledge of AE attenuation can help to separate located AE signals from diffuse background noise, provided than an appropriate choice of array has been made.

AE waves may be thought of as waves spreading out like ripples on a pond or, in three dimensions, like light from a point source. As is commonly done with light waves, and somewhat less commonly with sound waves, it ought to be possible to represent the cylindrical or spherical spreading of the wave by a number of rays each emanating from the source in a radial direction [1, 2]. Several other approaches have been made to understanding AE wave propagation using, for example, the Finite Element Method (FEM) and the Boundary Element Method (BEM). Although these approaches have experienced enhancements over the years, they tend to be computationally expensive, complex in implementation and, in some cases, are restricted to low frequencies and/or to particular classes of idealised wave [7-9]. One feature of AE, which is a consequence of its generation, is that it can rarely be considered to be of a single mode.

The simple geometric option to describing wave propagation, known as “Ray Tracing”, has greatly benefited from computerisation, and is a widely used technique in computer graphics to generate a realistic images by calculating the level and colour of light at

each point as a result of tracing the path of the light through pixels in an image plane as they interact with the optical surface. Modern ray-tracing algorithms have the capability of simulating a wide variety of optical effects, such as reflection, refraction and scattering. These capabilities can be used to simulate wave propagation in two or three dimensional virtual objects and virtual probes can be placed on the surface(s) of interest [10].

Ray-tracing is beginning to become a popular technique in non destructive test (NDT) modelling, especially in X-ray and ultrasonic testing [11, 12]. However, perhaps due to the complex wave propagation of AE signals compared to the other NDT techniques, relatively little work has been published investigating AE using the ray-tracing technique [7, 11-14].

1.2 Aims and objectives

The overall aim of this study is to establish a computationally efficient way to predict the attenuation of AE, using 3D solid modelling and ray-tracing techniques.
In order to do this, the following objectives were devised:

To integrate ray-tracing and ray-generation algorithms into a flexible solid-modelling framework

To introduce various rules for the propagation of the waves and to count rays arriving at a virtual sensor

To carry out a set of detailed experiments on the objects modelled to match the observed transmission properties with those arising from the simulations

To use the measured and simulated results to recommend the most consistent way of describing the propagation of an impulse source in small and larger objects of various materials with a range of interfaces

1.3 Research methodology

To meet the above objectives, the computer programming was done in visual C++ [15], incorporating the ACIS 3D solid modelling kernel [16, 17], a rendering program (HOOPS)[18] , and Microsoft foundation classes (MFC)[19] to create the necessary algorithms and tools for AE ray-tracing and the user interface. The simulation was developed in two stages, the first of which followed purely geometric rules and was used to achieve convergence and to establish the required resolution for interaction of the rays with the solid model. The second stage allowed a range of physical considerations to be introduced, including scattering, reflection and the phase(s) of the rays.

The AE attenuation experiments were carried out on a series of simple small blocks, investigating the effect of source position and surrounding media. Some tests were also carried out on larger, more practically significant structures, again with a range of realistic environments. Matlab software [20] was used to analyze the signals obtained from experiments.

1.4 Thesis structure

A brief summary of the chapters is given below:

Chapter 1: Introduction.

This chapter gives a description of how the present work was inspired and outlines the essential approach of describing AE attenuation using a ray tracing technique.

Chapter 2: Literature Review.

This chapter is divided into three sections. The first section summarises the state of knowledge of AE techniques, focusing on general aspects of AE wave propagation and

attenuation. The second section summarises the state of knowledge on ray tracing techniques. The last section reviews recent published research relevant to AE and ray simulation.

Chapter 3: Simulation Programme.

This chapter explains the methodology for the novel graphical user-friendly AE ray tracing programme, and discusses the physical approach used in developing the programme.

Chapter 4: Apparatus and Experimental Procedure.

This chapter is divided into three sections. The first section introduces and describes the features and specification of the AE monitoring apparatus. The second section describes the calibration of the AE sensors to quantify the natural variability of the AE results. The last section describes the experimental approach and the various procedures used to obtain data for comparison with the AE ray-tracing programme.

Chapter 5: Results and Analysis: Geometrical Simulation.

This chapter investigates the capability of the ray-tracing methodology to predict the geometric AE attenuation in different solid model shapes and sizes, using different source positions and materials.

Chapter 6: Results and Analysis: Physical Simulation Including Effect of Environment.

This chapter extends the capability of the ray-tracing methodology in predicting the AE attenuation, taking into account physical factors, and the effects of different external and internal environments.

Chapter 7: Conclusions and Future Work.

This chapter lists the significant findings of the thesis, and suggests directions for future work.

1.5 Contribution to knowledge

This work presented here contributes to knowledge in three key areas:

- It establishes an approach to the simulation of AE wave propagation using a solid model and virtual sensors as an alternative to computationally-intensive and less flexible numerical analysis approaches.
- It contains a set of carefully-measured practical data on a variety of objects with a variety of source-sensor paths and a range of interfacial conditions using a standard AE source. This data specifically allows the effects of interfacial acoustic impedance, material and geometry to be investigated using the framework of the simulation and therefore contributes to a general understanding of propagation modes in practical structures.
- It determines the key factors influencing AE attenuation and the relative roles of surface and bulk waves as a means to providing a more structured way of reconstituting the temporal and spatial features of AE sources, given records from an array of sensors and a known (or unknown) source position.

CHAPTER 2: LITERATURE REVIEW

AE is the term commonly used to describe the elastic waves generated by a rapid release of energy from localized sources within, or on the surface of a solid. The waves generated are in the ultrasonic range between 20 kHz and 1 MHz (as opposed to the audible frequency range, approximately 20 Hz - 16 kHz) [21]. The AE energy propagates through the solid and on the surface in all directions, and any suitable sensor sufficiently near to the source will detect the waves and convert them to electrical signals [2]. In principle, the AE signal can provide much information about the source of the emission, particularly its intensity and its temporal structure, but what is detected will depend on the propagation of the wave, which is in turn dependent on the source-sensor distance, the material(s) and the structure being monitored [22].

The first documented observation of AE may have been made as far back as the 8th Century by the Arabian alchemist, Geber. However, AE, as an NDT technology, started in the early 1960s, when it was recognised that growing cracks and discontinuities in pressure vessels could be detected by monitoring AE signals during pressurisation [2].

Since then, AE analysis has been used and developed for a wide range of applications of NDT, condition monitoring and fault diagnosis including; detecting and locating faults in pressure vessels and leakage in storage tanks and piping systems, monitoring welding and corrosion-erosion processes, detecting partial discharges from components subjected to high voltage and the failure of protective coatings [23-28].

A vast literature has built up around both AE monitoring and ray tracing techniques in several interrelated areas. This literature is reviewed in the following way in this chapter. First, the elements of the AE propagation are reviewed, followed by the causes and mechanisms of AE attenuation. Second, the basis of ray tracing is described, followed by a critical analysis of the application of this technique. Third, recent published research relevant to AE and ray simulation is reviewed in detail. The Chapter culminates in an identification of the area of study in this thesis.

2.1 Acoustic emission wave propagation

The propagation of waves in an elastic medium can be treated mathematically by the solution of the general wave equation using appropriate boundary conditions [1]:

$$\frac{\partial^2 \emptyset}{\partial t^2} = c^2 \nabla^2 \emptyset \qquad (2.1)$$

where:

t : Time

c : Wave propagation velocity

∇^2 : Laplacian operator in Cartesian coordinates $= \frac{\partial^2}{\partial x^2} + \frac{\partial^2}{\partial y^2} + \frac{\partial^2}{\partial z^2}$

$\emptyset$: Potential function representing two plane waves travelling in the positive and negative directions

If the deformation occurs in only one (say, *x*-) direction, the general solution for the potential function is:

$$\emptyset = f(x - ct) + F(x + ct) \qquad (2.2)$$

where:

f : Function corresponding to the plane wave travelling in the positive direction

F : Function corresponding to the plane wave travelling in the negative direction

Depending upon the geometry of the solid and the nature of the stimulus, AE waves can propagate in a number of different ways, and, unlike in ultrasonic NDT, these are generally beyond the control of the researcher. Different sources and structures lead to different amplitude, frequency, damping and dispersion characteristics, and scattering by inhomogeneities and multiple reflections from boundaries all add to the complexity [29, 30].

The wave particle directions in a propagating wave depend on the boundaries of the medium, and here bound categories can be identified, Figure 2.1. For unbounded media the wave particles can move relative to each other either along the direction of propagation, called a longitudinal wave, or rotating about the direction of propagation called a shear wave. For one bounding surface, the wave will propagate with two potential functions, associated with longitudinal wave particles and rotational wave particles, called Rayleigh waves and Love waves, respectively. For an infinite plate bounded by two surface, the stress wave will be uniform over any cross section of the plate perpendicular to the propagation direction, called Lamb waves [1]. There are two classes of Lamb waves, one where propagation involves compression and rarefaction (extensional waves) and the other involving bending motions (flexural waves). It should be emphasised that these types of waves result from the wave equation using idealised boundary conditions and idealised source functions. In practice, neither the medium, nor the boundaries nor the source is simple, and so these solutions provide a useful guide to what is seen by the sensor only. There have been various studies of AE wave propagation aimed at solving the basic problem of detecting what is the transfer function (time, frequency, amplitude) which is introduced by propagation from the source to the location of the sensor [31].

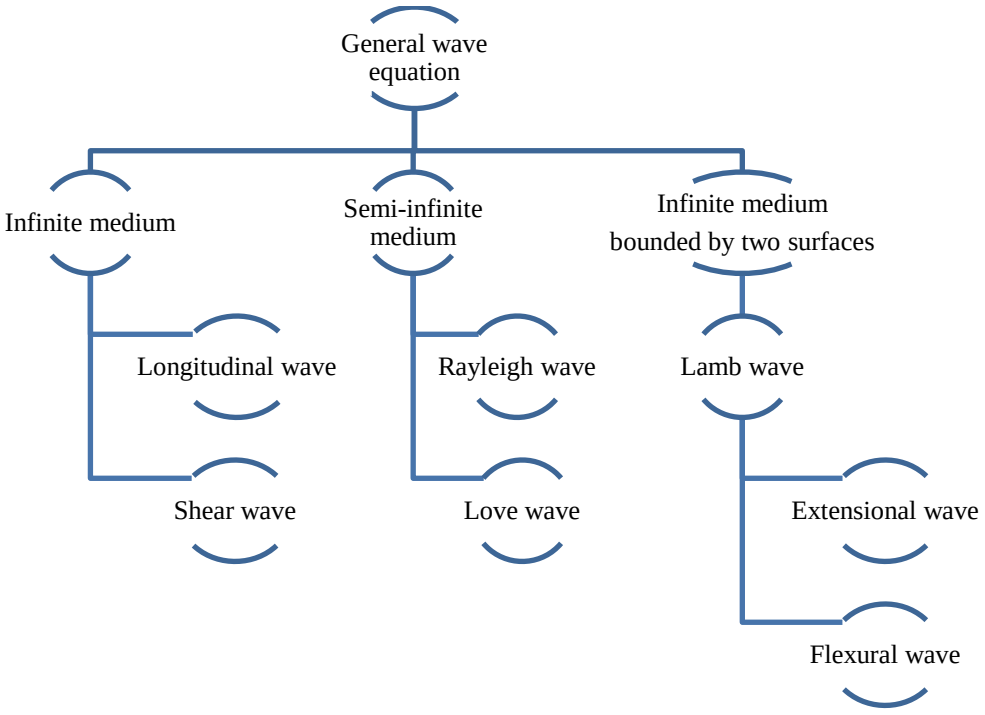

Figure 2.1: Wave modes according to the media

The traditional AE method only captures certain parameters (sometimes called AE features), including AE counts, peak levels and energies. Again, following the traditional approach, the AE features are correlated with the condition which is the subject of monitoring. The AE characteristics so used are usually only related to the captured signals and do not account for the source of the signal and wave propagation [22]. A common variant on this traditional approach uses arrays of sensors to locate the source, on the assumption that the source is a point in time and space and that the AE can be considered to propagate at a single, known speed. In an attempt to improve the accuracy of source location, a number of researchers (e.g. Holford et al. [32] and Shehadeh et al. [33]) have taken into account that more than one mode of propagation may be involved, and that the speeds may differ. Others (e.g. Nivesrangsan et al. [34]) have taken this a stage further, reconstituting the AE time series at given locations in situations, such as engines, where multiple, temporally extended sources are involved.

2.1.1 Wave modes

AE waves are similar to sound waves propagated in the bulk of a fluid (such as air) but are more complex because solid media can resist shear forces [1].

It is sometimes convenient to consider AE as being carried in one or more idealised mode, which can be divided into three basic wave types; body waves, which propagate through the bulk of the solid material, surface waves, which travel along the surface of a solid material, and guided modes, such as flexural waves, which involve both surfaces and the bulk [35]. The waves can travel along different paths at different speeds, depending on the properties of the propagation medium and the surrounding media, which generally cannot be independently controlled in real structures [28].

2.1.1.1 Body waves

The most common AE body wave types are longitudinal waves and shear waves.

In an infinite medium, the particle motion in a longitudinal wave is parallel to the wave propagation direction and consists of localised compression and tension of the medium, Figure 2.2(a). Longitudinal waves are also called compression, dilatational, pressure, irrotational, primary or P-waves [2, 22]

The velocity of longitudinal waves (c_1) is frequency-independent and given by the following expression [1, 22]:

$$c_1 = \sqrt{\frac{\lambda' + 2\mu}{\rho}} \tag{2.2}$$

where:

λ' : Lame's constant $= \frac{E_y}{(1+\nu)(1-2\nu)}$

μ : Rigidity modules $= \frac{E_y}{2(1+\nu)}$

E_y : Young's modulus for material

ν : Poisson's ratio for material

ρ : Density of the material

In shear waves, the particle motion is perpendicular to the wave propagation direction, Figure 2.2(b). Shear waves are also called transverse, distortional, secondary or S-waves.

The velocity of shear waves (c_2) is also independent of frequency and is given by the following expression [22].

$$c_2 = \sqrt{\frac{\mu}{\rho}} \tag{2.3}$$

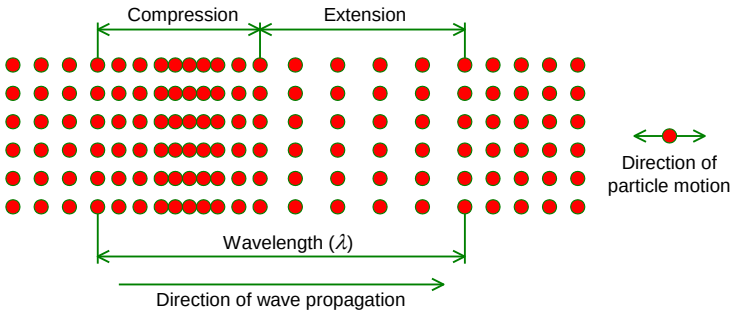

(a) Longitudinal wave

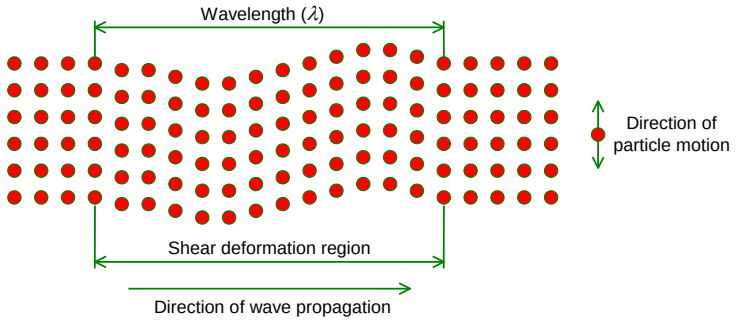

(b) Shear wave

Figure 2.2: AE wave types in infinite media: longitudinal wave and shear wave [34].

Once the velocity of a wave is known, its wavelength for a particular frequency can be calculated from the standard formula [22]:

$$\lambda = \frac{c}{f} \tag{2.4}$$

where:

c : Wave velocity (m/s)

f : Wave frequency (KHz)

λ : Wave length (mm)

The relative velocities of longitudinal waves and shear waves therefore depend only on Posisson's ratio and, in general:

$$c_2 \approx 0.6c_1 \qquad (2.5)$$

The simple behaviour of longitudinal and shear waves is widely exploited in ultrasonic NDT, where the type of wave injected can be controlled by the type of transducer and simple ray-tracing can be used to interrogate the body for defects. However, in AE applications, there is no control of the types of waves being generated or recorded, and generally no specific interest in locating internal reflectors.

2.1.1.2 Surface waves

Semi-infinite media, where there is a free surface, can also support a third wave type, where strain energy only travels along the surface of the material [21, 36]. Since AE sensors are surface mounted, it is common to assume that the AE energy is mostly carried in a surface wave for 2D source location [37]. Two types of surface waves can be recognised: Love waves and Rayleigh waves [1].

In Rayleigh waves, particles vibrate in an orbital fashion, individual particles moving in an elliptical path, in much the same way as particles in water waves, Figure 2.3 (a).

Love waves, propagate in a similar way to shear waves but strains only occur near the surface, with no vertical motion [1], Figure 2.3 (b). As these waves involve very high localised strains, they tend to be associated with very high energy generating events and damage to the structure in which they are propagated, such as in seismic waves [35].

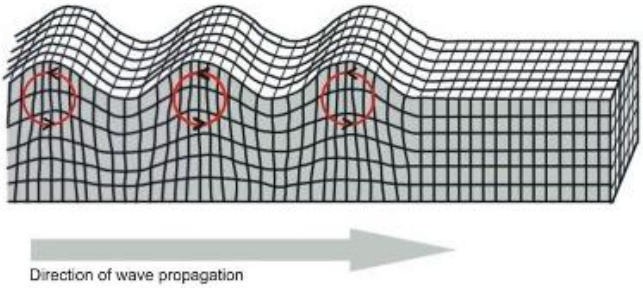

(a) Rayleigh wave

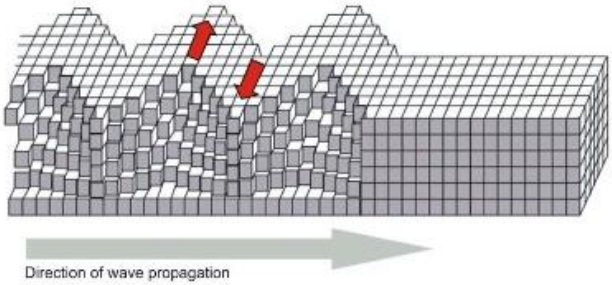

(b) Love wave

Figure 2.3: AE surface wave types in semi-infinite media: Rayleigh wave and Love wave [38]

Since surface waves spread out in only two dimensions (the horizontal plane) at lower frequencies than body waves, their amplitude falls off more slowly with distance travelled than body waves [35]. By the same token, surface waves have large amplitudes relative to the longitudinal and shear waves associated with a specific event [6]. Surface waves also propagate at a lower speed than shear waves and the approximate Rayleigh wave speed (c_r) can be estimated as [22]:

$$c_r \approx 0.92 c_2 \qquad (2.6)$$

2.1.1.3 Lamb waves

In an infinite medium bounded by two surfaces, such as a plate, wave propagation is more complicated due to interaction with the boundaries. When the wavelength is much smaller than the plate thickness, the wave propagates on the surface as a Rayleigh wave, and, as the plate becomes thinner the surface wave begins to interact with the bottom boundary producing guided modes called Lamb waves (plate waves) [2, 39].

Lamb waves can propagate in two possible types of mode; the symmetric (*S*) modes (extensional waves) and the asymmetric (*A*) modes (flexural waves) [40, 41] as illustrated in Figure 2.4. Some authors have suggested that the first arrival is an extensional mode and the second is a flexural mode. For an example, Holford and Carter [32] recognised two distinct Lamb wave modes in long structural steel girders, and suggested that the non-dispersive mode is essentially an extensional wave, which travels faster than the highly dispersive flexural mode. However, the extensional modes are not always faster than flexural, because both of the Lamb wave mode types can propagate at various speeds, which are dependent on both frequency and plate thickness, these values being represented in the form of a dispersion curve of velocity as a function of the frequency times plate thickness. For example, Figure 2.5 shows calculated dispersion curves for a steel plate of thickness 2.4 mm. For low values of frequency × thickness, there are only two Lamb wave modes (S_0, A_0), and the extensional mode is faster than the flexural mode, but eventually dips below the speed of the flexural mode. For high values of frequency × thickness, other Lamb wave modes (S_n, A_n) can be supported, although those modes (S_n, A_n) can travel faster than S_0 and A_0 modes, their amplitudes tend to be low and they are relatively unimportant in carrying AE energy [6]. In this work, AE is recorded in the frequency range between 100 and 350 kHz and the shaded area in Figure 2.5 covers this range of frequency with a plate thickness of 7 mm.

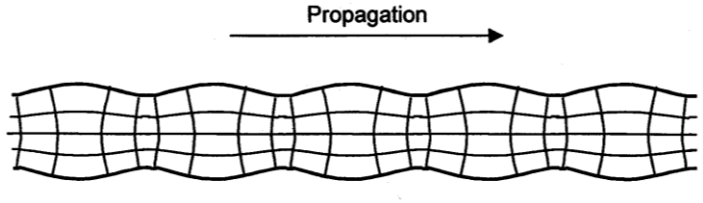

(a) Extensional wave

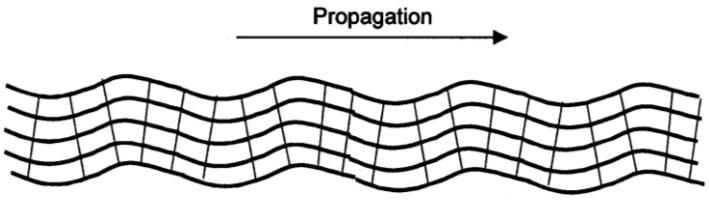

(b) Flexural wave

Figure 2.4 : Lamb wave types: extensional waves and flexural waves [34].

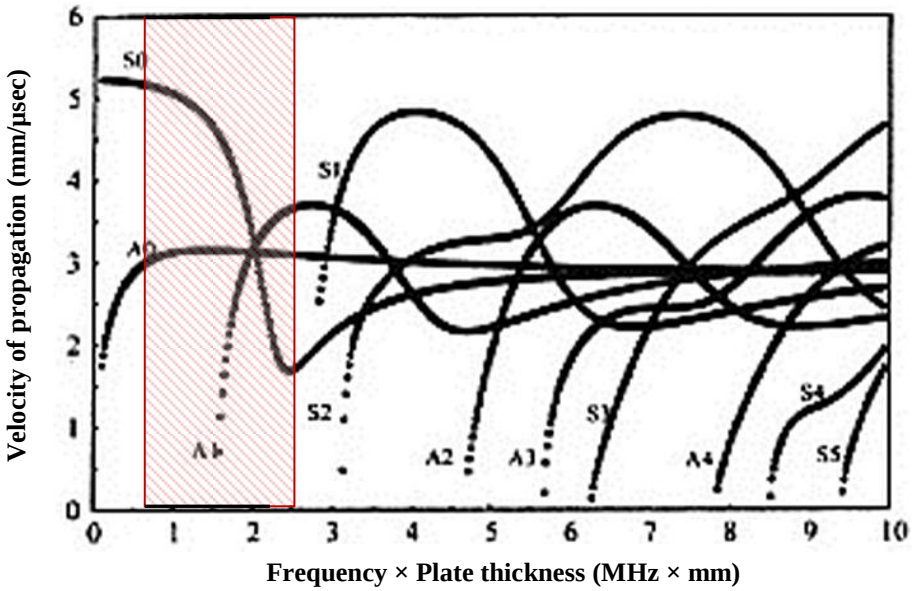

Figure 2.5: Dispersion curves for a steel plate; (*Sn)* symmetric Lamb waves; (*An)* asymmetric Lamb waves [42]

Generally, Lamb wave speeds (c_p) fall between those of longitudinal and shear waves. The average first Lamb wave disturbance propagates along a plate can be estimated as [2]:

$$c_p = c_2 \sqrt{\frac{2}{1-\nu}} \qquad (2.7)$$

Examples of wave speeds for longitudinal waves, shear waves, Rayleigh waves and Lamb waves (Flexural mode) in various solids can be seen in Table 2.1.

Materials	**Wave speed (m/sec)**			
	Longitudinal waves	**Shear waves**	**Rayleigh waves**	**Lamb waves**
Steel	5900	3200	3000	5100
Cast iron	5000	3000	2700	4700
Glass	5700	3400	3100	5300
Copper	4700	2300	2100	3800
Lead	2200	700	700	1200
Nickel	5600	3000	2800	4800
Brass	4400	2100	2000	3500
Aluminum	6300	3100	2900	5100

Table 2.1: AE wave speeds for various materials [2]

When a wave reaches an interface, some of the incident energy will be transmitted into the adjoining medium, some will be reflected, and some will propagate along the boundaries. Reflection, refraction and mode conversion can all occur when waves encounter boundaries

The reflection and refraction of waves depends on the angle of incidence and a material property known as the acoustic impedance (Z), defined as [2]:

$$Z = \rho \times c \tag{2.8}$$

where:

ρ : Material density (kg/m^3)

c : Wave speed (m/s)

The acoustic impedance can be used in some cases to determine the percentage of energy transmitted and reflected between two media [2]. For two materials of different acoustic impedance, Z_1 and Z_2, the percentage of energy reflected, E_r can be given by:

$$E_r = \frac{(Z_1 - Z_2)^2}{(Z_1 + Z_2)^2} \tag{2.9}$$

When the acoustic impedances of two media are well-matched ($Z_1 \approx Z_2$), the incident wave (V_1) is largely transmitted to the other medium (Figure 2.6 a). On the other hand, when the acoustic impedances are dissimilar ($Z_1 \gg Z_2$ or $Z_1 \ll Z_2$) the incident wave is mostly reflected (Figure 2.6 b). The acoustic impedances of typical materials of structural interest can be seen in Table 2.2.

However, the amount of actual energy reflected may be different than the theoretical calculated, as the energy may be dissipated at a boundary or in the material in several ways. Moreover the formula above refers only to a perfect boundary between two infinite media. It is difficult to obtain the actual proportion of reflected energy except by experiment [34].

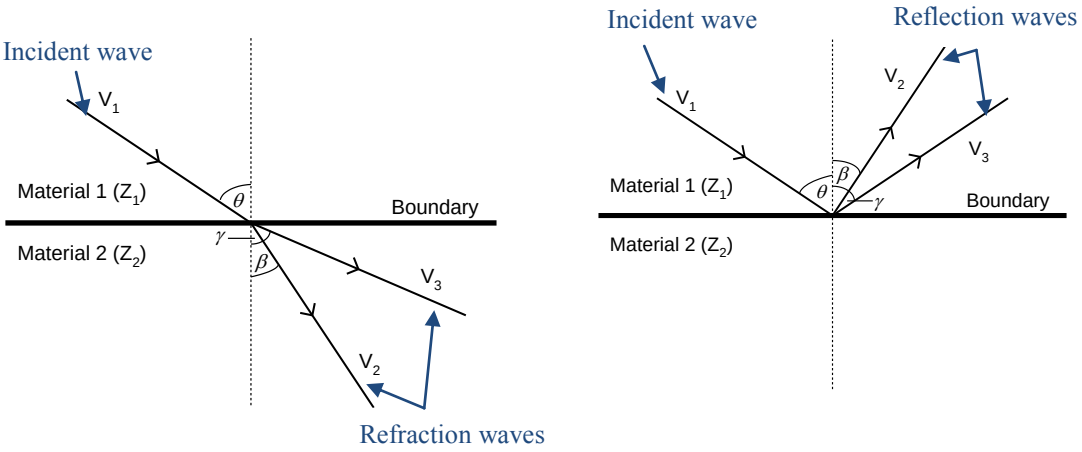

(a) Refraction **(b) Reflection**

Figure 2.6: Reflection, refraction and mode conversion of waves at boundaries.

Material	**Acoustic impedance, $Z(\mathbf{kg/m^2s})$**
Steel	46×10^6
Cast iron	36×10^6
Stainless steel	45.7×10^6
Air	4.3×10^2
Dry sand	2.6×10^5
Water	1.483×10^6
Clay	1.8×10^6
Glass	13.1×10^6
Resin	4.92×10^6

Table 2.2: Acoustic impedance of selected materials [43]

When waves are incident on a layer sandwiched between materials of different impedance, Figure 2.7, the problem can be treated using the impedance translation theorem [44], whereby the input impedance (Z_{input}) can be calculated from the loading impedance (Z_{load}) and the impedance (Z_0) of the layer itself as follows [43].

$$Z_{input} = Z_0 \frac{Z_{load} - iZ_0 tan(kd)}{Z_0 - iZ_{load} tan(kd)} \qquad (2.10)$$

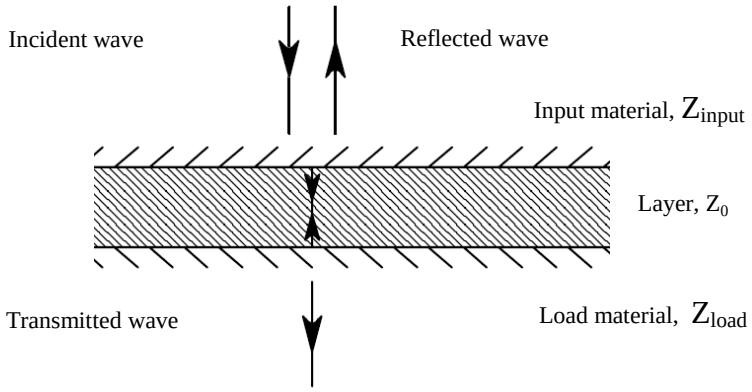

Figure 2.7: Schematic diagram of reflection and transmission through layered medium

In the particular case where the $Z_{input} = Z_{load} = Z$, the reflection and transmission coefficients are given by:

$$T = \frac{1}{\sqrt{\xi^2 \sin^2(k_v d) + 1}} \tag{2.11}$$

$$R = \frac{\xi^2 \sin^2(k_v d)}{\sqrt{\xi^2 \sin^2(k_v d) + 1}} \tag{2.12}$$

where ξ, is a measure of the impedance contrast between the layer impedance (Z_0) and the surrounding host material impedance (Z)

$$\xi = \frac{1}{2}\left|\frac{Z_0}{Z} - \frac{Z}{Z_0}\right| \tag{2.13}$$

Both longitudinal waves and shear waves are reflected or refracted when they impinge on a boundary. In the most general case, four separate waves are generated, a wave of each type is reflected, and a wave of each type is refracted. One reflected wave is of the same type and same angle as the incident and the second is of different type with an angle given by Snell's law [1]:

$$\frac{sin\theta}{V_1} = \frac{sin\beta}{V_2} = \frac{sin\gamma}{V_3} \qquad (2.14)$$

where:

θ, β, γ : propagation angles (°), as shown in Figure 2.6

V_1, V_2, V_3 : wave velocities (m/s)

Mode conversion can occur at a boundary where the acoustic impedances of the two media are different and the angle of incidence is not normal to the interface, leading, for example, to shear waves transforming to Rayleigh waves and vice versa [45].

The reflection coefficient for Rayleigh waves is much lower than for body waves. For example, Bremaecker et al. [46] found that only about 40% of the energy is preserved and the rest goes into body waves and Clement et al. [47] found that only 20 – 50% of the energy was preserved.

The refection coefficients for Lamb waves are more difficult to estimate because of the complex range of possible mode conversions. Several studies have measured and calculated the reflection coefficients for different Lamb modes [36, 48, 49], and, because the low order flexural mode (A_0) produces higher amplitudes than the extensional mode (S_0), flexural mode behaviour has become the most important mode in AE studies [2, 6]. Cho et al [49] investigated multi-mode reflection on a steel plate both experimentally and numerically at different frequencies. They found the incident energy to be transferred from the incident mode to other converted modes beyond a certain cut off frequency and to do so quite rapidly with increasing frequency up to a point where the incident mode reflection begins to increase again through reverse mode conversion. Figure 2.8 shows the flexural mode reflection behaviour as a function of frequency × thickness, in a range where the extensional mode S_0 reflection factor is close to zero. The factor for the flexural mode A_0 starts at unity then rapidly decreases to a minimum point (close to zero) then begins to increase again, most of the energy of the incident mode A_0 converting to A_1. The shaded area in Figure 2.8 covers the range of frequency used in the current work with a plate thickness of 7 mm.

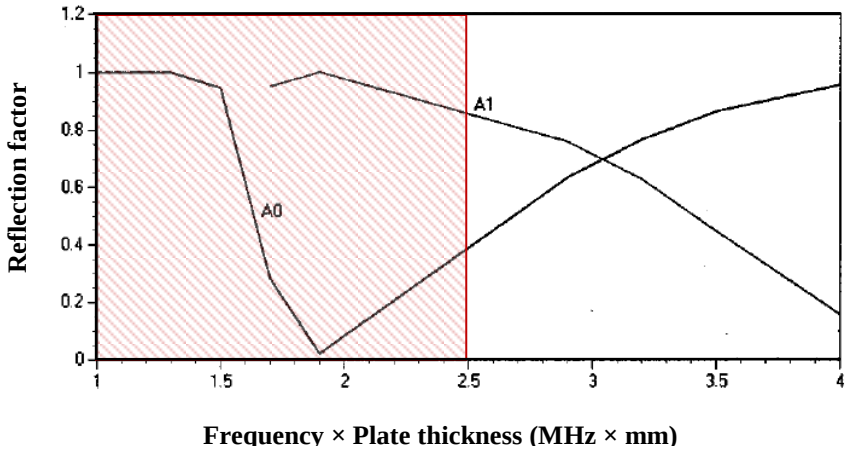

Figure 2.8: Variation of reflection factor on steel plate (from [49])

It is important to distinguish between wave modes to increase the accuracy of source location. However, most of the published wave mode analysis has been developed for plane waves, and so only applies reasonably at relatively large distances from the source. It is difficult to distinguish between wave modes at short source-sensor distances, due partly to the influence of curvature of the wavefront at short distances, but also because separation due to velocity differences is small [30].

A number of researchers have attempted to distinguish between wave modes in practical measurements, taking into account that the speeds may differ. For instance, Shehadeh et al. [33], working with a steel pipe 5.5 m long and with 7.35 mm wall thickness observed a change in shape of the waveform between relatively short distances from the source (Figure 2.9) and longer distances (Figure 2.10). They found a relatively low amplitude, fast wave (Wave 1) and a relatively high amplitude, slow wave (Wave 2). Whereas they avoided suggesting that Wave 1 is an extensional Lamb wave mode, and Wave 2 is a flexural wave, the characteristics of the two components were similar to those suggested as such by other researchers [30, 32]. On the other hand, Nivesrangsan [34] studied AE propagation in small diesel engines and found the effects of wave attenuation in cast iron, reflection, refraction and mode conversion in such a small structure with such a complex shape and number of interfaces to make it impracticable to separate components of AE wave propagation.

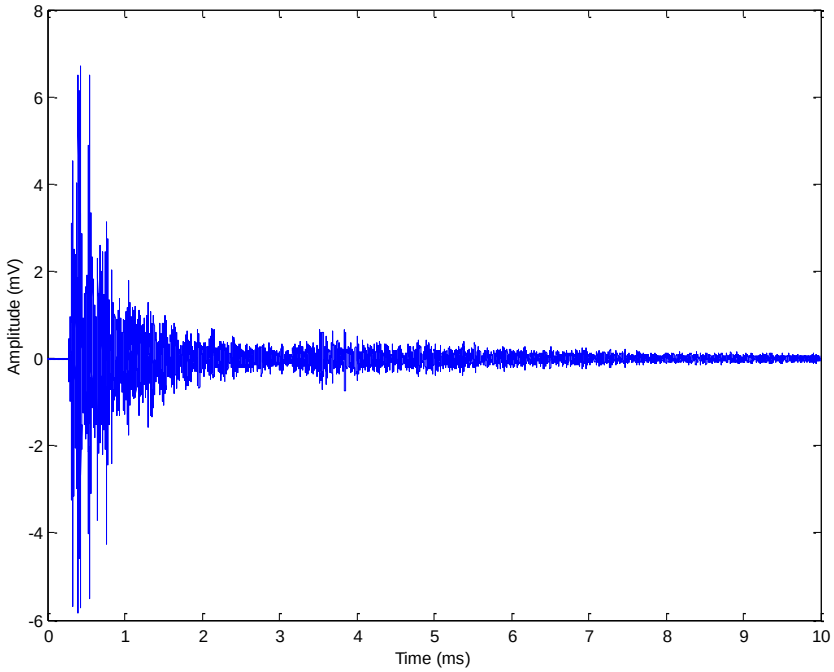

Figure 2.9: Typical raw AE signal acquired from long steel pipeline at 40 cm source -sensor distance (from Shehadeh et al.[28])

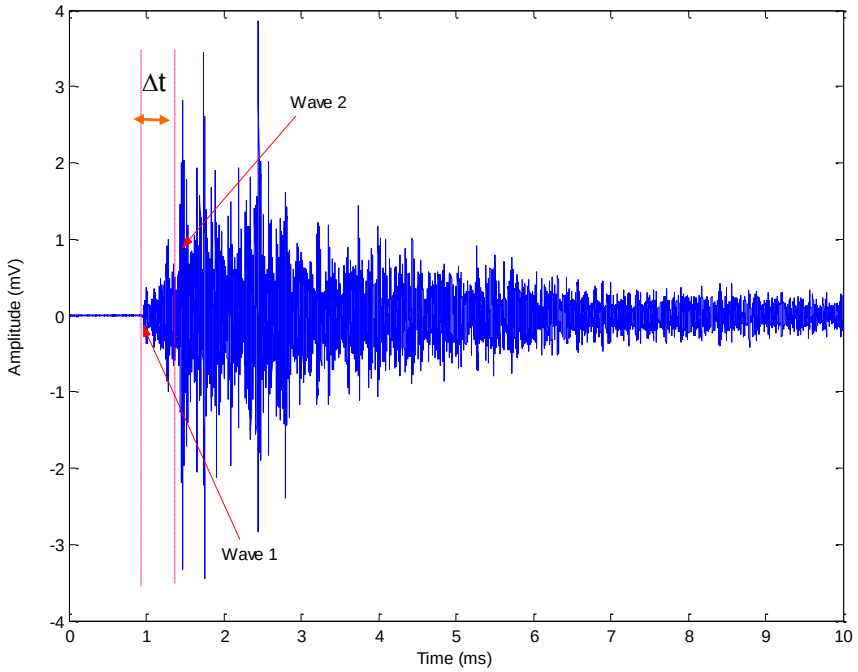

Figure 2.10: Typical raw AE signal acquired from long steel pipeline at 400 cm source -sensor distance (from Shehadeh et al. [28])

2.1.2 AE attenuation

As mentioned earlier AE waves can propagate in a number of different ways, which are generally beyond the control of the researcher. This means that an AE wave originating from a source is always distorted in some way when it reaches a sensor and careful calibration is required in order to ensure that source characteristics can be separated from characteristics that are introduced by the structure. This is particularly important when sources are extended temporally and are distributed spatially.

The amplitude of an AE signal detected by a sensor is considerably lower than the intensity that would have been observed in close proximity to the source, a phenomenon normally referred to as attenuation. To estimate and locate AE signals it is often valuable to know how much the signal is attenuated in the specimen, structure or material. If nothing else, a knowledge of attenuation is important to ensure that sensors can be placed appropriately on large or complex structures [28, 50, 51].

In most structures, there are four main mechanisms of attenuation [1, 2]; geometric attenuation, scattering and diffraction, internal friction (absorption) and attenuation from dispersion. Not all attenuation mechanisms are associated with energy loss, some involving no more than redistribution of energy in different modes.

2.1.2.1 Geometric attenuation

Geometric spreading effects are fundamental to wave propagation [6]. When AE waves are generated by a localised source in an infinite medium, the wave propagates as a spherical surface outward in all directions from the source. The geometric attenuation arises from the law of conservation of energy, under which the energy of the wavefront remains constant along the propagation path. Since the radius of this sphere is equal to the distance that the wave has travelled from the source, the amplitude of the wave, A, must decrease with increasing distance $(A \propto 1 / r)$. In plates, wave propagation can be considered to be two-dimensional, expanding as a cylindrical wavefront. In this case, the wave amplitude (A) decreases inversely as the square root of the propagation

distance, r, $\left(A \propto \sqrt{1 / r}\right)$ in order to maintain a constant energy at the wavefront. This approach does not, of course, consider any of the possible effects of reflection.

In theory, for a structure that is large in all dimensions (infinite half-space), an AE wave generated on the surface would simply spread and continue to attenuate. However, in realistic structures, the boundaries force the AE wave to remain in a restricted space such that attenuation from beam spreading is limited. In a small, well-defined structure such as a rod, the attenuation from geometric beam spreading is minimal and stress waves may travel great distances [52-54].

2.1.2.2 Attenuation from scattering, diffraction and interference

Scattering and diffraction, the second major cause of attenuation, occurs when AE waves propagate through media with complex boundaries and discontinuities such as holes, inclusions, cavities, cracks and slots. Scattering occurs when waves propagate through a finite void or inclusion while diffraction occurs when waves encounter a sharp edge such as a crack. These effects can generally cause a decrease in the amplitude of waves with distance, depending on the type and distribution of scattering centres [55]. There may also be interference effects, since, when a wave propagates through any type of medium, individual particles along its path are subject to periodic displacement [43]. In simple terms, when two waves of the same wavelength meet while travelling in the same medium, they will reinforce each other or cancel each other depending upon whether or not they are in phase, or out of phase, this phenomenon being knows as interference [56, 57], Figure 2.11.

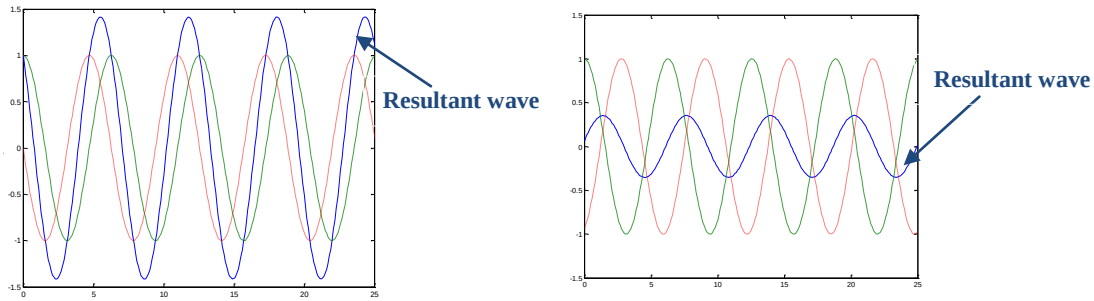

a) Constructive interference. **b) Destructive interference.**

Figure 2.11: Schematic representation of interference (continuous line) for (a) constructive interference and (b) destructive interference

Constructive interference occurs where the interacting waves have a displacement in the same direction, i.e. their phase difference is between $-\frac{\pi}{2}$ and $\frac{\pi}{2}$, whereas destructive interference occurs where the interacting waves have a displacement in the opposite direction, i.e. their phase difference is between $\frac{\pi}{2}$ and $\frac{3\pi}{2}$.

The source of interference is often reflected waves and both the path difference and the nature of the reflection affect whether interference between reflected and incident waves will be constructive or destructive. When a sound wave in a solid encounters a phase boundary of low acoustic impedance (e.g air interface), the reflected wave will reverse, i.e. a phase change of π. On the other hand, when a wave hits a boundary with a medium of higher acoustic impedance there is no phase change upon reflection [58, 59].

2.1.2.3 Internal friction

When a solid material is strained, some of the mechanical energy associated with particle motion is converted to thermal energy due to the presence of internal forces which tend to resist the motion of the material [60]. This dissipation of energy is normally referred to as internal friction, material damping or damping capacity [1, 61]. The internal friction of liquids and gases can be treated analytically, but the behaviour of solids is much more complex and varies considerably with the nature of the solid [62, 63].

The effect of internal friction on AE can be described by an exponential decrease of amplitude with distance, giving much steeper attenuation close to the source [30]. Internal friction is normally measured using cyclic loading (for example using a torsion pendulum) or by setting up a free vibration in a specimen, and can be quantified by either of the two dimensionless quantities, specific damping capacity or logarithmic decrement [63]. The first of these is defined as the ratio of energy lost per loading cycle due to friction to the total strain energy of the material at its maximum strained position in the cycle, this ratio is called the specific loss or specific damping capacity, ψ [64]:

$$\psi = \Delta W / W \qquad (2.15)$$

where:

ΔW : The energy dissipated in taking a specimen through stress cycle

W : The elastic energy stored in the specimen when the strain is maximum

The second quantifier is the logarithmic decrement, δ, of a specimen of the material undergoing free vibration. The earliest measurements used this method, e.g. Hopkinson et al. [65], Fopple et al. [64] and Hudson et al. [63], all of which showed the internal friction of steel to be very low (between 0.0001 to 0.0004) compared to other materials. Table 2.3 shows a selection of values of internal friction for various materials measured at frequencies between 0.3 and 10 cycles per second.

Material	**Internal friction**
Steel	1.7×10^{-3}
Copper	3.2×10^{-3}
Glass	9.5×10^{-3}
Wood	27×10^{-3}

Table 2.3: Measured internal friction for various materials [1]

2.1.2.4 Dispersion

Dispersion is a phenomenon affecting waves in which the frequency depends on speed [59]. AE waves exhibit dispersion when propagating in structures in which the wavelength is comparable to one or more dimensions of the structure [2]. It also can occur due to scattering and mode conversion at inhomogeneities such as fibre reinforcement in composites [66, 67].

Surgeon et al. [68] and Holford et al. [32] recognized the fact that Lamb waves are dispersive, the wave velocity being related to the ratio of the wavelength and plate thickness [69]. Prosser [70] found that flexural waves in graphite/epoxy composite plate attenuated more than extensional waves and attributed this greater attenuation to dispersion.

Dispersion is not generally a dominant AE attenuation mechanism [71], but can affect Lamb waves in particular. Rayleigh waves show no dispersion in homogeneous elastic solids, but become dispersive when the wave velocity or density vary with depth [72]. Pollock et al. [30] have suggested that geometric spreading dominates the attenuation for all kinds of structures over small distance and, for long distances, internal friction dominates [32]. Shehadeh et al. [73] studied the attenuation in a long steel pipeline and found it depend on the external and internal environments.

2.1.2.5 Measuring attenuation

Normally, the effects of attenuation must be measured on the actual structure of interest [55] and this can be performed using a simulated AE source [74]. The most widely used simulated AE source is the breaking of a pencil lead, with either a 0.3 or 0.5 mm diameter, 2H or HB lead, being pressed against a structural member, ASTM standard [75]. When the pencil lead is pressed against the material, it creates a small, local deformation that is suddenly relieved when the lead breaks (step unload). Using this method, simulated AE sources can be created at various sites on a structure to determine the best possible position for the placement of sensors and to make sure that all areas of interest are within the detection range of the sensors.

The attenuation curve is an important aid in determining sensor placement for the specific application. In many acoustic emission applications, the goal of the inspection is to monitor the entire structure. In this case, it is important that all parts of the structure are within the detection range of at least one sensor. In global monitoring tests of this kind, the test procedure typically specifies how the attenuation curve can be used to determine acceptable maximum sensor spacing [6].

In addition, if the distance between source and sensor is only a few wavelengths, the arrival of low amplitude waves can be obscured by lack of separation of higher amplitude waves. The region near to the source, known as, the near-field (Fresnel) zone [76], poses particular challenges due to the multiple wave reflections causing complex constructive and destructive interference and waves travelling at different speeds which have had less opportunity to separate from each other [77, 78]. When analyzing the elastic wave fields for AE applications, most of the techniques neglect near-field effects to simplify the algorithms [79]. However, some researchers, for instance Finck [76], found that the effect of the near field cannot generally be neglected if the distance from the source is less than approximately 3.5 wavelengths of the longitudinal wave for a tensile crack source or less than 6 wavelengths of the longitudinal wave for a double couple source.

Holford and Carter [32], have measured attenuation on long structural steel I-beams and found it to be sharpest in the near-field zone at around 10 dB over 0.5 m (20 dB/m) and lower over longer source-sensor distances (1 dB/m). They attributed the higher attenuation in the near-field zone to geometric spreading, and that in the far-field zone to absorption or internal frication. Graham and Alers [80] have measured attenuation on plates and a pressure vessel including various materials such as steel, aluminium and alumina ceramic using a white noise generator as an AE source. They found the attenuation on the large pressure vessel to follow the expected form for geometrical spreading and to vary with the inverse of distance from the source in the near field zone. In the far-field zone, the attenuation is caused by absorption with a limited amount of dispersion and the AE attenuation in steel tubes has been described using a simple power law [2]:

$$A = A_o x^{\alpha_l} \quad (2.16)$$

where:

A : Maximum measured signal amplitude (V) at a receiver sensor at distance x from the source

A_o : Maximum reference amplitude (V) at the source position

α_l : Loss coefficient

and it was found that the loss coefficient, α, for steel tube of 150 mm diameter was 8.1 dB/m for the near field and 1.9 dB/m for the far field.

Also, Nivesrangsan et al. [50], during a study of a small diesel engine, noticed that the variability in total energy of an AE signal becomes much greater at sensor positions close to the source, which explained by the sensor being within a zone where multiply reflected waves travelling at different speeds will have had less opportunity to separate from each other.

AE wave attenuation is often measured empirically [2, 61] using a logarithmic scale (decibel), where the relative amplitude (A_r) is given by:

$$A_r = 20 \times \log_{10}\left(\frac{A}{A_o}\right) \quad (2.17)$$

The amplitudes can be measured in volts provided that the amplifiers are consistently calibrated. Then, wave attenuation can be determined from a plot of the relative amplitude versus distance and can be expressed as decibels per unit distance [2], determined by:

$$\alpha_t = \frac{20}{D} \times \log_{10}\left(\frac{A_1}{A_2}\right) = \frac{A_r}{D} \quad (2.18)$$

where:

α_t : Attenuation coefficient (dB/m)

A_1 : Amplitude of the signal at Sensor 1 (V)

A_2 : Amplitude of the signal at Sensor 2 (V)

D : Distance between Sensor 1 and Sensor 2 (m).

When comparing attenuation between different structures, it is usually convenient to derive a single parameter from measurements and, for this purpose, it is possible to consider each wave to be a representative of the front of a one-dimensional simple harmonic wave travelling through an absorptive, homogenous medium. In this case, the displacement, γ, of any particle can be described as a function of time, *t*, and position, *x*, along the direction of travel by [2]:

$$\gamma = Ae^{-\alpha_l x}e^{j(k_v x-\omega t)} \tag{2.19}$$

where:

A : Amplitude of the wave at $x = 0$

α_l : Loss coefficient

k_v : Wave vector

ω : Angular frequency

For a single wavefront, where the phase can be ignored, this equation leads to a simple absorption law [81]:

$$E_x = E_o e^{-kx} \tag{2.20}$$

where:

E_x : AE energy at distance *x* from the source ($V^2.sec$)

E_o : AE energy of the source ($V^2.sec$)

k : Attenuation factor (m^{-1})

x : Source-sensor distance (m).

Some investigators have cast Equation 2.20 in linear form, which is useful in determining attenuation from structural measurements:

$$\ln(E_x) = \ln(E_0 e^{-kx}) = \ln(E_0) + \ln(e^{-kx}) \tag{2.21}$$

$$\ln\left(\frac{E_x}{E_0}\right) = -kx \tag{2.22}$$

Figure 2.12 shows an example of a measured AE attenuation in a small diesel engine compared with a strip of cast iron, where the maximum distance between the source and sensor was 40 cm [34]. As can be seen, there is a significant difference in the attenuation between the two structures, which can be conveniently summarised in the factor, *k*.

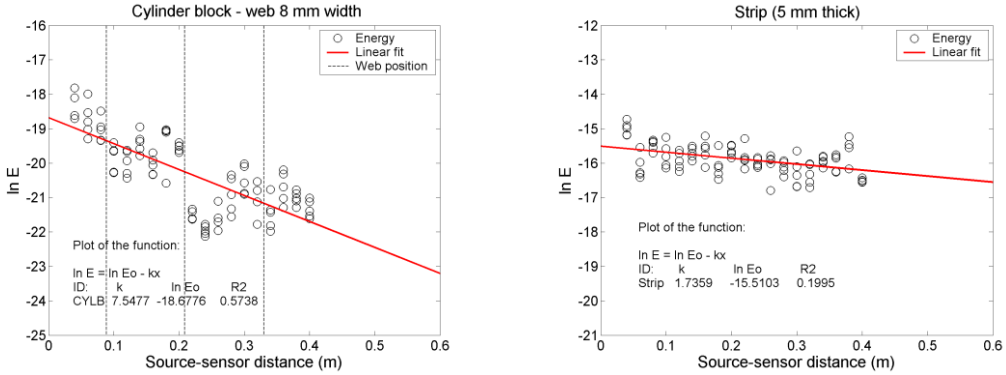

(a) Cylinder block – web 8 mm width **(b) Strip - 5 mm thick**

Figure 2.12: Examples of attenuation characteristics on two cast iron structures (from Nivesrangsan et al. [34]).

2.1.3 Acoustic emission modelling

Computer simulation is widely use in NDT applications, offering benefits in: demonstrating system performance, studying how a system works, improving diagnosis, data reconstruction, allowing virtual testing, and improving probe design [82]. Computer simulation has been used for many of the common NDT methods including ultrasonic, radiography and eddy current [11], although it has only relatively recently been used for AE.

The earliest studies provided analyses of the AE waveform in elastodynamic propagation models to find analytical solutions from a set of parameters and initial conditions [2, 83-87]. Most of the time, methods like the Finite Element Method (FEM) and the Boundary Element Method (BEM) [7, 88-90] provide accurate results at single frequencies.

Although such methods have been enhanced over the years, they tend to be complex in implementation [7], burdensome computationally [2], can need very long computer

processing times depending on the number of the numerical cells [9], and, in some cases, are restricted to low frequencies, because the computational load grows rapidly as a function of the frequency [7, 8, 91].

To take just one example, Dietzhausen et al. [87] investigated numerically the dynamic behaviour of a composite bar in tension undergoing fibre failure using a finite element programme (ABAQUS) to show the connection between the deformation and the characteristics of the AE time signal. The time signals, the surface displacements, and the surface velocities were determined numerically and compared with experimental results. The results of the simulation showed agreement with the experiments only to a certain degree.

2.2 Ray tracing techniques

Ray tracing offers an efficient alternative to solving the wave equation for the propagation of sound in structures or other media. By the same token, it can also be used to describe AE wave propagation and can offer a simpler alternative to modelling the elasto-dynamic wave field. When used in conjunction with a solid model, ray tracing becomes a simple geometric technique and offers the easiest to use and simplest modelling tool available for wave simulation in 2D or 3D [92].

Ray-tracing with solid models has its origin in computer graphics, where it has been used to generate realistic images by calculating the level and colour of the light at each point on an object, a process known as rendering. This is achieved by tracing the path of the light through pixels in an image plane as they interact with the optical surface and has the capability of simulating a wide variety of optical effects, such as reflection, refraction and scattering [92, 93] Figure 2.13 illustrates schematically how ray-tracing can be used to render a simple scene.

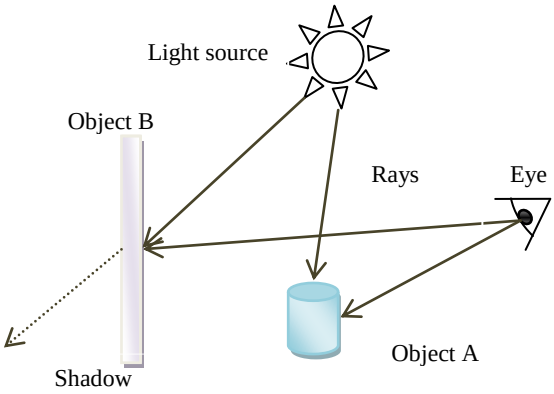

Figure 2.13: Schematic diagram of the principles of rendering by ray tracing.

The term ‘ray-tracing’ is often associated with images such as those produced in computer graphics, but, in acoustics, it is more usually taken to mean the production of diagrams illustrating ray paths and not the images produced when rays return to a transducer [94]. Figure 2.14 shows some example ray-traced images with multiple reflections. It works by assuming that the wave particles can be modelled as a large number of rays, and that there exists some distance, possibly very small, over which such a ray is locally straight.

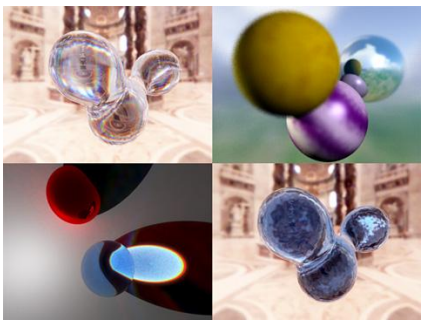

Figure 2.14: Sample ray-traced images [95].

A typical ray tracing algorithm will advance the ray over an appropriate short distance, and then use a local derivative (e.g Snell's law) to calculate the ray's new direction. From this location, a new ray is sent out and the process is repeated until a complete path is generated. The basis of ray tracing in computer graphics is that an observer sees

a point on a surface as a result of the interaction of the surface at that point with rays emanating from elsewhere in the scene [93].

When the simulation is carried on inside a solid object consisting of a uniform medium, rays are always assumed to travel in straight lines between intersections with objects. The ray can be tested for intersection with faces and edges of the solid at each step, adjusting the ray's direction if an intersection is found [92] and the ray may be reflected or transmitted with refraction. Following basic physics, the reflected ray lies in the plane of the incident, which plane also contains the normal of the incident ray and the angles of incidence and reflection are equal, the reflected ray being on the other side of the normal from the incident ray [10]. Similarly, the refracted ray also lies in the plane of the incident and the angle of refraction depends on the angle of incidence so that the ratio $sin\theta_1/sin\theta_2$ is constant. The value of this ratio depends on the two media involved, and also on the wavelength [10, 94].

2.2.1 Ray tracing applications

An early example of ray tracing in geometric optics is Rene Descartes' treatise, published in 1637, in which he used the laws of reflection and refraction to trace through a spherical drop of water and so explain the shape of a rainbow. It was not until thirty years later when Issac Newton discovered that white light contains light of all wavelengths that the colour of the rainbow was explained [10]. Early examples of ray tracing in computer graphics include those where rays were traced backwards from the eye to the object for the generation of shadows. At this time, researchers were severely limited by hardware capabilities and were forced to simulate shading by varying densities of parallel straight lines, or other patterns [10].

In the 1960s, computers become more powerful and researchers could tackle more demanding numerical problems at which point ray tracing started to be used to calculate the paths of waves or particles through systems with regions of varying propagation velocity.

Ray-tracing developments have been largely driven by graphics applications, producing accurate simulations of optical effects in image realisation, such as shadows, mirrors in 3D animations and video games [96, 97]. The term is now used for a range of engineering techniques, especially in wave simulation, where ray tracing means the production of ray diagrams, as opposed to the production of images, for applications such as solar radiation [98], indoor radio wave penetration between rooms through walls, ceilings and floors, taking into account the effect of different materials [99, 100], in petroleum engineering [9] and in X-ray tomography [101].

The propagation sound wave can be thought of as a wave spreading out like ripples on a pond or it may be thought of as a number of rays, Figure 2.15, where each ray is representative of part of the wavefront, rather than the complete wave field.

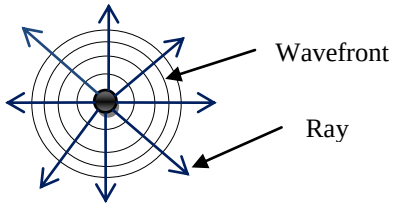

Figure 2.15: Sound waves and ray representation.

Generally, the sound wave equation can be solved in one of two ways. Numerically using wave theory, where the wave propagation is represented in terms of characteristic functions called normal modes [91]. An alternative approach is to use ray theory where the ray is postulated as a wavefront, on which the phase or time function of the solution is constant, and rays are projected from the source [102]. Like its analogue in optics, an acoustic ray solution presents a picture of the propagation in the form of a ray diagram. Such a geometrical model is well suited to sound of high frequency or short wavelength because the radius of curvature of the ray and the pressure amplitude change appreciably over distances of one wavelength [102]. The standard ray method has several advantages, e.g computational efficiency and possibility of simulating wave propagation [103]. However, it does not describe phenomena like interference and diffraction, which require consideration of the phase of the wave [10] .

Table 2.4 compares the relative advantages of the two approaches, although perhaps the most persuasive advantage of ray theory in the context of AE analysis is that it allows the solution to concentrate on some particular points on the surface of the medium (where the sensors are), thus avoiding solving the entire temporal-spatial wave field.

Wave theory	Ray theory
Gives a formally complete solution	Does not handle interference and diffraction problems
Solution is difficult to interpret	Rays are easily drawn. Sound distribution is easily visualised.
Requires a computer program, except in limiting cases when analytic answers exist, and presents computational difficulties in all but simplest boundary conditions.	Rays can be drawn by hand using Snell's law. However, a computer program is normally used.
Valid at all frequencies but practically is useful for low frequencies (few modes)	Valid for high frequencies.

Table 2.4: Comparison of wave and ray theory [102].

2.2.1.1 Application of ray tracing to seismic waves

Seismic waves are elastic disturbances generated by sudden movements of the Earth's crust. These waves propagate spherically outwards from the source, a result of transient stress imbalances in the rock which vibrate the ground [104]. Seismic techniques are similar to AE techniques in that they address the same concept but at a different scale [35], and seismic wave modes are conventionally divided into two types; body waves and surface waves.

Ray tracing helps to compute paths through a geophysical model, following them back to known earthquake locations and improves the interpretation of seismic measurements [105]. Also, it can be applied to different stages of oil exploration and production to

study the seismic wave propagation in layered media [9]. In early applications, the focus was on calculating seismic ray paths, wavefronts, and travel times, referred to as kinematic ray tracing. Such numerical approaches have been used for a long time in seismology and have given a number of valuable results [103]. Cerveny et al. [106] developed the numerical technique of dynamic ray tracing, which yields wavefront curvature and geometric spreading attributes. This numerical approach is referred as the standard ray method. One of the weaknesses of this technique applied to interpreting geological structures stems from the fact that calculating along each ray is quite independent of neighbouring rays, a single ray can see only the elastic properties and interface behaviour exactly along the ray path [103].

Another approach, known as two-point ray tracing has developed in two ways: The shooting method, obtains the ray path from source to receiver by adjusting the shooting ray direction and tracing it until it hits sufficiently close to the receiver. Each ray accepted by the iteration process corresponds to an event, i.e. an arrival with specific travel time [103, 107]. The bending method fixes the two ends and taking some initial estimate of the ray path, modifies it until it satisfies a minimum travel-time criterion [108].

2.2.1.2 Application of ray tracing to acoustic waves

Ray tracing of acoustic waves has three distinct types of application, depending on whether the propagation medium is air, water or a solid.

Sound waves travel in air as longitudinal pressure waves, and can only propagate in a compressible medium. The speed of sound in air is around 340m/s, but this varies with pressure and moisture content. Krokstad et al. [109] presented a computerized ray tracing technique in a simple geometric model to aid in understanding acoustical response in rooms, by tracing sound rays from a source following the law of reflection. Schroeder et al. [110] developed a more realistic prediction of the sound rays by tracing the sound in a large number of rays emitted in all directions from a source point, where each ray carries a certain amount of energy, reduced after each reflection

according to the absorption coefficient of the surface. Rindel et al. [8] also developed a room acoustical model using ray-tracing and showed that the scattering of sound from surfaces is very important in such simulations, suggesting the need for better information about the scattering properties of materials and structures. Wu et al, [111] and Hodgson et al. [112] developed a model for predicting the noise levels inside power stations using ray tracing techniques, and modelled an existing nuclear power generating station.

Ray tracing has also been used in ocean acoustics to calculate the path of sound through the ocean over very large distances, including reflections and refractions off the ocean surface and bottom. In the beginning, this was a geometric investigation using shooting rays. As acoustic wave velocity varies with depth, the water medium was divided into a large number horizontal layers each layer being considered as a homogenous medium with Snell's Law being applied to the boundaries between each of the layers, leading to curved ray paths [91, 113].

Most of the research on the propagation of acoustic waves in solids has been applied to ultrasonic waves for NDT where the user controls the wave type. Several software tools have been created using ray tracing for various applications in ultrasonics [114-116]. For example, the French Atomic Energy Commission (CEA) has developed a package called CIVA [117] which simulates the ultrasonic transducer as a distribution of particle velocity sources over the emitting surface, each source radiating a hemispherical wavelet. To model the propagation and the various reflections/refractions encountered by the wavelet, the pencil method [118] considers the evolution of a pencil of rays emitted by the source and centred on the geometrical path linking the source and the point of interest. Finally, the signal received by the probe is obtained by summing up all the scattered contributions. The amplitude of one contribution is proportional to the probe sensitivity at the location of the source. The model assumes transmission-reception reciprocity for the transducers so that this sensitivity is directly deduced from the transmitted field computation [119]. For dealing with the interaction boundaries and calibration reflectors (side holes, cracks) the high frequency Kirchhoff approximation was used, which assumes that the surface can be replaced at each point by its tangent plane.

2.2.1.3 Ray tracing in AE

AE wave propagation is more complex and complicated than in ultrasonics [2], even in a simple homogeneous structure like a plate. This is because AE waves are generated by relatively uncontrolled events in comparison with the waves used in ultrasonic NDT, where the waves are generated in a controlled way using ultrasonic transducers, which also act as sensors.

The essential theory of AE ray tracing was set out in 1981 in a series of articles by Ceranoglu and Pao [120-122]. They provided a numerical method of calculating the transient displacement response at any point on the surface for five different types of point source at the surface or interior of a plate. However, due to the limited hardware capability at the time, only small numbers of rays were considered, with few reflections.

Reverse ray tracing has also been suggested as a means of improving the accuracy of AE source location using an azimuth AE sensor which allows the direction, as well as the time of arrival, of a disturbance to be recorded [123]. The azimuth AE sensor [124] combines several sensor elements in one package with an electronic circuit to analyze the effect of an arriving AE wave on each element to determine the azimuth approach angle of the wave. Although little detail is provided, reverse ray tracing was reportedly achieved by using a parallel processing arrangement and provided an accurate measurement of the true location of AE sources on, for example, aircraft panels.

Giordano et al. [125] have used ray theory to model AE propagation in a finite linearly viscoelastic plate. A microfailure event was represented as a point source and ray tracing was used to develop the physical model of wave propagation. The model involved three main assumptions. Firstly, the rays were considered to represent plane waves, there was total reflection of longitudinal waves on the boundary surface, and the reflected rays were of the same type with the same angle. Secondly, the propagation medium was assumed to follow a Maxwell viscoelastic model, although the overall formulation holds for a generic linearly viscoelastic medium. Thirdly, the AE point source was modelled as a simple strain energy release due to a failure event. The predicted AE amplitudes showed close agreement with experimental results.

Schubert [14] has developed a new technique termed 'acoustic emission tomography', which provides an image of AE source and wave speed distribution in a region surrounded by sensors. Although he demonstrates this technique on simulated data for straight, non-reflected waves, Schubert recognises that the addition of ray-tracing algorithms to the algebraic reconstruction tomographic technique could further improve accuracy [14, 126, 127]. The technique consists of two main components; the localisation algorithm and the tomography algorithm. The localisation algorithm, is based on a simple straight ray model, in which the travel time of a wave from the source to the sensor is given by their relative geometrical distance divided by the fixed wave speed of the matrix medium. The acoustic travel time under different angles of incidence is obtained in a way similar to the well-known procedures of X-ray tomography. The transmission data are then passed to a tomography algorithm which constructs an image of local changes of a certain physical quantity inside the structure under test.

Wilcox et al. [128] suggested a modular framework to predict the received time domain waveform at a sensor as a result of an AE event. Their "QAE-Forward" framework is based around guided waves (such as Lamb Waves) and is an implementation of ray theory in which the change in the generated wave is described as a series of transfer functions, whose product $H(\omega)$ is the Fourier Transform of the received time-domain signal. The elements (modules) cover excitation, propagation and detection, with the possibility to introduce noise. The entire framework can be described by:

$$H(\omega) = \sum \left[E(\omega) \times P(\omega) \times B \times A(\omega) \times S(\omega) \prod_{reflection} R(\omega) \prod_{Trnsmission} T(\omega) \right] \qquad (2.23)$$

where the summation is taken over all rays and modes, E describes the excitation of the relevant modes by the source, P describes the propagation, B the beam spreading, A the "material attenuation and leakage into the surroundings", S the sensor sensitivity, R the reflection coefficient(s) and T the transmission coefficients of any media which the waves cross on their way to the sensor. Wilcox et al. point out that, once all of the

transfer functions have been calculated or measured, the time series of the recorded signal can be obtained by performing an inverse Fourier Transform on $H(\omega)$.

Scholey et al. [13], employed the above QAE-Forward framework to characterise the propagation of Lamb waves in aluminium alloy and carbon fibre reinforced plastic plates. They measured the phase velocities of the Lamb wave modes using a laser vibrometer, and found good agreement with those estimated using a global matrix method. They also made attenuation measurements on both plates using the same arrangement. Using these measured transfer functions (P and A), they were then able to make reasonable predictions of Lamb wave propagation in both the aluminium alloy and CFRP plates. In later work, Scholey et al. used this phase velocity and attenuation information for aluminium alloy and CFRP plates to estimate the performance of different AE configurations in terms of their "hit success" and source location error.

The geometrical application of ray tracing in conjunction with a solid model was first demonstrated by Lim et al. [7]. These authors simulated rays representing bulk AE waves ("internal rays") with solid models of various simple cast iron shapes and a diesel engine cylinder block to predict attenuation, defined as the loss of AE energy from source to sensor. They compared the attenuation curves from a simulated array of AE sensors with experimental data measured by Nivesrangsan et al. [50]. The simulations showed reasonable agreement in relative magnitude with measured attenuation curves for the various shapes, showing the potential of this approach. Later, Shehadeh et al. [73] used the same implementation to elucidate the effects of external and internal environments on the propagation of AE in pipelines, again comparing reasonably well with experimental observations. However, in both cases, the implementation was severely limited in its resolution and the current research was motivated by the opportunity to develop ray tracing in conjunction with solid modelling to give more stable and higher accuracy representations of experimental observations.

2.3 Identification of thesis topic

The literature reviewed in this chapter has shown that a complete generic description of AE propagation from source to sensors has yet to be developed. The ray-tracing approach has a distinct advantage over the solution of the entire wave field, in that it permits a focus only on the parts of the wavefront that interact with the sensor or sensors.

Other researchers have used ray-tracing to address the problem of AE propagation, most notably the work of Cernoglu and Pao and of Wilcox and co-workers. However, the approach taken here, in which ray-tracing has been combined with solid modelling has the potential to be very useful for small or complex structures in which multiple modes and reflections can make more analytical approaches rather unwieldy. The work aims to build on that put forward by Lim et al., and its application to experimental measurements by Nivesrangsan et al. and Shehadeh et al. The initial challenge is to improve the accuracy and resolution of the ray-tracing / solid-modelling approach. Once solved, the following challenges are in implementing different types of wave and incorporating a number of different physical representations, including reflection coefficients, material absorption and phase delay.

CHAPTER 3: SIMULATION PROGRAMME

This chapter explains the approach taken to designing the simulation programme and describes its essential elements. The programme was developed to predict AE attenuation in solids using 3D ray tracing, and it was decided at the outset to take a computer graphics approach in which a solid model of the object was used and the rays were made to interact with this model according to a set of rules that could be defined by the user. Since the programme was to be developed in conjunction with a set of experiments, it was essential that it was flexible, allowing a range of shapes, sizes, materials and surrounding environments to be used with easy incorporation of a range of physical rules.

3.1 Programme elements

The main target of the simulation programme is to predict the transmission path length of the AE rays using 3D solid modelling and ray tracing techniques, and to determine possible transmission paths from source to sensor arrays in order that the effect of different attenuation phenomena on the overall energy loss can be assessed.

As mentioned in the previous chapter, the programme implemented uses the same internal ray simulation methodology developed by Lim et al [7]. The programme was entirely re-written, and the following new functionality:

- Increase robustness greatly and to increase number of internal rays that can fired from around 4,000 to around 60,000 (depending on the number of reflections) to give more stable results for the internal rays. The major challenge here was to introduce convergence criteria which allowed a stable simulation result to be obtained without excessive computational.

- Introduce two different ray prediction functions, surface rays and combined rays the major challenge in introducing surface rays was to ensure that the generated rays travelled exactly along the surface of the solid model and to deal with the conditions at the edges.

- Introduce additional attenuation realism, allowing the effects of geometrical spreading, reflection and material absorption to be independently varied for internal and surface rays. The main challenge here was to introduce a sufficient (but not excessive) range of simulation parameters which could be adjusted to obtain fitting between the simulation and the measurements.

These functions are all discussed in detail in the following.

The simulation used a range of parameters, some parameters were varied to optimise performance while others were varied to modify the simulation physically. Table 3.1 shows the different user defined input parameters with a brief explanation for each.

Element	Description
Source position:	Source position on the model, in Cartesian coordinates (x,y,z)
Sensor position:	Sensor centre position on the model, in Cartesian coordinates
Ray type:	Choice from surface, internal or combined rays.
Internal velocity:	Internal ray velocity, depending on material (m/s)
Surface velocity:	Surface ray velocity, depending on the material (m/s)
Internal resolution:	Represented by the number of longitude and latitude lines whose intersection points determine the direction of the internal ray vectors
Surface resolution:	Represented by the number of surface rays vectors over 360°
Sensor Diameter:	Surface sensor diameter (mm)
Time:	Time variable representing the real simulation time. Defines the maximum ray length
Maximum ray reflections:	The number of ray reflections allowed before a rays is terminated
Sensor locker:	Toggle to allow simulation to be on one sensor or more. When the locker is on, the user needs to define the sensor step and sensor range
Sensor step:	The distance between each sensor in an array
Sensor range:	The total distance between the first and last sensor in an array
Upper reflection coefficient:	The reflection coefficient at the upper surface, depending on the upper surrounding medium
Lower reflection coefficient:	The reflection coefficient of lower surface, depending on the lower surrounding medium
Damping coefficient:	Coefficient of material absorption

Table 3.1: Programme input parameters.

The simulation distinguished between two types of rays called surface rays and internal rays, to indicate if the rays propagate parallel to the surface or not. These rays represent generalised wavefronts, and are not associated with specific AE modes, although the interpretation of the results in terms of known AE propagation modes is discussed later.

3.2 Programme implementation

The programme was implemented in C++ compiled via Visual Studio 2005. The 3D solid model was realised in ACIS version 18-SP3 and rendered by HOOPS version 16.20. The graphical user interface (GUI) was built using Microsoft Foundation Classes (MFC) 2005. To provide the user with a visual output, the simulation was able to display how the AE energy is transmitted over the 3D solid model. The implementation also had the capability to deal with different shapes (e.g. block, pipe), and to load different 3D CAD files in standard format to give flexibility for the user to draw the model using any CAD software.

3.3 Programme methodology

Figure 3.1 shows the overall programme flow chart, which can be summarised in five main steps, seen in Figure 3.2: Source Generation, Filtering, Path Generation, Sensor Representation and Data Recording. The following sections describe each of these steps in turn.

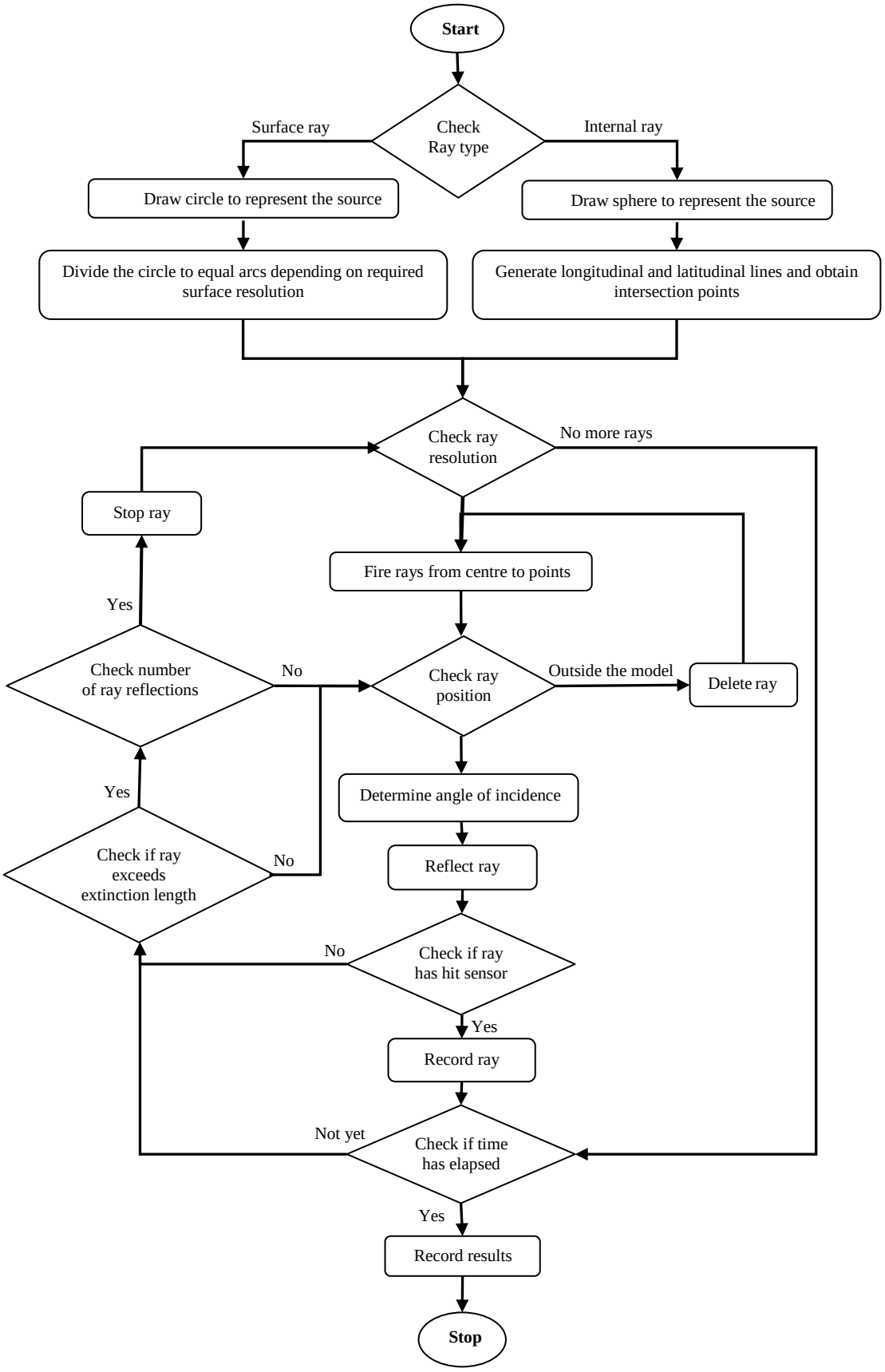

Figure 3.1: Programme flow chart.

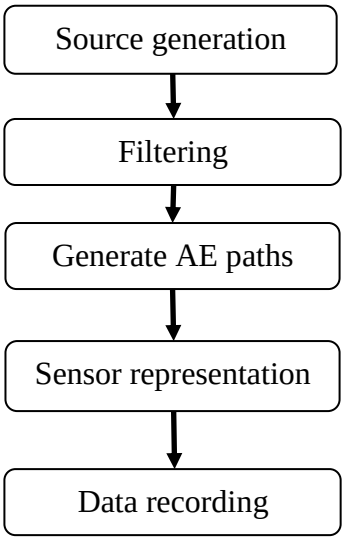

Figure 3.2: Simplified programme flow chart.

3.3.1 Source generation

The ray type (i.e. surface or internal) and resolution chosen as input defines the algorithm to be executed. For internal rays, the ray resolution determines the number of longitude and latitude lines over a fixed spherical source radius of 5 mm. The centre of this sphere is the source position and the default ray resolution is 125, which generates 125 longitude and 125 latitude lines. The intersections between these lines generates 15,625 positions on the surface of the sphere and the vectors between the centre and these points define the direction of each ray, Figure 3.3.

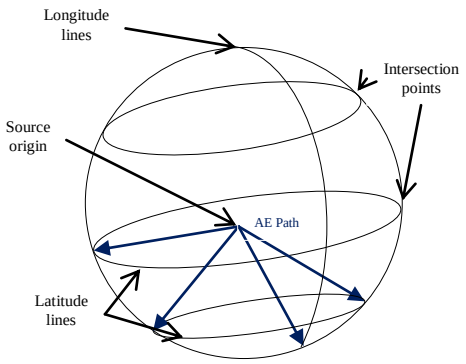

Figure 3.3: Internal ray source generation.

The surface ray resolution simply determines the number of segments the source circle is divided into. The ray vectors are again generated from the centre to appropriate points on the circumference of the source circle as shown in Figure 3.4.

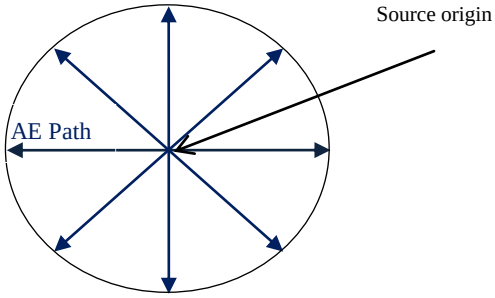

Figure 3.4: Surface ray source generation.

3.3.2 Filtering

Because the simulation relies on the interaction between the ray vectors and the surfaces or the edge of the solid model of the structure, it is necessary to ensure that each vector goes into the model or on the surface of the model. If not, the ray is terminated at the outset.

According to the user-defined parameter, internal or surface rays are kept in the system memory and the rest are terminated. This step is essential for internal rays to avoid wasting computational time, the program classifying the ray vectors into two categories; internal rays which can travel inside the model, and outside rays, terminated rays, as shown in Figure 3.5. For surface rays, this step can be skipped as all the rays generated are on the model surface.

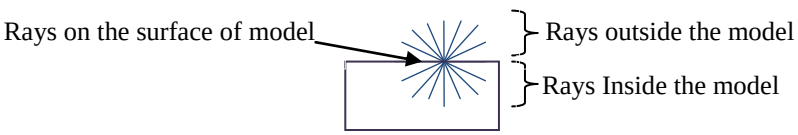

Figure 3.5: Ray filtration.

3.3.3 Path generation

The validated rays are then used to create the ray paths using functions that propagate the ray and detect when it encounters a surface or an edge, or hits the sensor. When the internal rays encounter a surface, or when surface rays encounter an edge, the ray is reflected such that the angle of incidence equals the angle of reflection, as shown in Figure 3.6. The number of reflection is associated with that ray and recorded with its total length.

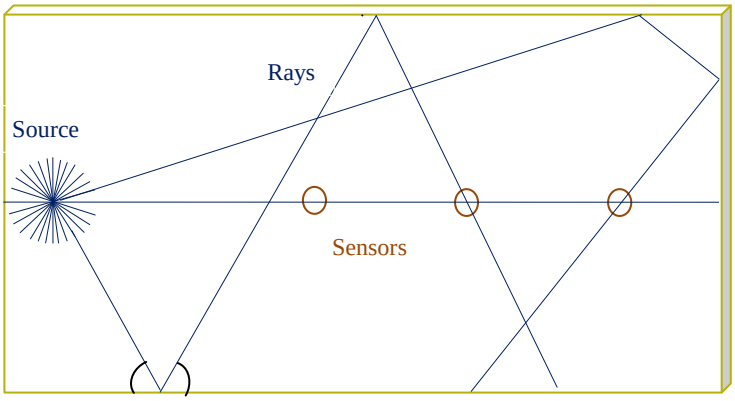

Figure 3.6: Schematic diagram of surface ray generation and path generation.

For rays that hit curved surface or edge, the programme calculates the tangent at the intersection point to obtain the angles of incidence and reflection, as seen in Figure 3.7.

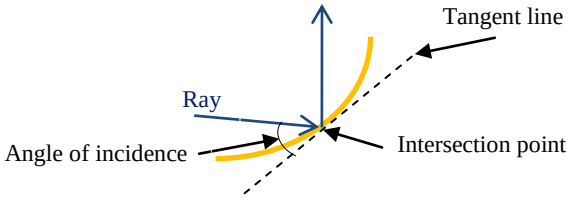

Figure 3.7: Schematic diagram for reflection at non-planer surface.

To avoid the need for spiral rays, cylindrical objects are modelled as flat plates, Figure 3.8. In this case, spiral rays are obtained by reflection of the rays at the edge of the plate without loss in energy. As a proxy for re-entry of the ray at the opposite edge of the plate.

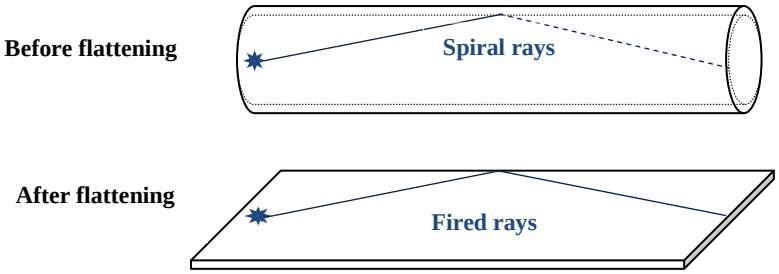

Figure 3.8: Schematic diagram for simulating spiral surface rays.

Validated rays are terminated when they hit the sensor, exceed the permissible number of reflections, or when they have travelled the maximum allowed total distance within the solid or on its surface dictated by the speed of the wave and the time.

3.3.4 Sensor representation

A spherical face is constructed using the sensor diameter (user input) and intersected with the selected surface model on which the sensor is positioned. The resulting intersection circle between the model surface and the sphere creates a circle representing the AE sensor surface contact. The default sensor diameter was set to 10 mm. If multiple sensor positions are required, the sensor generating function creates an array that holds each position, as shown in Figure 3.9.

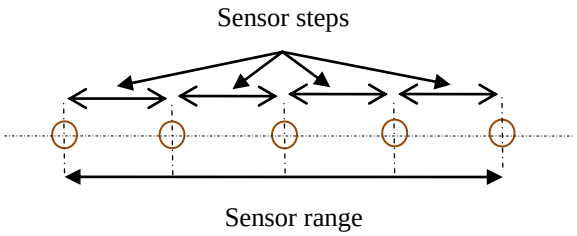

Figure 3.9: Sensor representation.

3.3.5 Data recording

The accuracy of simulation depends quite heavily on the (real) time for which the simulation is run and also the resolution of the rays, which, in turn, significantly affects the computational time. Accordingly, the GUI was designed to allow the user to change and visualise various parameters of the simulation, as shown in Figures 3.10, 3.11 and 3.12, in order to perform a feasibility study on the trade-off between resolution and computational time. After running a simulation, it was also possible to view the traces of the rays both locally (Figure 3.13) and globally (Figure 3.14).

The algorithm records two different types of data during the simulation. First, one record is kept for each ray fired, including the total number of times it is reflected from a surface (or edge, in the case of surface rays), the total distance it travels and the proportion of its original energy which remains at the end of the simulation period. Second, a record is also kept for each sensor position during a simulation, recording the distance between the source and the sensor, the number of rays fired after filtering, N_f, and the number of the rays that hit the sensor, $N_{h,}$. Appendix B shows an example of the programme output.

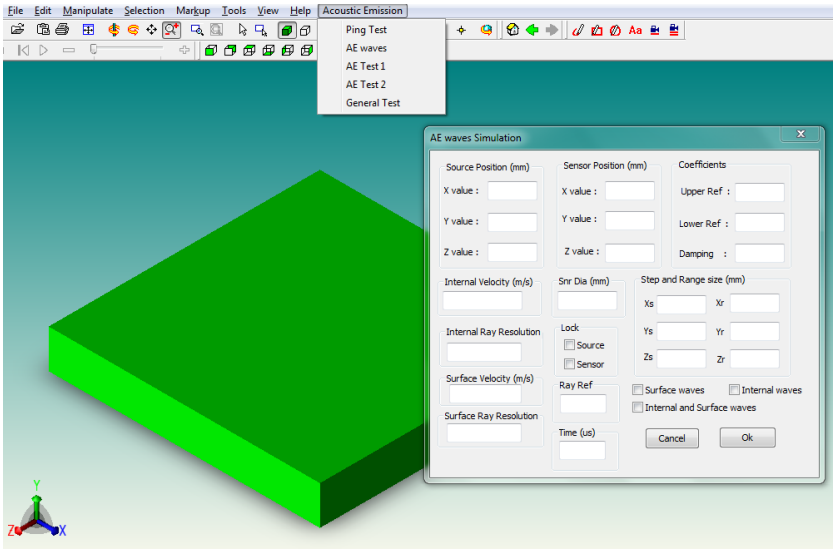

Figure 3.10: Graphical user interface with block solid model opened.

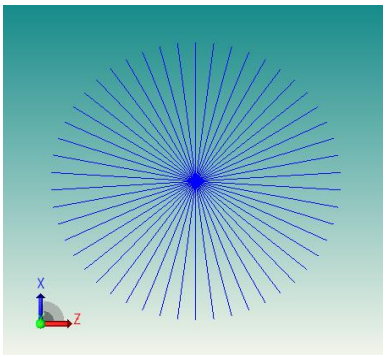

Figure 3.11: Surface source ray generation (2D) visualization.

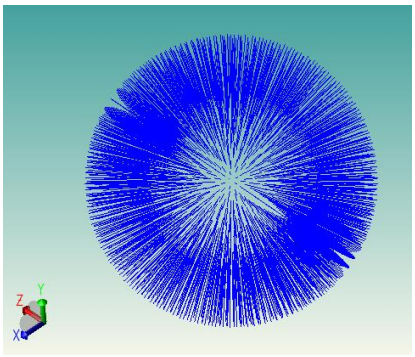

Figure 3.12: Internal source ray generation (3D) visualization.

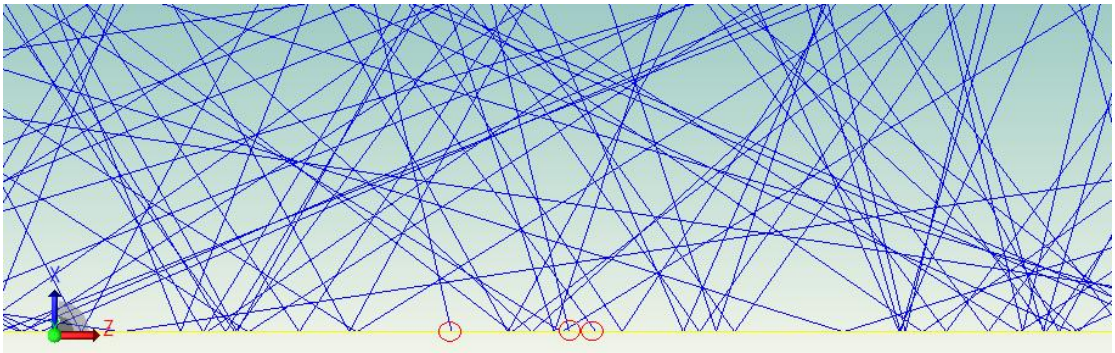

Figure 3.13: 2D AE ray path section visualization.

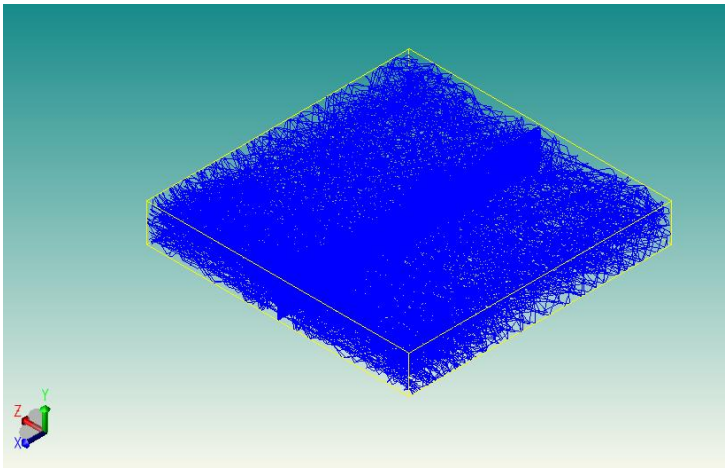

Figure 3.14: AE ray path 3D visualization.

3.4 Programme calculations

To enable the simulation to converge to a solution which resembles the practical measurements, it was first necessary to find a common way of describing the attenuation curves. Since the AE must travel from the source to the sensor, the ability to detect a given source decreases with distance between the source and the transducer [2, 7, 21, 22]. AE Attenuation can result from a range of processes, such as scattering, spreading, absorption and dispersion. As an AE wave propagates from its origin, the most significant initial reduction in amplitude is due to geometrical expansion of the wavefront [2], although, in small objects, reflection and interference between reflected waves can obscure much of the attenuation effect. Various authors use various functions of source-sensor distance to describe their measured attenuation, and this work follows those (e.g [11]) who have taken the pragmatic approach of using a simple absorption law form (whilst recognising that the physical processes involved are not uniquely absorption):

$$E(x) = E_o e^{-kx} \qquad (2.20)$$

where $E(x)$ is the recorded energy of the AE wave a distance x from the source and k is an effective attenuation coefficient. This allows the measured and simulated attenuations to be described by a single coefficient and to be referenced to a source energy, E_0. Using a reproducible source of fixed energy, such as a pencil-lead break, therefore allows the value of k to be determined experimentally by calculating the energy from the recorded signal at a given member of an array [21].

For obtaining the simulated energy, it is possible to consider each ray to be a representative of the front of a one-dimensional simple harmonic wave travelling through an absorptive, homogenous medium. In this case, the displacement, γ, of any particle can be described as a function of time, *t*, and position, *x*, along the direction of travel by [2, 21]:

$$\gamma = Ae^{-\alpha_l x} e^{j(k_v x - \omega t)} \tag{2.19}$$

where:

A : is the amplitude of the wave at $x = 0$

α_l : is the loss coefficient

k_v : is the wave vector

ω : is the angular frequency

Squaring the displacement leads to the energy [56]. Thus, the overall AE energy arriving at a virtual sensor can be taken as the sum of the energies of each ray which hits it, and the effect of resolution can be accounted by expressing this as a proportion of the number of rays fired.

$$\frac{E}{E_0} = \frac{1}{N_f}\left[\sum_{j=1}^{N_h}\left(e^{-\alpha x_j} \times {R_U}^{n_{Uj}} \times {R_L}^{n_{Lj}} \times e^{i(\phi)}\right)\right] \times \left[\sum_{j=1}^{N_h}\left(e^{-\alpha x_j} \times {R_U}^{n_U j} \times {R_L}^{n_{Lj}} \times e^{i(\phi)}\right)\right]^* \tag{3.1}$$

where:

$\frac{E}{E_0}$: proportion of the original energy arriving at the sensor

N_f : number of rays fired

N_h : number of rays hitting the sensor

x_j : distance travelled by ray *j*

α : Internal material friction

n_{Uj} : number of times ray *j* hit the upper surface

n_{Lj} : number of times ray *j* hit the lower surface

R_U : upper reflection coefficient (proportion of energy reflected when a ray encounters the upper face of the solid model)

R_L : lower reflection coefficient (proportion of energy reflected when a ray encounters the lower face of the solid model)

ϕ : Phase shift

As the programme contains many elements that can have an effect on the simulation result, simulations were run in two phases: In the first phase, only the effect of beam spreading was considered (i.e the energy arriving at the sensor was obtained by the proportion of rays hitting the sensor). In this phase, it was possible to examine how the simulation results converge and the trade-off between resolution and accuracy. In the second phase, simulations more closely represented the physical effects of interface environments, phase and absorption. These two simulation phases are to referred herein after as "geometric simulation" and "physical simulation".

3.4.1 Geometric simulation

In order to focus on the first order effects of shape and on the ratio of surface to body waves likely to be contributing to the measured energy, a number of simplifying assumptions were initially made in calculating the simulated energy. First, it was assumed that the AE wave is a simple harmonic wave, either propagating at the speed of Longitudinal waves, or at the speed of Rayleigh waves. Secondly, it was assumed that

there is 100% reflection at edges and faces, i.e. $R_L = R_U = 1$. Thirdly, it was assumed that the path differences are large enough that the phase differences are evenly distributed between zero and 2π, so that the effect of phase, including phase changes on reflection, affect all summations equally. Finally, to focus on the effects of geometry, it was assumed that there is no material absorption, i.e. that $\alpha = 0$. Very long path-lengths (and long simulation times) are avoided in this simulation by using an extinction criterion, which is a time after which a ray will be terminated if it has not hit a sensor.

Given the above simplifications, (E/E_0) recorded by the simulated sensor can be taken to be proportional to the proportion of the rays fired which hit the sensor, i.e. the hit ratio (N_h/N_f). Thus, the effective attenuation coefficient for the geometrical simulation (k') can be obtained from the hit ratios of a simulated array of sensors at distances x from the simulated source:

$$\ln\left(\frac{N_h}{N_f}\right) = \ln\left(\frac{E}{E_o}\right) = -k'x \qquad (3.2)$$

At this stage there are three main factors affecting the simulation predictions; ray resolution (number of fired rays), ray extinction time maximum allowed (ray length) and number of allowed reflections. These factors were adjusted in a systematic way for both internal and surface rays to give stable results to compare with the experiments.

3.4.2 Physical prediction

The physical simulation introduced additional factors, which can be used to calculate the remaining energy from a fired source on arrival at surface sensor. These are material absorption, interference and losses of reflection.

3.4.2.1 Superposition effect

Some rays arriving at the sensor will reinforce each other and some will attenuate each other depending on their phase difference. In order to focus on the effect of the superposition on the prediction result, it was initially assumed that there is 100% reflection at edges and faces ($R_L = R_U = 1$) and no internal friction ($\alpha = 0$).

The phase (ϕ) can be written in terms of three components, the wave vector (k_v) only, the propagation time (t) and the number of phase reversals ($n_j\pi$), because, when sound waves in solids strike low acoustic impedance boundaries (e.g air), the phase will reverse [58, 59]. The three components are summarized in equation 3.3.

$$\phi = k_v x_j + \omega t + n_j \pi \tag{3.3}$$

where:

ω	:	angular frequency
x_j	:	distance travelled by ray *j*
n_j	:	Number of hits by ray *j*
k_v	:	wave vector or wave number, $k_v = 2\pi/\lambda$, (rad/sec)
λ	:	wavelength
t	:	propagation wave time (sec), $t = x_j \,/\, v$
v	:	wave speed

3.4.2.2 Reflection coefficient

The reflection coefficients (proportion of incident energy reflected) for the internal rays at the upper surface R_U and lower surface R_L depend on the relative acoustic impedances of the two media, Z_1 and Z_2. This was calculated using the simplified equation [2]:

$$R = \frac{(Z_1 - Z_2)^2}{(Z_1 + Z_2)^2} \times 100 \tag{2.9}$$

The reflection coefficient for surface rays is much lower for body waves. When hits an edge only 20 – 40% of the energy is reflected and the rest goes into body waves, Rayleigh waves [46, 47]. Thus for the simulation a fixed refection coefficient (R = 0.4) was used.

The phase effect and internal material friction were initially neglected in the simulation to study the effect of the reflection coefficient separately.

$$\frac{E}{E_0} = \sum_{j=1}^{N_h} (e^{-\alpha x_j} \times {R_U}^{n_{Uj}} \times {R_L}^{n_{Lj}}) \tag{3.4}$$

3.4.2.3 Internal material friction

Internal material friction involves a range of physical effects that convert strain energy into heat [60]. As mentioned in Chapter 2, this has been measured for number of materials and the results were used in the simulation.

As before, the phase effect and reflection coefficient were initially neglected in the simulation to study the effect of the internal material friction separately

$$\frac{E}{E_0} = \sum_{j=1}^{N_h} e^{-\alpha x_j} \tag{3.5}$$

CHAPTER 4: APPARATUS AND EXPERIMENTAL PROCEDURE

This chapter describes the experimental apparatus, materials and methods that were used to obtain practical attenuation measurements to help develop the ray-tracing model. The chapter is divided into three parts. The first part describes the requirements, features and specifications of the AE monitoring apparatus and the signal processing techniques that were used for all experiments. The second part describes the calibration of the AE sensors and the third part outlines the experimental procedures. Three series of experiments were carried out with the following objectives:

- to study the effect of size and shape of the structure on attenuation in a variety of small steel blocks
- to study the effect of changing the environment on one face of the small steel blocks
- to study attenuation in a series of larger, but simple, structures of more practical interest with different external and internal environments.

4.1 Apparatus

Figure 4.1 shows schematically a typical AE acquisition system and experimental set-up as used in this work. The system generally comprised a test object (here shown as a solid block), simulated sources (pencil lead [75]), an array of AE sensors with their associated preamplifiers, a signal conditioning unit, a data acquisition card, and a computer with software for controlling the acquisition and storage of data. The equivalent actual set-up is shown in Figure 4.2.

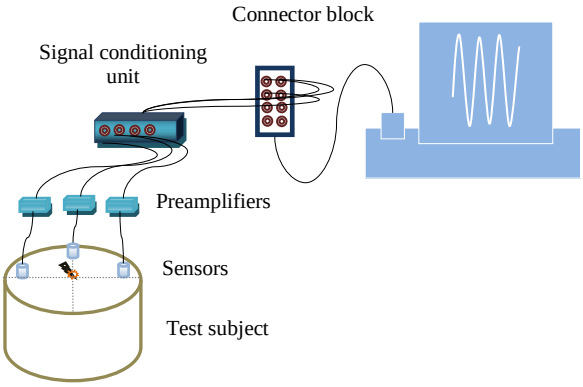

Figure 4.1: Schematic of typical AE system setup

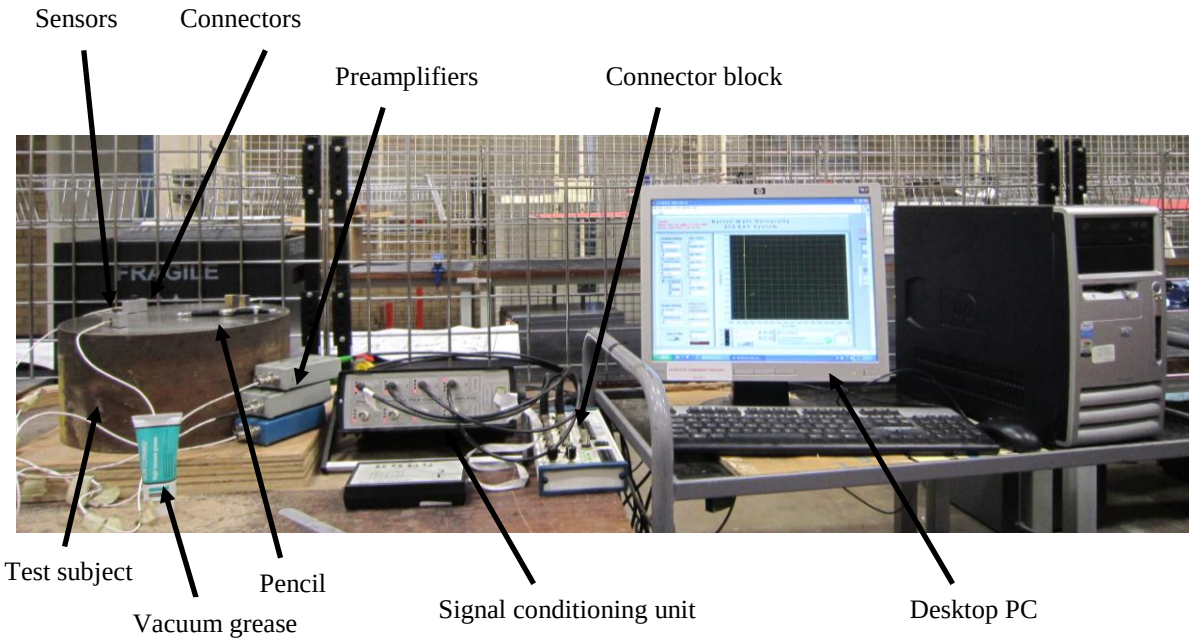

Figure 4.2: Actual AE system set-up equivalent to Figure 4.1

4.1.1 Simulated AE source

All experiments used a commercial mechanical pencil and an in-house machined guide ring to generate simulated AE sources, the so-called Hsu-Nielsen source. To improve the reproducibility of the generated AE, a modified guide ring (Nielsen shoe) as originally suggested by Higo and Inaba [75] was used, as shown in Figure 4.3. The source was compliant with ASTM standard (E976–99) which recommends that the

pencil lead should be of a fixed type (0.5 or 0.3 mm diameter, 2H or HB pencil lead) with a projecting length of 2-3 mm and, accordingly, a 0.5 mm 2H lead was used to generate all the simulated AE sources. For reproducibility and repeat tests, the lead was broken under the same conditions, at the same position on the test surface, using the same angle and the same orientation of the pencil, as far as could be judged visually.

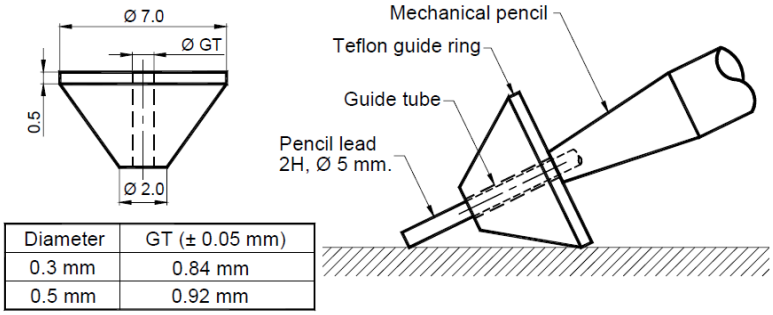

Diameter	GT (± 0.05 mm)
0.3 mm	0.84 mm
0.5 mm	0.92 mm

Figure 4.3: Drawing and dimensions of guide rings and pencil.

4.1.2 AE sensors and coupling

Three commercial "broadband" AE sensors of type Micro-80D (Physical Acoustics, PAC) as pictured in Figure 4.4 were used. These sensors are based on lead zirconate titanate (PZT), are omni-directional and produce a relatively flat but resonant frequency response between 175 and 1000 kHz, over an operating temperature range from -65 to $+177^{0}$C. The sensors are 10 mm in diameter and 12 mm high and were held onto the test object surface using an in-house designed magnetic clamp, or duct tape in some cases. In order to obtain good transmission of the AE from the test object to the sensor, the surface was kept smooth and clean and silicone vacuum grease was used as couplant to fill any gaps caused by surface roughness and to eliminate any air gaps which might otherwise impair AE transmission. The sensitivity of the sensor at each position was checked using a simulated source by breaking a pencil lead close to it, against an expected signal amplitude of around 4-5 volts using the fixed amplifier settings. Calibration certificates for the sensors used in this work are reproduced in Appendix A.

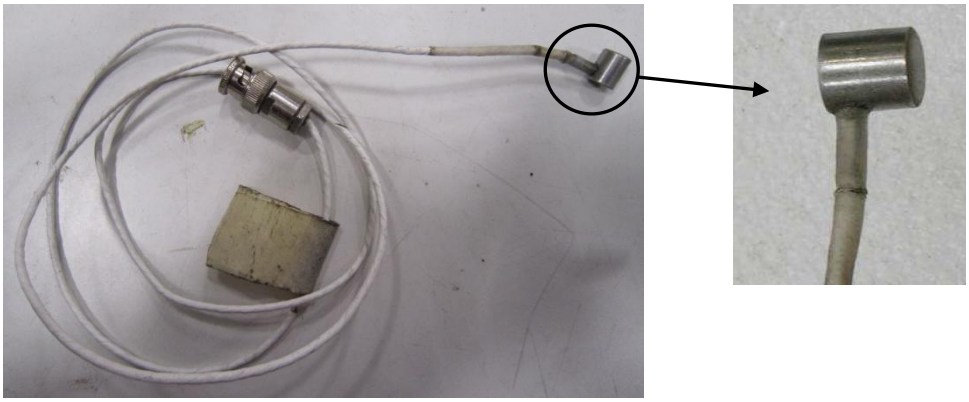

Figure 4.4: PAC Micro-80D broad band sensor.

4.1.3 Preamplifiers

Preamplifiers were used to amplify the AE signal from the Micro-80D sensor to a level which can be comfortably transmitted by a short length of coaxial (BNC) cable and converted by an Analogue to Digital Converter (ADC).

In this work two preamplifier models were used, both models from Physical Acoustics Corporation (PAC 2/4/6 and PAC 1220), shown in Figure 4.5. Model 2/4/6 had a switchable 20/40/60 dB gain, and PAC 1220 had a switchable 40/60 dB gain, and both had internal band pass filters from 0.1-1.2 MHz. The preamplifiers were powered by a + 28 V (0.2A) power supply and used a single BNC connection for both power and signal.

All of the data acquired in this work were in raw format with the preamplifier gain set at either 40dB or 60dB, more often the lower. Each experiment was done with a fixed gain.

(a) PAC 2/4/6 preamplifier **(b) PAC 1220A preamplifier.**

Figure 4.5: AE preamplifiers.

4.1.4 Signal conditioning unit

A programmable 4-channel signal conditioning unit (SCU) of in-house construction was used to power (+28 V) the AE sensors and pre-amplifiers. The unit could also be used to perform analogue RMS processing with additional amplification or attenuation, if necessary, using four gain switches of -12, -6, 0 and +6 dB. Again, each experiment was done with a fixed gain.

Figure 4.6: AE signal conditioning unit.

4.1.5 Data acquisition (DAQ) system

The experiments in this research were focused on acquiring raw AE signals in the bandwidth 0.1 to 1 MHz and the system was based on an in-house built desktop PC with a 12 bit, National Instruments (NI), PCI-6115 board. This board could be used to acquire simultaneously the raw AE signal at 10 M samples/s for up to four channels and used a full length PCI slot. It is a multifunction analogue, digital and timing device without on-board switches or jumpers and could be configured and calibrated by software.

Figure 4.7: AE Connector block

The software-programmable gain could be set to 0.2, 0.5, 1, 2, 5, 10 or 50 covering an input range from ± 200 mV to ± 42 V. The data could be sampled from 20k samples/s up to 10 M samples/s for each channel with a total on board memory of 32 MB. The board supported only differential input configurations and had over-voltage protection at ± 42 V. For source location applications, it could be used to record raw AE signals (sampled at 5 M samples/s) over up to four channels.

4.1.6 AE data handling

The LabView software package was used in this research to control the DAQ system, specifically to control sampling frequency, number of acquired data points per channel, set the number of channels, number of records, input range and pre-trigger data. Figure 4.8 shows the graphical user interface for the programme, developed by

Nivesrangsan [55], the signals displayed having been acquired from four AE sensors at different positions for a pencil lead break source, for which the upper channel was the trigger sensor.

The MATLAB software package was used for handling the AE signals. AE waveforms (amplitude-time) can be very complex but, in the current work, all data were from a step-unload (pencil lead break) so no sophisticated analysis was required to determine the energy of the signal in a way that avoided any reflections.

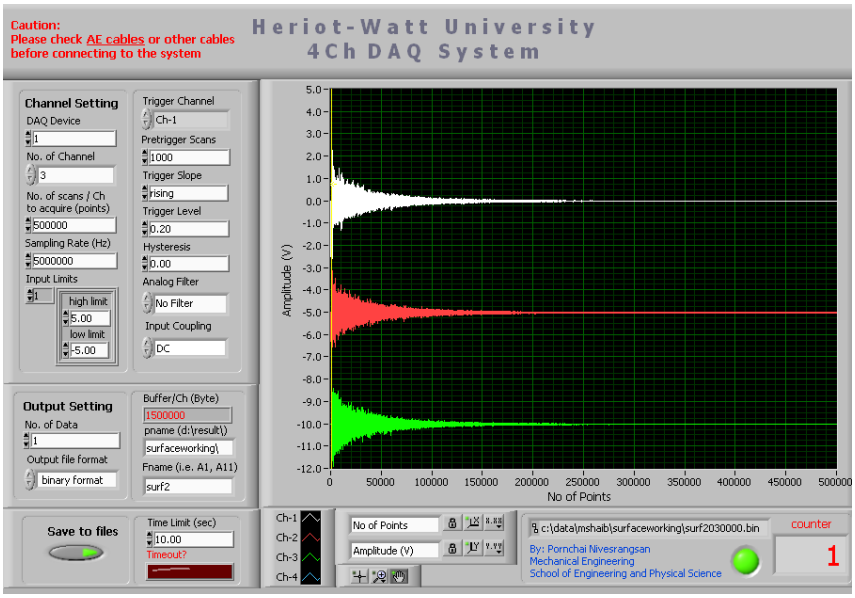

Figure 4.8: LabView front panel for 4-channel DAQ system.

The recorded AE signals were discrete time-series, and the raw signal was squared and integrated after eliminating the noise. To do this, a threshold was set at 1.5 times the maximum noise in the first 900 points. The wave arrival was recognized by the time at which the signal level first exceeds this threshold. The energy was calculated by integrating the square of the amplitude for the duration between the first and the last threshold crossings.

4.2 Sensor calibration and sources of variation

AE sensors are mechanical-electrical transducers which convert the mechanical disturbance to an electrical signal [78]. This indirect measurement will be influenced by the sensor's response to the forcing transient waves, which is influenced by the sensor construction, including the piezoelectric properties of the sensing element as well as its size, shape and backing, which govern the amplitude sensitivity and associated self-resonance. Also, the propagation path from source to sensor and the nature of the coupling between the sensor and the surface will affect what is recorded [129].

In order to study the AE attenuation, the sensors have to be calibrated to identify any factors other than distance from the source which might affect the accuracy of the data. According to the British Standards AE sensor calibration can be done using a large steel block with a pencil lead break source [130]. Accordingly, the three Micro-80D AE sensors used in this work were first tested back-to-back on a large cylindrical steel block of dimensions of 30.7 cm diameter and 16.6 cm height, supported by wooden blocks. Pencil leads (0.5 mm diameter, hardness 2H) were used to simulate an AE source by breaking the lead on the centre of the top of the cylinder, with an array of three sensors each mounted on the top surface at the same radial distance of 10 cm from the source.

The main aims of the calibration were to measure the random variation in recorded AE due to; variations in individual pencil lead breaks, variations in surface-sensor coupling and variations in sensor sensitivity

First, the three sensors were systematically moved around four different positions on the steel cylinder surface separated circumferentially by 90^{o} as shown in the Figure 4.9. Next, to assess the consistency of the pencil lead break, the three sensors were mounted at the same radial distance, 10 cm, from the source and 100 lead breaks acquired without moving or removing any of the sensors.

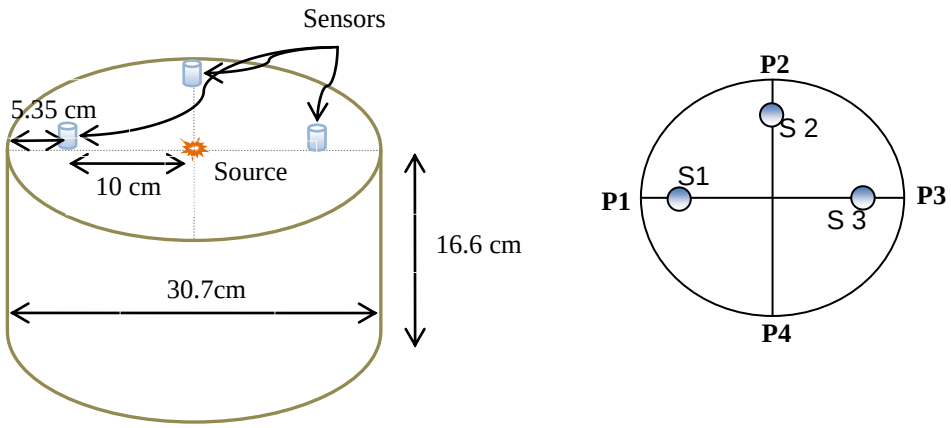

(a) Schematic view **(b) Plan view**

Figure 4.9: Typical schematic and plan view of sensors and positions on steel block.

With the three sensors in each position, 10 pencil lead breaks were recorded and the sensors were taken off and remounted in the same positions and another 10 breaks recorded. This process was repeated for a total of ten times so that 100 pencil lead breaks were recorded for each sensor at each position. Next, sensors were moved to another position and the whole process repeated, Table 4.1.

Array 1	S1, P1; S2, P2: S3,P3
Array 2	S1, P2: S2, P3; S3, P4
Array 3	S1, P3; S2, P4: S3,P1
Array 4	S1, P4: S2, P1; S3, P2

Table 4.1: Sensor and position arrays for calibration

AE signals were acquired at a sampling rate of 5 MHz for 5×10^5 points with a preamplifier gain of 40 dB and SCU gain at -6. The energy was calculated as described in Section 4.2.6.

Figure 4.10 shows magnified raw signals in the time domain for pencil lead breaks on the cylindrical block for each of the three sensors (S1, S2 and S3). There is a reflection corresponding to the return time from the edge (distance of 10.7 cm, caused by a surface wave in around 3×10^{-5} sec) which causes a slight increase in sensor amplitude.

However all sensors responses have ring down to around 10% of their maximum amplitude within time.

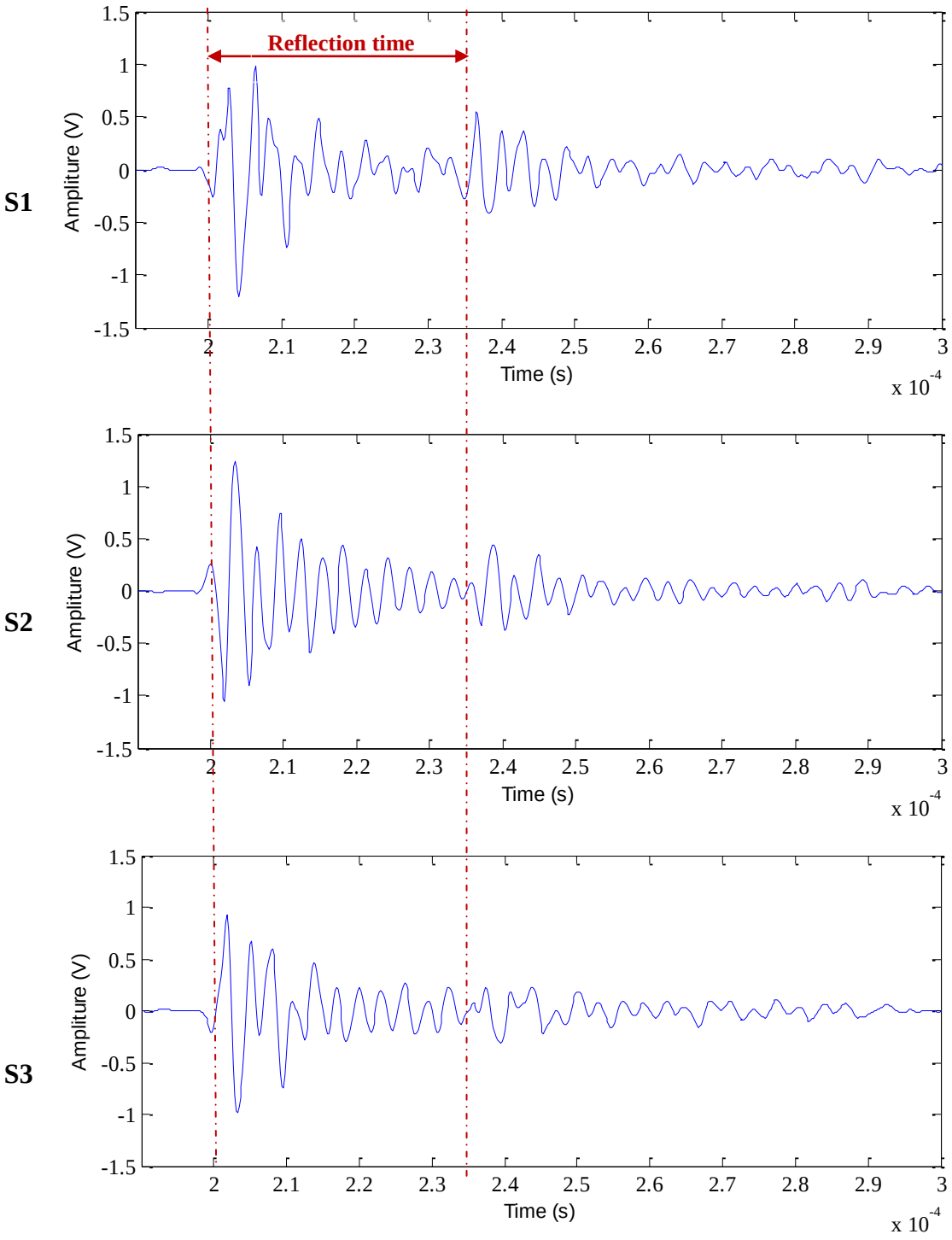

Figure 4.10: Typical magnified view of raw AE signal for pencil lead break on the cylindrical steel block for three sensors S1, S2 and S3 respectively

Figures 4.11 to 4.13 show the average and range of AE Energy recorded for the 10 pencil lead breaks for each of the 10 remounts, for each of the three sensors for each of the four positions. There is clearly significant variation in recorded energy for a given sensor in a given position, both due to the variation in lead break and the variation in coupling, which needs to be considered even before assessing any variation between sensors and positions.

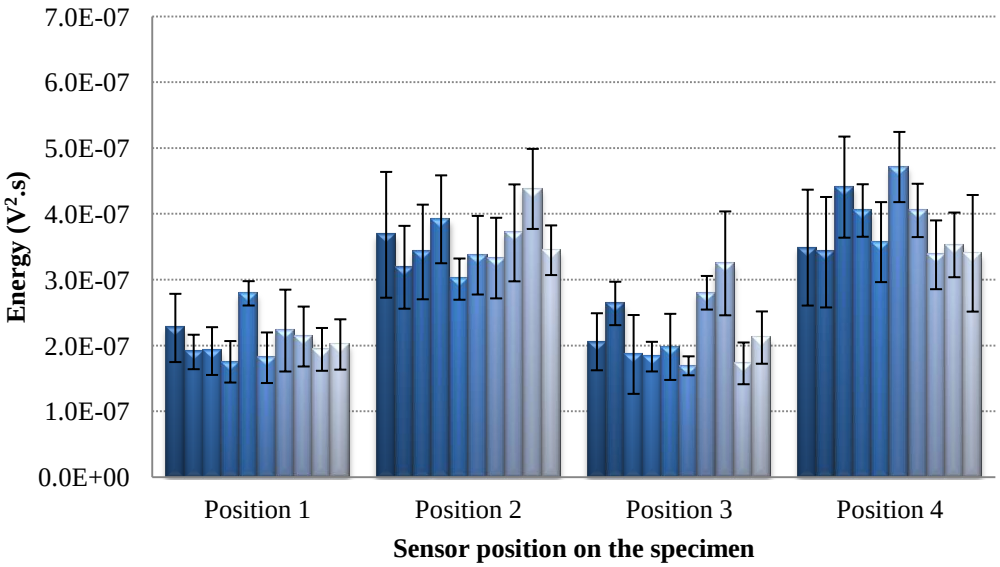

Figure 4.11: AE energy recorded at sensor S1 at each of the four positions on the cylindrical block

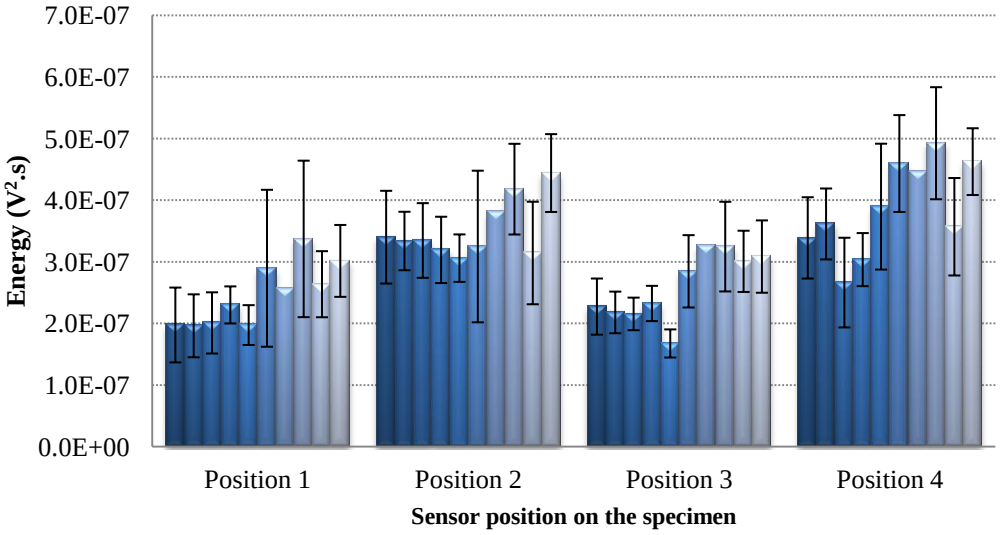

Figure 4.12: AE energy recorded at sensor S2 at each of the four positions on the cylindrical block

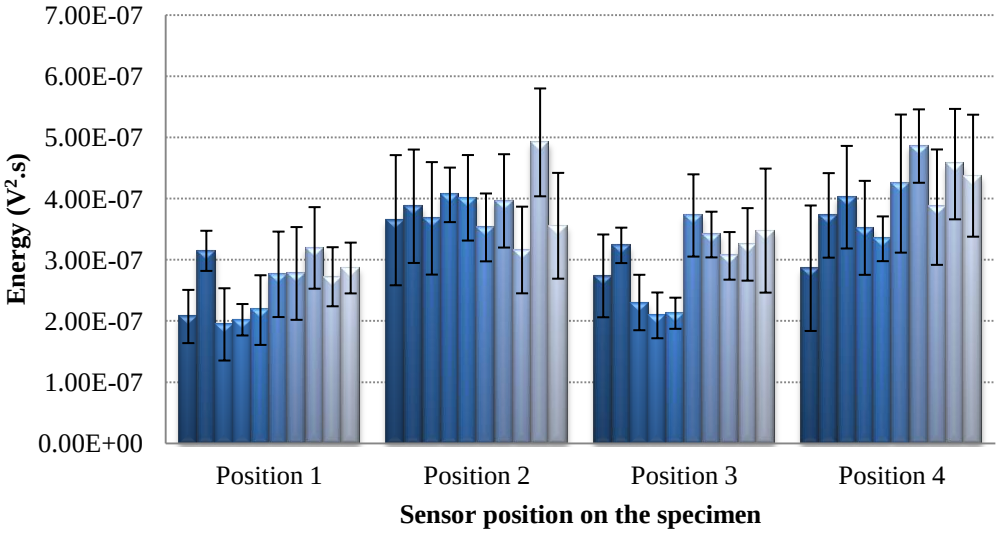

Figure 4.13: AE energy recorded at sensor S3 at each of the four positions on the cylindrical block

Figures 4.14 to 4.17 show the energy data re-grouped to compare the records for each sensor at each position. For each sensor, grouping the individual placements at a given position, the variance between placements (consistency of coupling) can be compared with the variance within a given placement (consistency of pencil lead breaks).

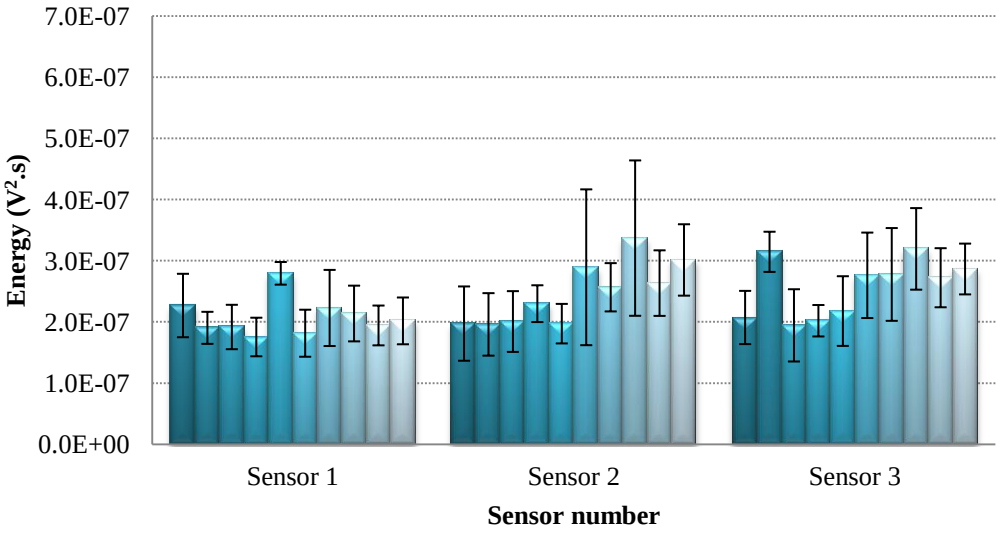

Figure 4.14: AE energy for each sensor recorded at position 1 on the cylindrical block.

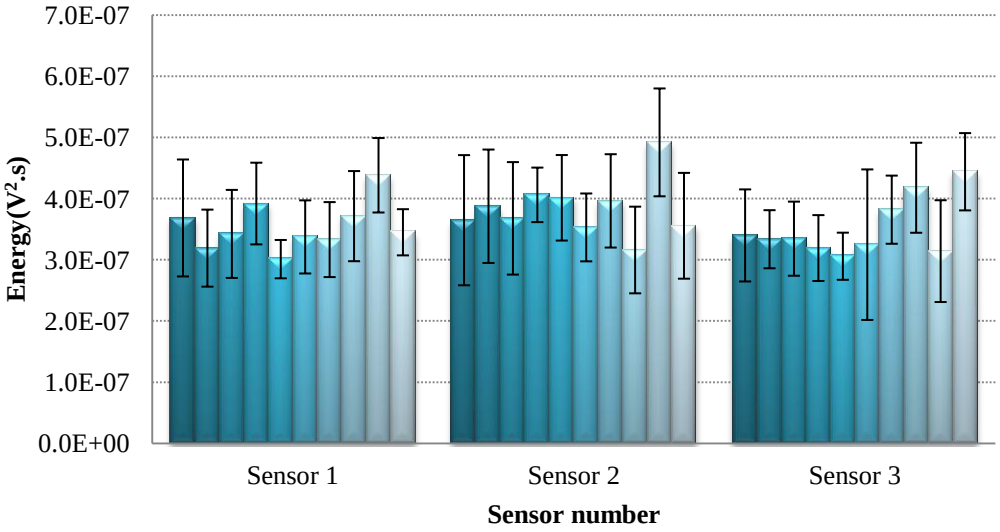

Figure 4.15: AE energy for each sensor recorded at position 2 on the cylindrical block.

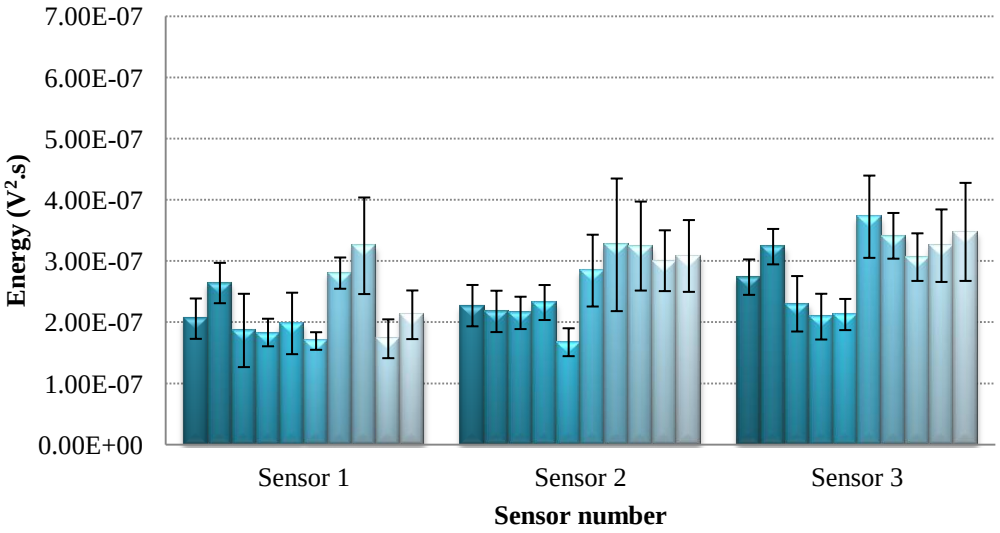

Figure 4.16: AE energy for each sensor recorded at position 3 on the cylindrical block.

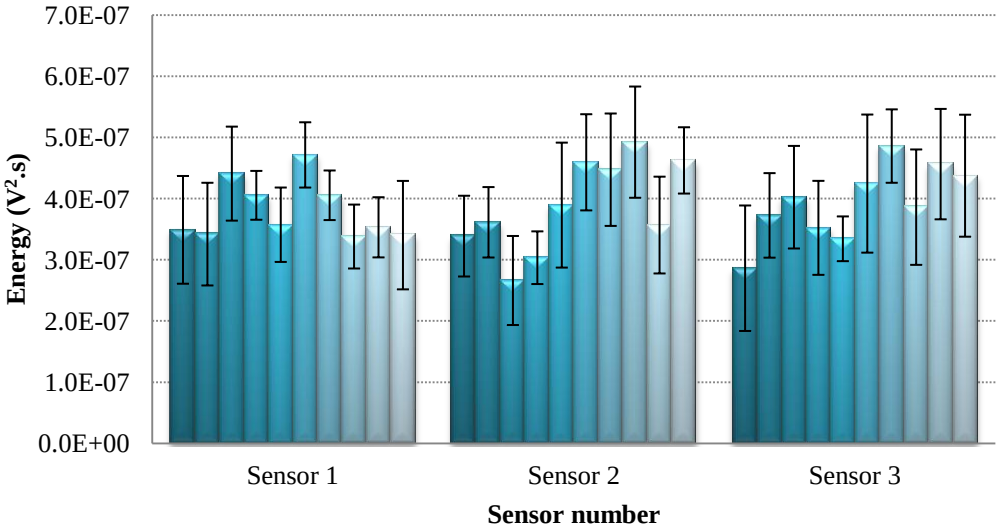

Figure 4.17: AE energy for each sensor recorded at position 4 on the cylindrical block.

In order to analyse the data more systematically, an analysis of variance (Anova) was carried out grouping the data in a range of ways. The significance of a source of variance is assessed using the indicator F-Value, the ratio of the between-group variance and the within-group variance. This is compared with $F_{critical}$ at a threshold of 0.05 (95% confidence level), meaning that, if the F-Value less than $F_{critical}$, there will be no significant effect of the tested source of variance [131]. The degree to which the F-Value is below or above the $F_{critical}$ is reflected in the P-Value, while will be equal to 0.05 if F-Value = $F_{critical}$.

In the first analysis, the data were grouped according to the individual placements at each individual position, so the variation from coupling (between-groups) can be compared with the variation from pencil lead breaks (within-groups). Table 4.2 shows the result of 12 such Anova tests and it can be seen that, in the majority of the cases, F-Value is well above $F_{critical}$, indicating that the placement of the sensor is more important source of variation than is the pencil lead break.

Position number	Sensor number	F-Value	$F_{critical}$	P-Value
1	1	2.01	1.99	0.047
1	2	4.96	1.99	2.06×10^{-5}
1	3	1.44	1.99	0.18
2	1	2.18	1.99	3.53×10^{-9}
2	2	13.11	1.99	9.66×10^{-25}
2	3	3.79	1.99	4.3×10^{-5}
3	1	3.77	1.99	0.08
3	2	26.14	1.99	1.59×10^{-21}
3	3	11.46	1.99	9.39×10^{-12}
4	1	4.5	1.99	1.64×10^{-5}
4	2	10.11	1.99	1.36×10^{-10}
4	3	12.14	1.99	1.45×10^{-12}

Table 4.2: Summary of Anova results for remounting the sensors

In the second analysis, the data were re-grouped according to the individual sensors for different positions, to assess the variance due to the sensor (between-groups) against the variance of the pencil lead break and coupling (within-groups). However, grouping in this way does not permit the effect of remounting the sensors (between-groups) to be isolated. Table 4.3 shows the result of 4 Anova tests, which show the majority of the F-Value to be well above $F_{critical}$, indicating that the sensor is a bigger source of variation than the coupling or the pencil lead break. Appendix A, contains the original calibration certificates for three sensors.

Position number	F-Value	$F_{critical}$	P-Value
P1	3.55	3.03	0.07
P2	40.67	3.03	3.02×10^{-16}
P3	30.08	3.03	1.29×10^{-12}
P4	18.45	3.03	3.95×10^{-8}

Table 4.3: Summary of Anova results for different sensor sensitivity

To conclude, the energy recorded for a given installation can vary due to the pencil-lead break by about 20%. Removal and re-installation can increase the variation in the energy to about 40% (including the effect of lead break) attributed to changes in coupling conditions and magnetic clamp tightening force. The overall recorded energy can vary due to sensor, coupling conditions and pencil lead by about 50%. Finally, it has been noticed that changing the sensor position has a more significant effect than the

effect of lead break, sensor coupling and sensor, and this was attributed to changes in the degree of the wood support directly underneath the sensor.

The possibility of variation of sensitivity due to the different factors needs to be taken into account in each of the objects by repeating the pencil lead test and remounting the sensor at the same position. Also, the supports underneath the test objects will be kept as small as possible and at the corners of the test object.

4.3 Attenuation in small steel blocks with air environment

In many applications, for example machinery, it is of interest to measure AE on relatively small objects with a number of interfaces. In order to evaluate the potential of AE simulation to describe propagation in such objects, a variety of experiments were carried out with a linear array of sensors on four small solid blocks of steel of different shapes, as follows (Figure 4.18):

- Plate (100 cm width × 100 cm length × 0.65 cm height)
- Strip (20 cm width × 93.3 cm length × 2 cm height)
- Block (35 cm width × 35 cm length × 5 cm height)
- Cylinder (30.6 cm diameter × 16.5 cm height)

The blocks were each placed on a wooden surface as shown in Figure 4.17, and the experiments consisted of deploying a standard Hsu-Nielsen source at a fixed point on the upper surface of the block and acquiring the raw AE at different source-sensor distances, with sensors mounted in groups of three along various straight lines on the same surface as the source.

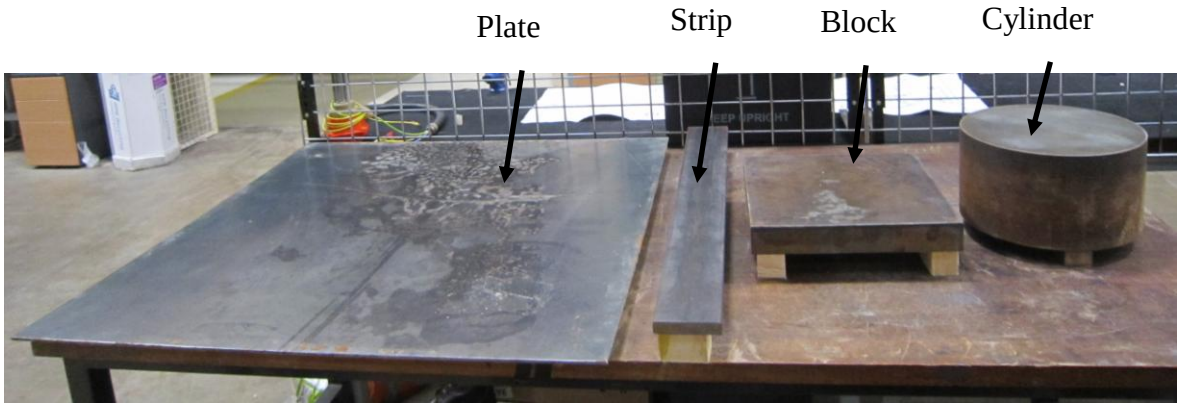

Figure 4.18: The four solid steel geometric shapes tested

In order to produce a range of AE propagation conditions on each of the small blocks, three different source positions were chosen on the same surface of the block as the sensors, at the centre, at the edge and at the corner, in addition, same experiments were carried out with the source on the end face. For each source position, sensor arrays were constructed to give a range of source-sensor distances along the lines shown schematically in Figure 4.19.

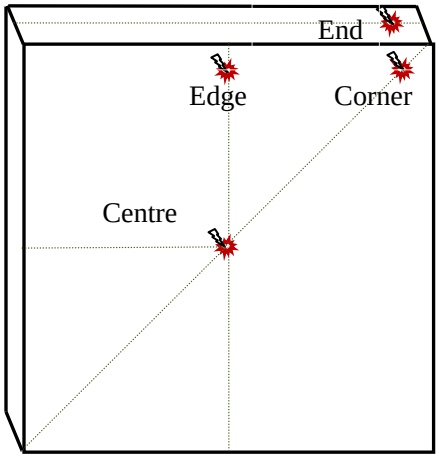

Figure 4.19: Schematic view of source positions and sensor lines on steel block

As the effect of removal and replacement the sensor has a significant effect on measured AE energy. It was necessary to establish the repeatability of AE energy measurement for a given installation. Thus, the AE attenuation experiments were designed to use different sets of sensor arrays and the re-installation of arrays. The same three sensors,

preamplifiers and magnetic clamps were used for all of the systematic tests. Seven pencil lead breaks were recorded for each set of sensor positions and the sensors were taken off and remounted in the same positions and another seven breaks recorded. This process was repeated a total of three times so that 21 breaks were recorded for each sensor at each position, the data being captured at a sampling rate of 5 MHz for a fixed period of 0.1 Sec (500,000 points). Table 4.4 summarises the experimental arrangements, showing the three sensor positions, the sensor steps and total number of sensor positions.

Steel shape	**Source position**	**Distance of first sensor position from the source (cm)**			**Sensor step distance (cm)**	**Total number of sensor positions**
		S1	**S2**	**S3**		
Block	**Centre**	2.5	7.5	12.5	2.5	6
	Edge	3	18	23	5	6
	Corner	3	17	31	7	6
	End	3	18	23	5	6
Plate	**Centre**	5	15	25	5	6
	Edge	5	35	65	10	9
	Corner	7	49	91	14	9
Strip	**Centre**	5	15	25	5	6
	Edge	5	35	65	10	9
	End	5	35	65	10	9
Cylinder	**Centre**	2	6	10	2	6
	Edge	5	15	25	5	6

Table 4.4: Summary of small steel block measurements

4.4 Effect of external environment on attenuation in the small blocks

In applications where propagation in small blocks is of interest, the surfaces of the structure are often exposed to different environments. Such is the case for an an engine, for example, where AE propagating in the bulk or on the surface might encounter surfaces where the environment is air, water or oil. In order to examine such interface effects on AE attenuation in the small blocks, three different types of "external" environment were used on the lower surface; dry sand (particle size around 200 micron), water and wet sand (20% water, 80% dry sand). For the air and water tests the blocks were suspended on wooden supports at the corners, and, for the sand tests, the blocks were embedded, as shown in Figures 4.20 to 4.22. These tests were only carried out on the three parallelepipedal blocks; the plate, the strip and the slab.

Three source positions were used on the upper surface at the edge, centre and corner and, again, arrays were set up along various lines to give a range of source-sensor distances. As before, seven pencil lead breaks were taken at each sensor position and the sensors removed and replaced twice more, giving a total of 21 breaks for each sensor position. Again as before, the data were captured at a sampling rate of 5 MHz for a fixed period of 1ms (500,000 points). Table 4.5 summarises number the experiment arrangement, showing the three sensor positions, the sensor steps and total number of sensor positions.

(a) Dry fine sand

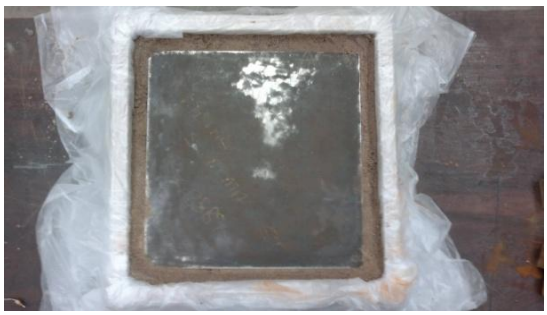

(b) Wet fine sand

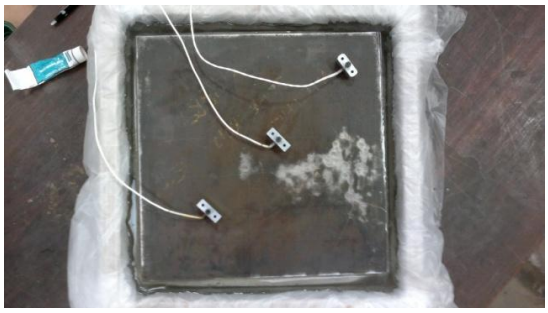

(c) Water

Figure 4.20: Set-up for the three environments for the steel slab.

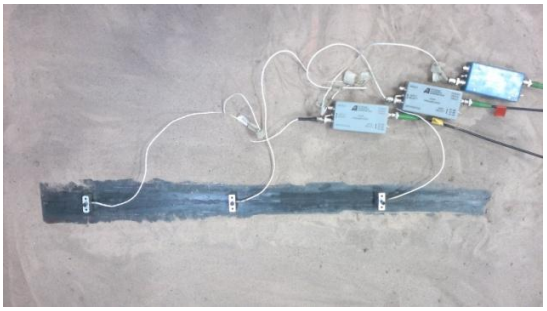

(a) Dry fine sand

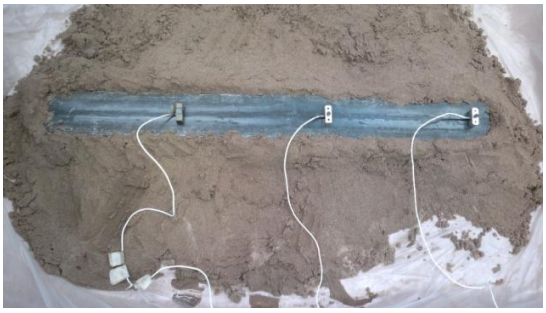

(b) Wet fine sand

(c) Water

Figure 4.21: Set-up for the three environments for the steel strip.

(a) Dry fine sand

(b) Wet fine sand

(c) Water

Figure 4.22: Setup for the three environments for the steel plate.

Surrounding environment	Steel shape	Source position	Distance of first sensor position from the source (cm)			Sensor step distance (cm)	Total number of sensor positions
			S1	S2	S3		
a) Air b) Dry sand c) Wet sand d) Water	Block	Centre	2.5	7.5	12.5	2.5	6
		Edge	3	18	23	5	6
		Corner	3	17	31	7	6
	Plate	Centre	5	15	25	5	6
		Edge	5	35	65	10	9
		Corner	7	49	91	14	9
	Strip	Centre	5	15	25	5	6
		Edge	5	35	65	10	9

Table 4.5: Summary of small steel block measurements for different environments

4.5 Attenuation in practical structural elements

This section deals with tests carried out on some simple practical structural elements to supplement the tests on the idealised objects described in Sections 4.4 and 4.5. The structures were; a plate of laminated glass, a relatively short section of carbon steel pipeline and a large cylindrical stainless steel vessel. In each case, a range of environments was chosen, typical of its application.

4.5.1 AE attenuation in a laminated glass plate

Glass is widely used in modern architecture and this object was chosen for its similarity to the steel plate studied as one of the idealised shapes. Accordingly, the glass was cut to the same planar dimensions to the steel plate. Laminating involves bonding (in this case) two sheets of glass together using an adhesive interlayer, so, besides the difference in material, the glass plate had an additional interface at the mid-section although this was very thin.

The glass sheet used was a 100 cm × 100 cm square consisting of two 4 mm sheets laminated with an inter-layer to give a total measured thickness of 8.8 mm.

As before, seven pencil lead breaks were taken at each sensor position and the sensors removed and replaced twice more, giving a total of 21 breaks for each sensor position. Again as before, the data were captured at a sampling rate of 5 MHz for a fixed period of 1 ms (500,000 points), Table 4.4 summarises the experiment arrangement. Because the material is not magnetic, small magnets were placed on the opposite face of the glass to hold the sensors in place, as shown in Figure 4.23.

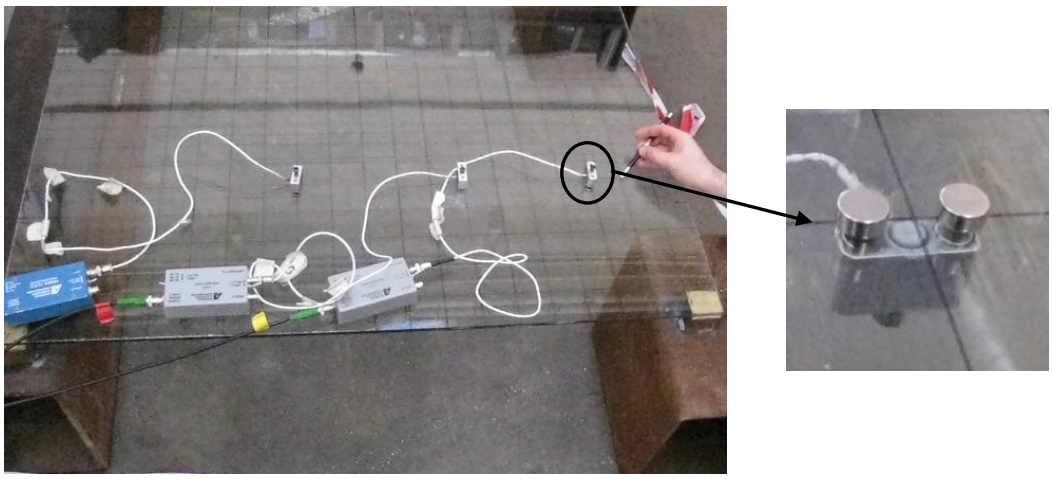

Figure 4.23: Measurement setup for laminated glass showing sensors in position and the small magnets used to hold down the sensors.

Source position	Distance of first sensor position from the source (cm)			Sensor step distance (cm)	Total number of sensor positions
	S1	S2	S3		
Centre	5	15	25	5	6
Edge	5	35	65	10	9
Corner	7	49	91	14	9

Table 4.6: Summary of laminated glass measurements

4.5.2 Attenuation in a large cylindrical vessel

A cylindrical stainless steel vessel, 2.5 m long with an external diameter of 2.2 m and wall thickness of 8 mm, was chosen to study the AE attenuation in a large structure, again as an extension to the plate morphology. The experiments were carried out with the vessel suspended on four relatively small steel columns, as shown in Figure 4.24.

Two source positions were used, one 30 cm from the top of the cylindrical part of the vessel and one 120 cm from the bottom of the cylindrical part of the vessel, approximately half-way up.

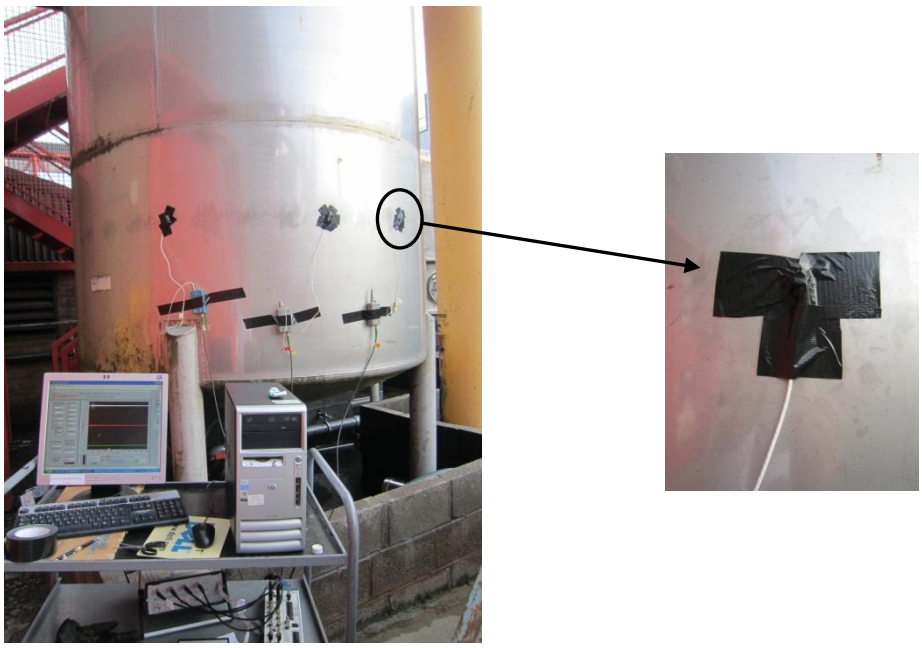

Figure 4.24: Measurement setup for stainless steel vessel showing AE system and sensors in position and the duct tape for the sensor clamping.

Two arrays were used, an axial one along the outer surface of the vessel at the same circumferential position as the source at the top of the vessel, and a circumferential one at approximately half way up the vessel at the same axial position as the source at the middle of the vessel, Figure 4.25. Each array was produced by moving the sensors in groups of three as follows; the first sensor was mounted 10 cm from the source and was moved incrementally in 10 cm steps along the (circumferential or axial) array line four times, the second sensor was mounted 60 cm from the source and moved in 20 cm steps along the array line for a further four positions and the third sensor was mounted 140 cm from the source and moved in 20 cm steps. This gave a total of twelve different array positions along a total axial or circumferential distance of 2 m, Table 4.7.

Sensor array	Internal environment	Distance of first sensor position from the source (cm)			Sensor step distance (cm)			Total number of sensor positions
		S1	S2	S3	S1	S2	S3	
Longitudinal	**Air**	10	60	140	10	20	20	12
Circumferential	**Air**	10	60	140	10	20	20	12
Longitudinal	**Water**	10	60	140	10	20	20	12
Circumferential	**Water**	10	60	140	10	20	20	12

Table 4.7: Summary of vessel tank measurements

Again because the surface was non-magnetic, the sensors were attached using adhesive tape with vacuum grease couplant, as shown in Figure 4.24 and seven pencil lead breaks were taken at each sensor position and the sensors removed and replaced twice more, giving a total of 21 breaks for each sensor position, as before. Again as before, the data were captured at a sampling rate of 5 MHz for a fixed period of 1 ms (500,000 points). The entire experiment was carried out twice, once with the vessel empty and once with it filled with water to a level of 10cm below the top of cylindrical section.

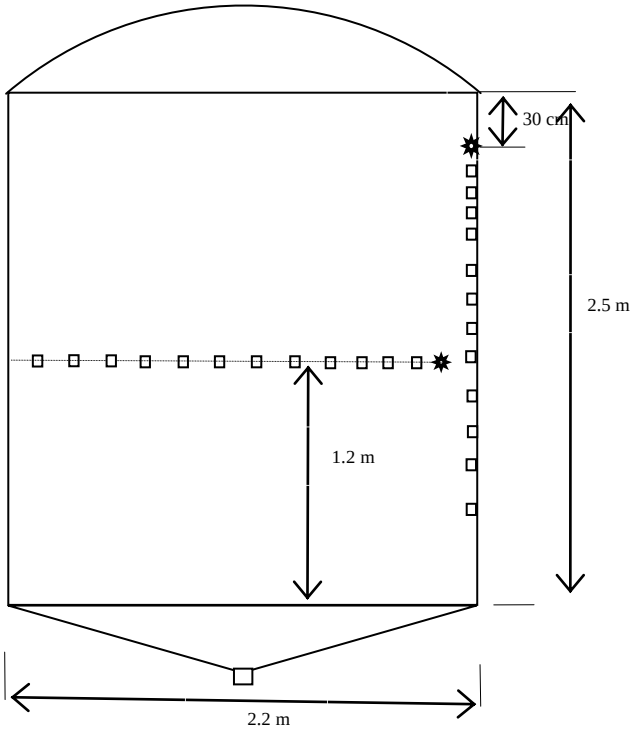

Figure 4.25: Sensor arrays for stainless steel vessel experiments.

4.5.3 Attenuation in a long steel pipe

The final practical structure in this study is a length of seamless steel line pipe, 5.5 m long with an external diameter of 48.4 mm and wall thickness of 7.35 mm, thus more resembling the strip than the plate idealised structure. The experiment formed part of a different study by Shehadeh [73], although the techniques used were sufficiently similar that the results can be used here. The experiments were carried out with the pipe

suspended on wooden blocks and only one sensor (PAC Micro80D) was used in 13 different positions, the measurement being repeated 10 times at each position, without removal and replacement of the sensor. The pencil lead breaks were performed on the surface of the pipe at 30 cm from the end of the pipe. For the first 10 positions, the spacing was 20 cm and this was increased to 1 m for up to 5 m source-sensor distance, Figure 4.26. As in the current work, the data were sampled at 5 MHz for a fixed period of 0.01 Sec. The experiment was repeated six conditions of internal and external environments, as summarises in Table 4.8. For each condition, sensors were mounted along the pipeline, which was embedded in the external environment as shown in Figure 4.27.

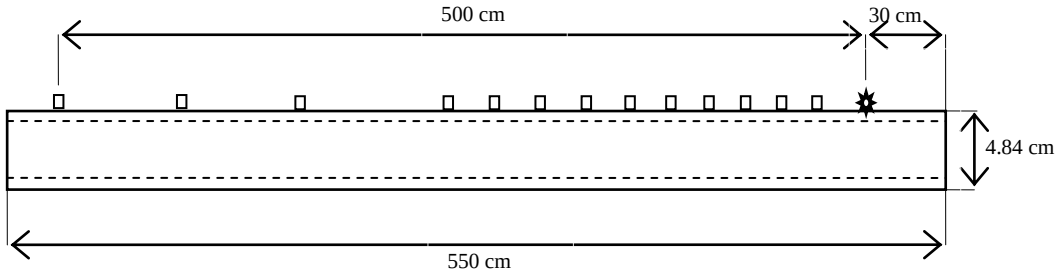

Figure 4.26: Schematic layout of plain pipe experiment.

Internal environment	External environment	Distance of first sensor position from the source (cm)	Space between first 10 positions(cm)	Space between last 3 positions (cm)
Air	**Air**	**20**	**20**	**100**
Air	**Dry sand***	**20**	**20**	**100**
Air	**Wet sand****	**20**	**20**	**100**
Air	**Soaked sand*****	**20**	**20**	**100**
Water	**Wet sand**	**20**	**20**	**100**
Water	**Air**	**20**	**20**	**100**

Table 4.8: Summary of pipeline measurements, * sand particle size 180 micron, ** 20% water and 80% dry sand, * 27% water and 73% sand**

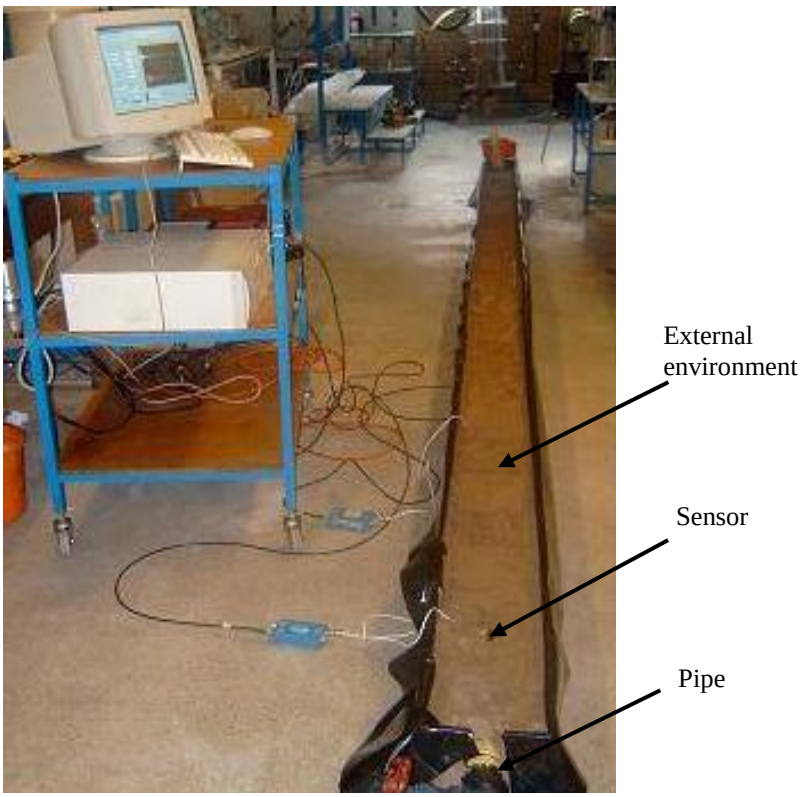

Figure 4.27: Measurement setup for buried pipeline tests showing data acquisition system and sensors in position [28]

4.6 Summary of the experiments and approach to simulation

Table 4.9 summarises all the experimental configurations on which simulations will be performed. The experimental conditions, the number of repeat tests, the number of sensor positions, the number of records per position and the maximum direct source-sensor distance of are also shown.

The analyses of these results are discussed in the following three chapters. As the purpose of the experiments was to help develop and establish a simulation approach, the analysis was carried out in stages with the following objectives. The simulation only distinguishes between waves which propagate in the bulk material (internal waves) and those which propagate on the surface (surface waves), each ray essentially representing part of a spherical or cylindrical wavefront, respectively.

The first question to be answered is whether this approach could be used to explain the very different attenuation results obtained with different shapes of relatively small extent in which a lot of reflected energy might be expected to arrive at a sensor as well as those of relatively large extent where there is much more geometric attenuation. This is pursued in Chapter 5, applied to experiments 1, 3, 4 and 5 for the cases where the external and internal environments are air and using a "geometric" simulation, where all rays arriving at a surface or an edge are assumed to be 100% reflected and no material attenuation or interference are considered.

The next question to be answered is whether a consistent answer can be obtained to the question of what proportion of the source energy goes into internal and external waves, and this is pursued in Chapter 6, using the geometric simulation applied to experiments 2, 3, 4 and 5 for the varied internal and external environments. Here, the objective is to find a consistent set of values for reflection coefficients and internal frication, guided by literature data.

No.	Experiment details	No. of repeat tests	No. of sensor positions	No. of records per position	Maximum source-sensor distance (cm)
1	**Simple geometric shapes with different source positions**				
	1.1 Steel block (slab)				
	1.1.1 Source at the centre	3	6	7	15
	1.1.2 Source at one edge	3	6	7	28
	1.1.3 Source at one corner	3	6	7	38
	1.1.4 Source on one end	3	6	7	28
	1.2 Steel plate				
	1.2.1Source at the centre	3	6	7	30
	1.2.2 Source at one edge	3	9	7	85
	1.2.3 Source at one corner	3	9	7	112
	1.3 Steel strip				
	1.3.1 Source at the centre	3	9	7	30
	1.3.2 Source at one edge	3	9	7	85
	1.3.3 Source at one end	3	9	7	45
	1.4 Steel cylinder				
	2.4.1 Source at the centre	3	6	7	12
	2.4.1 Source at the edge	3	6	7	26
2	**Simple steel shapes with three different environments on lower surface**				
	2.1 Steel block				
	2.1.1 Source at the centre	3 × 3	6	7	15
	2.1.2 Source at one edge	3 × 3	6	7	28
	2.1.3 Source at one corner	3 × 3	6	7	38
	2.2 Steel plate				
	2.2.1Source at the centre	3 × 3	6	7	30
	2.2.2 Source at one edge	3 × 3	9	7	85
	3.2.3 Source at one corner	3 × 3	9	7	112
	2.3 Steel strip				
	2.3.1 Source at the centre	3 × 3	9	7	30
	2.3.2 Source at one edge	3 × 3	9	7	85
3	**Laminated glass**				
	3.1 Source at the centre	3	6	7	30
	3.2 Source at one edge	3	9	7	85
	4.3 Source at the end	3	9	7	112
4	**Stainless steel vessel (empty and filled with water)**				
	4.1 Axial sensor array	2 × 2	12	7	200
	4.2 Circumferential sensor array	2 × 2	12	7	200
5	**Pipe**				
	5.1Varied external and internal conditions	1 × 6	13	10	500

Table 4.9: Summary of experiments to be simulated.

CHAPTER 5: RESULTS AND ANALYSIS: GEOMETRICAL SIMULATION

This chapter uses a simplified version of the ray-tracing algorithm in order to determine some basic numerical performance criteria, including the required density of fired rays and the number of iterations required for convergence, as well as providing some indication of the relative contributions of surface and body waves to the disturbance recorded at the sensor. The simulation, therefore, simply generates two types of rays, body rays and surface rays, and only considers the effect of geometric spreading. The comparison of these simple simulations with the experimental results is used to inform the next stage of simulation. The chapter starts with some general comments on the simulations and is then divided into two main sections where simulated and measured results are compared, the first dealing with the four small solid steel shapes (block, plate, strip and cylinder) and the second dealing with the more practical structures (laminated glass plate, pipeline and large vessel). The final section discusses the findings in preparation for the physical simulation.

5.1 Data treatment and simulation

All of the experimental and simulated results in this section were treated in a similar way in order to make the matching of simulation and experiment congruent. The following sections outline the general basis of treatment of data and production of the graphical outputs.

5.1.1 Wave speed

AE propagation in structures is often treated theoretically assuming one or more idealised modes, implying simple sources and structures [30], Table 5.1. Such an approach considers the structure to be a homogeneous elastic continuum and that the

modes do not interact or interfere, which may not be applicable in real situations [51, 68, 132, 133].

Wave speed (m/sec)		
Longitudinal wave	**Shear wave**	**Rayleigh wave**
5900	3200	3000

Table 5.1: Simple mode AE wave speeds for steel [2].

Another approach is to determine the wave speed experimentally from a known source position using surface mounted sensors with a known separation distance and measuring the arrival time difference between the signals. However, wave propagation in small structures over small distances is complicated and it is difficult to know which wave types are involved because the effects of wave reflection, refraction and mode conversion are unpredictable. Furthermore, the shorter the structure, the smaller the arrival time differences at a sensor and the smaller the differences in arrival time between waves of different speeds. In this work, the largest of the small shapes has been used (100cm × 100cm × 0.65cm) along with some of the larger structures to identify one slower and one faster wave in each of the three materials (steel, glass and stainless steel). A threshold of 0.016 of the maximum amplitude of the whole signal was used to identify arrival times of the slow wave automatically and a threshold of 0.18 of the maximum amplitude was used for the fast wave.

5.1.2 Attenuation measurements

A pencil-lead break is known to give a relatively reproducible step unload impulse on the surface [2]. Multiple pencil lead breaks were performed for each (known) source-sensor distance in each configuration with data being captured at a sampling rate of 5 MHz for a period of 1ms (500,000 points) which was enough to capture the entire ring-down without an excessive "tail" which could contribute to noise.

In order to compare the simulated and measured energies, it is necessary to assume a curve shape which will give a reasonable fit to the data. For this purpose, a set of curves was chosen and analysed using a power law curve (the expected shape for geometric attenuation) and an exponential curve (the expected shape for attenuation due to internal friction). At this stage, the curve type chosen was for numerical convenience only, and does not carry any implications for the mechanisms of attenuation, nor about the wave modes involved.

The exponential and power curves were fit to all of measured and simulated data. A threshold was taken at 50% confidence level, simply to produce a quantifier against which the two type of fit could be evaluated. Power curve fitting has 25 of the 317 fits below this level, with an average R^2 of 71.1%, whereas the exponential curve fitting gave a slightly better result with 23 curves below the confidence level, and an average R^2 of 73.8%.

Table 5.2 summarises the attenuation measurements for the plate with the source at the centre, for the four environments. The effective attenuation coefficients, k_1, k_2 and k_3 are given for each of the repeat tests along with the corresponding correlation coefficients for both power law and exponential fitting. In order to make the trends clearer, the mean effective attenuation coefficient $\bar{k}$ for each of the conditions was obtained by taking a weighted mean

$$\bar{k} = \frac{{R_1}^2 k_1 + {R_2}^2 k_2 + {R_3}^2 k_3}{{R_1}^2 + {R_2}^2 + {R_3}^2} \qquad (5.1)$$

As can be seen the exponential curve fits showed a better distinction between the different environments. In addition, the power law curve fitting gave a higher weighting to data points near to the source [131], in the near zone, as can be seen, for example, in Figures 5.1 and 5.2. Accordingly, it was decided to use exponential curve fitting as a means of comparing simulated and measured results.

Curve fitting	Environment	Effective attenuation coefficient, k (m^{-1})			Strength of linear correlation, R^2			Weighted mean, $\bar{k}$ (m^{-1})
		k_1	k_2	k_3	R_1^2	R_2^2	R_3^2	
Power	**Air**	0.67	**0.38**	0.4	0.66	**0.59**	0.77	0.48
	Dry sand	0.93	0.79	0.98	0.83	0.55	0.37	0.93
	Wet sand	0.98	1.18	1.06	0.57	0.69	0.71	1.08
	Water	1.3	**1.24**	1.2	0.84	**0.86**	0.85	1.24
Exponential	**Air**	4.43	**2.93**	2.84	0.58	**0.70**	0.81	3.31
	Dry sand	6.46	6.18	7.04	0.8	0.66	0.38	6.47
	Wet sand	7.79	8.97	7.49	0.76	0.79	0.67	8.12
	Water	9.87	**8.88**	9.43	0.96	**0.88**	0.9	9.41

Table 5.2: Summary of measured attenuation in steel plate source at the centre, using exponential and power curves fitting. Curves in bold type are shown in Figure 5.1 and 5.2.

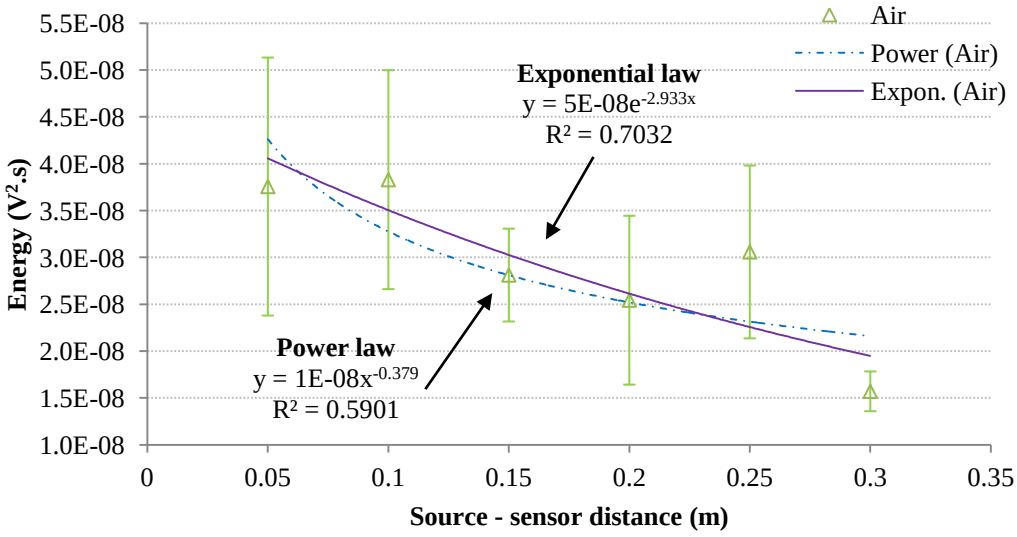

Figure 5.1: Measured AE attenuation in plate with source at the centre in air environment showing exponential and power curve fits.

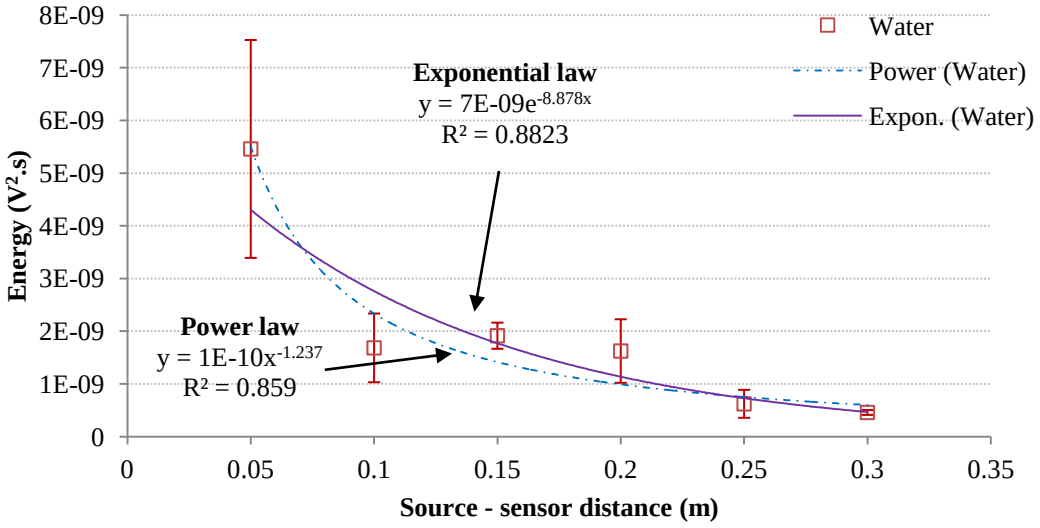

Figure 5.2: Measured AE attenuation in plate with source at the centre in water environment showing exponential and power curve fits.

5.1.3 Simulated energy

For a full physical simulation of AE propagation, the rays emanating from the source can be taken to represent spherical or circular wavefronts for the body and surface waves, respectively. Each ray can lose energy by absorption or during reflection and, when waves following different paths recombine at the sensor, they may be out of phase with each other and so can interfere destructively or constructively. For example, the overall energy loss of body waves represented by the N_h waves that encounter the sensor can be expressed by:

$$\frac{E}{E_0} = \frac{1}{N_f}\left[\sum_{j=1}^{N_h}\left(e^{-\alpha x_j} \times {R_U}^{n_{Uj}} \times {R_L}^{n_{Lj}} \times e^{i(\phi)}\right)\right] \times \left[\sum_{j=1}^{N_h}\left(e^{-\alpha x_j} \times {R_U}^{n_U j} \times {R_L}^{n_{Lj}} \times e^{i(\phi)}\right)\right]^* \quad (3.1)$$

In order to focus on the effects of geometry and on the ratio of surface to body waves likely to be contributing to the measured energy, four assumptions have been made in calculating the simulated energy in this chapter:

1- The AE wave is a simple harmonic one, either propagating at the speed of body wave (longitudinal wave), or at the speed of surface wave (Rayleigh waves)

2- The path differences are large enough to ensure that the phase differences are evenly distributed between zero and 2π, so that the effect of phase, including phase changes on reflection, affect all summations equally

3- There is 100% reflection at all edges and faces, i.e. $R_U = R_L = R = 1$

4- There is no material absorption, i.e. $\alpha = 0$

As a justification of assumption 2, Figures 5.3 and 5.4 show the histogram of phase differences (calculated from the path differences, frequencies and wave speeds) for all internal and surface rays hitting a sensor for simulations on each of the shapes.

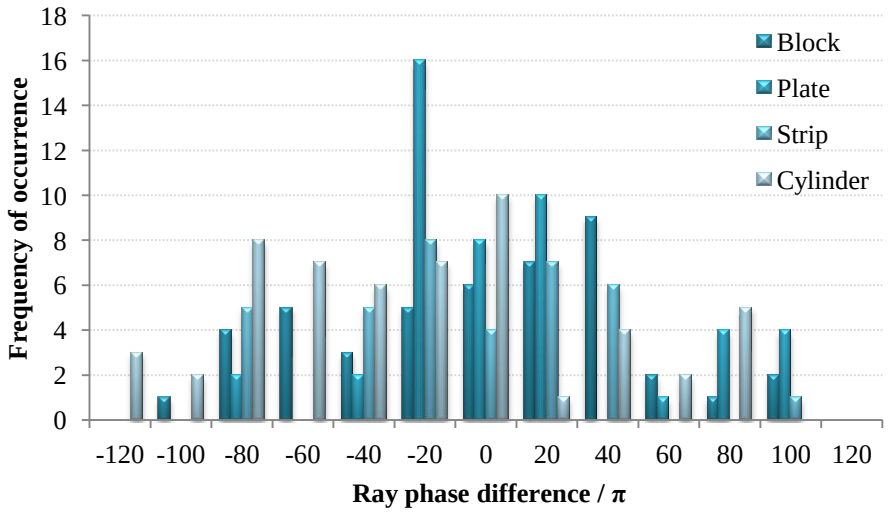

Figure 5.3: Histogram of the internal ray phase differences at the 2nd sensor for block, plate, strip and cylinder with source at the centre

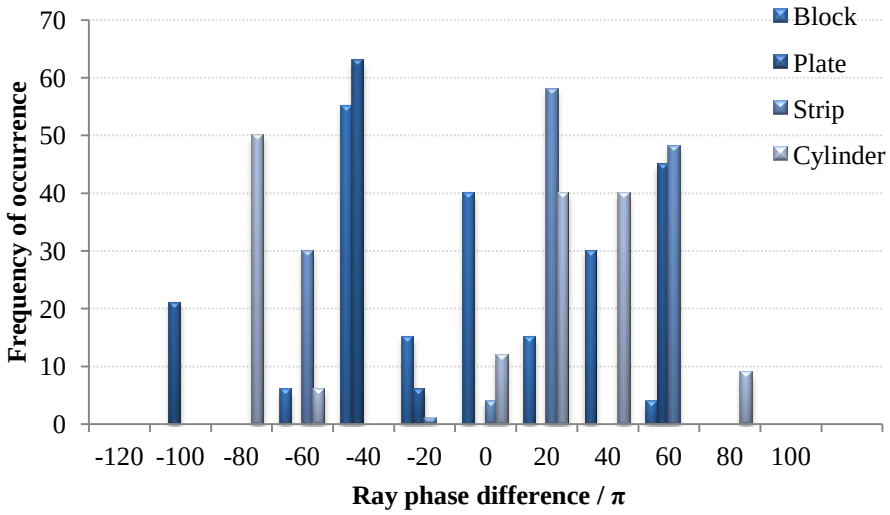

Figure 5.4: Histogram of the surface ray phase differences at the 2nd sensor for block, plate, strip and cylinder with source at the centre

Given the above simplifications, (E/E_0) recorded by the simulated sensor can be taken to be equal to the proportion of the rays fired which hit the sensor, i.e. the hit ratio (N_h/N_f). Thus, the effective exponential attenuation coefficient for the geometrical simulation can be obtained from the hit ratios of a simulated array of sensors at distances (x) from the simulated source:

$$\ln\left(\frac{N_h}{N_f}\right) = \ln\left(\frac{E}{E_o}\right) = -k'x \qquad (3.4)$$

5.2 Small solid shapes

As described in Chapter 4, up to four source positions, illustrated schematically in Figure 4.18, were used for each of the blocks, giving a total of 12 different attenuation tests over the four shapes, as summarised in Table 5.3.

Shape	Source position (see Figure 4.18)			
	Centre	Edge	Corner	End
Block	✓	✓	✓	✓
Plate	✓	✓	✓	×
Strip	✓	✓	×	✓
Cylinder	✓	✓	×	×

Table 5.3: Summary of attenuation measurements on small steel shapes

These small test objects were deliberately chosen at the beginning, because AE waves in small objects quickly establish complex interference patterns making attenuation rather difficult to assess.

5.2.1 Measurements on small solid shapes

Figure 5.5 shows plots of source-sensor distance versus arrival times, as measured on the steel plate with the source at the centre. The slope of the best-fit straight line through these data indicates that the speeds of the fast and slow waves were 5119 m/s and 3177 m/s, respectively.

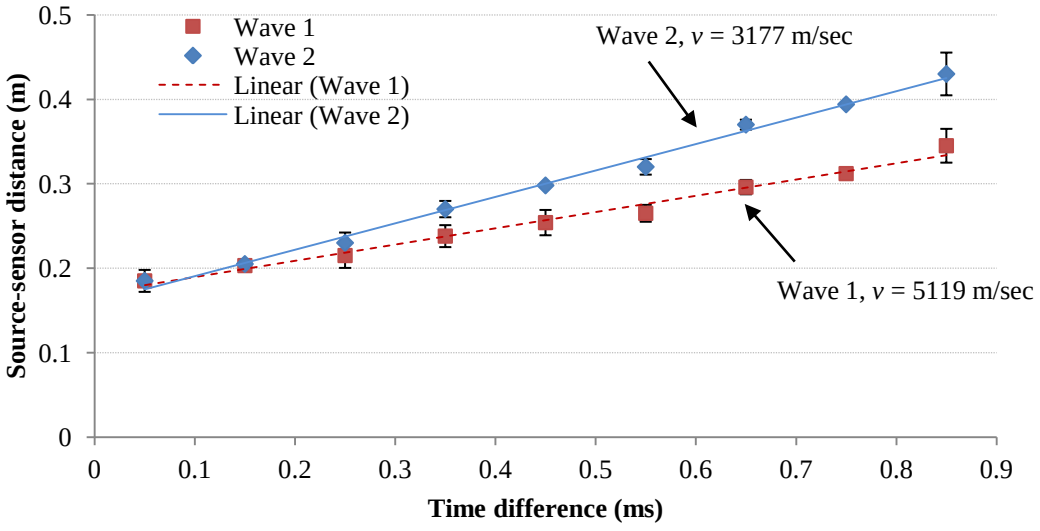

Figure 5.5: Wave speed estimation for tests on steel plate with source at the centre.

Figures 5.6 to 5.9 show examples of the measured AE energy level plotted on a logarithmic scale against source-sensor distance for each of the four small steel shapes; block, plate, strip and cylinder, respectively. Three sensors were mounted in two arrays to give six different source-sensor distances and the results of the repeat tests are shown separately, with the range of values recorded by each of the pencil lead breaks being shown as error bars. As can be seen, the fit to the exponential curve is generally good except for three of the experiments, two on the block and one on the plate. Also, although there is some variation in exponential decay constant (k) between the repeat tests, the values of k are identifiably different for each of the solid shapes, being significantly larger on the cylinder than on any of the other shapes, due to the wave reflecting from edges and from bottom of the cylinder.

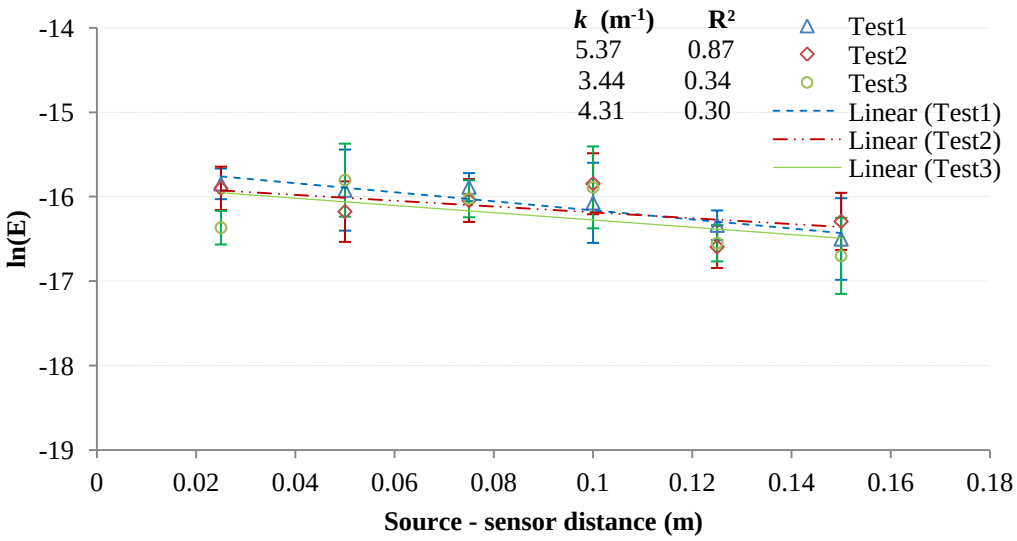

Figure 5.6: Experimental AE attenuation in steel block, source at the centre.

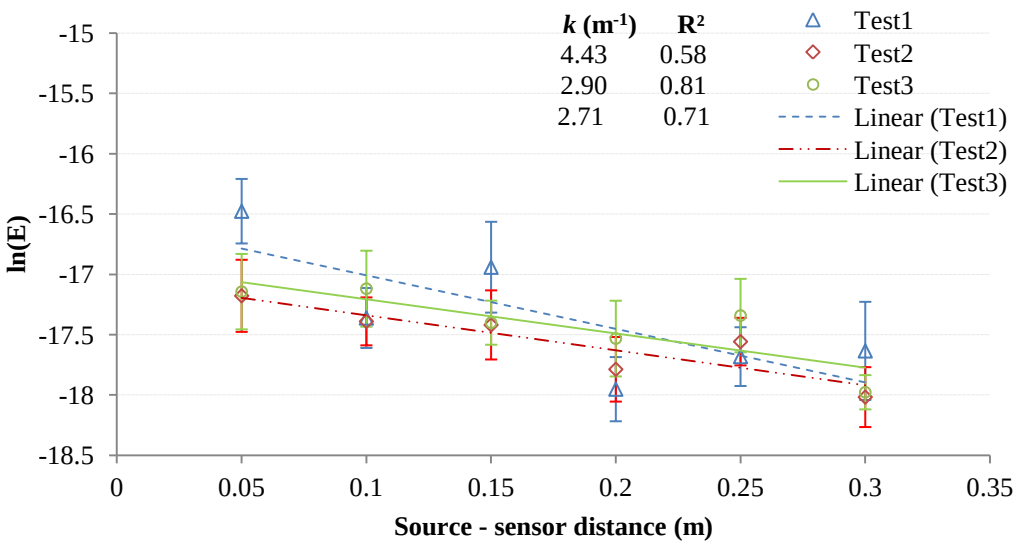

Figure 5.7: Experimental AE attenuation in steel plate, source at the centre.

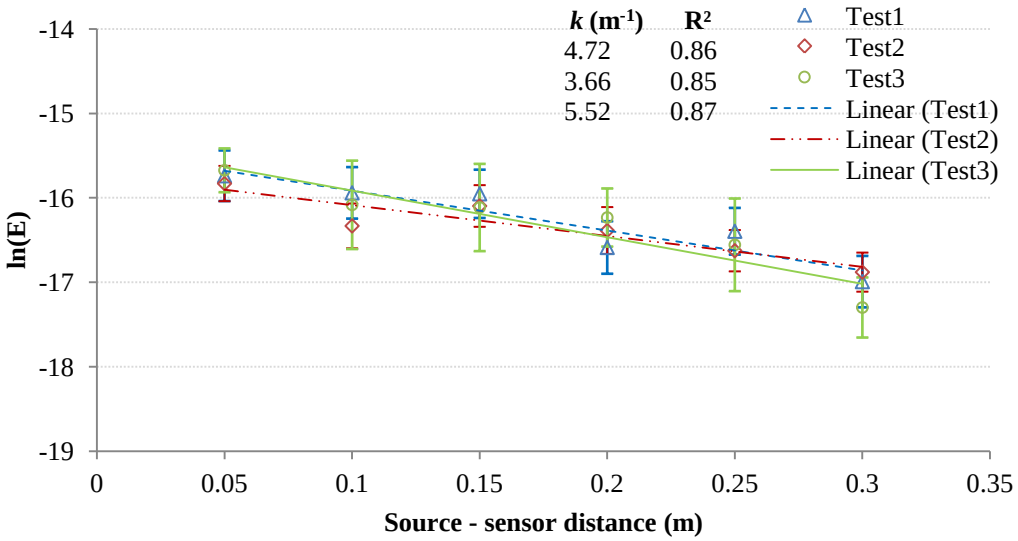

Figure 5.8: Experimental AE attenuation in steel strip, source at the centre.

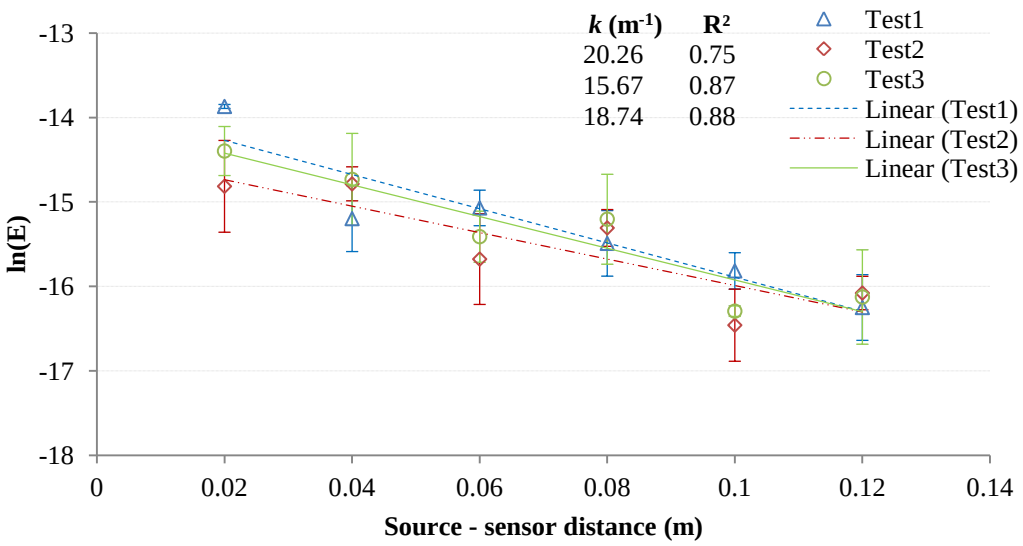

Figure 5.9: Experimental AE attenuation in steel cylinder, source at the centre.

5.2.2 Simulation results on small solid shapes

There are three main factors that can affect the simulation predictions; resolution (number of fired rays), ray extinction time (maximum allowed path length) and number of reflections allowed. To simplify the sensitivity analysis, the number of reflections allowed was not limited separately, although the extinction time will ultimately prevent excessive numbers of reflections. Thus, the number of rays fired and extinction time were varied systematically for simulated sensor positions in the same range as the experiments for each of the small objects. For each simulation, the slope of the logarithm of the energy recorded versus position (i.e. k') was calculated by fitting a straight line to the simulated energy profile.

Tables 5.4 to 5.11 show the effect of resolution and extinction time on the value of k' for bulk and surface rays on the block, plate, strip and cylinder, all with the source at the centre. As can be seen, there are two dimensions of convergence to a stable value of k' in the simulation; for a given resolution there is eventual convergence with increasing extinction time, and for a given converged extinction time, there is eventual convergence with increasing resolution. The shaded areas in the tables show the values of resolution and extinction time for which convergence has been achieved in both

dimensions. The simulated attenuation coefficients for bulk rays and surface rays on the four shapes studied all comfortably converged within the 11,000 fired rays and 1400 μsec extinction time envelope. For surface rays, at the highest resolution, the extinction times at which convergence was achieved were; 900μsec for the block, 1200 μsec for the plate 600 μsec for the strip, which is in approximate proportion to their widths, and 200 μsec for the cylinder.

Given a surface wave speed of 3177 m/s the extinction distances correspond to between 4 and 10 object widths. For bulk rays, convergence requires higher resolutions and, at the highest resolution, extinction times of about 600 μsec were needed. Given that the sample depths are about one tenth to one hundredth the width, this means that the average internal ray undergoes many more reflections than a surface ray, which is to be expected. The situation is more intense for the thinner objects where a smaller proportion of multiply reflected rays are removed by extinction and the simulations rapidly become filled with rays which would not, in real cases, reach a sensor. An average of 10 ray reflections occurred at convergence for the cylinder (surface area = 740 cm^2), 20 ray reflections for the block (surface area = 1225 cm^2), 30 ray reflections the strip (surface area = 1866 cm^2) and 50 ray reflection for the plate (area = 10000cm^2).

	No. of fired rays						
Extinction time (μsec)		**625**	**2,500**	**5,625**	**10,000**	**15,625**	**22,500**
	100	5.8	6.8	1.8	11.4	9.4	9.1
	200	2.05	3.9	3.5	7.04	4.17	4.08
	300	1.86	3.9	4.1	4.2	3.97	4.07
	600	2.38	4.07	4.11	3.7	3.91	3.92
	900	2.24	3.2	4.12	3.02	3.91	3.91
	1200	2.22	3.03	4.13	3.01	3.9	3.91
	1400	2.22	2.03	4.13	3.01	3.9	3.91

Table 5.4: Convergence of AE simulation for internal rays on block with source at centre (*k'* values in m^{-1})

	No. of fired rays						
Extinction time (µsec)		625	2,500	5,625	10,000	15,625	22,500
	100	6.04	6.85	8.17	7.55	8.81	8.42
	200	5.23	6.16	6.56	6.33	5.41	4.45
	300	5.73	5.68	5.51	3.93	4.39	4.44
	600	5.46	5.82	4.84	3.45	4.61	4.42
	900	5.46	5.61	4.95	4.05	4.42	4.41
	1200	5.46	5.61	4.95	3.92	4.4	4.4
	1400	5.46	5.61	4.95	3.82	4.42	4.4

Table 5.5: Convergence of AE simulation for internal rays on plate with source at centre (*k′* values in m^{-1})

	No. of fired rays						
Extinction time (µsec)		625	2,500	5,625	10,000	15,625	22,500
	100	8.5	10.73	10.47	11.64	8.96	9.7
	200	2.16	4.18	6.04	4.5	4.06	4.25
	300	2.85	4.35	4.18	4.56	4.05	3.97
	600	2.67	4.32	3.33	4.94	3.59	3.51
	900	2.64	4.32	3.34	3.88	3.46	3.53
	1200	2.68	4.32	3.32	3.86	3.46	3.53
	1400	2.68	4.32	3.32	3.81	3.46	3.53

Table 5.6: Convergence of AE simulation for internal rays on strip with source at centre (*k′* values in m^{-1})

	No. of fired rays						
Extinction time (µsec)		625	2,500	5,625	10,000	15,625	22,500
	100	0	0	0	0	0	0
	200	11.9	13.6	17.9	18.1	17.2	17.2
	300	16.1	16.5	19.9	16.8	17.7	16.3
	600	16.1	16.5	15.9	17.1	16.5	16.5
	900	16.1	16.5	17.9	16.8	16.5	16.5
	1200	16.1	16.5	17.9	16.8	16.5	16.5
	1400	16.1	16.5	17.9	16.8	16.5	16.5

Table 5.7: Convergence of AE simulation for internal rays on cylinder with source at centre (*k′* values in m^{-1})

	No. of fired rays					
Extinction time (µsec)	250	1,000	2,500	4,800	7,500	11,000
100	7.64	6.43	6.14	6.75	5.59	6.13
200	5.83	6.2	5.2	5.14	5.17	5.07
300	5.64	5.44	5.13	4.95	4.86	4.84
600	5.12	4.73	5.41	4.14	4.15	4.14
900	5.13	4.67	4.52	4.04	4.07	4.05
1200	5.07	4.71	4.52	4.06	4.06	4.05
1400	5.07	4.71	4.52	4.06	4.06	4.05

Table 5.8: Convergence of AE simulation for surface rays on block with source at centre (*k'* values in m^{-1})

	No. of fired rays					
Extinction time (µsec)	250	1,000	2,500	4,800	7,500	11,000
100	0	0	0	0	0	0
200	4.85	4.87	4.76	4.7	4.7	4.65
300	4.85	4.37	4.72	4.72	4.7	4.65
600	2.94	3.59	4.3	3.99	3.86	3.81
900	2.94	3.53	3.79	3.73	3.71	3.72
1200	4.85	3.43	3.68	3.67	3.71	3.71
1400	2.85	3.43	3.68	3.67	3.71	3.71

Table 5.9: Convergence of AE simulation for surface rays on plate with source at centre (*k'* values in m^{-1})

	No. of fired rays					
Extinction time (µsec)	250	1,000	2,500	4,800	7,500	11,000
100	0	0	0	0	0	0
200	4.22	4.69	4.56	4.57	4.52	3.9
300	4.08	3.32	4.23	4.25	4.21	4.16
600	5.16	4.1	4.46	3.8	3.5	3.52
900	4.22	4.52	3.93	3.72	3.81	3.81
1200	4.25	4.35	3.92	3.72	3.82	3.82
1400	4.25	4.35	3.92	3.72	3.83	3.82

Table 5.10: Convergence of AE simulation for surface rays on strip with source at centre (*k'* values in m^{-1})

	No. of fired rays						
Extinction time (μsec)		250	1,150	2630	4,800	7,500	11,000
	100	18.2	17	19	19.2	19.2	19.2
	200	15.7	16.8	15.5	16.3	16.3	16.3
	300	15.7	16.8	17.5	16.3	16.3	16.3
	600	17.7	15.8	16.5	16.3	16.3	16.3
	900	15.7	16.8	16.5	16.3	16.3	16.3
	1200	15.7	16.8	16.5	16.3	16.3	16.3
	1400	15.7	16.8	16.5	16.3	16.3	16.3

Table 5.11: Convergence of AE simulation for surface rays on cylinder with source at centre (*k′* values in m^{-1})

Figures 5.10 to 5.13 show examples of the relationship between the hit ratio and source-sensor distance for internal rays, surface rays and the two combined at convergence; 15625, 7500 and 23125 fired rays and 900 μsec for the internal, surface and combined rays, respectively. These are plotted in a similar manner to the corresponding attenuation measurements (Figures 5.2 to 5.5) and, as can be seen, the fit for surface rays to an exponential curve is generally good, whereas, for internal rays, the evolution is not always smooth and not always exponential. Also, the contribution from internal rays is usually significantly less than from surface rays.

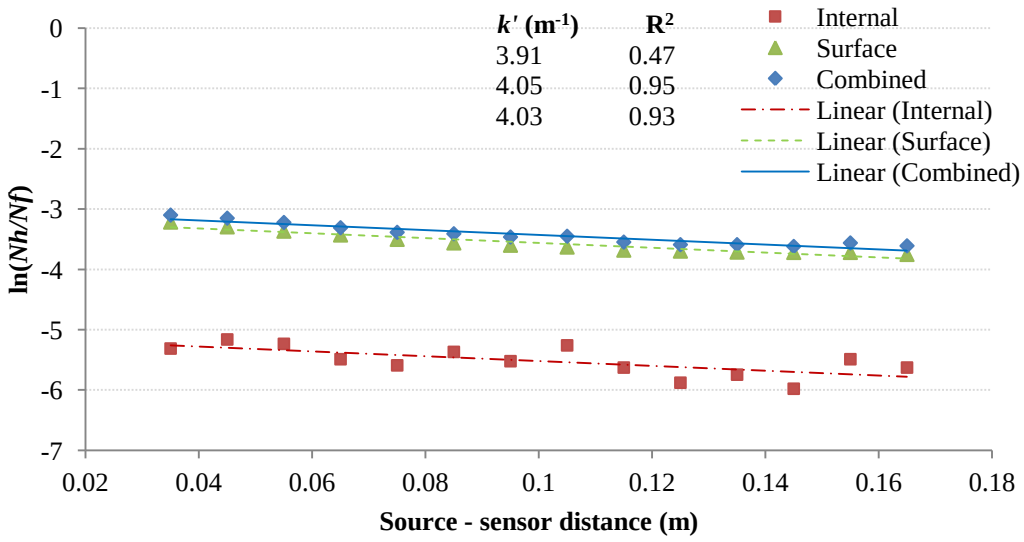

Figure 5.10: Predicted internal, surface and combined ray attenuation on steel block, source at the centre, at 15625, 7500 and 23125 fired rays and 900 μsec

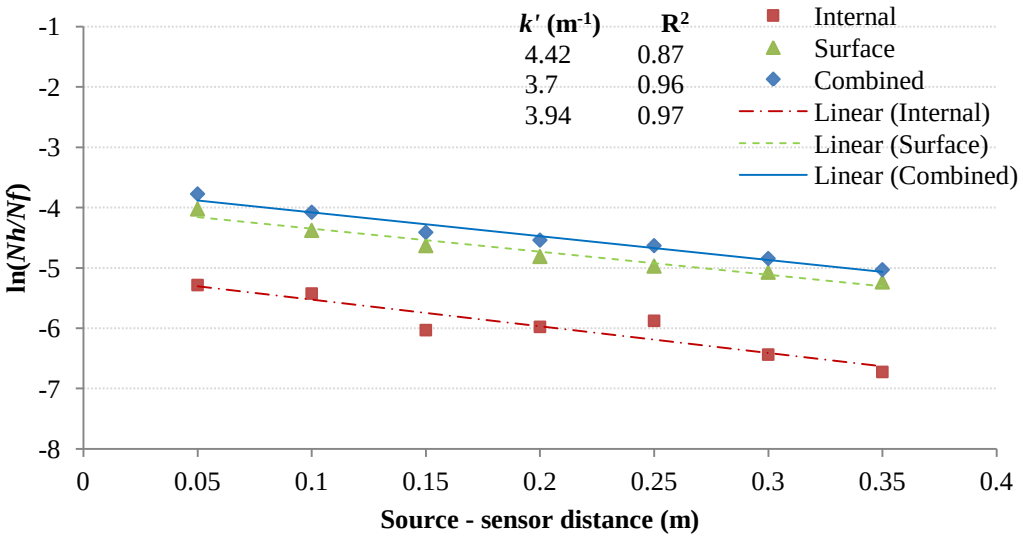

Figure 5.11: Predicted internal, surface and combined rays attenuation on steel plate, source at the centre, at 15625, 7500 and 23125 fired rays and 900 µsec

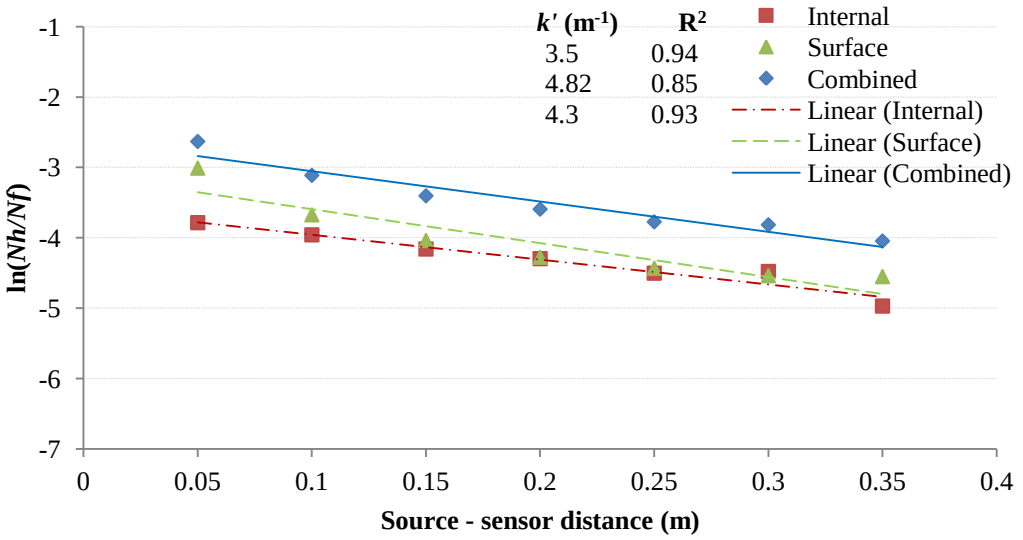

Figure 5.12: Predicted internal, surface and combined rays attenuation on steel strip, source at the centre, at 15625, 7500 and 23125 fired rays and 900 µsec

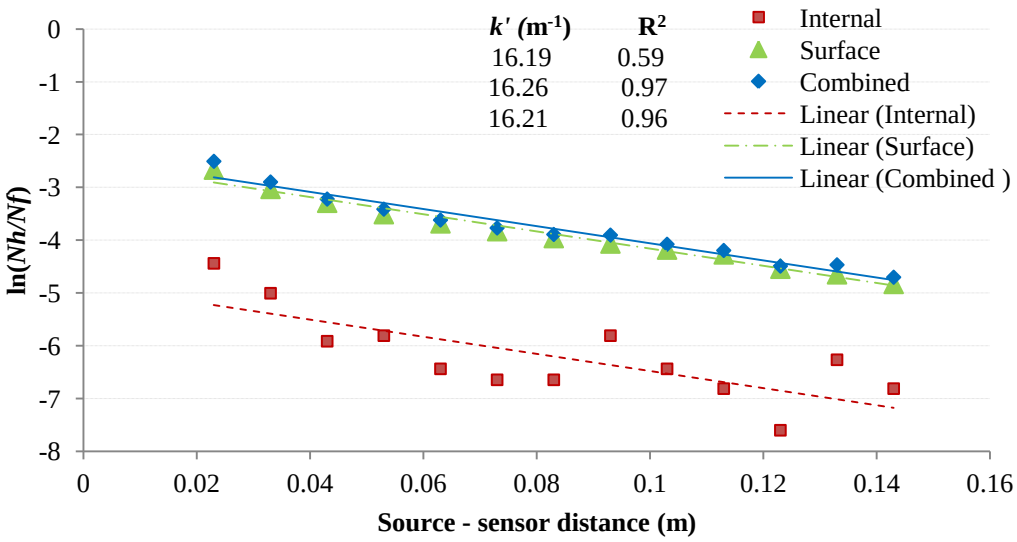

Figure 5.13: Predicted internal, surface and combined rays attenuation on steel cylinder, source at the centre, at 15625, 7500 and 23125 fired rays and 900 µsec

5.2.3 Comparison of measured results with simulations

All the attenuation measurement and simulation curves are shown in Appendix C. Table 5.12 summarises all of the measured attenuation coefficients for the block, plate, strip and cylinder, respectively. The effective attenuation coefficients, k_1, k_2 and k_3 are given for each of the repeat tests along with the corresponding correlation coefficients and the weighted means accordingly to Equation 5.1 are also found. Although there is some scatter in the log-linear plots, clear differences are discernible between the observed attenuation behaviour for the different configurations. Firstly, comparing the four shapes with the source at the centre, it appears that only the cylinder has significantly different attenuation than the others. Secondly, when the source is at an edge rather than at the centre, the attenuation is less and, when the source is at a corner, it is less still. Finally, when the source is on the end of a block, the attenuation only appears to be slightly less than it is for the source at the centre and more than it is for the source at the edge.

Similar attenuation effects, *k'*, can be seen in the simulations for internal rays, surface rays and combined rays, Table 5.13. Figures 5.14 and 5.15 show the weighted mean measured attenuation coefficients plotted against the simulated coefficients for

combined rays with and without the values for the cylinder. Both plots show a strong correlation, which suggests that the simulated and measured results are being driven by the same geometric changes. It might also be noted that the simulated attenuation coefficients are consistently lower (by about 20%) than the measured ones, which suggest that other mechanism than geometric spreading are active even in the small objects.

Shape	**Source**	**Effective attenuation coefficient, k (m^{-1})**			**Strength of linear correlation, R^2**			**Weighted mean, $\bar{k}$ (m^{-1})**
		k_1	k_2	k_3	R_1^2	R_2^2	R_3^2	
Block	**Centre**	5.37	3.44	4.31	0.87	0.34	0.3	4.72
	Edge	1.55	2.84	2.22	0.22	0.47	0.27	2.37
	Corner	1.01	1.47	2.43	0.1	0.47	0.54	1.90
	End	3.14	2.79	4.64	0.52	0.65	0.71	3.59
Plate	**Centre**	4.43	2.9	2.84	0.58	0.81	0.71	3.30
	Edge	2.27	1.73	1.49	0.9	0.81	0.76	1.85
	Corner	1.39	1.27	1.01	0.89	0.88	0.84	1.23
Strip	**Centre**	4.72	3.66	5.52	0.86	0.85	0.87	4.64
	Edge	2.41	1.69	2.15	0.79	0.86	0.93	2.08
	End	2.92	1.21	1.44	0.57	0.37	0.24	2.08
Cylinder	**Centre**	20.27	15.67	18.74	0.75	0.87	0.88	18.13
	Edge	3.42	4.76	3.09	0.55	0.68	0.57	3.82

Table 5.12 : Summary of measured attenuation results on small solid shapes

Shape	Source	Effective attenuation coefficient, k' (m^{-1})			Strength of linear correlation, R^2		
		Internal rays	Surface rays	Combined rays	Internal rays	Surface rays	Combined rays
Block	Centre	3.91	4.05	4.03	0.47	0.95	0.93
	Edge	1.38	2.77	2.43	0.63	0.4	0.43
	Corner	2.18	2.56	2.51	0.14	0.56	0.58
	End	1.5	5.5	4.3	0.04	0.95	0.93
Plate	Centre	4.2	3.7	3.94	0.87	0.96	0.97
	Edge	2.51	2.31	2.36	0.85	0.86	0.86
	Corner	2.26	1.64	1.7	0.74	0.81	0.8
Strip	Centre	3.53	4.82	4.3	0.94	0.85	0.93
	Edge	1.9	2.15	2.42	0.93	0.94	0.94
	End	2.71	2.07	2.13	0.32	0.93	0.82
Cylinder	Centre	16.19	16.21	16.26	0.59	0.97	0.96
	Edge	5.12	6.38	6.22	0.42	0.97	0.94

Table 5.13: Summary of geometric simulated attenuation results on small solid shapes

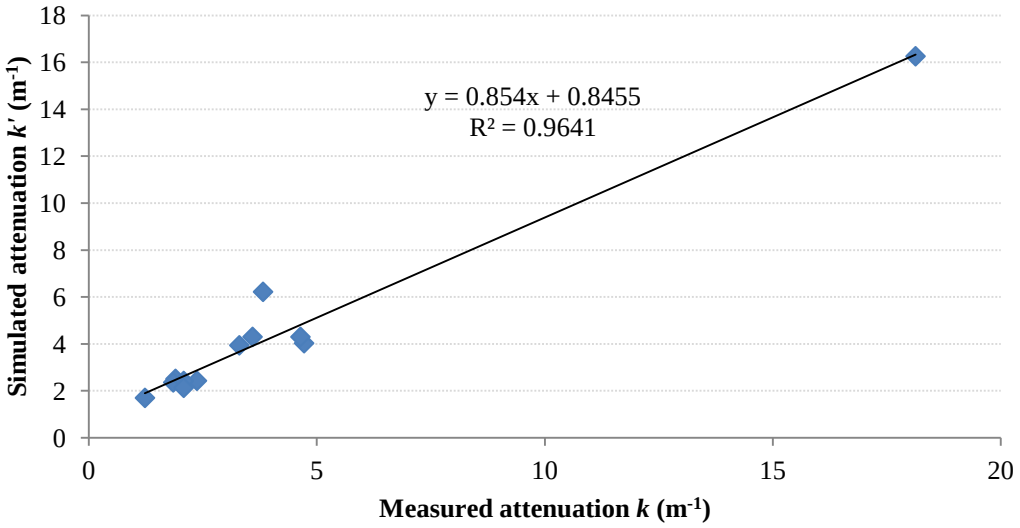

Figure 5.14: Weighted measured attenuation coefficients plotted against the simulated coefficient for combined rays with the values for the cylinder

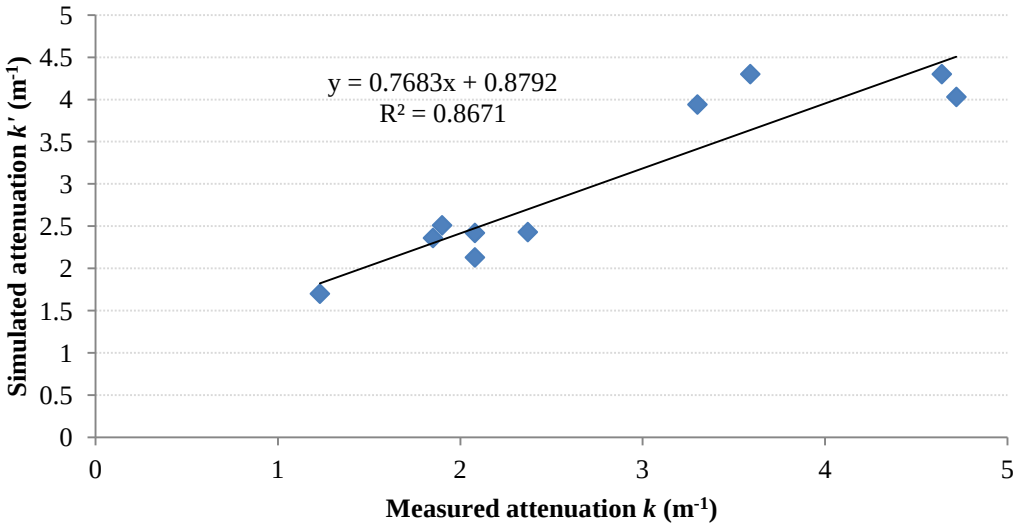

Figure 5.15: Weighted measured attenuation coefficients plotted against the simulated coefficient for combined rays without the values for the cylinder

5.3 Practical structures

Essentially the same approach was taken with the practical structures as for the idealised solid shapes, with the wave speeds first being determined and then the attenuation curves for both the measurements and simulations compared.

5.3.1 Laminated glass

Figure 5.16 shows the arrival times versus source-sensor distance for both the fast and slow waves on the laminated glass using a threshold of 0.02 of the maximum amplitude of the raw signal for Wave 1 and 0.35 of the maximum amplitude for Wave 2. Thus, the speeds of the fast and slow wave are 5574 m/s and 3363 m/s, respectively.

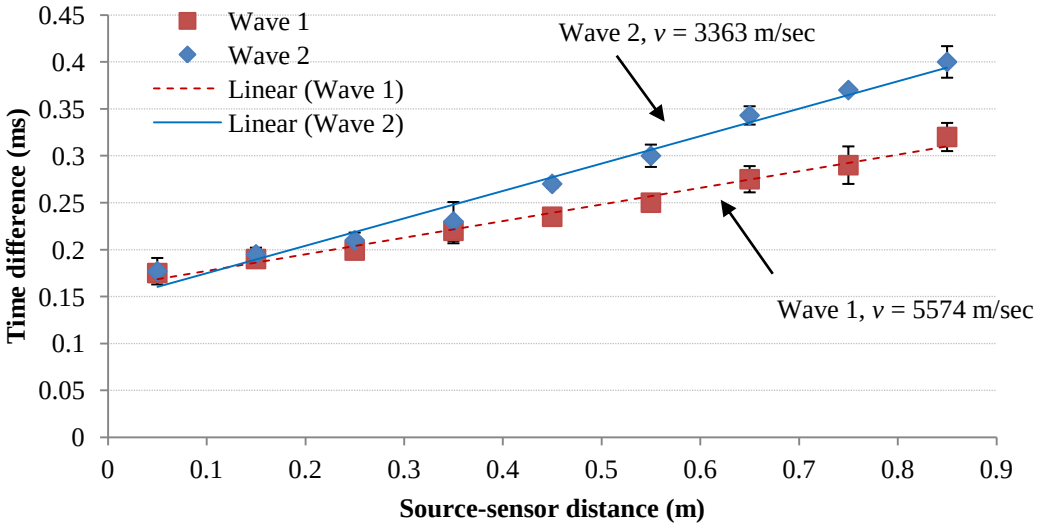

Figure 5.16: Wave speed estimation for laminated glass.

No additional tests with environments were done for the laminated glass, so Figures 5.17 to 5.19 show the experimental AE attenuation on the laminated glass for the three repeat tests for each of the source positions, centre, edge and corner, respectively. As can be seen, the fit and consistency between *k*-values was best with the source at the edge and variable with the source at the centre or corner. Even so, the *k*-value can be seen to be largest when the source is at the centre and smallest when the source is at the corner, which is consistent with the measurements on a similar size of steel plate.

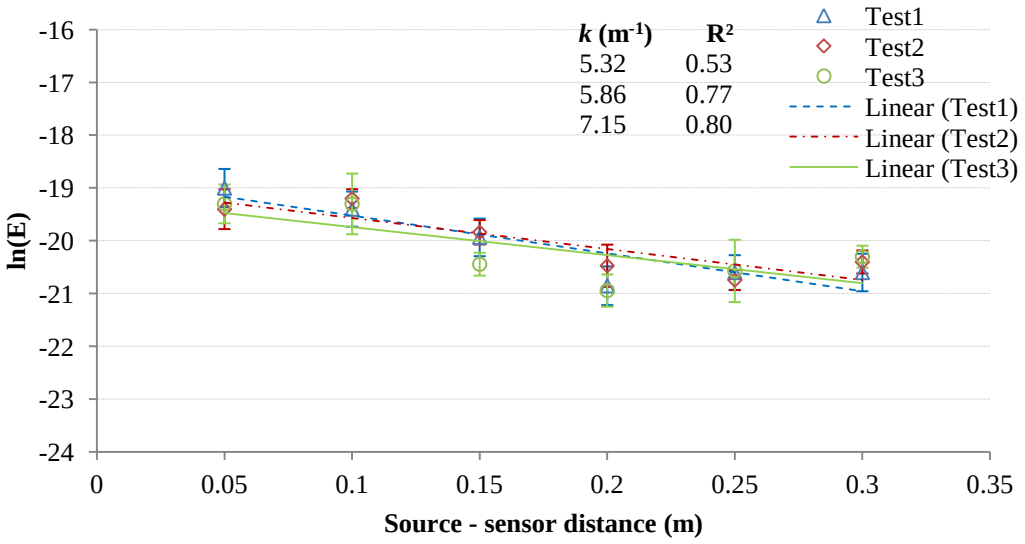

Figure 5.17: Experimental AE attenuation on laminated glass plate, source at the centre

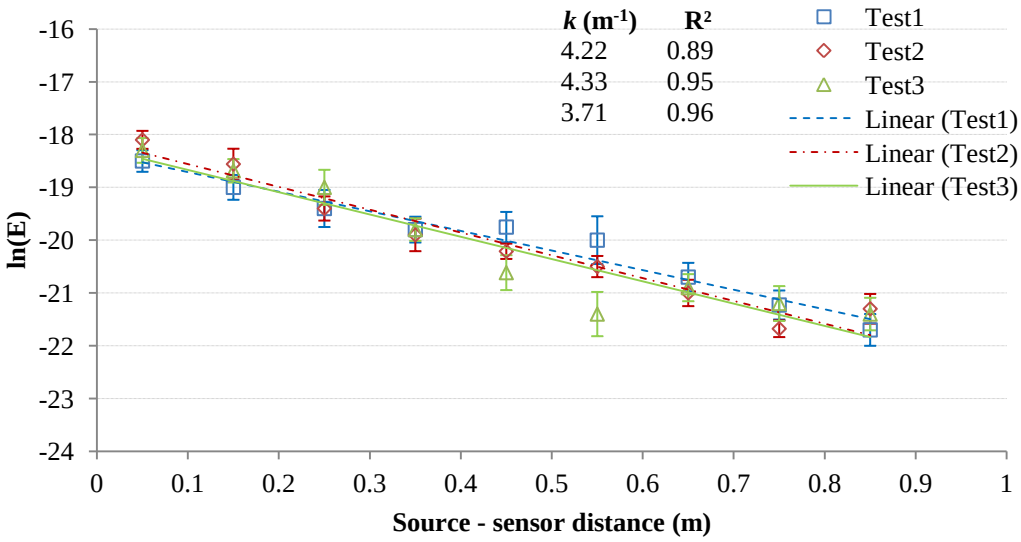

Figure 5.18: Experimental AE attenuation on laminated glass plate, source at the edge.

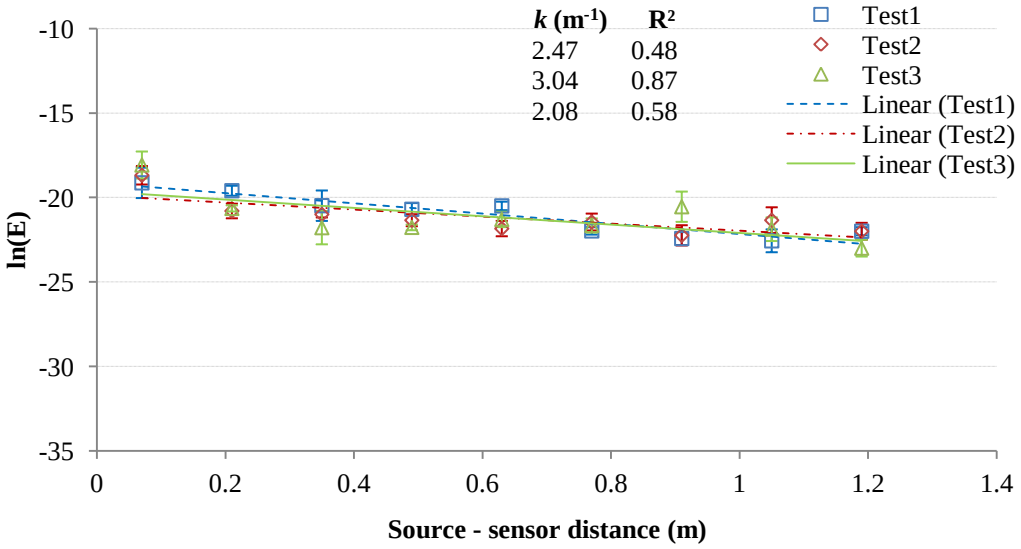

Figure 5.19: Experimental AE attenuation on laminated glass plate, source at the corner.

For the geometric attenuation simulation, the convergence behaviour (resolution and extinction time) for laminated glass was similar to the steel plate. Figures 5.20 to 5.22 show the simulated AE attenuation values for the laminated glass for converged internal rays, surface rays and the two combined. The same extinction criteria as for the small blocks was used here.

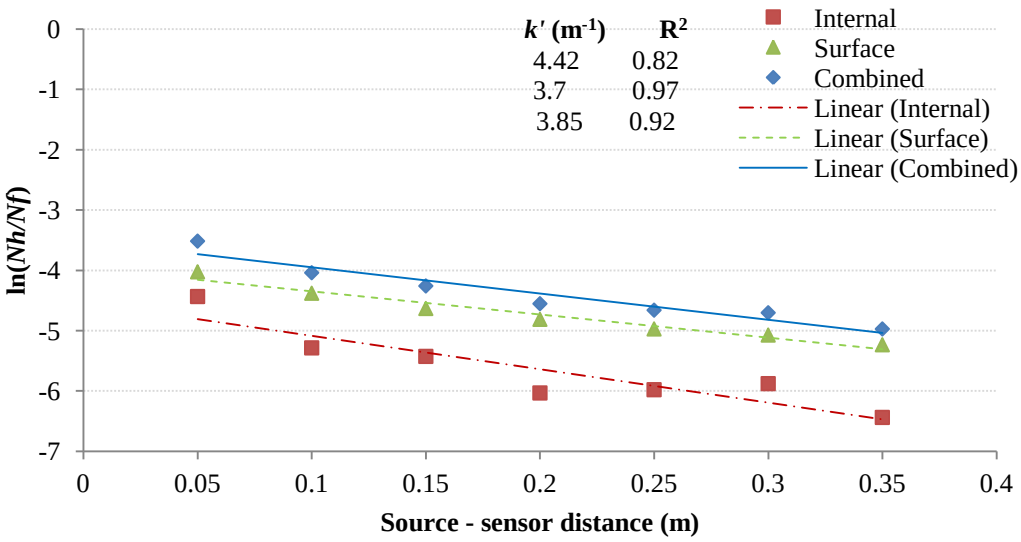

Figure 5.20: Simulated internal, surface and combined ray attenuation on laminated glass plate, source at the centre, at 15625, 7500 and 23125 fired rays and 900 µsec

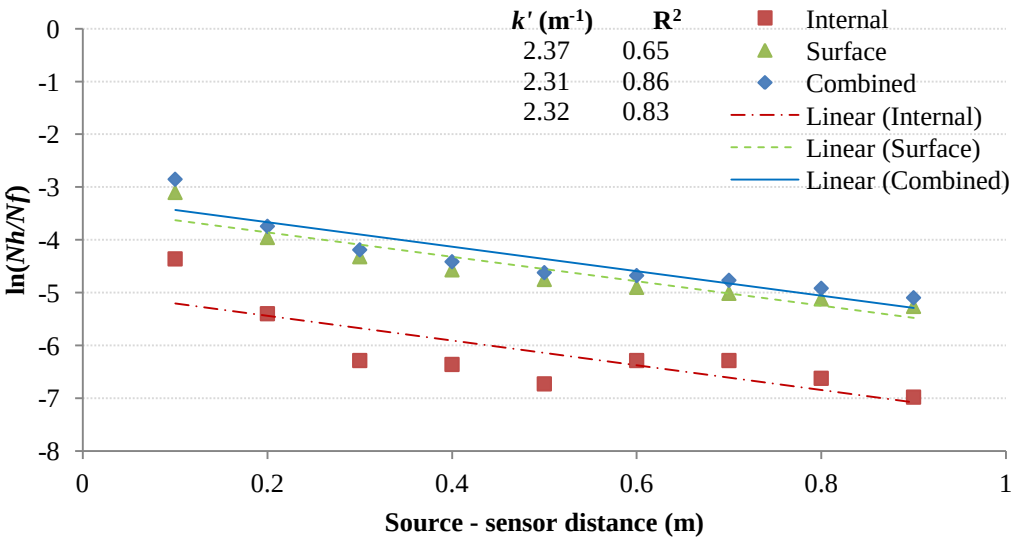

Figure 5.21: Simulated internal, surface and combined ray attenuation on laminated glass plate, source at the edge, at 15625, 7500 and 23125 fired rays and 900 µsec

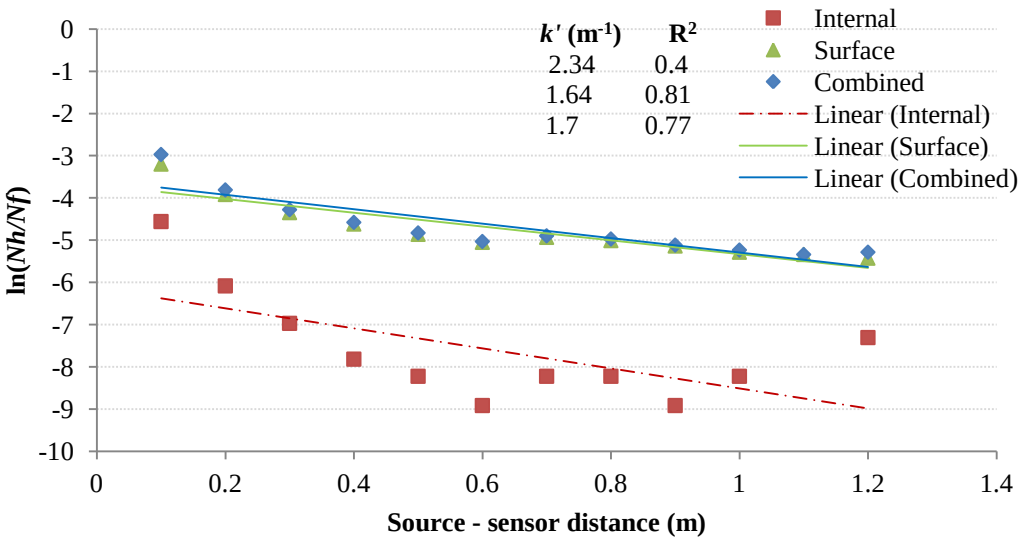

Figure 5.22: Predicted internal, surface and combined rays attenuation on a laminated glass plate, source at the corner, at 15625, 7500 and 23125 fired rays and 900 µsec

Tables 5.14 and 5.15 summarise all of the attenuation measurements and geometric simulations for the laminated glass. Again, clear differences are discernible between the observed attenuation behaviour for different source positions. It appears that, when the source is at an edge rather than at the centre, the attenuation is less and, when the source is at a corner, it is less still. These effects are seen in both the experimental and simulated results and are evident in both the surface and internal ray geometric simulations, and the simulations show suggest that surface rays dominate the response.

Source	Effective attenuation coefficient, k (m^{-1})			Strength of linear correlation, R^2			Weighted mean, $\bar{k}$ (m^{-1})
	k_1	k_2	k_3	R_1^2	R_2^2	R_3^2	
Centre	5.32	5.86	7.15	0.53	0.77	0.8	6.22
Edge	3.71	4.33	4.22	0.96	0.95	0.89	4.08
Corner	2.47	2.08	3.04	0.48	0.58	0.87	2.61

Table 5.14: Summary of measured attenuation results for each of the three positions on a laminated glass.

Source	Effective attenuation coefficient, k' (m^{-1})			Strength of linear correlation, R^2		
	Internal rays	Surface rays	Combined rays	Internal rays	Surface rays	Combined rays
Centre	4.2	3.7	3.85	0.82	0.97	0.92
Edge	2.37	2.31	2.32	0.65	0.86	0.83
Corner	2.34	1.64	1.7	0.4	0.81	0.77

Table 5.15: Summary of geometric simulated attenuation results in laminated glass with 50 internal ray reflections and 10 surface ray reflections.

The simulation results in Table 5.15 are very close to those for the steel plate, despite the measured attenuation being higher. However, by reducing the allowed number of reflections to 35 for internal rays and 5 for surface rays, the simulations are much closer to the measured results (Table 5.16), although the surface rays still dominate the response.

Source	Effective attenuation coefficient, k' (m^{-1})			Strength of linear correlation, R^2		
	Internal rays	Surface rays	Combined rays	Internal rays	Surface rays	Combined rays
Centre	6.4	5.55	5.67	0.66	0.94	0.97
Edge	5.02	2.97	3.15	0.76	0.84	0.84
Corner	3.61	2.34	2.64	0.86	0.91	0.90

Table 5.16: Summary of geometric simulated attenuation results in laminated glass with 35 internal reflections and 5 surface reflections.

5.3.2 Large stainless steel vessel

Figure 5.23 shows the fast and slow wave speeds for the stainless steel tank to be 5213 m/s and 3188 m/s, respectively.

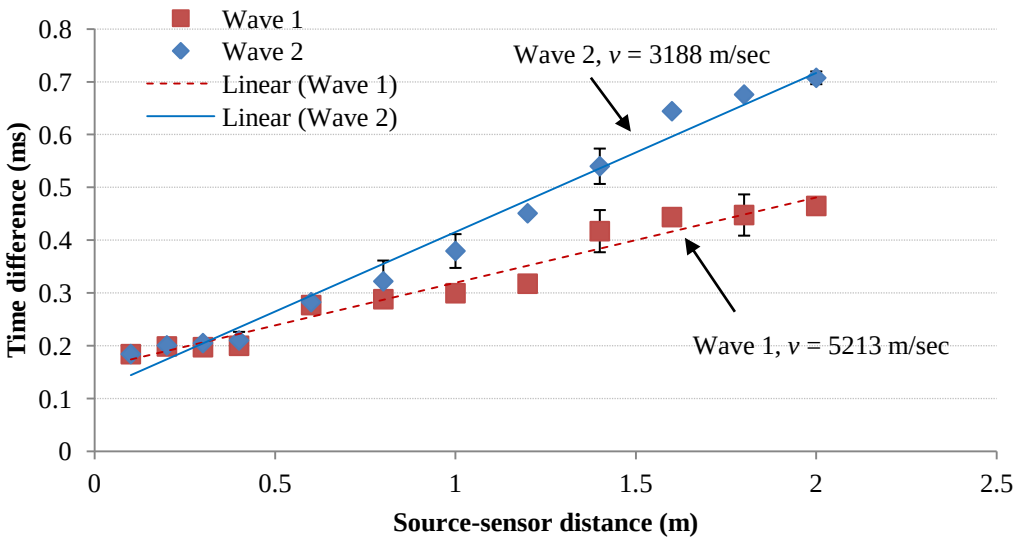

Figure 5.23: Wave speed estimation on the stainless steel vessel.

Figures 5.24 and 5.25 show the experimental AE attenuation for the vessel for the longitudinal and circumferential arrays, respectively. As can be seen, the results for the longitudinal sensor array are more consistent and fit the exponential decay rather better than for the circumferential array. The longitudinal sensor attenuation coefficient also seems to be higher than the circumferential one.

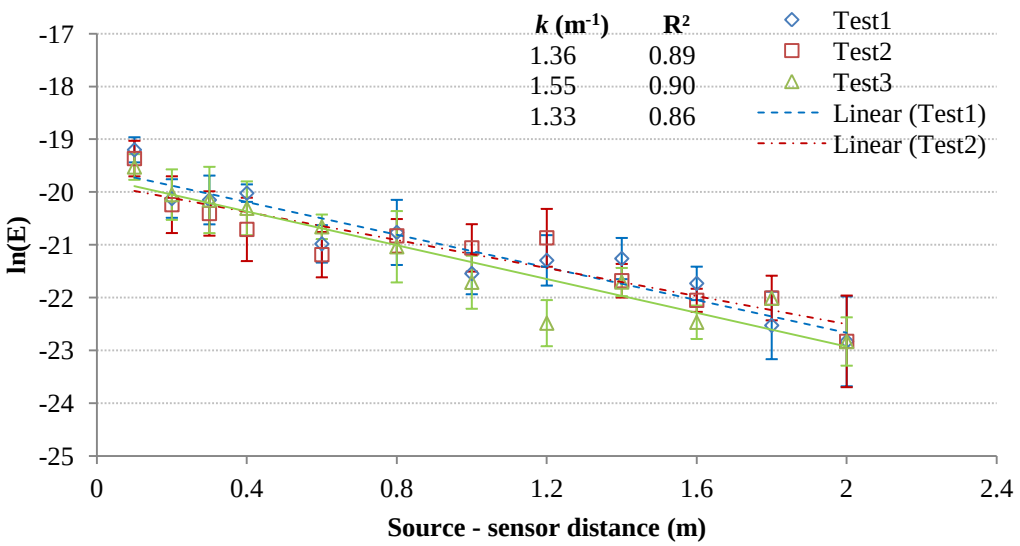

Figure 5.24: Experimental attenuation curves for stainless-steel vessel, longitudinal sensor array.

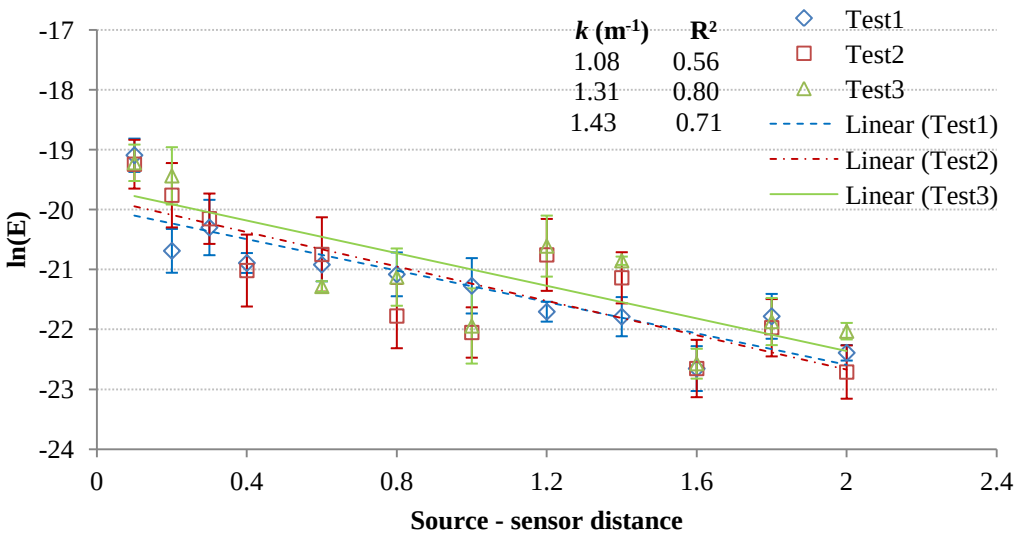

Figure 5.25: Experimental attenuation curves for stainless-steel vessel, circumferential sensor array.

Tables 5.17 and 5.18, show the effect of resolution and extinction time on the value of k' for bulk and surface rays on the vessel with the longitudinal sensor array, the shaded areas in the tables showing the values of resolution and extinction time for which convergence has been achieved. The surface area for the cylinder is much higher than the other structures that have been considered, around 18m^2, and it was necessary to increase the extinction time to 1200µsec to allow a longer path length (6.3m). For the internal rays, the number of allowed reflections was increased to 100 and, to simplify the simulation of surface rays, the vessel was considered to be a plate with the axial seam allowing 100% reflection.

	No. of fired rays					
Extinction time (µsec)		**625**	**2,500**	**6,400**	**10,000**	**12,100**
	300	2.67	0.98	1.75	2.19	2.15
	600	1.09	0.98	0.88	1.48	1.46
	900	1.09	0.98	0.88	1.55	1.55
	1200	1.09	0.98	0.88	1.58	1.58
	1400	1.09	0.98	0.88	1.58	1.58

Table 5.17: Convergence of AE simulation for internal rays on vessel with longitudinal sensor array (k' values in m^{-1})

	No. of fired rays					
Extinction time (μsec)		**1,000**	**2,500**	**4,800**	**7,500**	**10,000**
	300	0	0	0	0	0
	600	1.13	1.18	1.19	1.19	1.19
	900	1.13	1.18	1.19	1.19	1.19
	1200	1.13	1.18	1.19	1.19	1.19
	1400	1.13	1.18	1.19	1.19	1.19

Table 5.18: Convergence of AE simulation for surface rays on vessel with longitudinal sensor array (*k'* values in m^{-1})

Figures 5.26 and 5.27 show the resulting simulations for the longitudinal and circumferential arrays, respectively, for internal rays, surface rays and combined rays.

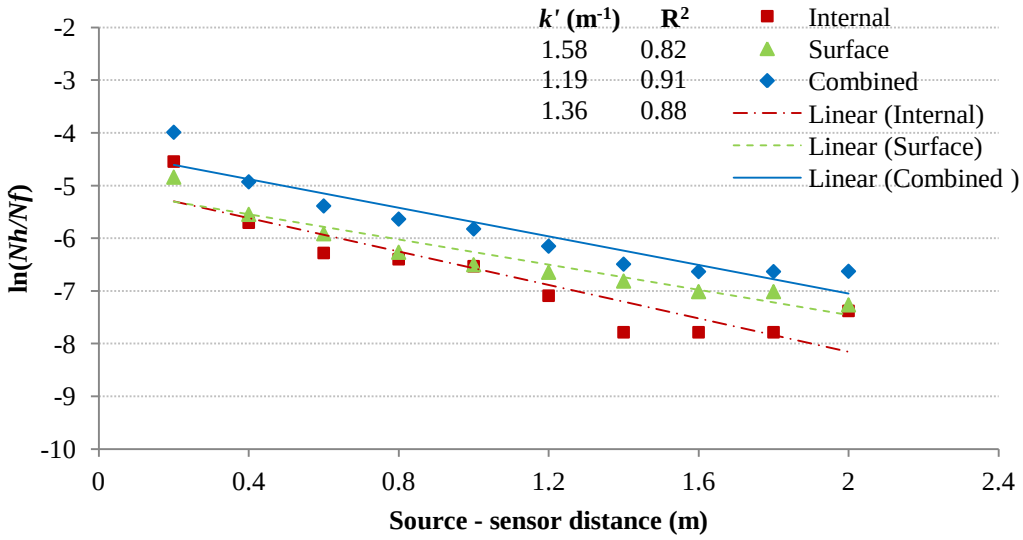

Figure 5.26: Simulated attenuation for internal, surface and combined rays on stainless steel vessel, with longitudinal sensor array, at 10000, 7500 and 17500 fired rays and 1200 μsec extinction time.

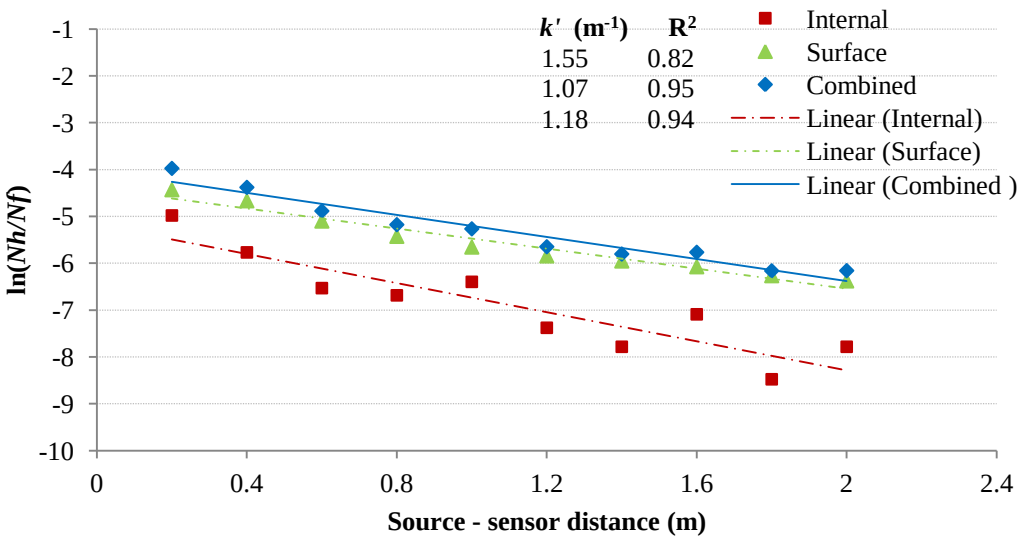

Figure 5.27: Simulated attenuation for internal, surface and combined rays on stainless steel vessel, with circumferential sensor array, at 10000, 7500 and 17500 fired rays and 1200 µsec extinction time.

Tables 5.19 and 5.20 summarise the attenuation coefficients for the vessel. Again, the agreement between simulated and measured values is good, even to the extent of the slight increase in attenuation coefficient for the longitudinal array.

Sensor array	Effective attenuation coefficient, k (m^{-1})			Strength of linear correlation, R^2			Weighted mean, $\bar{k}$ (m^{-1})
	k_1	k_2	k_3	R_1^2	R_2^2	R_3^2	
Longitudinal	1.36	1.55	1.33	0.89	0.90	0.86	1.41
Circumferential	1.08	1.31	1.43	0.56	0.80	0.71	1.29

Table 5.19: Summary of measured attenuation coefficients for stainless steel vessel

Sensor array	Effective attenuation coefficient, k' (m^{-1})			Strength of linear correlation, R^2		
	Internal rays	Surface rays	Combined rays	Internal rays	Surface rays	Combined rays
Longitudinal	1.58	1.19	1.36	0.82	0.91	0.88
Circumferential	1.55	1.07	1.18	0.82	0.95	0.94

Table 5.20: Summary of simulated geometric attenuation coefficients for stainless steel vessel

5.3.3 Long steel pipe

Figure 5.28 shows the experimental AE attenuation measurements on the long pipe, only one sensor was used, moved to 13 different positions, the 10 pencil lead breaks being taken at each position, without removal and replacement of the sensor at the same position.

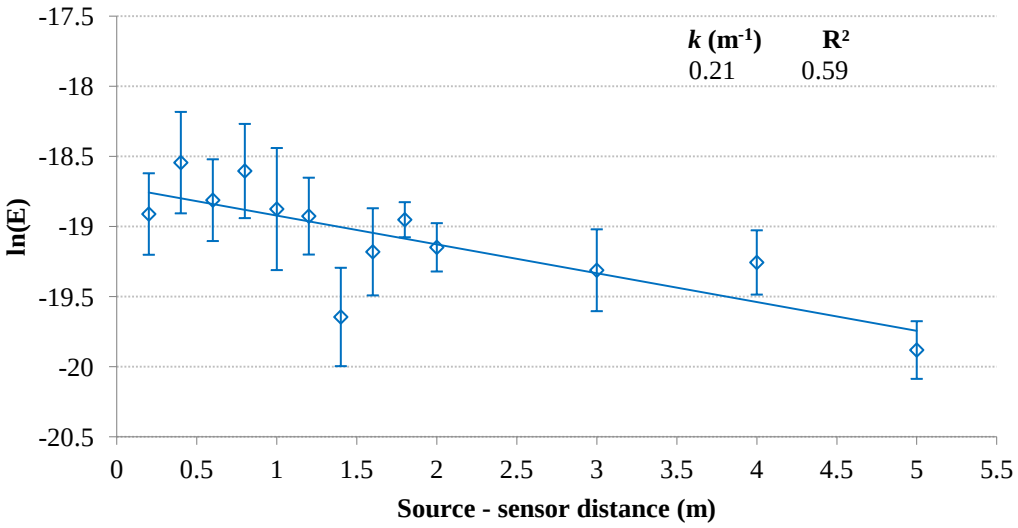

Figure 5.28: Experimental attenuation curve for long steel pipe, source at the end [28]

As with the vessel, it was necessary to consider the pipe to be a flat plate for the purposes of simulation. Tables 5.21 and 5.22 show, as before, the effect of resolution and extinction time on the convergence of *k* for bulk and surface rays on the pipeline, at the fast and slow wave speeds 5219 m/s and 4022 m/s [73], respectively.

	No. of fired rays					
Extinction time (µsec)		**625**	**2,500**	**64,00**	**10,000**	**12,100**
	300	2.35	2.02	3.02	3.33	2.56
	600	1.42	1.58	1.31	1.67	1.72
	900	0.4	1.58	0.84	1.1	1.12
	1200	0.4	0.32	0.6	0.53	0.53
	1400	0.4	0.32	0.6	0.53	0.53

Table 5.21: Convergence of AE simulation for internal rays on pipeline (*k'* values in m^{-1})

	No. of fired rays					
Extinction time (µsec)		**1,000**	**2,500**	**4,800**	**7,500**	**10,000**
	300	0	0	0	0	0
	600	0	0	0	0	0
	900	0	6.4	5.36	5.68	5.86
	1200	0.19	0.49	0.61	0.55	0.55
	1400	0.19	0.49	0.61	0.54	0.55

Table 5.22: Convergence of AE simulation for surface rays on pipeline (k' values in m^{-1})

Figure 5.29 shows the simulated attenuation curve at convergence. This time, there is a substantial difference in the simulated and measured values of the attenuation coefficient, the simulations indicating significantly much more attenuation than the measurements.

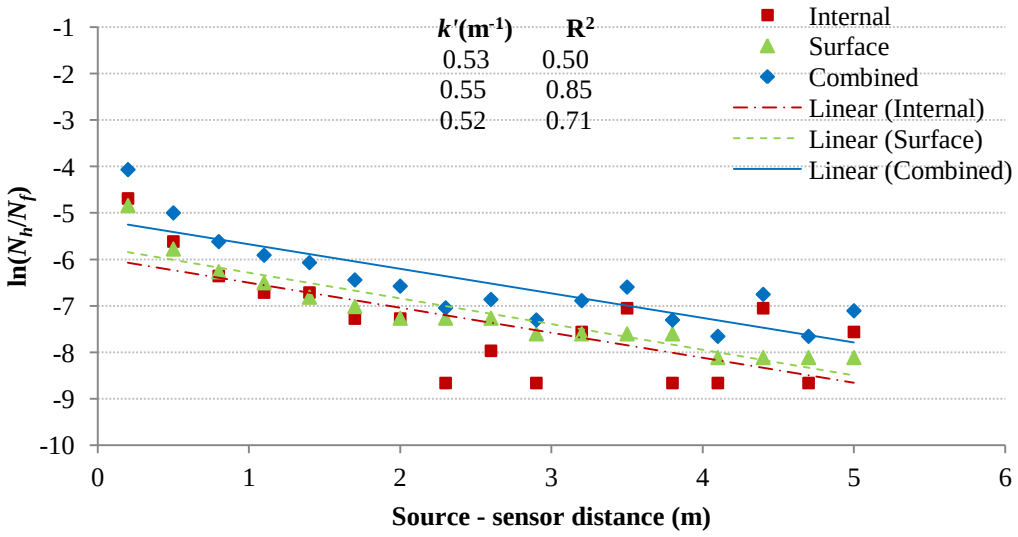

Figure 5.29: Simulated internal, surface and combined ray attenuation on pipeline, at 10000, 7500 and 17500 fired rays and 1200 µsec extinction time

5.4 Discussion

The values of the attenuation coefficient described in this chapter are summarized in Figures 5.30 to 5.32. Overall, the simulated results show a remarkable similarity to the measured ones, mirroring the effects of shape and material and even some of the subtle changes such as the axial and circumferential effects in the stainless steel vessel. In general the larger shapes than the smaller ones, such as the pipeline and vessel showed lower attenuation, and the solid cylinder showed significantly greater attenuation than the other small objects. Generally, the simulated attenuation coefficient were about 20% lower than the measure one, a significant exception being the pipeline, where the simulated coefficients were more than double the measured ones.

The simulations show approximately the same attenuation for internal rays and surface rays, except in the larger structures where the internal rays are attenuated more. The differences between internal and surface rays are rarely greater than the experimental error in the measured values. There is little to distinguish the measured attenuation between the block and plate, although the internal simulation suggests less attenuation in the block, whereas the surface simulation suggests more. The measured attenuation in the strip is a little lower than for the other two rectangular cross-section shapes, although the surface simulation suggests more attenuation while the internal simulation suggests considerably less.

Although wave speeds are different, the simulation was not able to distinguish between the steel plate and the laminated glass, unless the extinction time and maximum allowed number of reflections was changed. The detailed interpretation of this is discussed further in the next chapter.

The pipe showed significantly lower attenuation than the large vessel, in both the experiment and the simulation and it is thought the reason for this was the difference between the source position in the two experiments. This was confirmed with a simulation of the pipeline with the source at the centre. Figure 5.33, shows clearly higher attenuation for the pipe with the source at the centre, close to the vessel attenuation.

The combined rays gave results very close to the simulation for the surface rays in most cases. This is because the surface rays travel in two dimensions and a higher proportion of those fired will hit a sensor mounted on the same surface without refelction.

Also, it has been noticed that there is a relationship between the solid model area (A), and the number of reflections of internal rays, large areas needing more reflections to give a stable AE attenuation prediction:

- $A < 1000\ cm^2$, 10 reflections
- $1000\ cm^2 < A < 10000\ cm^2$, 20 - 30 reflections
- $10000\ cm^2 < A < 20000\ cm^2$, 50 reflections
- $A > 20000\ cm^2$, 100 reflections

Overall, the set of simulation results have indicated that, although purely geometric effects can be replicated in the simulation, some improvements will be necessary using physically based simulation.

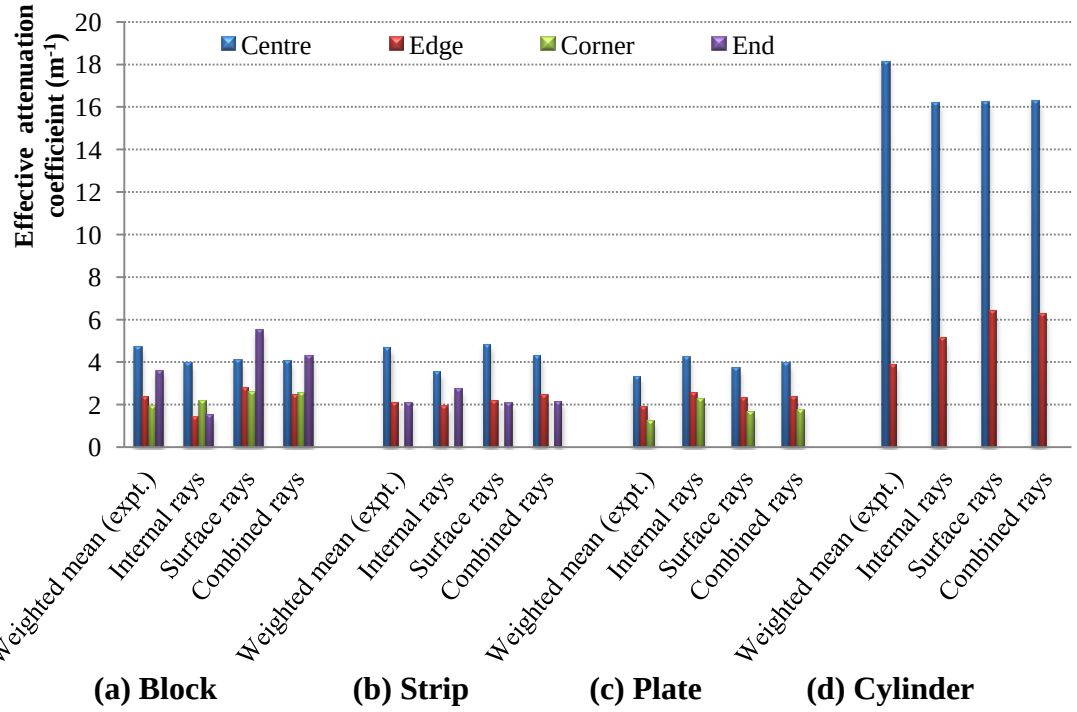

Figure 5.30: Comparison between experiments and simulation results for 4 small objects (block, strip, plate and cylinder).

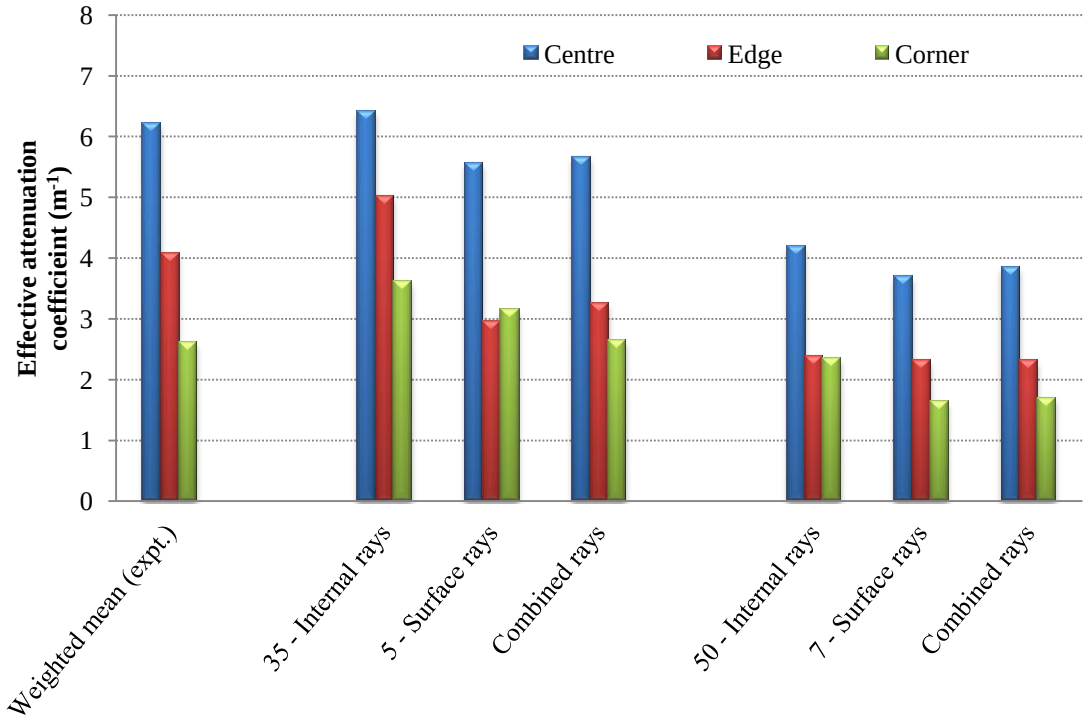

Figure 5.31: Comparison between experiments and simulation results for laminated glass with different allowed numbers of internal and surface ray reflections.

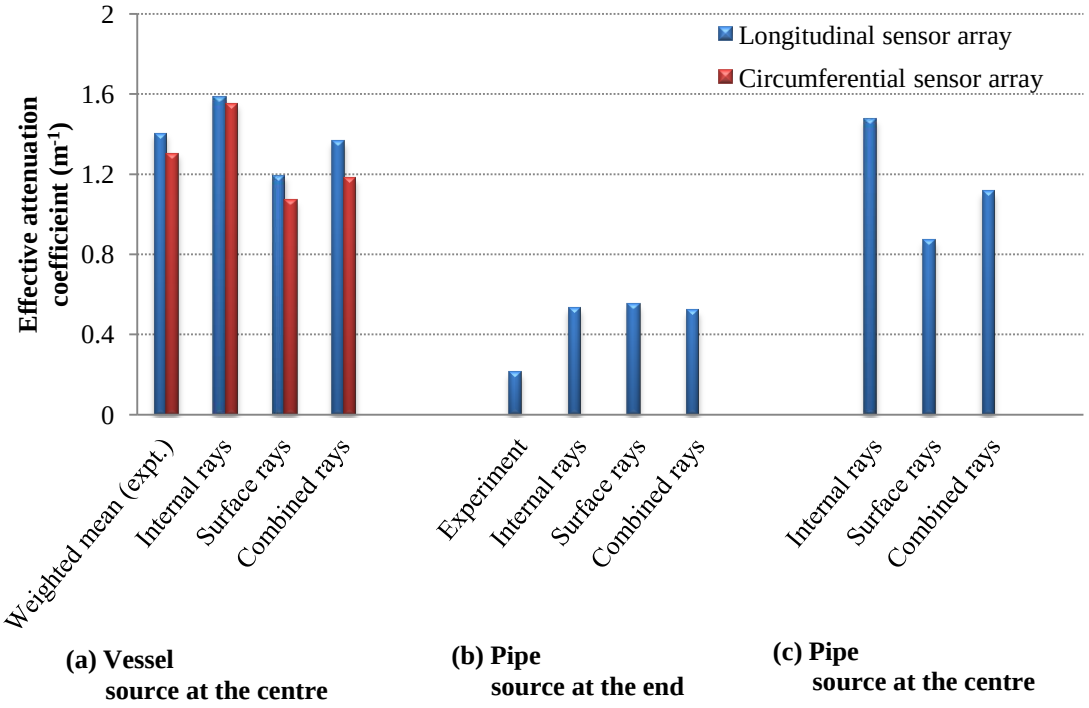

Figure 5.32: Comparison between experiments and simulation results for vessel and pipeline

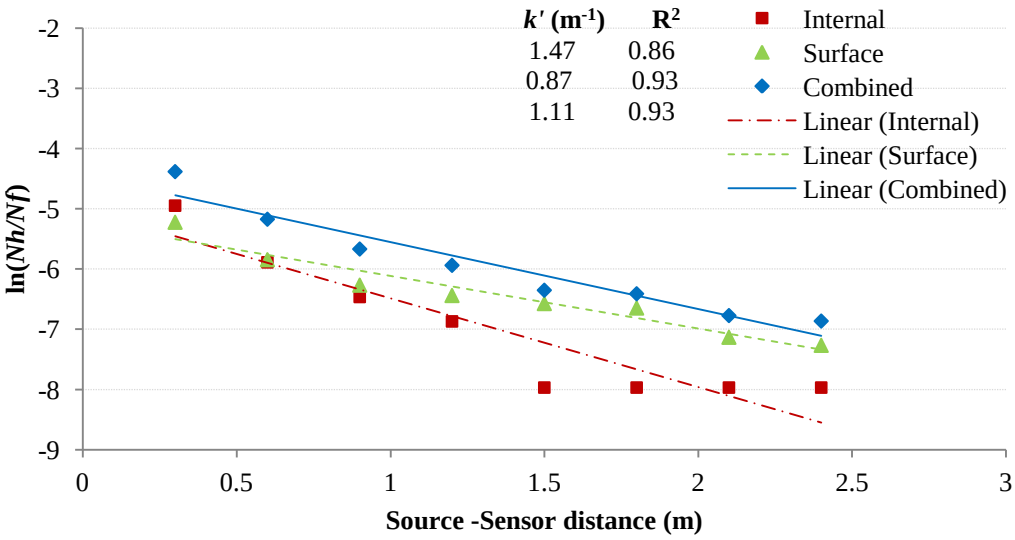

Figure 5.33: Simulated internal, surface and combined ray attenuation on pipeline when source is at the middle, at 10000, 7500 and 17500 fired rays and 1200 µsec extinction time

CHAPTER 6: RESULTS AND ANALYSIS: PHYSICAL SIMULATION INCLUDING EFFECT OF ENVIRONMENT

The previous chapter showed that a simple geometrically based simulation was able to explain much of the attenuation effect due to differences in shape, although it was difficult to assess the relative contributions of surface and body waves. However, attenuation depends not just on the geometry but also on the numbers and types of reflections, any interference due to waves travelling along different paths and any absorption by the material in which the wave is travelling [30]. This chapter extends the ray tracing algorithm to take these factors into account, and uses further experiments in which different surrounding environments were used with the range of shapes already studied.

As in Chapter 5, this chapter starts with some general comments on the modified simulation and is then divided into two main results sections, the first dealing with the small solid shapes with different surrounding environments, and the second dealing with the larger, practical structures, again with different surrounding environments.

6.1 AE attenuation on small structures with different environments

Further attenuation measurements were made on three of the small steel shapes (block, plate and strip) with one face immersed in each of four different environments: air (suspended on wooden blocks), fine dry sand (particle size around 200 micron), wet-sand (20% water content) and water. Table 6.1, summarises the 32 different attenuation tests in this part of the study.

Shape	Environment	Source position (see Figure 4.18)		
		Centre	Edge	Corner
Block	Air	✓	✓	✓
	Dry sand	✓	✓	✓
	Wet sand	✓	✓	✓
	Water	✓	✓	✓
Plate	Air	✓	✓	✓
	Dry sand	✓	✓	✓
	Wet sand	✓	✓	✓
	Water	✓	✓	✓
Strip	Air	✓	✓	×
	Dry sand	✓	✓	×
	Wet sand	✓	✓	×
	Water	✓	✓	×

Table 6.1: Summary of attenuation measurements on small steel shapes with different environments

6.1.1 Measurement results

Figures 6.1 to 6.4 show, as an example of the measured attenuation, the best exponential fits and associated correlation coefficients for the steel plate with the source at the edge for each of the three repeat tests for each of the four different environments. As can be seen, there is quite a degree of scatter within the each test (seven breaks) and between the three repeats, and the correlation coefficients are not always high. The raw experimental results (attenuation plots) for all of the conditions are given in Appendix D.

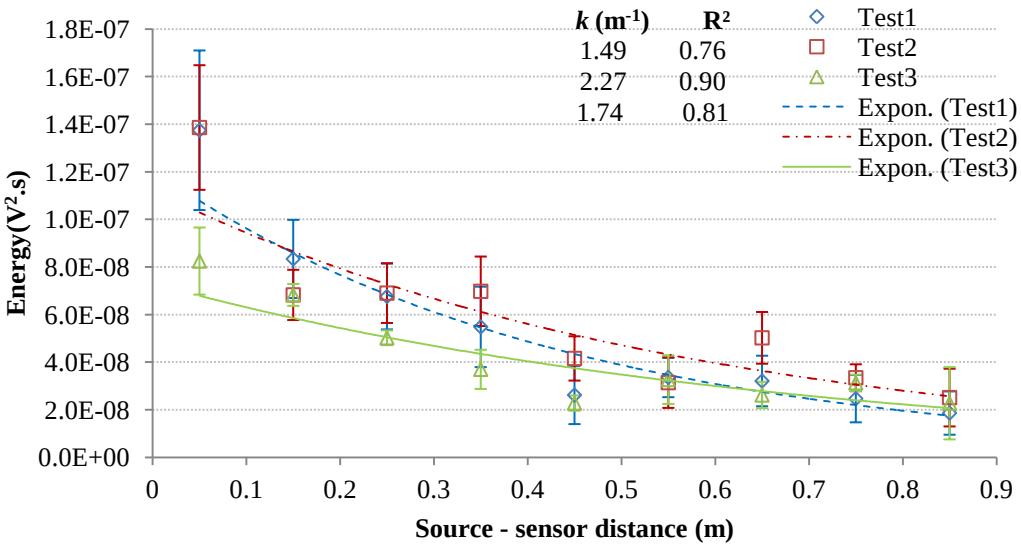

Figure 6.1: Experimental AE attenuation in steel plate, air environment, source at the edge

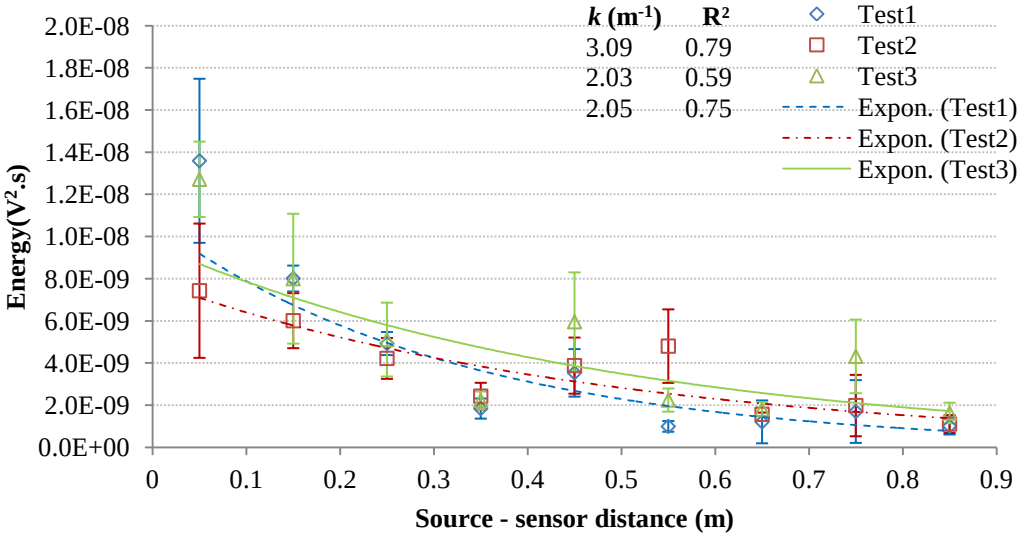

Figure 6.2: Experimental AE attenuation in steel plate, dry sand environment, source at the edge

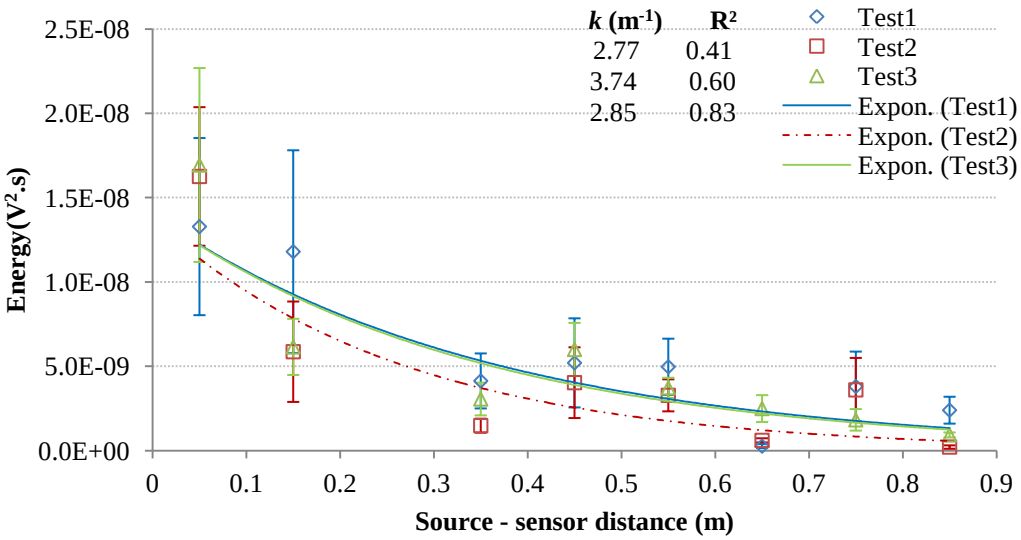

Figure 6.3: Experimental AE attenuation in steel plate, wet sand environment, source at the edge

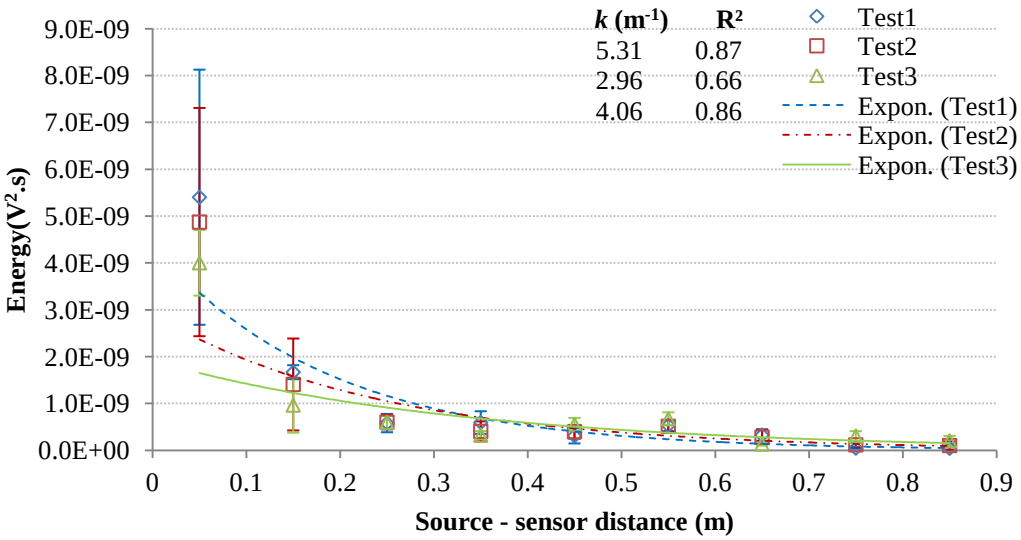

Figure 6.4: Experimental AE attenuation in steel plate, water environment, source at the edge

Table 6.2 summarises all of the attenuation curve fits for the plate with the four different environments with the source in each of the three positions, including the edge (Figures 6.1 - 6.4). The effective attenuation coefficients, k_1, k_2 and k_3 are given for each of the repeat tests along with the corresponding correlation coefficients. As before, in order to make the trends clearer, the mean effective attenuation coefficient, $\bar{k}$, for each of the conditions has been obtained by taking a weighted mean.

$$\bar{k} = \frac{{R_1}^2 k_1 + {R_2}^2 k_2 + {R_3}^2 k_3}{{R_1}^2 + {R_2}^2 + {R_3}^2} \qquad (5.1)$$

Tables 6.3 and 6.4 show the corresponding results for the strip and block, respectively. Even though there is some scatter in the exponential plots, especially on the small shapes (strip and block), clear differences are discernible in the measured attenuation behaviour between the different shapes and environments. In practice, for given configuration (source position and object) the attenuation increases as the environment goes from air to dry sand to wet sand to water. Occasionally, the sand behaves anomalously and possible reasons for this are discussed later.

Source position	**Environment**	**Effective attenuation coefficient, k (m^{-1})**			**Strength of exponential correlation, R^2**			**Weighted mean, $\bar{k}$ (m^{-1})**
		k_1	k_2	k_3	${R_1}^2$	${R_2}^2$	${R_3}^2$	
Centre	**Air**	4.43	2.90	2.84	0.58	0.81	0.71	3.31
	Dry sand	6.46	7.04	6.18	0.80	0.38	0.66	6.48
	Wet sand	7.79	8.97	7.49	0.76	0.79	0.67	8.12
	Water	9.87	8.88	9.43	0.96	0.88	0.90	9.41
Edge	**Air**	2.27	1.73	1.49	0.90	0.81	0.76	1.85
	Dry sand	3.09	2.05	2.03	0.79	0.75	0.59	2.43
	Wet sand	2.85	2.77	3.74	0.83	0.41	0.60	3.12
	Water	5.31	2.96	4.06	0.87	0.66	0.86	4.21
Corner	**Air**	1.39	1.27	1.01	0.89	0.88	0.84	1.23
	Dry sand	1.50	1.61	1.44	0.43	0.58	0.67	1.51
	Wet sand	1.84	2.00	2.19	0.81	0.69	0.85	2.01
	Water	3.8	2.99	2.77	0.93	0.81	0.82	3.21

Table 6.2: Summary of measured attenuation results for each of the four environments on the steel plate.

Source position	Surrounding environment	Effective attenuation coefficient, k (m^{-1})			Strength of exponential correlation, R^2			Weighted mean, $\bar{k}$ (m^{-1})
		k_1	k_2	k_3	R_1^2	R_2^2	R_3^2	
Centre	Air	4.72	3.66	5.52	0.86	0.85	0.87	4.64
	Dry sand	4.97	4.59	6.62	0.68	0.49	0.91	5.60
	Wet sand	3.72	4.34	4.41	0.79	0.34	0.24	3.99
	Water	4.87	6.74	5.34	0.57	0.97	0.73	5.82
Edge	Air	2.41	1.69	2.15	0.79	0.86	0.93	2.08
	Dry sand	1.68	1.97	2.14	0.68	0.71	0.87	1.95
	Wet sand	2.94	2.68	3.41	0.68	0.93	0.85	3.00
	Water	4.44	4.2	3.9	0.61	0.85	0.58	4.19

Table 6.3: Summary of measured attenuation results for each of the four environments on the steel strip.

Source position	Surrounding environment	Effective attenuation coefficient, k (m^{-1})			Strength of exponential correlation, R^2			Weighted mean, $\bar{k}$ (m^{-1})
		k_1	k_2	k_3	R_1^2	R_2^2	R_3^2	
Centre	Air	5.37	3.44	4.31	0.87	0.34	0.30	4.72
	Dry sand	7.16	8.73	4.68	0.18	0.44	0.43	6.80
	Wet sand	4.31	4.87	7.13	0.47	0.50	0.78	5.73
	Water	9.87	8.06	10.33	0.69	0.87	0.73	9.33
Edge	Air	1.55	2.84	2.22	0.22	0.47	0.27	2.37
	Dry sand	2.56	2.97	2.34	0.66	0.51	0.33	2.65
	Wet sand	3.29	6.31	3.8	0.15	0.76	0.53	5.07
	Water	4.2	5.8	6.61	0.77	0.88	0.85	5.58
Corner	Air	1.01	1.47	2.43	0.10	0.47	0.54	1.90
	Dry sand	2.81	3.39	2.15	0.61	0.59	0.48	2.83
	Wet sand	4.25	2.68	2.87	0.77	0.37	0.55	3.46
	Water	4.13	5.48	3.17	0.70	0.95	0.83	4.33

Table 6.4: Summary of measured attenuation results for each of the four environments on the steel block.

6.1.2 Simulation results

The physical simulation can take into account the three additional attenuation factors; phase difference, reflection coefficients and internal material friction. These are applied separately below to investigate the relative effects in the small solid blocks.

As mentioned in Chapter 3, the overall AE energy arriving at a virtual sensor can be taken as the sum of the energies of each ray which hits it:

$$\frac{E}{E_0} = \left[\sum_{j=1}^{N_h} \left(e^{-\alpha x_j} \times {R_U}^{n_{Uj}} \times {R_L}^{n_{Lj}} \times e^{i(\phi)}\right)\right] \times \left[\sum_{j=1}^{N_h} \left(e^{-\alpha x_j} \times {R_U}^{n_U j} \times {R_L}^{n_{Lj}} \times e^{i(\phi)}\right)\right]^* \quad (3.1)$$

6.1.2.1 Superposition effect

As mentioned in Chapter 5 (Figures 5.3 and 5.4) the geometric simulation of small objects, the ray path differences are large enough that the phase differences are several multiples of π and so the rays must be drawn from a population where the phase difference is evenly distributed between zero and 2π. Thus, the net interference effect, including phase changes on reflection, is an equal mixture from 100% constructive to 100% destructive and so it is possible to assign an average interference attenuation to all rays.

To assess this effect on the current measured data, the phase was taken to be

$$\phi = k_v x_j + \omega t + n_j \pi \quad (3.3)$$

In equation 3.1, the reflection coefficients taken to be unity and the material damping coefficient to be zero.

Tables 6.5 and 6.6 show the results simulated attenuation coefficients for internal and surface rays, respectively, for the steel plate with the source at the edge for a range of assumed frequencies as well as the average for all the frequencies. Four different simulations are represented, where k'_1, k'_2, k'_3 and k'_4 are the effective attenuation coefficients derived assuming only the first term, the first and second terms and all terms in equation 3.3, and without phase effect, respectively.

Frequency (kHz)	**Effective attenuation coefficient (m^{-1})**				**Strength of exponential correlation, R^2**			
	k'_1	k'_2	k'_3	k'_4	R_1^2	R_2^2	R_3^2	R_4^2
160	2.13	2.78	2.90		0.36	0.23	0.52	
200	2.00	2.10	2.60		0.29	0.40	0.55	
250	2.49	1.94	1.99		0.33	0.20	0.10	
300	2.27	2.72	2.32		0.46	0.32	0.39	
340	2.48	3.20	3.10		0.33	0.44	0.47	
Average	2.33	2.35	2.44	2.31	0.55	0.52	0.58	0.86

Table 6.5: Simulated attenuation coefficients for surface rays of a range of assumed frequencies and without phase effect (k'_4) on the steel plate, source at the edge

Frequency (kHz)	**Effective attenuation coefficient, k (m^{-1})**				**Strength of exponential correlation, R^2**			
	k'_1	k'_2	k'_3	k'_4	R_1^2	R_2^2	R_3^2	R_4^2
160	3.52	4.03	3.5		0.65	0.30	0.75	
200	2.1	3.42	2.57		0.88	0.31	0.69	
250	2.46	2.14	1.56		0.58	0.47	0.35	
300	3.76	2.19	2.91		0.75	0.20	0.36	
340	2.39	2.22	2.6		0.44	0.24	0.10	
Average	2.47	2.26	2.59	2.52	0.79	0.69	0.8	0.85

Table 6.6: Simulated attenuation coefficients for internal rays of a range of assumed frequencies and without phase effect (k'_4) on the steel plate, source at the edge

As was expected from Section 5.1.3, taking account of phase in the simulations has little effect either on the value of the effective attenuation coefficient or on the strength of the exponential correlations over the frequency rays of interest, and so phase is not taken into account in any of the remaining simulations in this chapter.

6.1.2.2 Reflection coefficient effect

Given the observed effect of the environment on the lower surface of the experimental results, it was important to introduce a routine to deal with phase boundary effects. It is known that the proportion of incident energy, R, reflected at a boundary between two media, 1 and 2, depends on their acoustic impedances, Z_1 and Z_2:

$$R = \frac{(Z_1 - Z_2)^2}{(Z_1 + Z_2)^2} \qquad (2.9)$$

The proportion of internal reflected energy for steel interfaced with air, dry sand, wet sand and water are obtained as 0.99, 0.97, 0.93 and 0.87 respectively, where the refection coefficient for wet sand can be in the middle between dry sand and water. For the surface rays, for example Rayleigh waves, boundaries are less clearly defined, but it is known that only around 20 - 40% of the energy is reflected at an edge and the rest is converted into body waves [46].

Figures 6.5 and 6.6 show the effect of lower reflection coefficient on the simulated attenuation curves for internal and surface rays respectively, without internal friction ($\alpha = 0$), for the same examples as were used in Tables 6.5 and 6.6. As can be seen, the relatively small, changes in the internal ray reflection coefficients affect the attenuation significantly. Also, the expected reflection coefficient for Rayleigh waves has a huge effect on the simulated surface wave attenuation.

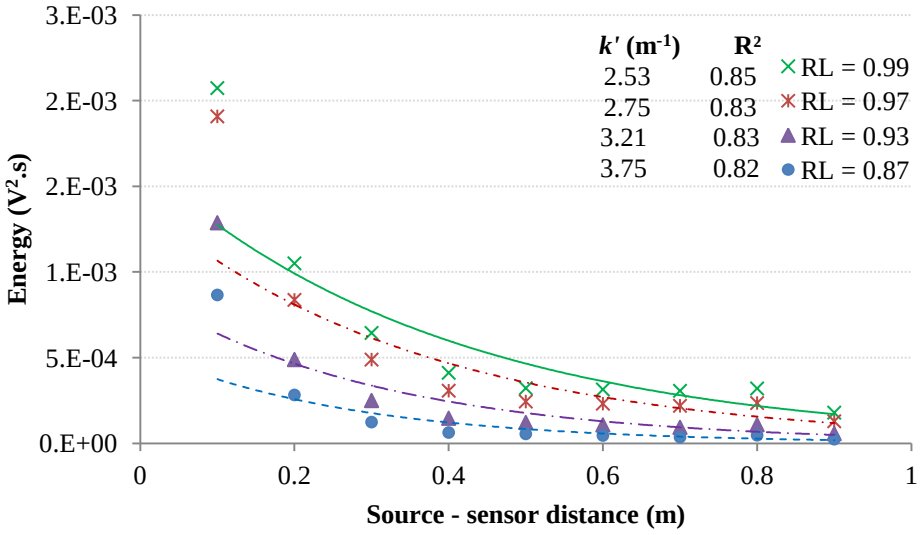

Figure 6.5: Effect of reflection coefficient of simulated attenuation of internal rays on steel plate, source at the edge

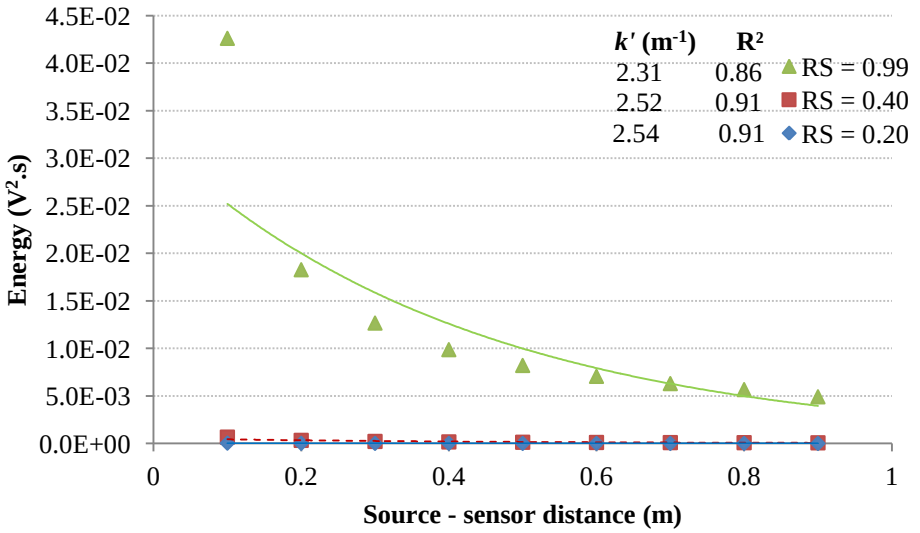

Figure 6.6: Effect of reflection coefficient of simulated attenuation of surface rays on steel plate, source at the edge

6.1.2.3 Internal material friction effect

Figures 6.7 and 6.8 show, for the same examples as Figures 6.5 and 6.6, of the effect of varying internal friction (α) on the simulation results, with 100% reflection ($R_U = R_L = 1$). As can be seen, varying α between 0 and 0.05 has very little effect on attenuation, and values of at least 0.5 are required to cause a significant increase.

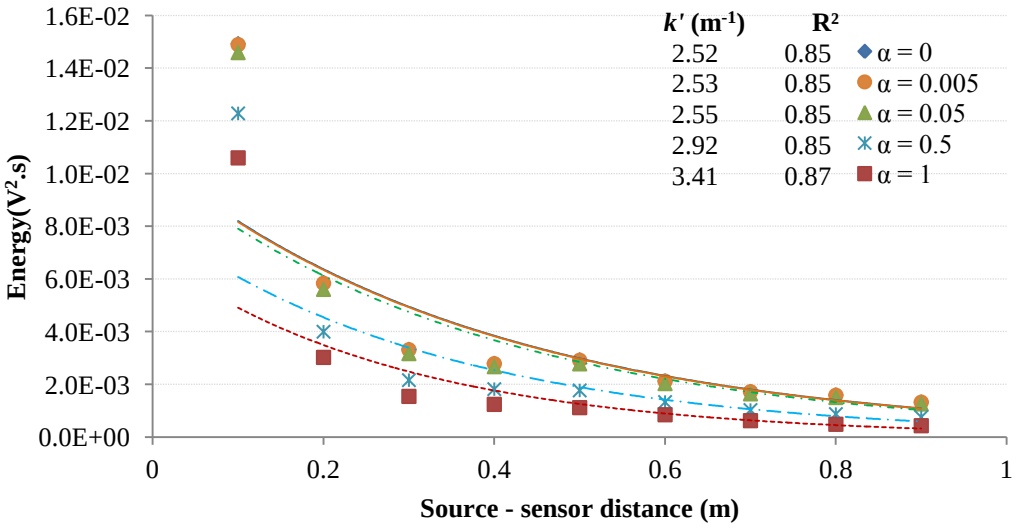

Figure 6.7: Effect of internal friction of simulated attenuation of internal rays on steel plate, source at the edge.

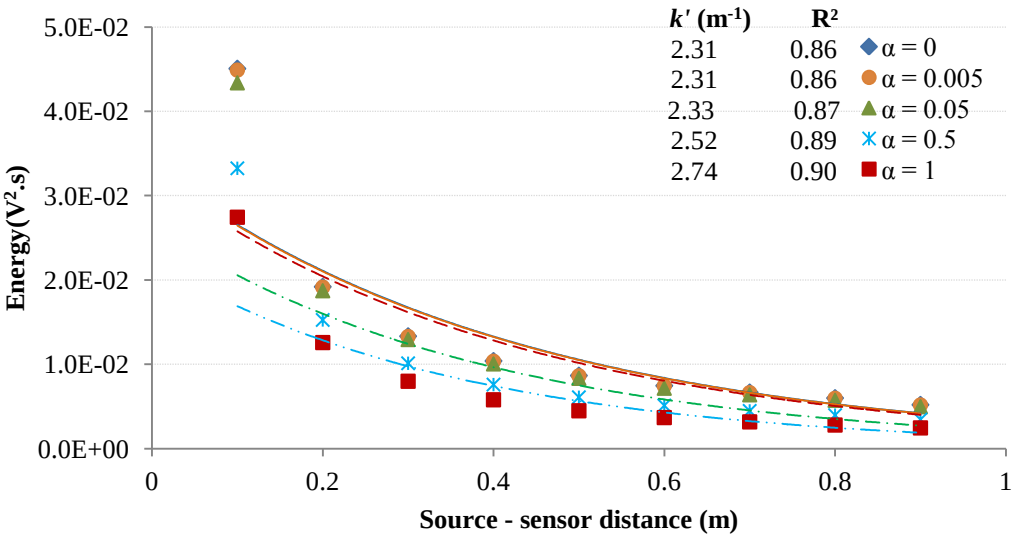

Figure 6.8: Effect of internal friction of simulated attenuation of surface rays on steel plate, source at the edge.

Tables 6.7 to 6.9 summarise all of the simulated attenuation coefficients for the three shapes and the four environments and the three source positions. In these simulations, the material damping coefficient was held at 0.005 and the proportion of energy reflected when a surface wave encounters an edge at 40%, mode conversion, these values are used as the basic of the discussion at the end of this chapter.

Source position	Lower reflection coefficient R_L	Effective attenuation coefficient, k' (m^{-1})			Strength of exponential correlation, R^2		
		Internal rays	Surface rays	Combined rays	Internal rays	Surface rays	Combined rays
Centre	**0.99**	4.46	4.47	4.46	0.88	0.96	0.88
	0.97	5.2		5.12	0.89		0.91
	0.93	6.04		5.75	0.86		0.9
	0.87	7.4		6.13	0.81		0.8
Edge	**0.99**	2.53	2.52	2.52	0.85	0.91	0.86
	0.97	2.75		2.68	0.83		0.86
	0.93	3.21		2.9	0.83		0.86
	0.87	3.75		3	0.83		0.86
Corner	**0.99**	2.27	2	2.25	0.75	0.89	0.76
	0.97	2.46		2.4	0.76		0.78
	0.93	2.83		2.65	0.76		0.79
	0.87	3.39		2.79	0.72		0.79

Table 6.7: Summary of simulated physical attenuation results for each of the four environments on the steel plate.

Source position	Lower reflection coefficient R_L	Effective attenuation coefficient, k' (m^{-1})			Strength of exponential correlation, R^2		
		Internal rays	Surface rays	Combined rays	Internal rays	Surface rays	Combined rays
Centre	**0.99**	3.55	4.9	3.8	0.95	0.93	0.96
	0.97	3.81		4.05	0.96		0.96
	0.93	4.32		4.47	0.97		0.96
	0.87	5.0		4.92	0.97		0.95
Edge	**0.99**	2.07	2.66	2.14	0.93	0.92	0.93
	0.97	2.22		2.29	0.93		0.93
	0.93	3.06		2.87	0.9		0.922
	0.87	4.02		2.97	0.88		0.92

Table 6.8: Summary of simulated physical attenuation results for each of the four environments on the steel strip.

Source position	Lower reflection coefficient R_L	Effective attenuation coefficient, k' (m^{-1})			Strength of exponential correlation, R^2		
		Internal rays	Surface rays	Combined rays	Internal rays	Surface rays	Combined rays
Centre	**0.99**	4.02	6.24	4.7	0.42	0.97	0.68
	0.97	5.2		5.56	0.52		0.75
	0.93	5.87		6.03	0.61		0.86
	0.87	6.98		6.47	0.69		0.91
Edge	**0.99**	2.01	5.62	2.25	0.78	0.84	0.8
	0.97	2.53		2.94	0.86		0.88
	0.93	3.61		4.14	0.85		0.89
	0.87	5.04		5.11	0.8		0.91
Corner	**0.99**	2.23	3.8	2.66	0.37	0.96	0.64
	0.97	2.48		2.85	0.42		0.69
	0.93	3.72		3.56	0.6		0.83
	0.87	5.32		3.9	0.68		0.9

Table 6.9: Summary of simulated physical attenuation results for each of the four environments on the steel block.

6.4 AE attenuation on practical structures with different environments

The general approach with the practical structures was to vary the environment to reflect those which might actually be encountered. Thus, the vessel was tested empty and filled with water and the pipeline was also tested empty and with water inside, but also with various external environments to simulate pipeline burial. The glass plate already contained a phase boundary between the laminated plates, so the simulations were modified to include this.

6.4.1 Laminated glass

Laminated glass is a combination of two glass sheets bonded together with a layer of resin (PVB) bonded with the application of heat and pressure to form a single piece.

Figures 6.9 to 6.12 show the effect of material damping (α = 0.1), (the material damping for glass varies between 0.01 and 0.1 [1, 134]) and proportion reflected (0.2 for internal rays and 0.4 for surface rays) on the simulated attenuation curves, without taking into account the possibility that the transmitted rays might continue to the bottom of the plate and be reflected back up.

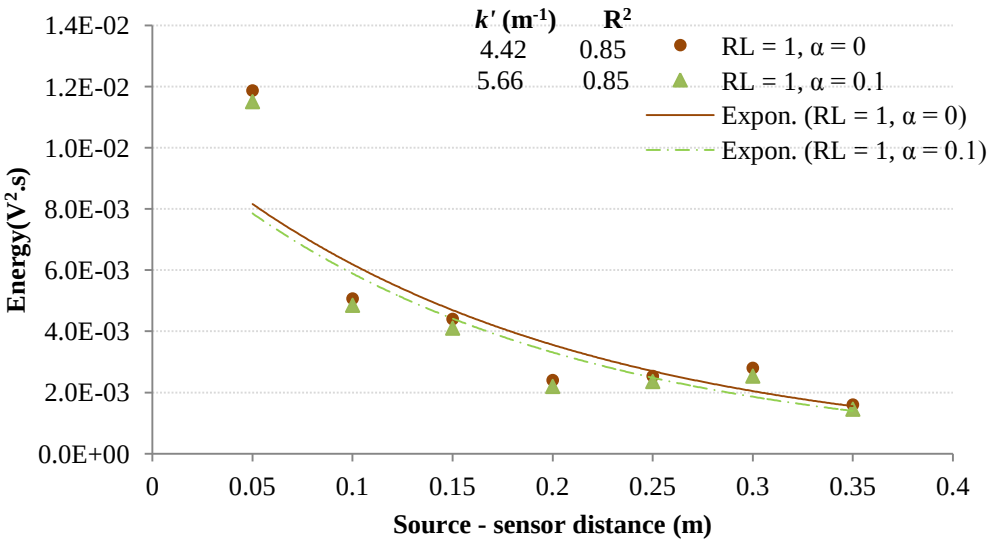

Figure 6.9: Physical simulation of internal ray attenuation on laminated glass, source at the centre, effect of internal friction only.

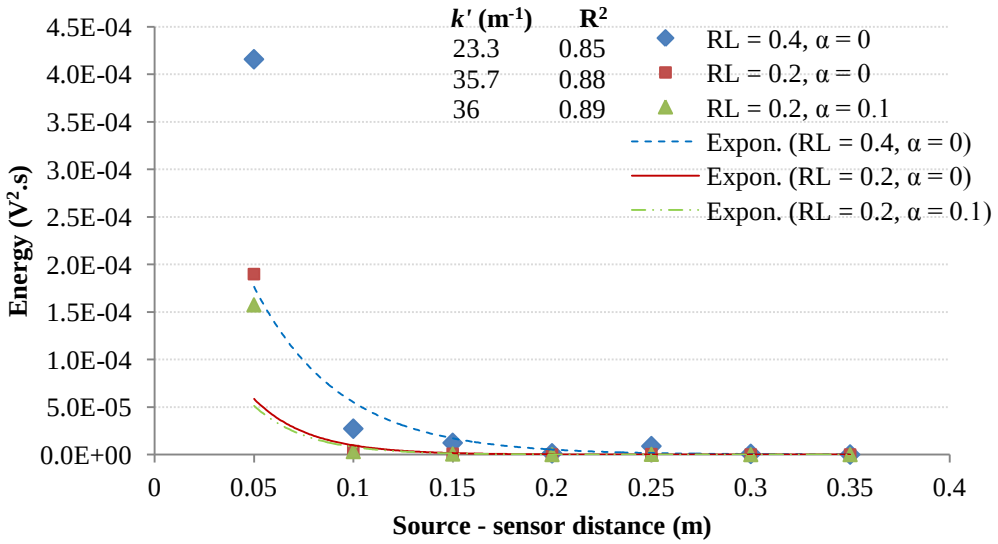

Figure 6.10: Physical simulation of internal ray attenuation on laminated glass, source at the centre, effect of internal friction and reflection coefficient.

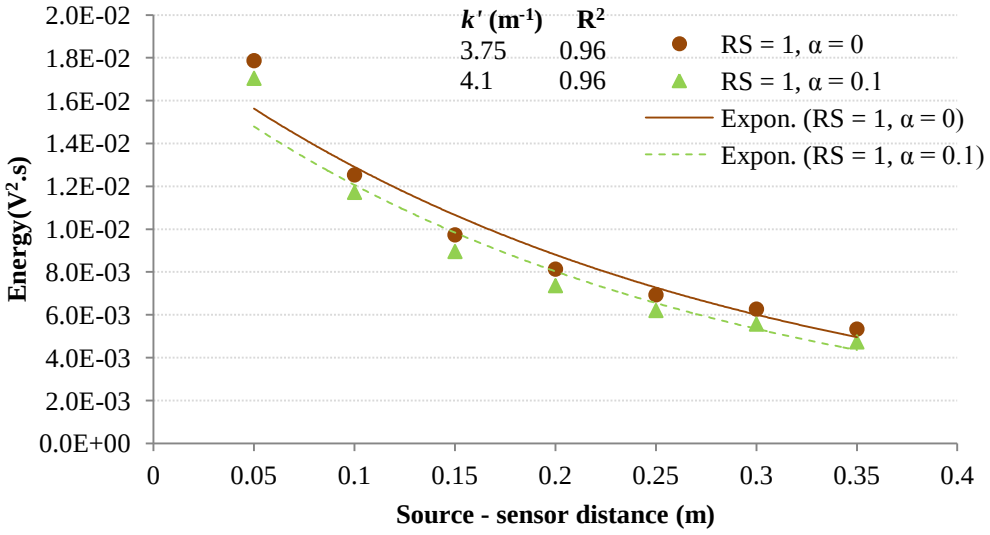

Figure 6.11: Physical simulation of surface ray attenuation on laminated glass, source at the centre, effect of internal friction only.

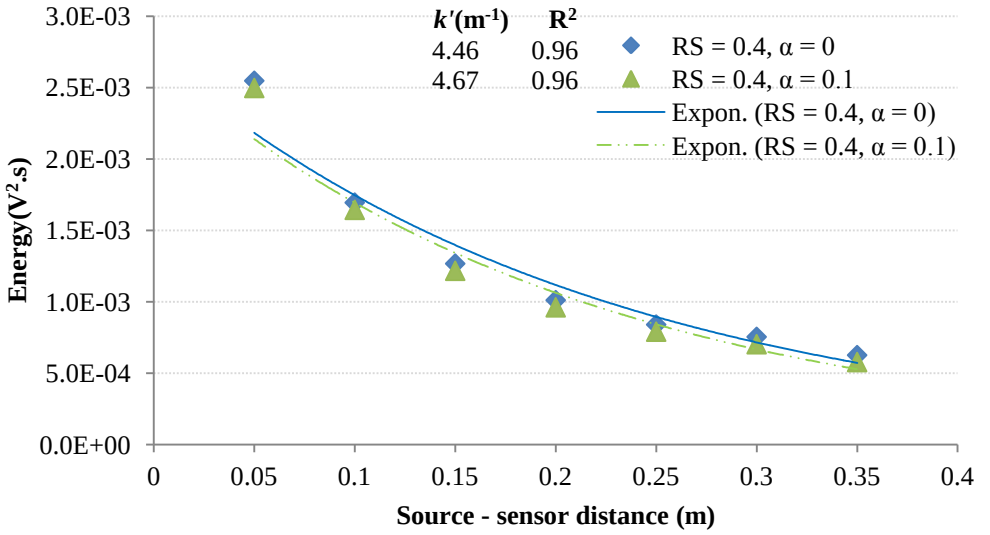

Figure 6.12: Physical simulation of surface ray attenuation on laminated glass, source at the centre, effect of internal friction and reflection coefficient.

Tables 6.10 and 6.11 summarise all of the attenuation measurements and simulations using R = 0.2 and α = 0.1 for internal rays and R = 0.4 for surface rays, as can be seen, the combined rays values of *k′* match the measure values better than the geometric simulation (Table 5.15) although they are close to the modified geometric simulations with reduced number of reflections (Table 5.16). In physical simulation, internal rays

make almost no effect on the total energy at the sensor but enhanced material damping is required to attenuate the surface rays sufficiently to match the measure values.

Source	Effective attenuation coefficient, k (m^{-1})			Strength of exponential correlation, R^2			Weighted mean, $\bar{k}$ (m^{-1})
	k_1	k_2	k_3	R_1^2	R_2^2	R_3^2	
Centre	5.32	5.86	7.15	0.53	0.77	0.8	6.22
Edge	3.71	4.33	4.22	0.96	0.95	0.89	4.08
Corner	2.47	2.08	3.04	0.48	0.58	0.87	2.61

Table 6.10: Summary of measured attenuation results for each of the three positions on a laminated glass.

Source position	Effective attenuation coefficient, k' (m^{-1})			Strength of exponential correlation, R^2		
	Internal rays	Surface rays	Combined rays	Internal rays	Surface rays	Combined rays
Centre	36	4.67	4.8	0.89	0.96	0.95
Edge	13.9	2.7	2.9	0.37	0.92	0.88
Corner	10	2.15	2.22	0.1	0.9	0.88

Table 6.11: Summary of physical attenuation results for each of the three positions on a laminated glass.

6.4.2 Large stainless steel vessel

Figures 6.13 and 6.14 show the measured attenuation on the vessel for the circumferential sensor array for each of the three repeat tests with the vessel empty and filled with water, respectively.

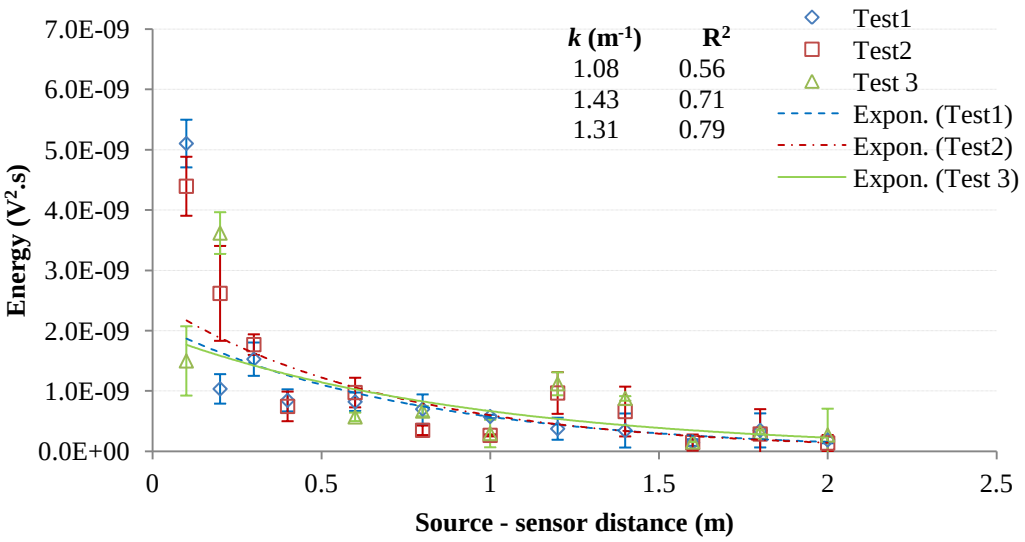

Figure 6.13: Measured attenuation at circumferential sensor array in large vessel, empty

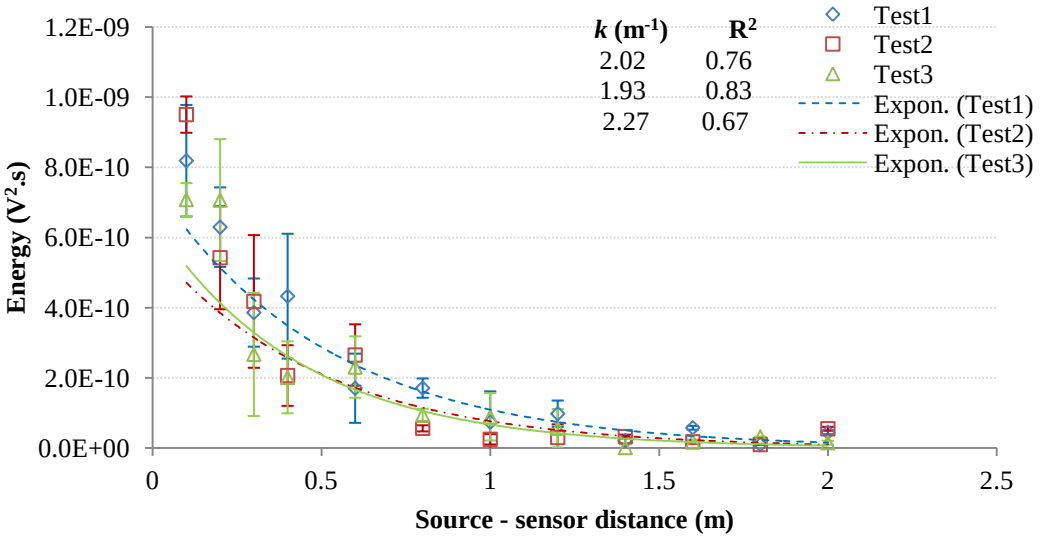

Figure 6.14: Measured attenuation at circumferential sensor array in large vessel, full of water

Table 6.12 summarises the 12 experimental results for each of the three tests with different source positions with the two arrays with the tank full of water and empty. Clearly, the internal water has a significant effect on attenuation and, as before, the attenuation in the circumferential array is slightly less than in the longitudinal array for both environments.

Sensor array	Internal Environment	Effective attenuation coefficient, k (m^{-1})			Strength of exponential correlation, R^2			Weighted mean, $\bar{k}$ (m^{-1})
		k_1	k_2	k_3	R_1^2	R_2^2	R_3^2	
Longitudinal	**Air**	1.33	1.6	1.55	0.86	0.89	0.9	1.50
	Water	2.52	2.17	2.05	0.9	0.93	0.7	2.26
Circumferential	**Air**	1.08	1.43	1.31	0.52	0.71	0.79	1.29
	Water	2.02	1.93	2.27	0.76	0.83	0.67	2.06

Table 6.12: Summary of measured attenuation coefficients on stainless steel vessel, full of water and empty.

Figure 6.15 shows the simulated attenuation curves for internal and surface rays with internal friction $\alpha = 0.005$ and two different reflection coefficients for the internal rays, 0.87 for lower (inner) surface and 0.99 for the upper (outer) surface, and 100% reflection of surface rays. These coefficients are summarised in Table 6.13 along with the parallel results for the circumferential array. Clearly, the simulations do not account for the observed increase in attenuation due to the water and this because there is no mechanism to attenuate the dominant surface rays due to the internal water.

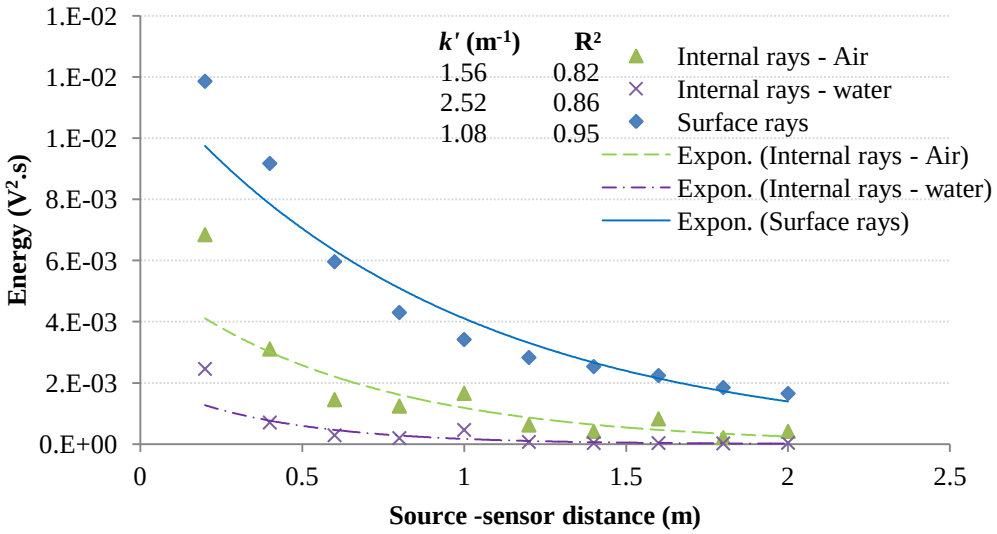

Figure 6.15: Simulated attenuation on stainless steel vessel for circumferential sensor array

Sensor array	Lower reflection coefficient R_L	Effective attenuation coefficient, k' (m^{-1})			Strength of exponential correlation, R^2		
		Internal rays	Surface rays	Combined rays	Internal rays	Surface rays	Combined rays
Long.	**0.99**	1.55	1.2	1.38	0.75	0.91	0.85
	0.87	2.42		1.2	0.75		0.90
Circum.	**0.99**	1.56	1.08	1.18	0.82	0.91	0.94
	0.87	2.52		1.14	0.86		0.95

Table 6.13: Summary of simulated attenuation coefficients for stainless steel vessel.

6.4.3 Long steel pipe

Table 6.14 summarises the experimental AE attenuation on the steel pipeline for the two different internal environments (air and water) and the four different external environments. It is clear that both internal and external environments have an effect on attenuation.

Internal environment	External environment	Effective attenuation coefficient, k (m^{-1})	Strength of exponential correlation, R^2
Air	**Air**	0.21	0.61
Air	**Dry sand**	0.45	0.37
Air	**Wet sand**	0.65	0.68
Air	**Soaked sand**	1.46	0.83
Water	**Air**	0.64	0.88
Water	**Wet sand**	0.92	0.83

Table 6.14: Summary of measured attenuation results for pipeline with different internal and external environments

Table 6.15 summarises the simulated coefficients for the pipeline, for internal and surface rays and the two combined, with the source near the end. The internal material friction, α, was kept at 0.005 and six different reflection coefficients, were used, 0.99, 0.97, 0.93, 0.87 and 0.86 to represent the effect of air, dry sand, wet sand, water and soaked sand respectively. As before 100% reflection was used for the surface rays. As can be seen, the simulated attenuation continues to be high for the air-filled pipe and, because the surface rays dominate, there is no effect of wither internal or external environment on the combined rays.

Lower reflection coefficient R_L	Upper reflection coefficient R_U	Effective attenuation coefficient, k' (m^{-1})			Strength of exponential correlation, R^2		
		Internal rays	Surface rays	Combined rays	Internal rays	Surface rays	Combined rays
0.99	**0.99**	0.56	0.56	0.56	0.64	0.86	0.7
0.99	**0.97**	0.67		0.57	0.63		0.64
0.99	**0.93**	0.76		0.6	0.45		0.55
0.99	**0.86**	0.86		0.55	0.32		0.76
0.87	**0.99**	0.93		0.55	0.30		0.78
0.87	**0.93**	1.19		0.55	0.27		0.83

Table 6.15: Summary of simulated attenuation coefficients for pipeline with different internal and external environments.

6.5 Discussion

Figures 6.16 to 6.18 show the measured (weighted mean) and simulated attenuation coefficients for the three small shapes with the different environments and different source positions. Generally, the same trends with change of shape and source position are exhibited by the physical simulations, as they were with the geometric simulations discussed in Chapter 5. Moreover, the tendency to increase attenuation as the impedance matching between steel and the lower surface becomes closer is reflected in both the experiments and simulations. The somewhat anomalous experimental results for the block and strip with a wet sand environment with the source at the centre are not reproduced in the simulations (nor in the experiments with the source elsewhere or with the other shape), and it may be that these relatively small samples are more susceptible to incomplete bedding down when the source is at the centre.

Not surprisingly, the greatest effect of the immersed environment is seen in the sample with the greatest area to volume ratio (i.e. the plate), both in the simulations and in the experiments. With the source at the centre, the internal ray simulations give almost exactly the same coefficients as the experiments, although the simulations for air, both for surface and internal rays, suggest rather more attenuation than the experiment, whereas those with other environments suggest less attenuation. With the source away from the centre, both simulated and measured coefficients show a significant decrease in attenuation coefficient, but also an increase in the difference between measured and

simulated internal ray coefficients, for the air environment. Also, the surface ray coefficients are closer to the internal rays for air as the source moves away from the centre. Overall, the plate experiments and simulations indicate that attenuation is better described using an internal ray model than a surface ray model when the source is at the centre, and with one surface immersed in a wet environment. Although ray tracing does not lend itself to describing Lamb wave propagation, the effect of the environment on one surface could be introduced by artificially increasing the absorption coefficient, α, on a surface wave, as will be discussed later.

In contrast to the plate, the internal ray simulations on the block all yield smaller attenuation coefficients than the surface ray simulations. Leaving aside the anomaly with wet sand mentioned above, the internal ray simulations give lower coefficients than the experiments when the source is at the centre or an edge, and slightly higher coefficients than the experiments when the source is at a corner. In all cases, the surface ray simulations give substantially higher attenuation coefficients than the experiments. When the two types of ray are combined, the simulated attenuation coefficients are very similar to the experimental ones, indicating that a suitable simulation model for such blocky shapes where Lamb waves are less important can be found by combining surface and internal simulations, perhaps with a few adjustments to the surface and internal ray reflection coefficients.

Finally, the strip behaviour seems to be intermediate between the block and the plate in that the internal simulations show lower attenuation that the experiments, but where the surface simulations have lower coefficients than the internal ones. It is suggested that an appropriate approach here would be to combine surface and internal simulations, but with added absorption for the surface simulations to account for Lamb wave propagation.

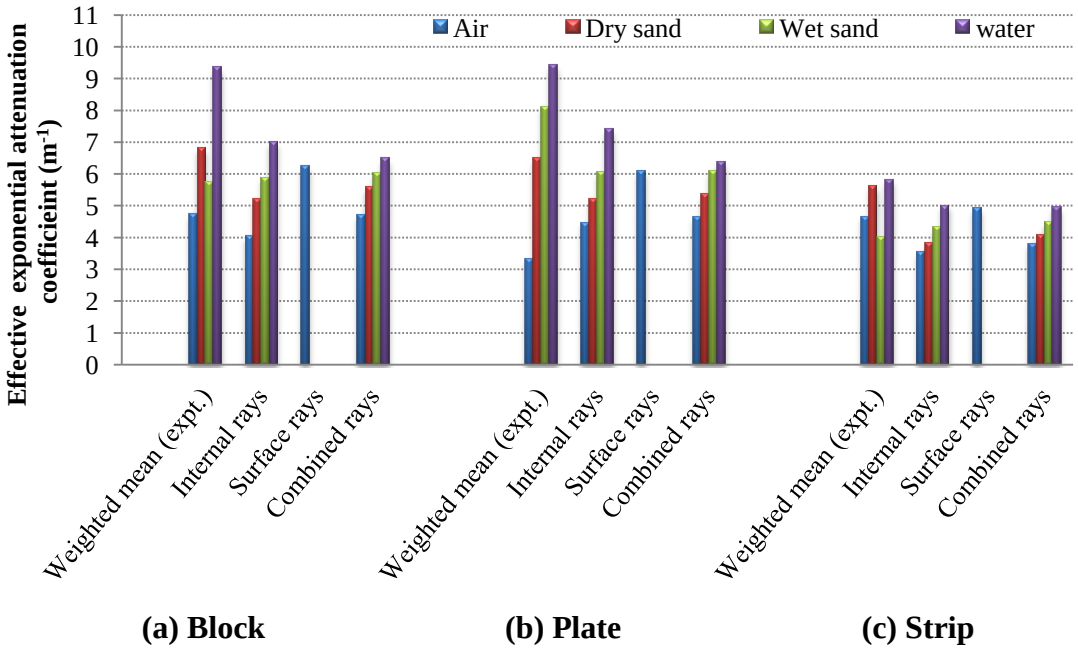

Figure 6.16: Comparison between experiments (expt.) and simulation results for the three small objects with four environments, source at the centre.

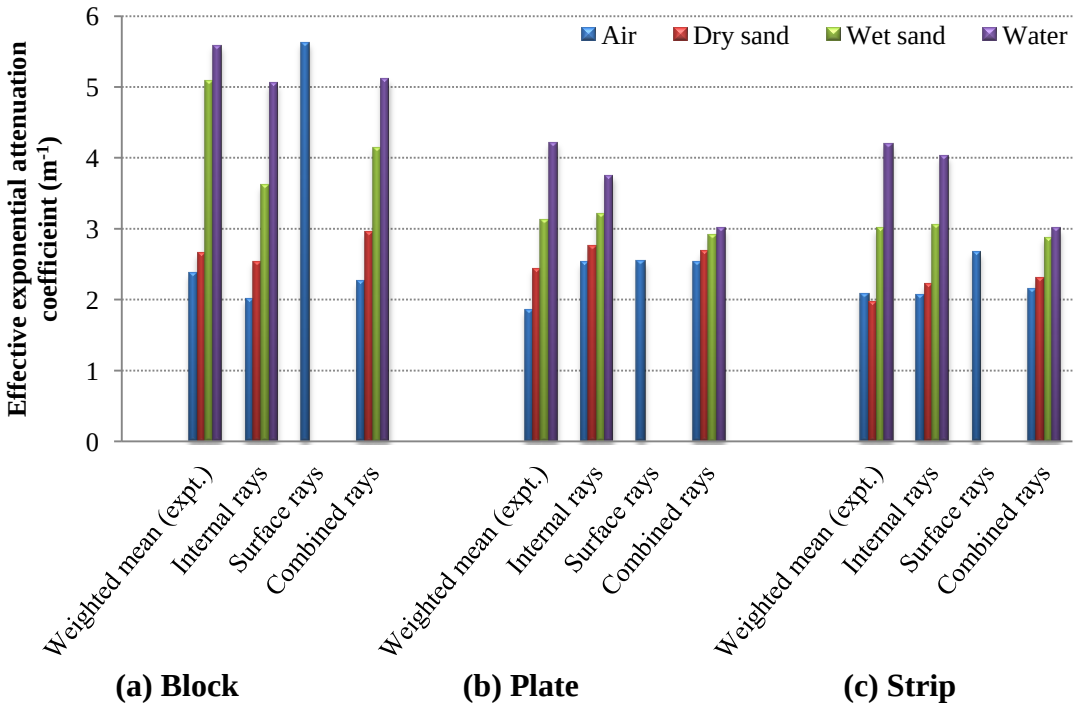

Figure 6.17: Comparison between experiments (expt.) and simulation results for the three small objects with four environments, source at one edge.

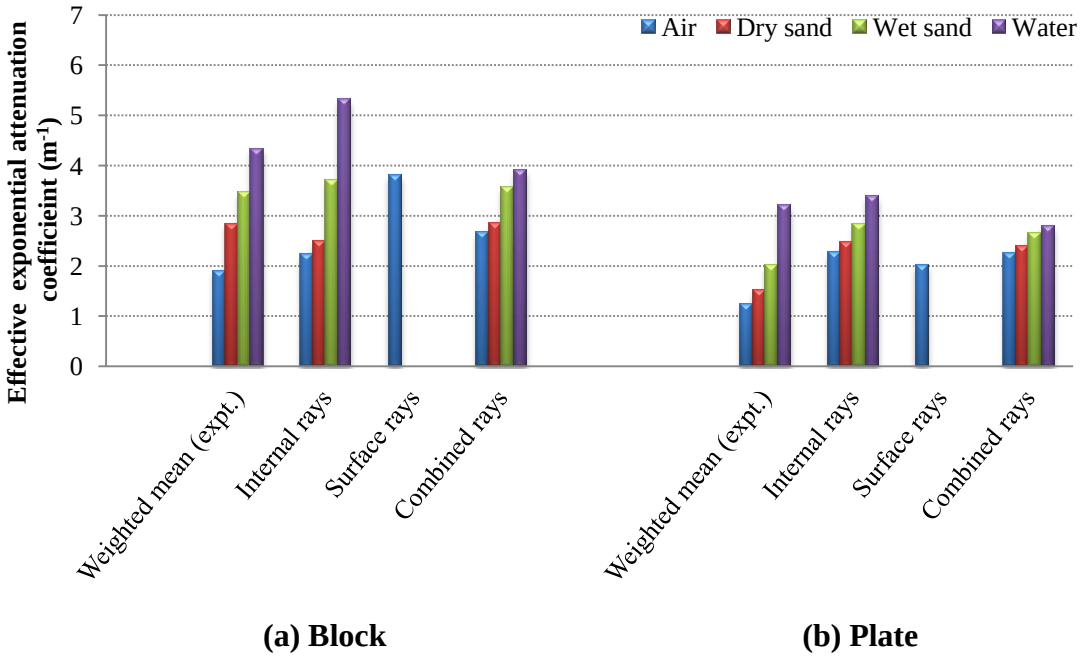

Figure 6.18: Comparison between experiments and simulation results for the three small objects with four environments, source at one corner.

Figure 6.19 shows the experimental and simulation results for the laminated glass and steel plate, tested in an air environment, using internal damping of the surface rays of 0.0005 and 0.1 for the steel plate and laminated glass, respectively. For all three positions, the measured attenuation is greater on the laminated glass than on the steel plate, an effect that is replicated reasonably well in the simulations when both surface and internal rays are considered. The difference in the simulations is almost entirely attributable to the reflection effect for the internal rays, the interface in the laminated glass allowing almost all the internal ray energy to leak into the lower plate. Although the simulation does not allow these leaked rays to reflect from the lower surface and be transmitted to the upper plate again, this probably would not affect the general finding quantitatively because the attenuation coefficients are so large, even using the impedance translation theorem [44], where only about 0.02 of the energy might be reflected.

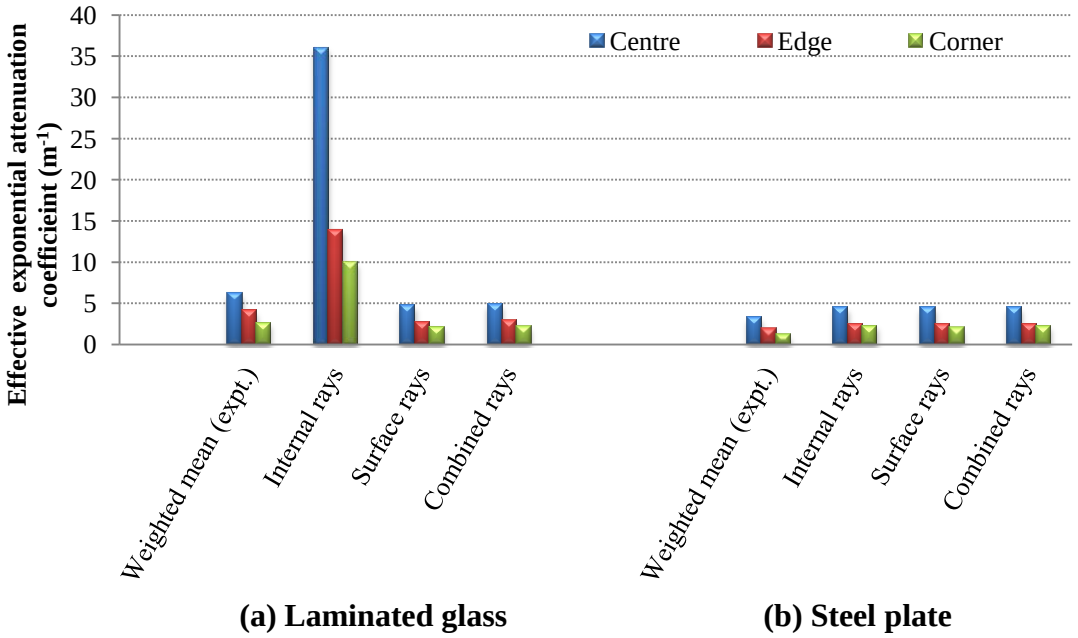

Figure 6.19: Comparison between experiments and simulation results for two plates tested in air (laminated glass and steel plate).

Figures 6.20 and 6.21 summarise the experiments and simulations on the stainless steel vessel and the pipe, respectively. For both objects, the effect of water filling is simulated qualitatively by the internal rays, but the surface rays are not affected by either the internal nor the external environment. In cylinders, the surface waves are only affected by beam spreading in the simulations (geometric attenuation), meaning that the simulated combined ray attenuation coefficients do no change with either internal or external environment.

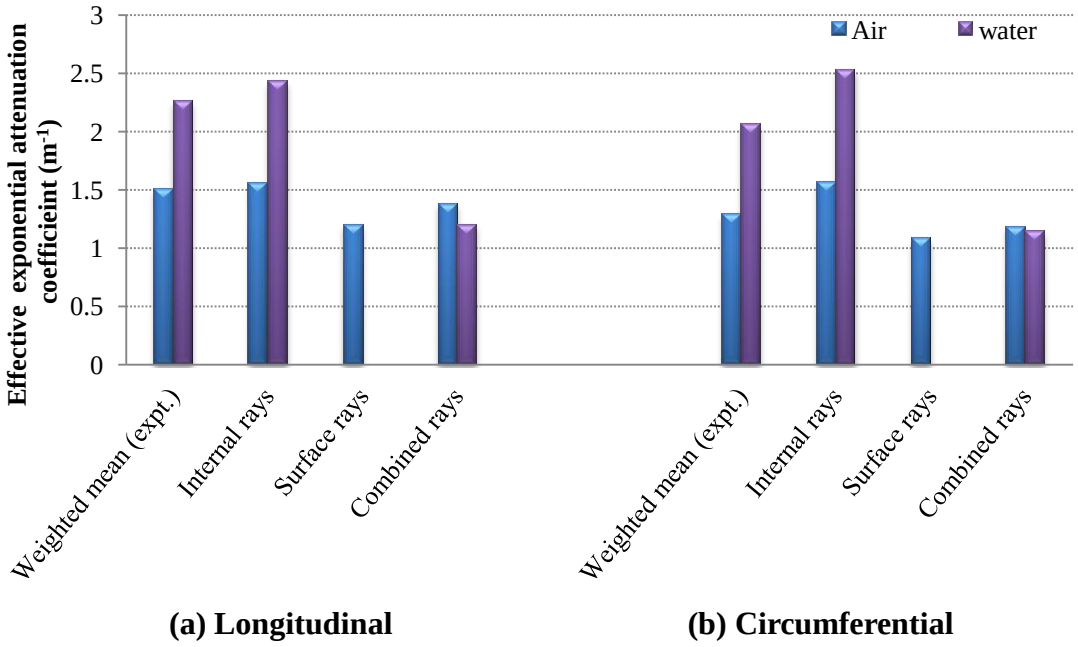

Figure 6.20: Comparison between experiments and simulation results for vessel with two different environments

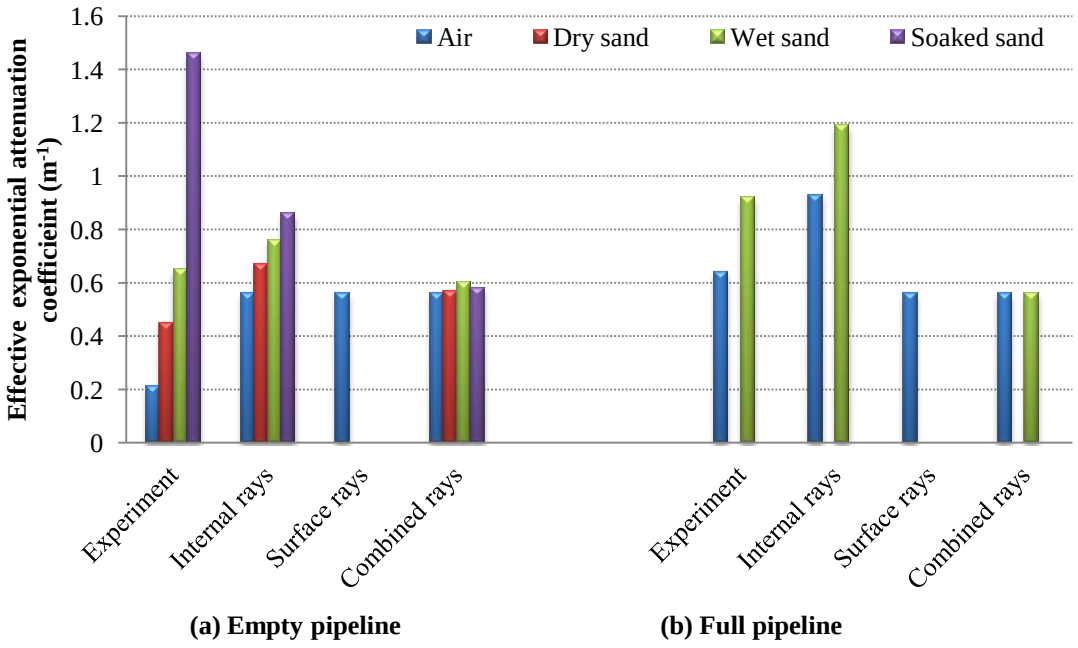

Figure 6.21: Comparison between experiments and simulation results for pipeline with different internal /external environments

The simplest way to introduce environments attenuation to surface wave is to include the surface damping effect, $e^{-\alpha_s x_j}$, which would be applied of the upper surface for Rayleigh waves and at the top and bottom surfaces for Lamb waves, allowing the effect in all the experiments to be modelled. Figures 6.22 and 6.23 show the effect of including the surface damping coefficient on the surface wave simulations. Table 6.19 summarizes the relative values of surface damping for the different environments.

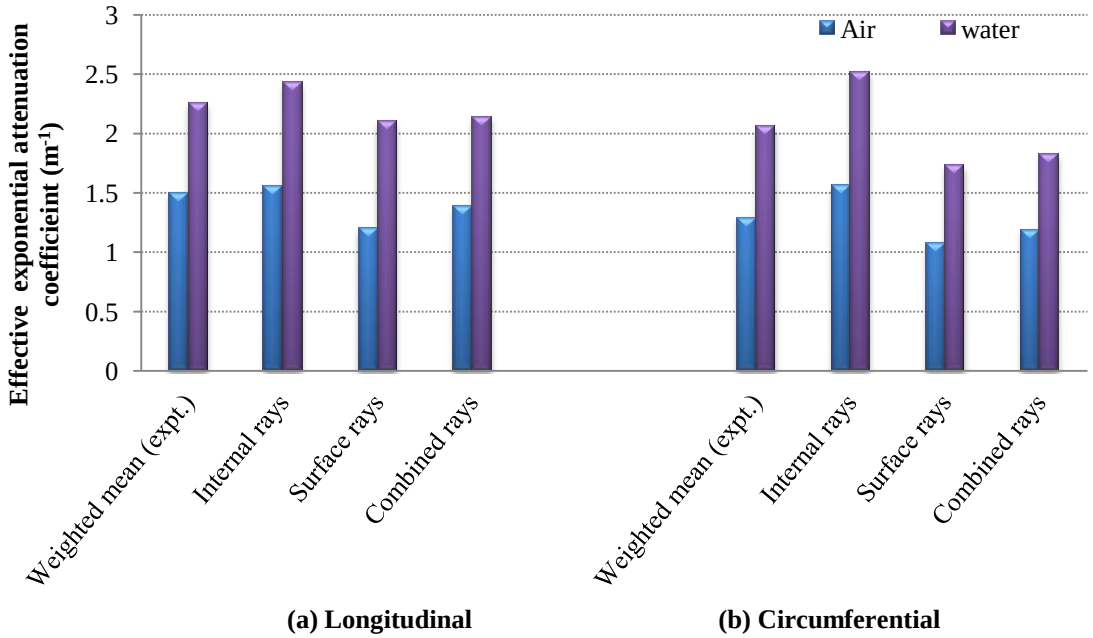

Figure 6.22: Comparison between experiments and simulation results for vessel with two different environments

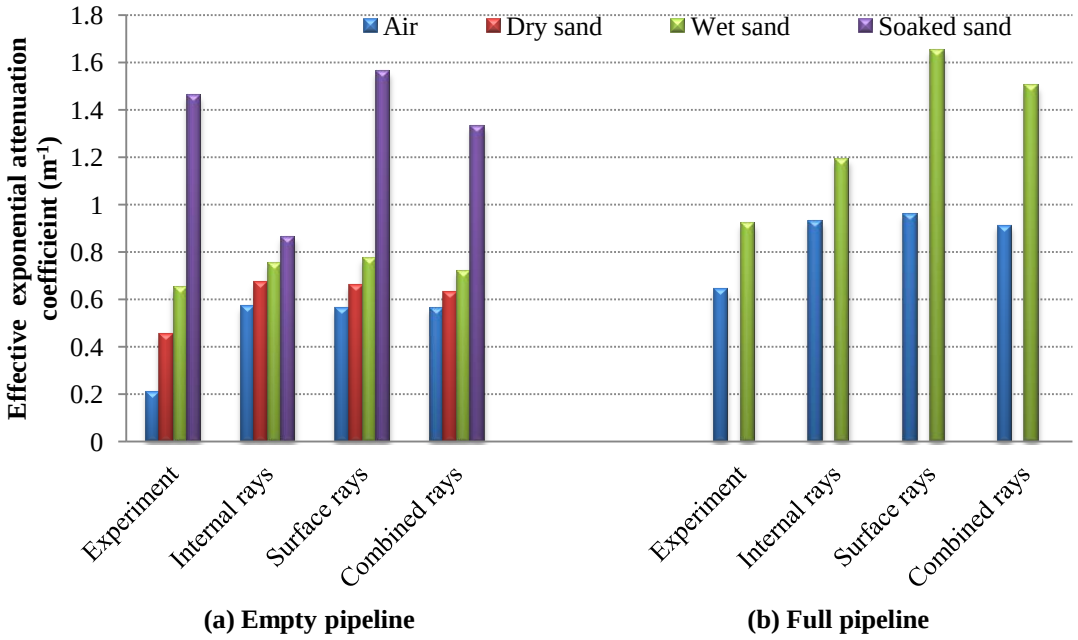

Figure 6.23: Comparison between experiments and simulation results for pipeline with different internal /external environments

Environments	**Surface damping, α_s**
Dry sand	0.05
Wet sand	0.1
Water	0.45
Soaked sand	0.5
Laminated glass	0.8

Table 6.16: Surface damping values, α_s, for different environments

These values of surface damping, α_s, were chosen to fit the experimental observations with different environments. The simulations were then re-run with lower surface damping for the small objects (steel plate, steel strip and laminated glass) most likely to support Lamb wave modes. The reflection coefficients for surface rays kept at 0.4, because the reflection for Lamb wave can vary between unity and zero [49]. Figure 6.24 summarises the experimental and modified simulations on the longer small objects (steel plate, steel strip and laminated glass) for the case with the source at the edge

(involving the greatest surface propagation distances). Comparing the modified simulations with the original one (Figures 6.17 and 6.19) show that the introduction of Lamb wave attenuation of the surface waves improves the differentiation between different environments for the steel plate and strip, and has also improve the simulation for the laminated glass. In general, there is sufficient evidence to suggest that a consistent attenuation model can cover most of the measurements.

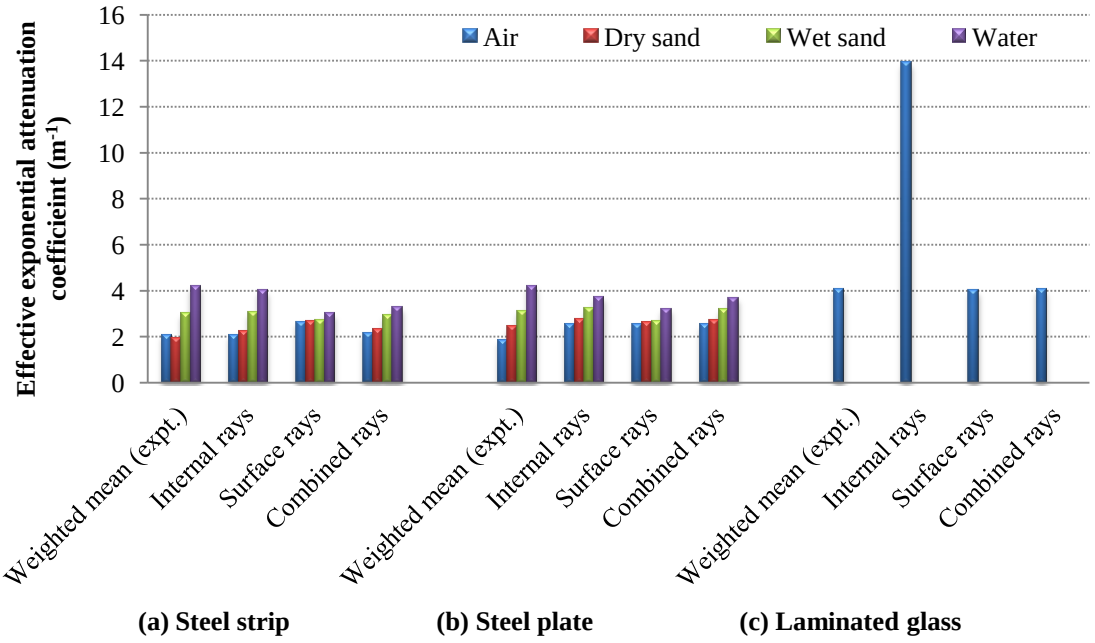

Figure 6.24: Comparison between experiments and modified simulation for steel strip, steel plate and laminated glass, source at the edge.

CHAPTER 7: CONCLUSIONS AND FUTURE WORK

The broad aim of this study was to develop a method of analysing AE propagation in solids which is an alternative to numerical solution of the wave equation. The value of such approach is that changes to the practical factors effecting attenuation can be investigated, practically to match simulations with measurements in real structures. As well as this, a predicted attenuation simulation can help to reconstruct the characteristics of an AE source, which has been recorded at one or more sensors at known distances, perhaps in a situation where the interface conditions are varying, e.g. a buried pipeline.

The method chosen was ray tracing in a solid model, and a set of simulations was carried out, modelling the attenuation in a set of models of relatively simple geometry, distinguished by an effective exponential coefficient, k', measured in m-1. In parallel, a set of measurements was carried out to determine the practical effective exponential coefficient, k (again measured in m-1), again for a set of test objects of simple geometry.

The conclusions are drawn first on the performance and flexibility of the computational technique. Secondly, the simulation parameters and procedures determined to give a good match to the measurements are summarised and, finally, the recommendations for future work are outlined.

7.1 Performance and flexibility of the simulation

The simulations involved launching two types of rays, namely “surface” and “internal” rays, each representing part of a wave front. The surface ray vectors are generated by a segmented circle and therefore represent circular wave fronts, i.e. 2-dimensional ray paths, which are traced on the surface of the model and are reflected when they hit the edges of this surface. The internal rays represent spherical wave fronts, the vectors being generated by the intersection of longitude and latitude lines over a sphere, the

centre of which is the source position. These 3-dimensional rays are traced inside the model structure and are reflected when they encounter the upper or lower surface.

A GUI was designed to allow the flexibility in changing various parameters of the simulation to perform a feasibility study and to view the traces of the ray paths both globally and locally, after running a simulation. Some of these parameters were varied to optimise performance and the others were varied to modify the simulation realism.

To match the simulation with the measurement, and adjust the program parameters, the simulation was run in two phases:

The first phase, called "geometric simulation", considered only the effect of beam spreading (i.e. the energy arriving at the sensor was obtained simply from the proportion of rays hitting the sensor). In this simple simulation, it was possible firstly to examine the convergence behaviour and the trade-off between resolution and accuracy by varying three parameters, the ray resolution, the extinction time and number of reflections.

The conclusions of this aspect are:

7.1.1 Computational efficiency is critical and major adjustments were required to the existing code in order to achieve any kind of convergence. To overcome memory leakage in the linked programming environments (C++ and ACIS), such measures as deleting pointers after each process, and using specific ACIS codes with less memory leakage (e.g. [16]) were taken. A number of other measures, such as avoiding rays becoming "boxed in" at corners, filtering non-viable rays at birth and limiting the simulation time were also effective in increasing the available resolution. Any increased complexity of the objects or of the simulation will require further efficiency measures to be taken or alternative platforms to be used.

7.1.2 To achieve convergence to a stable value of k' for the smaller solid shapes it was necessary to use a resolution of around 15,625 fired internal rays and around 7,500 surface rays, with a 900μsec extinction time, corresponding to an average ray length of

4.5m. This extinction time corresponds to typically around 7 reflections for the surface simulations. For internal simulations the number of reflections at convergence varied with the solid surface area, *A*, as follows:

- $A < 0.1$ m^2, 10 reflections
- 0.1 m^2 $< A < 1$ m^2, 20 - 30 reflections
- 1 m^2 $< A < 2$ cm^2, 50 reflections

7.1.3 For the two plates with the same surface area but different material (steel and laminated glass) the geometric simulations could only match the experimentally observed distinction by limiting the numbers of allowed reflections in the glass.

7.1.4 For the larger structures convergence was achieved with 10,000 fired internal rays and around 7,500 surface rays, at 900μsec extinction time, corresponding to around 100 reflections.

The second aspect of the geometric simulation was to investigate generally the capacity of the body plus surface wave concept to reflect the changes in *k* observed for the objects and source positions examined. Conclusions on this aspect are:

7.1.5 The simulations reproduced most of the geometrical changes observed in the small test objects and the stainless steel vessel, i.e. object shape and source position, certainly within the range of experimental error indicated by the repeat measurements.

7.1.6 For the pipeline, there was a significant discrepancy between simulation and experiment and this was traced to the position of the source, indicating that the simulation did not properly address the end condition.

The second phase, called “physical simulation”, took into account the additional attenuation mechanisms of material internal friction and energy losses on reflection. The investigation of the reflection losses was supplemented by some additional measurements in which one or both faces of the solid were subject to a range of

environments which were expected to affect impedance matching. Conclusions on this phase are:

7.1.7 The introduction of additional attenuation mechanisms obviated the need to use an extinction time as rays generally had lost all, or most, of their energy once the simulation time had been exceeded.

7.1.8 The additional mechanisms resulted in an under-constraint when it came to matching simulation with experiment. This required an approach where new mechanisms were introduced only as necessary to explain effects which could not be accounted for by a simpler model. A sensitivity analysis showed that energy loss on reflection was a more important mechanism than material internal friction, significant effects in the latter only being possible using internal friction exponential coefficients considerably in excess of those reported in the literature.

7.2 Simulation parameters

The investigation led to the following parameters and approaches for a successful simulation of the objects and environments examined.

7.2.1 The simulated and measured attenuation curves could conveniently be summarised using an effective exponential attenuation coefficient, *k'* or *k*, respectively, in

$$E_x = E_o e^{-kx} \qquad (2.22)$$

The fits achieved were a little better than using a power law curve fit and they were used for this reason rather than any implication about the attenuation mechanisms acting.

7.2.2 Absolute values of energy at the source, E_0, were considerably smaller for the simulations than the measurements, although they seemed to be consistent between surface and body rays.

7.2.3 A surface plus body wave approach was generally successful at matching *k'* and *k* in the majority of cases, using geometric spreading, internal friction and energy losses on reflection as the attenuation mechanisms.

7.2.4 For some of the larger structures, it was necessary to introduce a pseudo-internal friction mechanism for surface waves, which could be applied to the upper (generating) surface, or to both surfaces. It was only necessary to introduce lower surface wave pseudo-internal friction in structures where Lamb waves can be supported.

7.2.5 The path differences between successful waves were such that an even spread of phase differences across the range from 0 to 2π could be expected and so phase effects did not need to be taken into account for the structures examined for a source which is a point in space and time.

7.2.6 The final recommended parameters to give a consistent single approach for all of the tests are given by the following physical "laws" for total ray energy as a proportion of the rays fired:

Internal rays:

$$\frac{E}{E_0} = \sum_{j=1}^{N_h} [e^{-\alpha x_j} \times {R_U}^{n_{Uj}} \times {R_L}^{n_{Lj}}] \qquad (3.6)$$

where N_h is the number of rays hitting the sensor, α is the material internal friction coefficient (taken as 0.005), n_{Uj} and n_{Lj} are the numbers of reflections of the jth ray at the upper and lower surfaces, respectively, and R_U and R_L are the proportions of energy reflected at the upper and lower surfaces respectively. Table 7.1 shows the recommended reflection coefficient at different environments.

Environment	Reflection coefficients, R
Air	0.99
Dry sand	0.97
Wet sand	0.93
Water	0.87
Saturated sand	0.86
Resin (Laminated glass)	0.2

Table 7.1: Recommended reflection coefficient for different environments

Surface rays:

$$\frac{E}{E_0} = \sum_{j=1}^{N_h} \left[e^{-(\alpha+\alpha_U{}'+\alpha_L{}')x_j} \times R^{n_j} \right] \qquad (7.1)$$

where α_U' and α_L' are the pseudo-internal friction coefficients which damp surface waves at the upper and lower surfaces, respectively, n_j is the number of reflections of the jth ray at any edge, and R is the proportion of energy reflected at an edge (taken to be 0.4 for real edges, or 1 for seams when a cylinder is unrolled to be treated as a flat plate). Table 7.2 shows the recommended the pseudo-internal friction coefficients at different environments.

Environment	Pseudo-internal friction coefficients, α_U', α_L'
Air	0
Dry sand	0.05
Wet sand	0.1
Saturated sand	0.5
Water	0.45
Resin (Laminated glass)	0.8

Table 7.2: Recommended Pseudo-internal friction coefficients for different environments

7.3 Recommendations for future work

The following recommendations are suggested for further research:

- Introduce a mechanism for surface rays to spread to different faces of the solid model and deal with non-planar (e.g. cylindrical) surfaces.

- Using AE wave controlled sources than a pencil lead break might allow different source characteristics to be investigated, although the effect of sensor remounting will still exist.

- Improve the visualisation of complex ray patterns in 3D by introducing tagging and a zoom facility.

- Investigate AE wave spreading in more complex and more practical structures to separate noise from real signal and identify multiple and complex sources.

- Expand the simulations to take into account sources that are distributed in space and time. It is expected that this will introduce phase effects not seen in the current simulations.

REFERENCES

1) Kolsky H, "Stress Waves in Solids", Clarendon, Oxford, 1953.

2) Miller K and Hill E, "Nondestructive Testing Handbook, Vol. 6, Acoustic Emission Testing", Third Edition, American Society for Non-Destructive Testing, New York, 2005.

3) Matthews J, "Nondestructive Testing Monographs and Tracts", Vol. 2, London, 1983.

4) Vahaviolos S, "Acoustic Emission: Standards and Technology Update", ASTM, West Conshohocken, 1999.

5) Grosse C and Ohtsu M, "Acoustic Emission Testing", Springer, Berlin, 2008.

6) Hellier C, "Handbook of Nondestructive Evaluation", McGraw-Hill, London, 2003.

7) Lim T, et al., "Predicting AE attenuation within solids by geometric analysis", International Conference on Shape Modeling and Applications, Massachusetts, 2005, pp.156-162.

8) Rindel J, "The use of computer modeling in room acoustics", Journal of Vibroengineering, 2000, **3** (4), pp.219-224.

9) Hantschel T, et al. "Finite element analysis and ray tracing modeling of petroleum migration", Journal of Marine and Petroleum Geology, 2000, **17** (7), pp.815-820.

10) Glassner A, "An Introduction to Ray Tracing ", Third Edition, Academic Press, London, 1990.

11) Ginzel E, "NDT Modeling and overview", 2006, Available from: http://www.ndt.net/article/modellingNDT2007/2.pdf, (Viewed November 2012).

12) Aldrin J, NDT Modeling software, Available from: http://www.computationaltools.com/, (Viewed November 2012).

13) Scholey J, et al., "Acoustic emission in wide composite specimens", Trans Tech Publication, 2006, **13**, pp.325-332.

14) Schubert F, "Tomography techniques for acoustic emission monitoring", European Conference on NDT, 2006.

15) Deitel H, "C++ How to Program", Fifth Edition, Prentice Hall, London, 2005.

16) Spatial product documentation, Available from: http://doc.spatial.com/index2.php, (Viewed November 2012).

17) Corney J and Lim T, "3D Modeling with ACIS", Saxe Coburg, Stirling, 2001.

18) Tech Software 3D, Available from: http://www.techsoft3d.com, (Viewed November 2012).
19) Qi G, "Wavelet based acoustic emission characterization of composite materials", NDT & E International, 2000, **33**, pp.133-144.
20) Mathworks, MATLAB, "Signal Processing Toolbox User's Guide", Mathworks Inc., 2002.
21) Scott I, "Basic Acoustic Emission", Gordon and Breach, New York, 1991.
22) Holroyd T, "The Acoustic Emission and Ultrasonic Monitoring Handbook", Coxmoor Publishing Co, Northampton, 2000.
23) Verde C, "Accommodation of multi-leak location in a pipeline", Journal of Control Engineering Practice, 2005, **13**, pp.1071-1078.
24) Um J and Wright R, "Pipeline construction and reinstatement monitoring: Current practice, limitations and the value of airborne videography", The Science of the Total Environment, 1996, **186**, pp.221-230.
25) Papadakis G, "Major hazard pipelines: A comparative study of onshore transmission accidents", Journal of Loss Prevention, 1999, **12**, pp.91-107.
26) Montiel H, et al., "Historical analysis of accidents in the transportation of natural gas", Journal of Hazardous Materials, 1996, **51**, pp.77-92.
27) Whitaker M, et al., "Application of acoustic emission to the monitoring and end point determination of a high shear granulation process", International Journal of Pharmaceutics, 2000, **205**, pp.79-91.
28) Shehadeh M, "Monitoring of long steel pipes using acoustic emission ", PhD Thesis, Heriot-Watt University, Edinburgh, 2005.
29) Haque M, et al., "Application of Acoustic Sensing and Signal Processing for PD Detection in GIS", International Conference on Information, Communication and Signal Processing, 1997, pp.745-749.
30) Pollock A, "Classical wave theory in practical acoustic emission testing", Progress in Acoustic Emission III - Japanese Society for Non-Destructive Testing, 1986, pp.708-721.
31) Pao Y, "Theory of acoustic emission", Elastic Waves & Non-destructive Testing of Materials, ASME, California, 1978, **29**, pp.107-128.
32) Holford K and Carter D, "Acoustic emission source location", Key Engineering Materials, 1999, **167-168**, pp.162-171.

33) Shehadeh M, et al., "Acoustic emission source location in long steel pipes using cross correlation and wavelet transforms", 17th International Congress on Condition Monitoring And Diagnostic Engineering Management, Cambridge, 2004, pp-250. .259

34) Nivesrangsan P, "Multi-Source, Multi-Sensor Approaches To Diesel Engine Monitoring using Acoustic Emission", PhD thesis, Heriot-Watt University, Edinburgh, UK, 2004.

35) Hardy H, "Acoustic emission, microseismic activity: principles, techniques and geotechnical application", A. A. Balkema, Amsterdam, 2003.

36) Graff K, "Wave Motion in Elastic Solids", Dover, New York, 1991.

37) Babich V, et al., "Scatter of Rayleigh waves by tilted surface breaking cracks", NDT & E International, 2004, **37**, pp.105-109.

38) Initiation in primary seismology and the SOS-LIFE earthquake alarm working principle, Available from: http://lamit.ro/earthquake-early-warning-system.htm, (Viewed November 2012).

39) Sotja E, et al.,"Generation and analyses of guided waves in planar structures", Journal of Engineering, 2011, **3**, pp.532-537.

40) The American Society of Non-Destructive Testing, Ultrasonic Testing, Lamb wave, Available from: http://www.asnt.org/publications/errata/3UT03p100.pdf., (Viewed November 2012).

41) Choi S, et al., "Ultrasonic plate wave properties in thin steel plates", in International Conference on Control, Automation and Systems, Seoul, 2008, pp.1972-1975.

42) Jeong H, et al., "Detection of defects in a thin steel plate using ultrasonic guided wave", in 15th World Conference on Nondestructive Testing, Roma, 2000.

43) David J and Cheeke N, "Fundamentals and Applications of Ultrasonic Waves", CRC Series in pure and applied physics, CRC Press, London, 2002.

44) Brekhovskikh L, "Waves in Layered Media", Academic Press, New York, 1980.

45) Achenbach D, "Wave Propagation in Plastic Solids", Elsevier Science, Netherlands, 1975.

46) Bremaecker J, "Transmission and reflection of Rayleigh waves at corners", Geophysics 1958, **23** (2), pp.253-266.

47) Clement M, "The reflection and transmission of Rayleigh wave", MSc Thesis, University of British Columbia, 1961.

48) Liu Z, "Reflection and transmission of lamb waves at discontinuity in plate", in 16th World Conference on NDT, Montreal, 2004.

49) Cho Y and Rose J, "A boundary element solution for a mode conversion study on the edge reflection of Lamb waves", The Journal of the Acoustical Society of America, 1996, **99**, pp.2097-2109.

50) Nivesrangsan P, et al., "Acoustic emission mapping of engines for spatially located time series - Part 1: Preliminary studies", Mechanical Systems and Signal Processing, 2005, **19** (5), pp.1034-1054.

51) Schoorlemmer H, "Advanced real time source location applications", 26th European Conference on AE Testing, Berlin, 2004, pp.623-627.

52) Scruby C, et al., "Defect characterisation in three dimension by acoustic emission", Journal of Physics, Part D: Applied Physics, 1986, **19** (9), pp.1597-1612.

53) Neill G, et al., "Detection of incipient cavitations in pumps using acoustic emission", Proceedings of the Institution of Mechanical Engineers, Part E: Journal of Process Mechanical Engineering, 1997, **211**, pp.267-277.

54) Mba D, et al., "Detection of shaft seal rubbing in large scale power generation turbines with acoustic emissions, case study", Proceedings of Institute of Mechanical Engineers, Part A: J. Power and Energy, 2004, **218** (2), pp.71-81.

55) Nivesrangsan P, "Multi source, multi sensor approaches to diesel engine monitoring using acoustic emission", PhD Thesis, Heriot Watt University, Edinburgh, 2005.

56) Cummings K, et al., "Understanding Physics", Wily, 2004.

57) Hecht E, "Optics", Fourth Edition, Pearson Education, London, 2002.

58) Caruthers J, "Fundamentals of Marine Acoustic", Elsevier Oceanography, New York, 1977.

59) Cermer L and Heckl M, "Structure Borne Sound", Spring-Verlage, London, 1988.

60) Harris C, "Harris' Shock and Vibration Handbook", Six Edition, McGraw-Hill, London, 2009.

61) Maji A, et al., "Acoustic emission source location using lamb wave modes", Journal of Engineering Mechanics, 1997, **123** (2), pp.154-161.

62) Zener C, "Internal friction in solids", Proceedings of the Physical Society, 1940, **52** (1), pp.152-166.

63) Hudson D, "Internal friction in metals", PhD Thesis, California Institute of Technology, California, 1942.

64) Foppl O, "The practical importance of the damping capacity of metals, especially steels", Journal of Iron and Steel, 1936, **134**, pp.393-455.

65) Hopkinson B and Williams G, "The elastic hysteresis of steel", Proceedings of the Royal Society of London, Series A Containing Papers of a Mathematical and Physical Character, 1912, **87** (598), pp.505-511.

66) Aggelis G and Shiotani T, "Surface wave dispersion in cement based media: Inclusion size effect", NDT & E International, 2008, **41**, pp.319-325.

67) Aggelis G and Matikas A, "Effect of plate wave dispersion on the acoustic emission parameters in metals", Journal Computers and Structures, **98-99**, 2012.

68) Surgeon M and Wevers M, "One Sensor linear location of acoustic emission events using plate wave theories", Materials Science & Engineering A, 1999, **265** (1-2), pp.254-261.

69) Gorman M, "Plate wave acoustic emission", Journal of the Acoustical Society of America, 1991, **90** (1), pp.358-364.

70) Prosser W, "Advanced acoustic emission techniques in composite material research", Journal of Acoustic Emission, 1996, 14 (3-4), pp.1-11.

71) Thakkar N, "Monitoring of rail wheel interaction using acoustic emission", PhD Thesis, Heriot Watt University, Edinburgh, 2009.

72) Telford W, et al., "Applied Geophysics", Second Edition, Cambridge University Press, Cambridge 1990.

73) Shehadeh M, et al., "Aspects of acoustic emission attenuation in steel pipes subject to different internal and external environments", Mechanical Engineers, Part E: Journal of Process Mechanical Engineering, 2008, **222** (1), pp.41-54.

74) Nivesrangsan P, et al., "Acoustic emission mapping of engines for spatially located time series", 25th European Conference on AE Testing, Prague, 2002, pp.1151-1158.

75) Higo Y and Inaba H, "The general problems of acoustic emission sensors", American Society for Testing and Materials, Philadelphia, 1991, pp.7-24.

76) Finck F and Manthei G, "On near field effects in signal based acoustic emission analysis", Otto Graf Journal 2004, **15**, pp.121-133.

77) Dzenis Y and Qian J, "Analysis of microdamage evolution histories in composites", International Journal of Solids and Structures, 2001, **38** (10-13), pp.1831-1854.

78) Hsu N, et al., "An approach to acoustic emission signal analysis - Theory and experiment", Materials Evaluation, 1977, **35** (10), pp.100-106.

79) Hea T, et al., "Near field beam forming analysis for acoustic emission source localization", Elsevier, Ultrasonic, 2011, **52**, pp.587-592.

80) Graham L and Alers G, "Acoustic emission in the frequency domain", Monitoring Integrity by Acoustic Emission, American Society for Testing Materials, 1975, pp.11-39.

81) Carlin B, "Ultrasonic", McGraw-Hill, New York, 1960.

82) Maria A, "Introduction to Modeling and Simulation", Proceedings of the 29th Conference on Winter Simulation, Atlanta 1997.

83) Prosser W and Gorman M, "Accurate simulation of acoustic emission sources in composite plates", American Society for Non-Destructive Testing Spring Conference, New Orleans 1994.

84) Lindsey C, "Simulations of acoustic emission by turbulence", 2006, Available from: http://hmi.stanford.edu/TeamMeetings/Feb_2006/Proceedings/H5_CLindsey.pdf, (Viewed November 2012).

85) Banerjee S and Mal K, "Acoustic emission waveform simulation in multilayered composites", The Journal of Strain Analysis for Engineering Design, 2005, **40** (1), pp.25-32.

86) Mullins W, et al., "Examination on the use of acoustic emission for monitoring metal forging process: A study using simulation technique", Script Material, 1996, pp.967-974.

87) Dietzhausen H, et al., "Numerical simulation of acoustic emission in fibre reinforced polymers", Computational Materials Science, 1998, pp.23-30.

88) Gan H, et al., "Finite element formulation of acoustic scattering phenomena with absorbing boundary condition in the frequency domain", IEEE Symposium on Ultrasonic, 1992, pp.981-986.

89) Rindel J, "The use of computer modeling in room acoustics", Journal of Vibroengineering, 2000, **3**, pp.41-72.

90) Ippolito J, et al., "A 3-Dimensional finite element approach for simulating acoustic wave propagation in layered SAW devices", IEEE Symposium on Ultrasonic, Australia, 2003, pp.303 - 30.

91) Etter P, "Underwater Acoustic Modeling", Second Edition, Elsevier Science, London, 1996.

92) Suffern K, "Ray Tracing from the Ground up", A K Peters, Wellesley, 2007.

93) Kuchkuda R, "An Introduction to Ray Tracing", Theoretical foundations of computer graphics and CAD, 1988, pp.1039-1060.

94) Blake V, "The application of ray tracing techniques from computer graphics to the simulation of side scan sonar images", MPhil Thesis, Heriot Watt university, Edinburgh, 1994.

95) Adams R, "The damping characteristics of certain steels, cast irons and other metals", Journal of Sound and Vibration, 1972, **23** (2), pp.199–216.

96) Shirleya P, et al., "Fast ray tracing and the potential effects on graphics and gaming courses", Computers and Graphics Conference, 2008, pp.260-267.

97) Grynko Y and Shkuratov Y, "Ray tracing simulation of light scattering by spherical clusters consisting of particles with different shapes", Journal of Quantitative Spectroscopy and Radioactive Transfer, 2007, **106** (1-3), pp.56-62.

98) Ralf L and Philipp A, "Reverse ray tracing model for the performance evaluation on stationary solar concentrators", Solar energy 2006, **81**, pp.761-767.

99) Yang C, et al., "A ray tracing method for modeling indoor wave propagation and penetration", Antennas and Propagation Conference, 1998, pp.907-919.

100) Alves A, et al., "Efficient ray tracing method for indoor propagation prediction", International Conference on Microwave and Optoelectronics, 2005, pp.435-438.

101) Hampaia D, et al., "X-Ray propagation through polycarpellary optics studied through a ray tracing approach", Spectrochimica Acta Part B: Atomic Spectroscopy, 2007, **62** (6-7), pp.608-614.

102) Urick R, "Principles of Underwater Sound", Third Edition, McGraw Hill, London, 1983.

103) Gjoystdal H, et al., "Improved applicability of ray tracing in seismic acquisition, imaging and interpretation", Journal of Geophysics, 2007, **72** (5), pp.261-271.

104) Carpinteri A and Lacidogna G, "Earthquakes and Acoustic Emission", Taylor & Francis, London, 2007.

105) Cerveny V, "Seismic Ray Theory", Cambridge University Press, Cambridge, 2005.

106) Cerveny V and Hron H, "The ray series method and dynamic ray tracing system for three-dimensional inhomogeneous media", Bulletin of the Seismological Society of America, 1980, **70**, pp.47-77.

107) Yang, W., "A basic study on two-point seismic ray tracing", 2003, Available from: http://www.ees.nmt.edu/outside/courses/GEOP523/Docs/yang.pdf , (Viewed November 2012).

108) Moser T, et al., "Ray bending revisited", Bulletin of the Seismological Society of America, 1992, **82** (1), pp.259-288.

109) Krokstad et al., "Calculating acoustical room response by use of a ray tracing technique", Journal of Sound and Vibration, 1968, **8** (1), pp.118–125.

110) Schroeder M, "Digital simulation of sound transmission in reverberant spaces", Journal of the Acoustical Society of America, 1970, **47**, pp.424-431.

111) Wu S, "The linking of AutoCAD drafting package with a ray tracing program", 1989, **8**, pp.118-125.

112) Hodgson M, "Ray tracing prediction of noise levels in a nuclear power generation station", in Applied Acoustics, 1997, pp.19-29.

113) Tucker D and Gazey B, "Applied Underwater Acoustics", Pergamon Press Ltd, London, 1966.

114) UTman for ultrasonic weld inspection simulation, Available from: http://www.utsim.co.uk/, (Viewed November 2012).

115) Spectrum software, Available from: http://www.imperial.ac.uk/nde/products%20and%20services/spectrum, (Viewed November 2012).

116) 3D Ultrasonic simulation, Available from: http://www.utex.com, (Viewed November 2012).

117) Simulation software for non destructive testing, Available from: http://www-civa.cea.fr, (Viewed November 2012).

118) Gengembre N, "Pencil method for ultrasonic beam computation", 5th World Congress on Ultrasonic (WCU), 2003, pp.1533-1536.

119) Calmon P, et al., "CIVA: An expertise platform for simulation and processing NDT data", Ultrasonic, 2006, **44**, pp.975-979.

120) Ceranoglu A and Pao Y, "Propagation of elastic pulses and acoustic emission in a plate - Part 1: Theory", Journal of Applied Mechanics, 1981, **48** (1), pp.125-132.

121) Ceranoglu A and Pao Y, "Propagation of elastic pulses and acoustic emission in a plate - Part 2: Epicentral responses", Journal of Applied Mechanics, 1981, **48** (1), pp.133-138.

122) Ceranoglu A and Pao Y, "Propagation of elastic pulses and acoustic emission in a plate - Part 3: General responses", Journal of Applied Mechanics, 1981, **48** (1), pp.139-147.

123) Horn M, "Acoustic emission source location by reverse ray tracing", Patent no US5528557, USA, 1996.

124) Horn, M., "Method and apparatus for Acoustic emission monitoring", Patent no US4910718, USA, 1990.

125) Giordano M, et al., "Acoustic Emission wave Propagation in a viscoelastic Plate", Composite Science and Technology, 1999, **59**, pp.1735-1743.

126) Schubert F, "Basic principles of acoustic emission tomography", 26th European Conference on Acoustic Emission Testing, 2004, pp.15-17.

127) Schubert F, "Acoustic emission tomography - A new imaging technique for structural health monitoring", International Meeting of NDT Experts, 2005, pp.243-256.

128) Wilcox P, et al., "Progress towards a forward model of the complete acoustic emission process", Advanced Materials Research, 2006, **13-14**, pp.69 -76.

129) Nashed M, "Acoustic emission monitoring of propulsion system: A laboratory study on a small gas turbine", PhD Thesis, Heriot-Watt University, Edinburgh, 2010.

130) Esward J, et al., "An investigation into the establishment and assessment of a test facility for the calibration of acoustic emission sensors", Centre for Mechanical and Acoustical Metrology, National Physical Laboratory, 2002.

131) Peck R, et al., "Introduction to statistics and data analysis", Third Edition, Cengage Learning Inc, Florence, 2008.

132) Rajtar J and Muthiah R, "Pipeline leak detection system for oil and gas flowlines", Journal of Manufacturing Science and Engineering, Trans. ASME, 1997, **119**, pp.105-109.

133) Trofimov A, et al, "Experimental investigation of the attenuation of ultrasonic waves in liquids with change of temperature", Soviet Journal of Nondestructive Testing, 1990, **26** (8), pp.547-551.

134) Lilly J, "Recent advances in acoustical glazing", Journal of Sound and Vibration, 2004, pp.8-11.

APPENDIX A: AE SENSOR CERTIFICATES

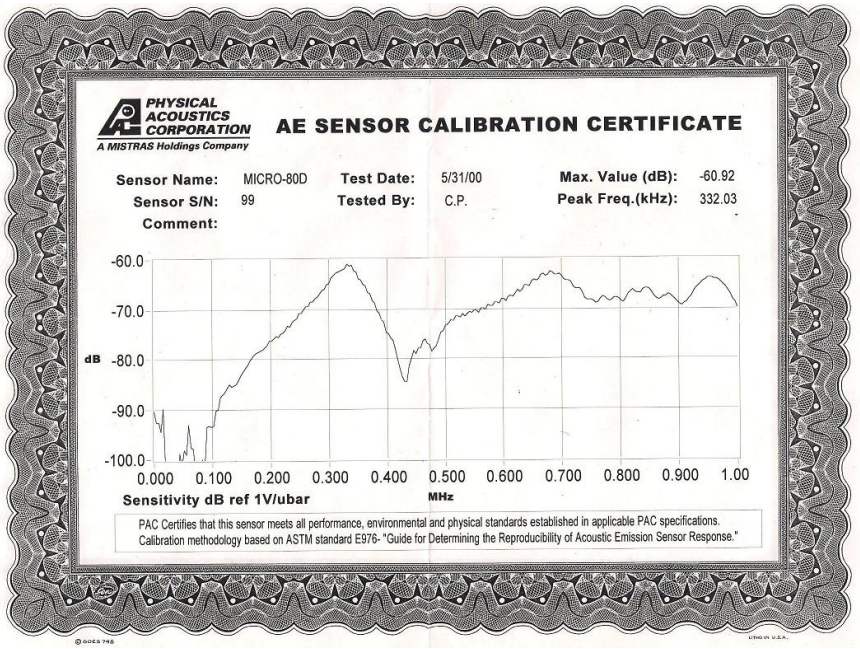

Figure A.1: AE sensor certificate for sensor 99.

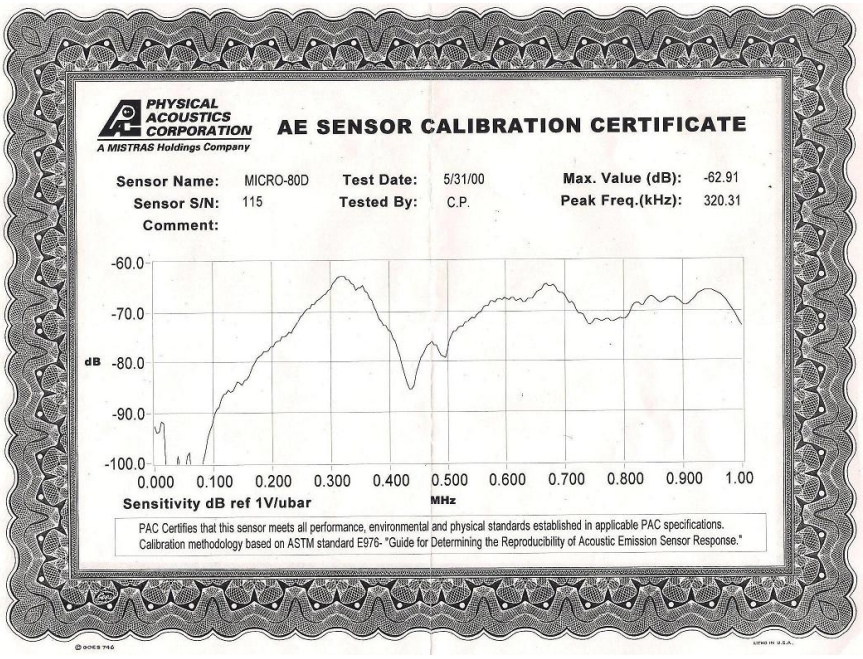

Figure A.2: AE sensor certificate for sensor 115.

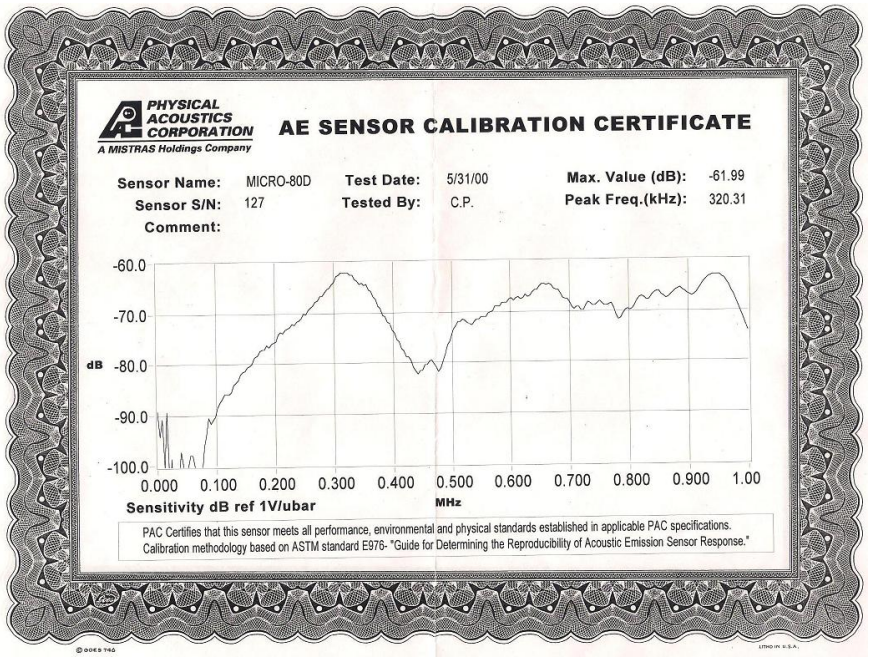

Figure A.3: AE sensor certificate for sensor 127.

APPENDIX B: PROGRAMME DATA RECORD

A copy of the AE data recording for predicted internal rays attenuation on steel plate, source at the edge, at 15625 fired rays, 900 μsecs and 50 maximum number reflection, 0.005 material impedance, 0.97 lower reflection and 0.99 upper reflection.

Source- sensor distance (m)	No of hits	Total no of rays fired inside the model	Hit ratio	Energy
0.90	10	7502	0.0013	5.127832
0.80	12	7502	0.0016	6.040742
0.70	13	7502	0.0017	5.956591
0.60	16	7502	0.0021	8.221238
0.50	22	7502	0.0029	11.94098
0.40	21	7502	0.0028	11.24406
0.30	25	7502	0.0033	12.24735
0.20	44	7502	0.0059	23.73602
0.10	112	7502	0.0149	73.06308

Table B.1: A copy of a short AE data recording for internal ray for plate, source at the edge

Sensor Index	Ray distance (m)	Energy	No of hits	No of reflection	Ray index
0	1.424405	0.718063	1	16	1767
0	1.158968	0.546956	1	29	3723
0	1.063225	0.424851	1	42	3725
0	1.166954	0.379837	1	47	3725
0	1.063925	0.361296	1	50	3726
0	1.063925	0.361296	1	50	3775
0	0.959496	0.4656	1	37	3776
0	1.063225	0.424851	1	42	3776
0	0.954899	0.727021	1	15	3779
0	1.424405	0.718063	1	16	5792
1	1.437593	0.696475	1	17	1709
1	1.624901	0.42366	1	42	2077
1	0.96374	0.719719	1	16	3722
1	1.259324	0.428722	1	41	3724
1	0.959496	0.460944	1	38	3725
1	1.270683	0.350095	1	50	3725
1	0.87963	0.380383	1	47	3774
1	0.855766	0.505155	1	33	3776
1	1.166954	0.391584	1	46	3776
1	1.158968	0.563872	1	28	3778
1	1.624901	0.42366	1	42	5370

1	1.437593	0.696475	1	17	5734
2	1.28396	0.479222	1	36	1519
2	1.624901	0.427939	1	41	2131
2	0.855766	0.500103	1	34	3725
2	0.87963	0.376579	1	48	3727
2	0.774681	0.380583	1	47	3773
2	0.767337	0.429778	1	41	3774
2	0.759947	0.485332	1	35	3775
2	0.752037	0.54807	1	29	3776
2	1.270683	0.360923	1	50	3776
2	0.742678	0.618921	1	23	3777
2	1.259324	0.441981	1	40	3777
2	1.624901	0.427939	1	41	5424
2	1.28396	0.479222	1	36	6032
3	1.225618	0.586987	1	26	1337
3	1.228047	0.424501	1	42	1395
3	1.28396	0.464845	1	37	1469
3	1.477735	0.592169	1	25	3722
3	0.742678	0.612732	1	24	3724
3	0.752037	0.542589	1	30	3725
3	0.759947	0.480479	1	36	3726
3	0.767337	0.42548	1	42	3727
3	0.774681	0.376777	1	48	3728
3	0.675786	0.429975	1	41	3773
3	0.655043	0.485587	1	35	3774
3	0.648308	0.59463	1	25	3776
3	0.643871	0.728152	1	15	3778
3	1.28396	0.464845	1	37	5982
3	1.228047	0.424501	1	42	6152
3	1.225618	0.586987	1	26	6216
4	2.172643	0.614512	1	23	605
4	1.172404	0.587143	1	26	1153
4	1.176204	0.636681	1	22	1154
4	1.186922	0.361074	1	50	1270
4	1.225618	0.569378	1	27	1285
4	1.228047	0.411766	1	43	1349
4	0.643871	0.720871	1	16	3723
4	0.648308	0.588684	1	26	3725
4	0.655043	0.480731	1	36	3727
4	0.675786	0.425675	1	42	3728
4	0.60212	0.365789	1	49	3770
4	0.575621	0.447975	1	39	3772
4	0.542819	0.594944	1	25	3775
4	0.544579	0.645147	1	21	3776

4	0.548936	0.699576	1	17	3777
4	1.477735	0.610484	1	24	3779
4	1.228047	0.411766	1	43	6106
4	1.225618	0.569378	1	27	6164
4	1.186922	0.361074	1	50	6271
4	1.172404	0.587143	1	26	6398
4	1.176204	0.636681	1	22	6399
4	2.172643	0.614512	1	23	6948
5	2.172643	0.608367	1	24	553
5	1.128497	0.563958	1	28	968
5	1.176204	0.617581	1	23	1102
5	1.172404	0.569529	1	27	1103
5	1.186922	0.350241	1	51	1230
5	0.548936	0.692581	1	18	3724
5	0.544579	0.638695	1	22	3725
5	0.542819	0.588995	1	26	3726
5	0.575621	0.443495	1	40	3729
5	0.60212	0.362131	1	50	3731
5	0.520335	0.365939	1	49	3768
5	0.479239	0.448191	1	39	3770
5	0.46878	0.48604	1	35	3771
5	0.457545	0.527087	1	31	3772
5	0.44503	0.571604	1	27	3773
5	0.440849	0.699955	1	17	3776
5	1.186922	0.350241	1	51	6231
5	1.176204	0.617581	1	23	6347
5	1.172404	0.569529	1	27	6348
5	1.128497	0.563958	1	28	6579
5	2.172643	0.608367	1	24	6896
6	3.109943	0.437911	1	40	292
6	1.102943	0.424767	1	42	901
6	1.128497	0.547039	1	29	922
6	1.114313	0.361205	1	50	960
6	1.759915	0.410673	1	43	3723
6	0.440849	0.692955	1	18	3725
6	0.44503	0.565888	1	28	3728
6	0.457545	0.521816	1	32	3729
6	0.46878	0.481179	1	36	3730
6	0.479239	0.443709	1	40	3731
6	0.520335	0.362279	1	50	3733
6	0.439436	0.366087	1	49	3765
6	0.424549	0.397011	1	45	3766
6	0.409136	0.430548	1	41	3767
6	0.392906	0.466921	1	37	3768

6	0.37548	0.506369	1	33	3769
6	0.361631	0.571843	1	27	3771
6	0.346134	0.645787	1	21	3773
6	0.33712	0.759419	1	13	3776
6	2.377226	0.443957	1	39	3779
6	2.438342	0.639067	1	21	3780
6	1.128497	0.547039	1	29	6533
6	1.114313	0.361205	1	50	6571
6	1.102943	0.424767	1	42	6634
6	3.109943	0.437911	1	40	7245
7	3.109943	0.424773	1	41	256
7	2.101313	0.56689	1	27	292
7	1.074919	0.564109	1	28	596
7	1.075794	0.499553	1	34	655
7	1.102943	0.412024	1	43	867
7	1.114313	0.350369	1	51	930
7	2.201652	0.686881	1	18	2501
7	0.269518	0.572106	1	27	3707
7	0.265562	0.595769	1	25	3708
7	0.233466	0.823934	1	9	3716
7	1.925007	0.69478	1	17	3721
7	2.438342	0.632676	1	22	3721
7	2.377226	0.439518	1	40	3722
7	0.33712	0.751824	1	14	3725
7	0.346134	0.639329	1	22	3728
7	0.361631	0.566124	1	28	3730
7	0.37548	0.501305	1	34	3732
7	0.392906	0.462252	1	38	3733
7	0.409136	0.426243	1	42	3734
7	0.424549	0.393041	1	46	3735
7	0.439436	0.362426	1	50	3736
7	0.375304	0.366204	1	49	3761
7	0.390623	0.351639	1	51	3761
7	0.356376	0.397146	1	45	3762
7	0.337011	0.430704	1	41	3763
7	0.316965	0.467098	1	37	3764
7	0.295947	0.506571	1	33	3765
7	0.292467	0.527522	1	31	3766
7	0.269431	0.572106	1	27	3767
7	0.265477	0.59577	1	25	3768
7	0.261698	0.620411	1	23	3769
7	0.23884	0.791203	1	11	3775
7	0.233391	0.823934	1	9	3776
7	1.759915	0.423374	1	42	3778

7	0.269518	0.572106	1	27	3828
7	0.265562	0.595769	1	25	3829
7	0.233466	0.823934	1	9	3837
7	2.201652	0.686881	1	18	4940
7	1.114313	0.350369	1	51	6541
7	1.102943	0.412024	1	43	6600
7	1.075794	0.499553	1	34	6876
7	1.074919	0.564109	1	28	6939
7	3.109943	0.424773	1	41	7209
7	2.101313	0.56689	1	27	7245
8	3.08314	0.372453	1	48	220
8	2.101313	0.561221	1	28	256
8	2.071493	0.444637	1	39	282
8	1.092683	0.74899	1	14	292
8	1.074875	0.663339	1	20	349
8	1.056926	0.4996	1	34	527
8	1.074919	0.547186	1	29	562
8	1.075794	0.484567	1	35	625
8	1.06955	0.376222	1	48	707
8	2.201652	0.693819	1	17	2561
8	0.152653	0.700964	1	17	3644
8	0.138225	0.760174	1	13	3647
8	0.129828	0.89393	1	5	3655
8	0.233466	0.815695	1	10	3664
8	0.265562	0.589812	1	26	3672
8	0.269518	0.566385	1	28	3673
8	0.298149	0.413685	1	43	3697
8	0.261794	0.467227	1	37	3698
8	0.224508	0.527701	1	31	3699
8	0.238993	0.506715	1	33	3699
8	0.215659	0.549541	1	29	3700
8	0.191543	0.59599	1	25	3701
8	0.206867	0.572285	1	27	3701
8	0.182206	0.620658	1	23	3702
8	0.172671	0.646347	1	21	3703
8	0.162818	0.673101	1	19	3704
8	0.152506	0.700964	1	17	3705
8	0.141562	0.729983	1	15	3706
8	0.149732	0.729953	1	15	3707
8	0.138092	0.760175	1	13	3708
8	0.1252	0.791652	1	11	3709
8	0.135213	0.791613	1	11	3710
8	0.120582	0.824399	1	9	3711
8	0.132878	0.824349	1	9	3712

8	0.131051	0.858436	1	7	3714
8	0.129703	0.893931	1	5	3716
8	0.233391	0.815695	1	10	3725
8	0.23884	0.783291	1	12	3726
8	0.261698	0.614207	1	24	3732
8	0.265477	0.589812	1	26	3733
8	0.269431	0.566385	1	28	3734
8	0.292467	0.522247	1	32	3735
8	0.295947	0.501505	1	34	3736
8	0.316965	0.462427	1	38	3737
8	0.337011	0.426397	1	42	3738
8	0.356376	0.393175	1	46	3739
8	0.375304	0.362542	1	50	3740
8	0.320184	0.381448	1	47	3756
8	0.333809	0.36628	1	49	3756
8	0.347434	0.351715	1	51	3756
8	0.28419	0.430817	1	41	3757
8	0.298053	0.413685	1	43	3757
8	0.311916	0.397234	1	45	3757
8	0.247563	0.486577	1	35	3758
8	0.26171	0.467227	1	37	3758
8	0.275856	0.448647	1	39	3758
8	0.224436	0.527701	1	31	3759
8	0.238916	0.506715	1	33	3759
8	0.200721	0.572303	1	27	3760
8	0.21559	0.549542	1	29	3760
8	0.191482	0.59599	1	25	3761
8	0.2068	0.572286	1	27	3761
8	0.182147	0.620658	1	23	3762
8	0.172615	0.646348	1	21	3763
8	0.162766	0.673102	1	19	3764
8	0.152457	0.700965	1	17	3765
8	0.141516	0.729983	1	15	3766
8	0.149684	0.729954	1	15	3767
8	0.138048	0.760175	1	13	3768
8	0.12516	0.791653	1	11	3769
8	0.13517	0.791613	1	11	3770
8	0.120544	0.824399	1	9	3771
8	0.132836	0.824349	1	9	3772
8	0.131009	0.858436	1	7	3774
8	0.129662	0.893931	1	5	3776
8	1.925007	0.716268	1	16	3780
8	0.233466	0.815695	1	10	3785
8	0.265562	0.589812	1	26	3793

8	0.269518	0.566385	1	28	3794
8	0.298149	0.413685	1	43	3818
8	0.261794	0.467227	1	37	3819
8	0.224508	0.527701	1	31	3820
8	0.238993	0.506715	1	33	3820
8	0.215659	0.549541	1	29	3821
8	0.191543	0.59599	1	25	3822
8	0.206867	0.572285	1	27	3822
8	0.182206	0.620658	1	23	3823
8	0.172671	0.646347	1	21	3824
8	0.162818	0.673101	1	19	3825
8	0.152506	0.700964	1	17	3826
8	0.141562	0.729983	1	15	3827
8	0.149732	0.729953	1	15	3828
8	0.138092	0.760175	1	13	3829
8	0.1252	0.791652	1	11	3830
8	0.135213	0.791613	1	11	3831
8	0.120582	0.824399	1	9	3832
8	0.132878	0.824349	1	9	3833
8	0.131051	0.858436	1	7	3835
8	0.129703	0.893931	1	5	3837
8	0.152653	0.700964	1	17	3887
8	0.138225	0.760174	1	13	3890
8	0.129828	0.89393	1	5	3898
8	2.201652	0.693819	1	17	5000
8	1.06955	0.376222	1	48	6806
8	1.075794	0.484567	1	35	6846
8	1.074919	0.547186	1	29	6905
8	1.056926	0.4996	1	34	6992
8	1.074875	0.663339	1	20	7180
8	2.101313	0.561221	1	28	7209
8	2.071493	0.444637	1	39	7235
8	1.092683	0.74899	1	14	7245
8	3.08314	0.372453	1	48	7295

Table B.2: A copy of a long AE data recording for internal ray for plate, source at the edge

APPENDIX C: GEOMETRIC SIMULATION

C.1 Experiment results

Figures from C.1 to C.8 show the relationship between the measured of AE energy level and source-sensor distance and the correlation coefficient, on four steel solid shapes: block, plate, strip and cylinder respectively.

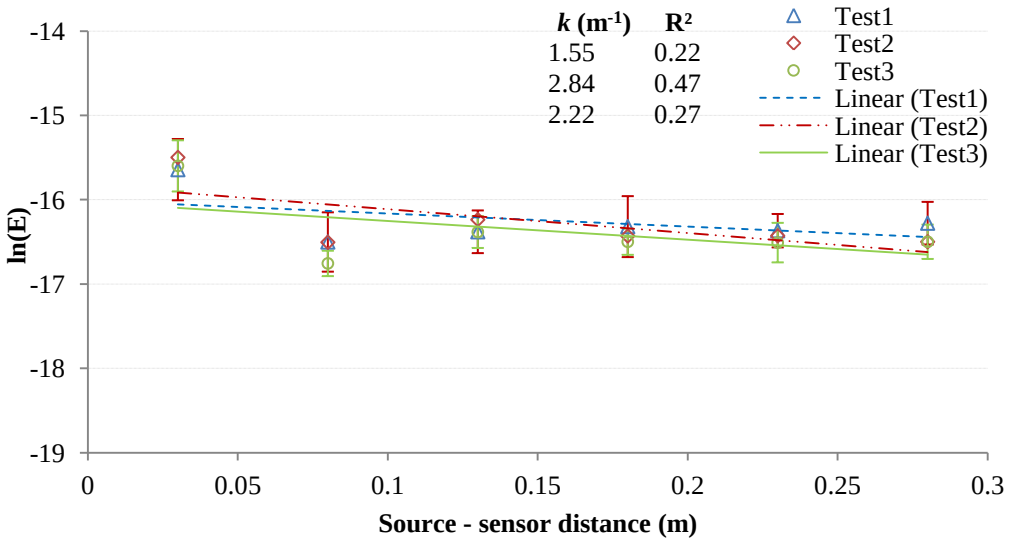

Figure C.1: Experimental AE attenuation in steel block, source at the edge.

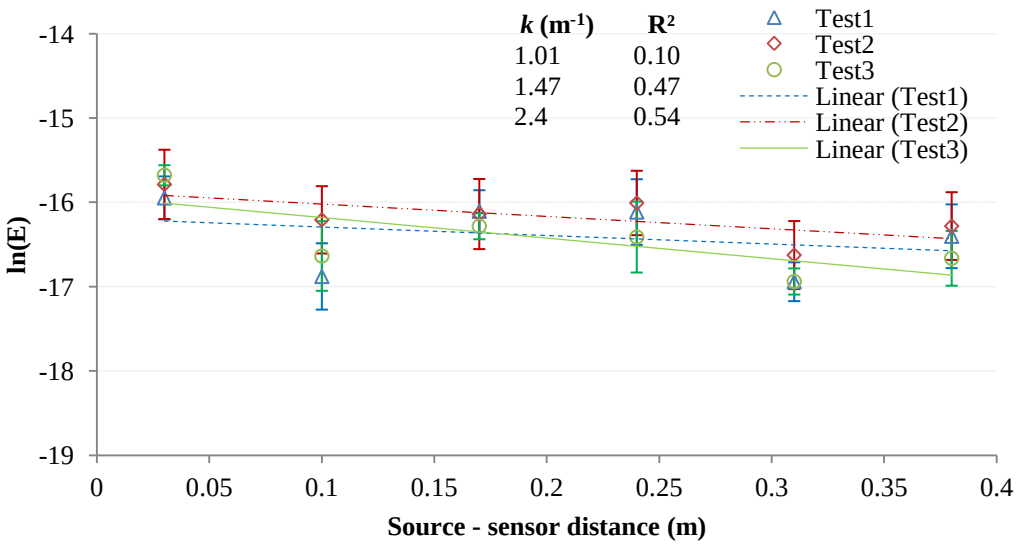

Figure C.2: Experimental AE attenuation in steel block, source at the corner.

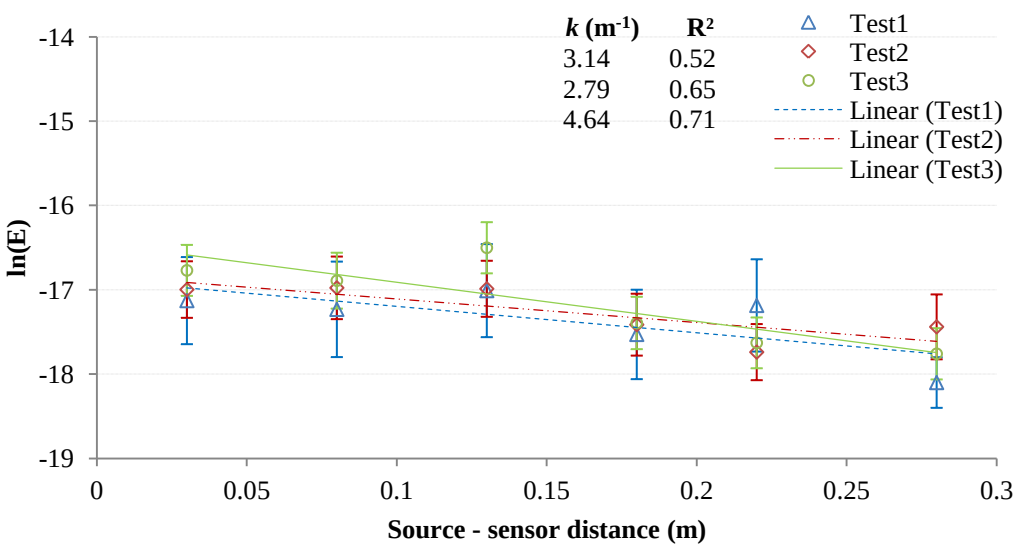

Figure C.3: Experimental AE attenuation in steel block, source at the end

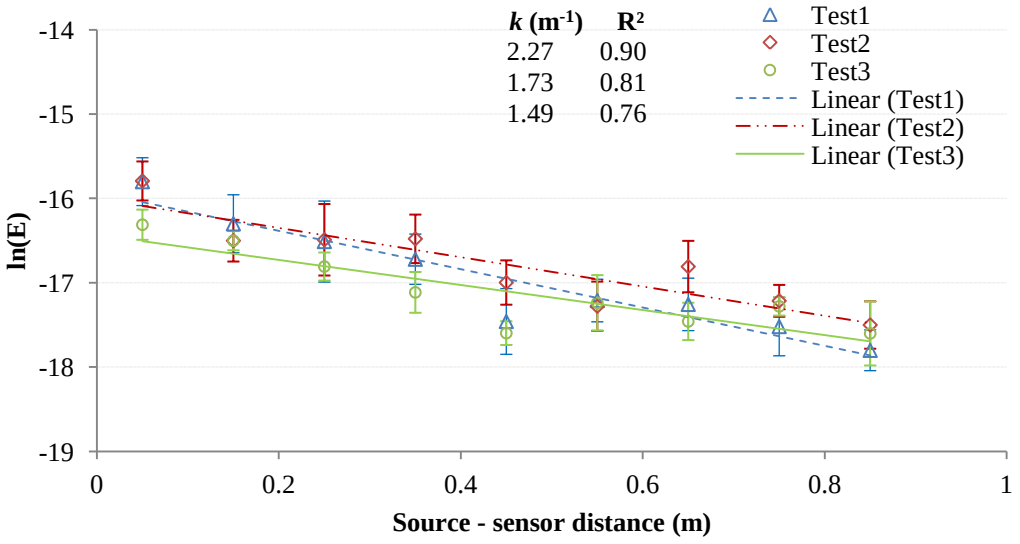

Figure C.4: Experimental AE attenuation in steel plate, source at the Edge.

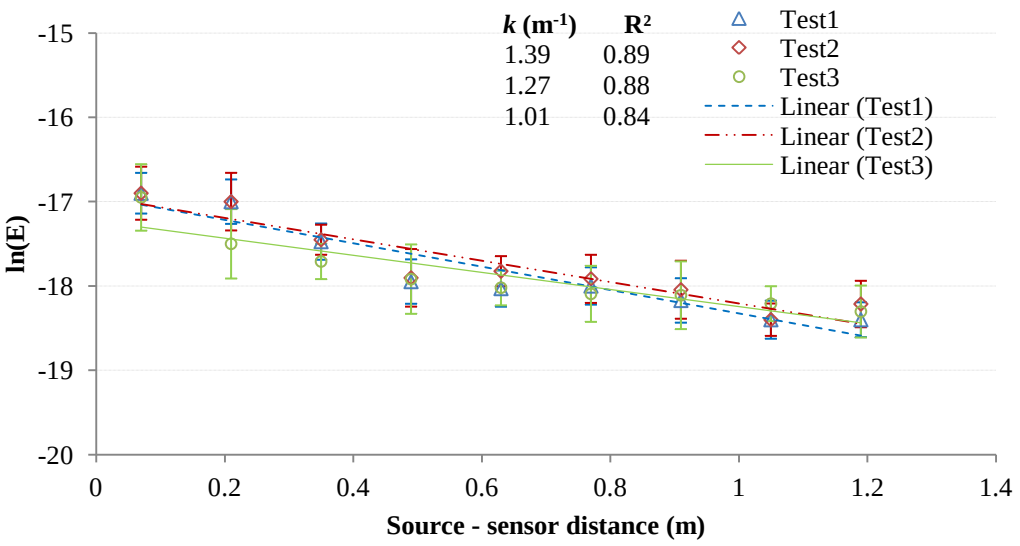

Figure C.5: Experimental AE attenuation in steel plate, source at the corner.

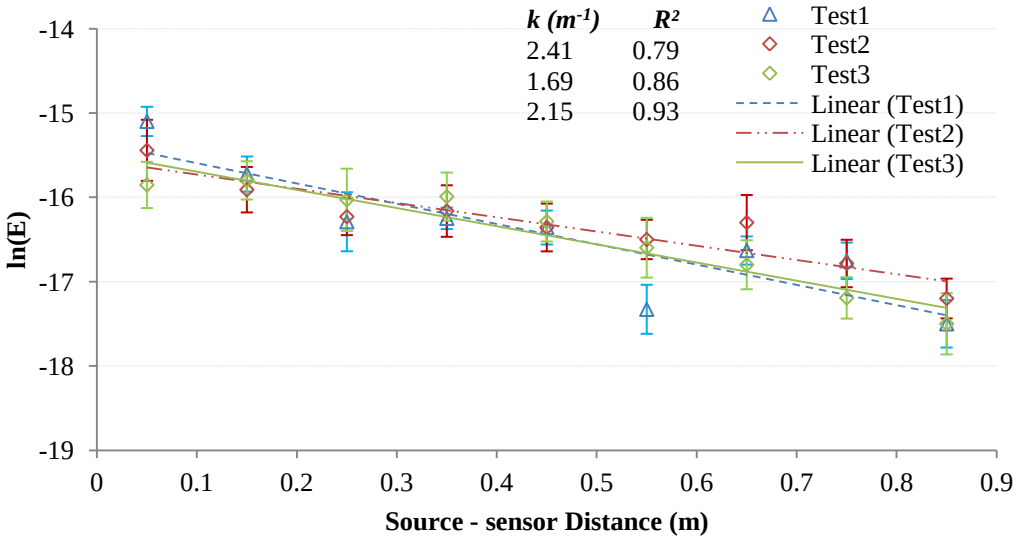

Figure C.6: Experimental AE attenuation in steel strip, source at the edge.

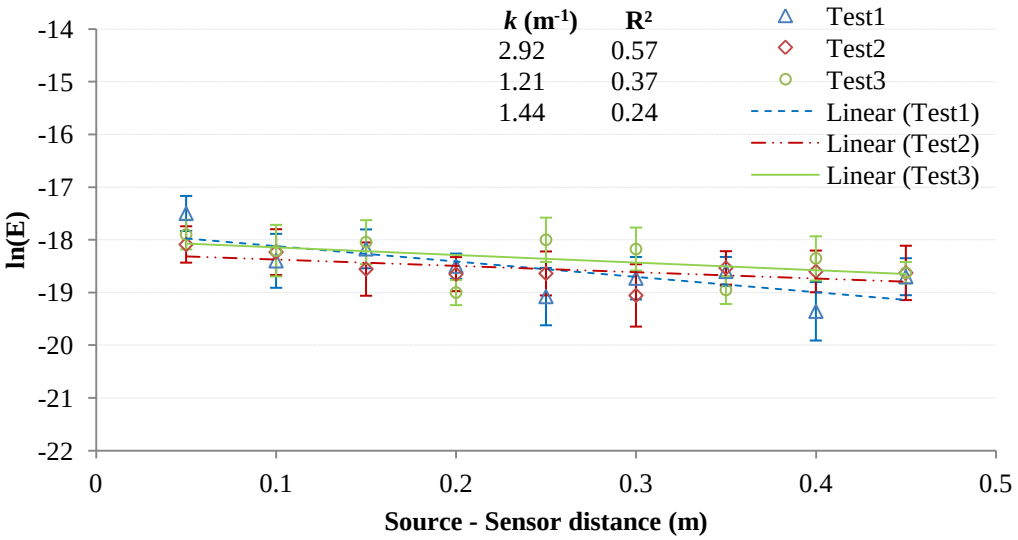

Figure C.7: Experimental AE attenuation in steel strip, source at the end.

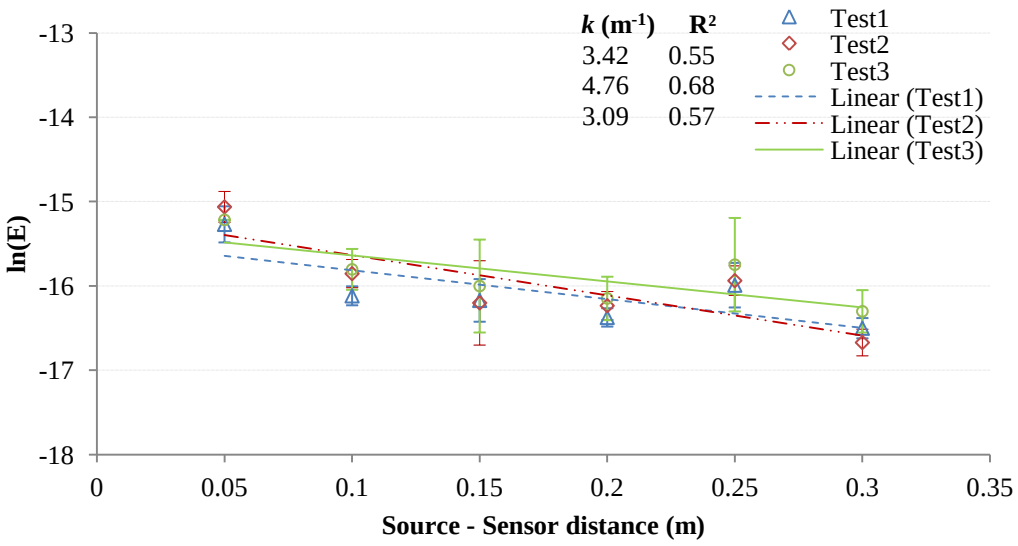

Figure C.8: Experimental AE attenuation in steel cylinder, source at the edge.

C.2 Simulation results

Figures from C.9 to C.18 show the ray tracing prediction of the AE attenuation for converged internal rays, surface rays and combined rays (surface and internal) at 15625, 7500 and 23125 fired rays and 900 µsecs for the internal, surface and combined rays respectively.

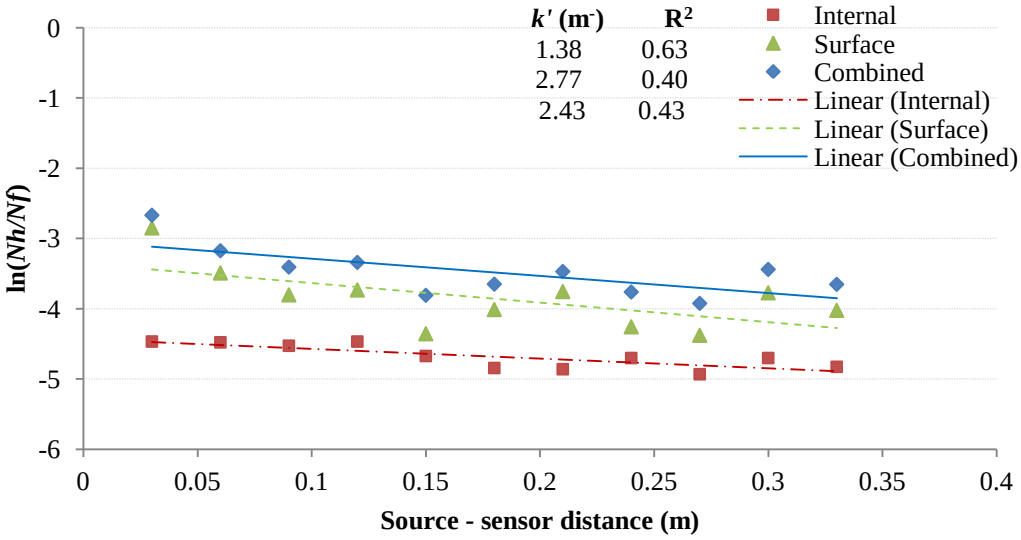

Figure C.9: Predicted internal, surface and combined rays attenuation on steel block, source at the edge, at 15625, 7500 and 23125 fired rays and 900 µsec

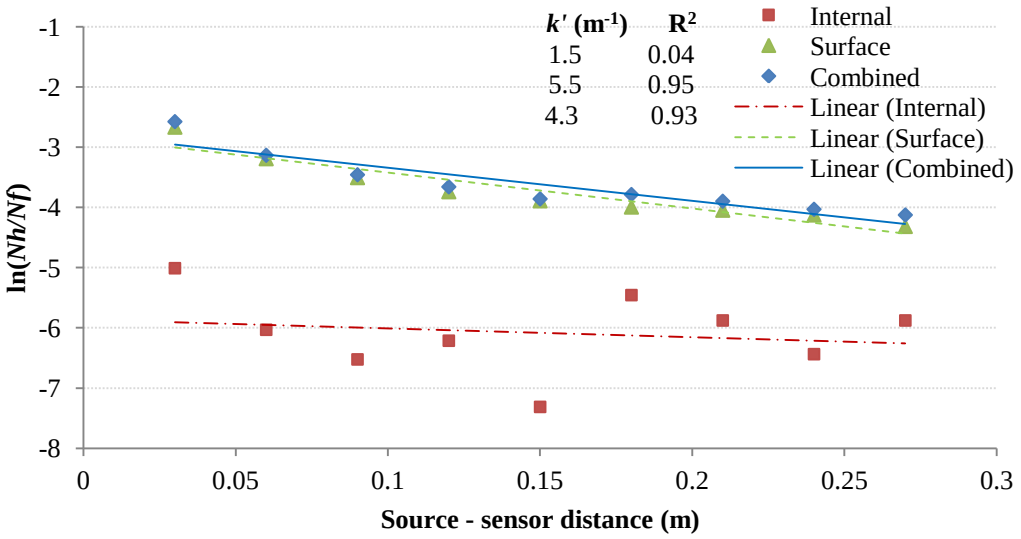

Figure C.10: Predicted internal, surface and combined rays attenuation on steel block, source at the end, at 15625, 7500 and 23125 fired rays and 900 µsec

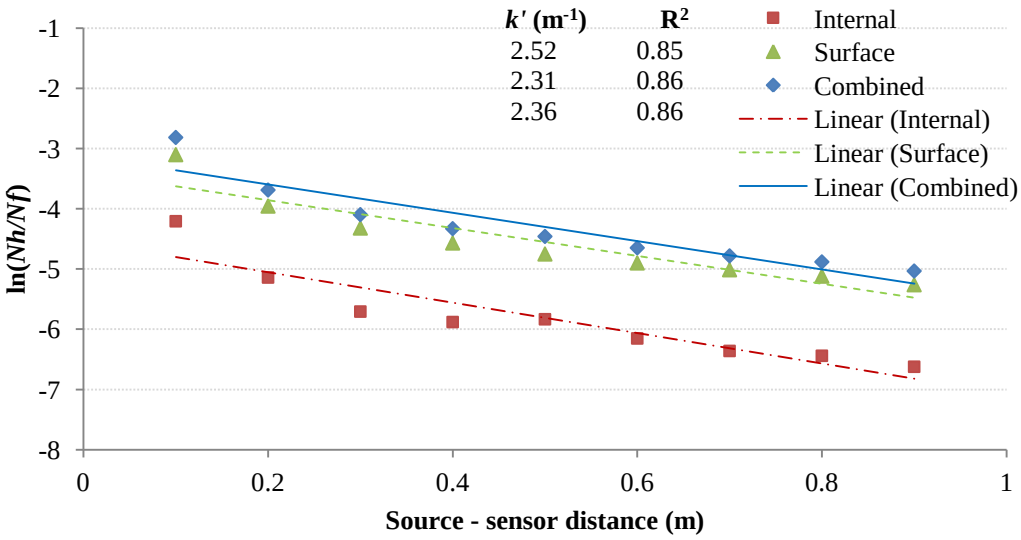

Figure C.11: Predicted internal, surface and combined rays attenuation on steel plate, source at the edge, at 15625, 7500 and 23125 fired rays and 900 µsec

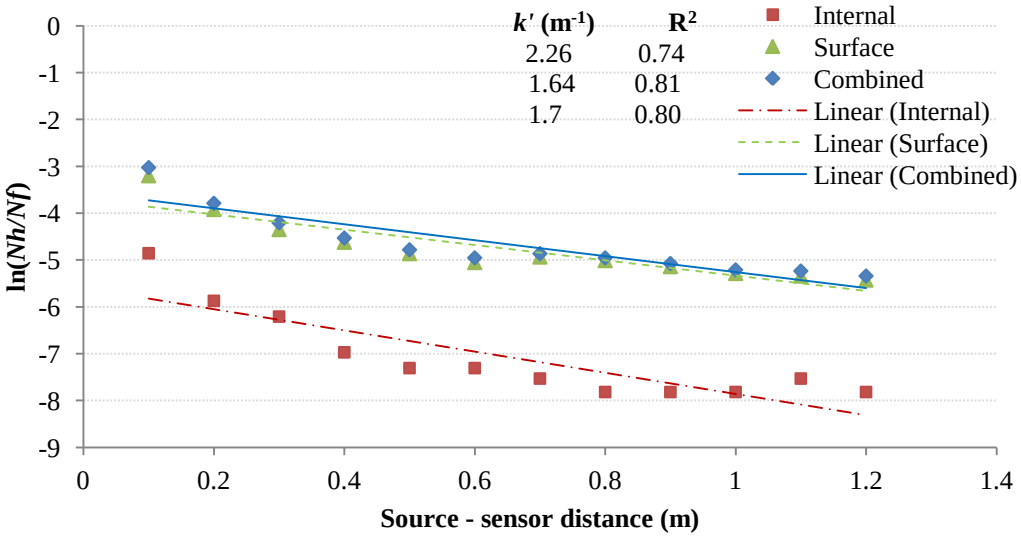

Figure C.12: Predicted internal, surface and combined rays attenuation on steel plate, source at the corner, at 15625, 7500 and 23125 fired rays and 900 µsec

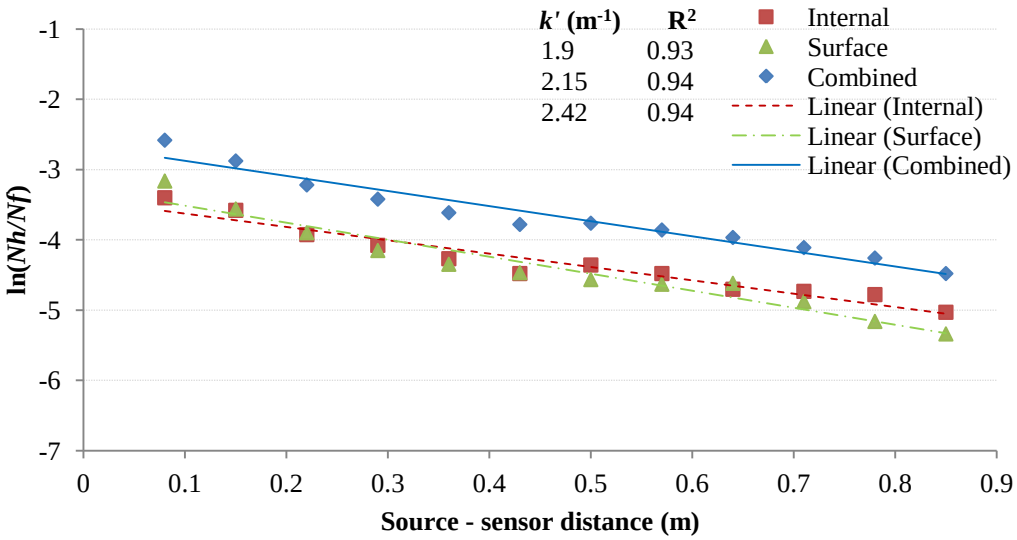

Figure C.13: Predicted internal, surface and combined rays attenuation on steel Strip, source at the edge, at 15625, 7500 and 23125 fired rays and 900 µsec

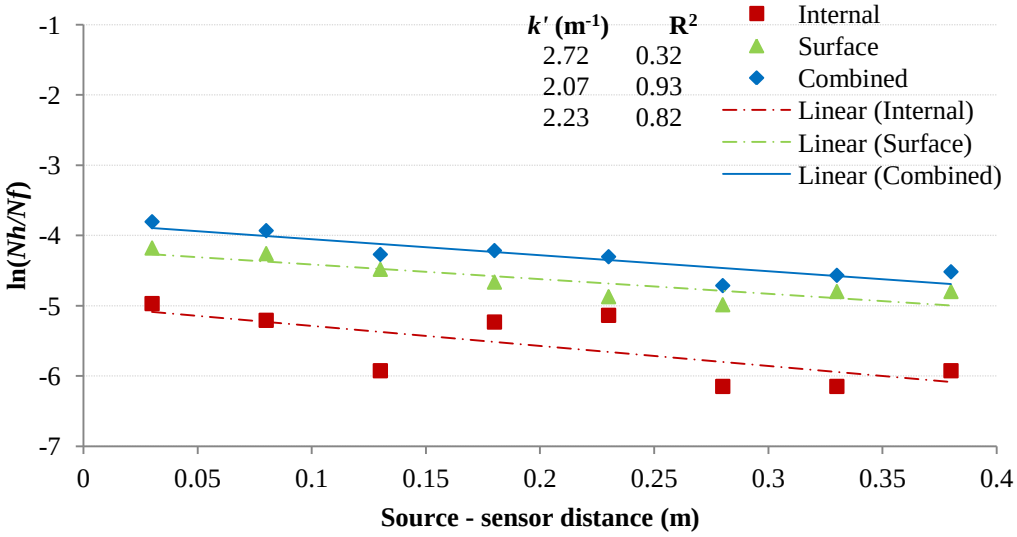

Figure C.14: Predicted internal, surface and combined rays attenuation on steel Strip, source at the end, at 15625, 7500 and 23125 fired rays and 900 µsec

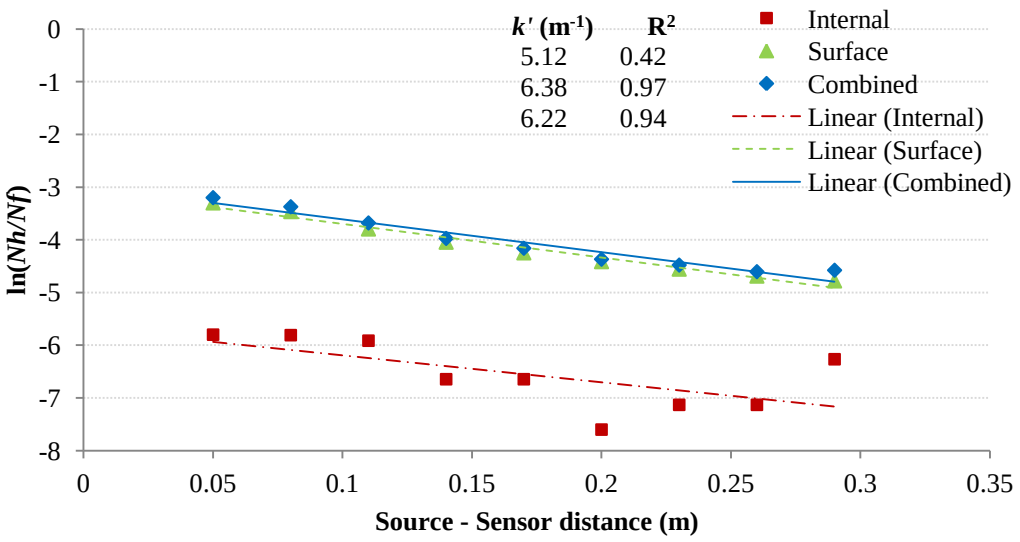

Figure C.15: Predicted internal, surface and combined rays attenuation on steel cylinder, source at the edge, at 15625, 7500 and 23125 fired rays and 900 µsec

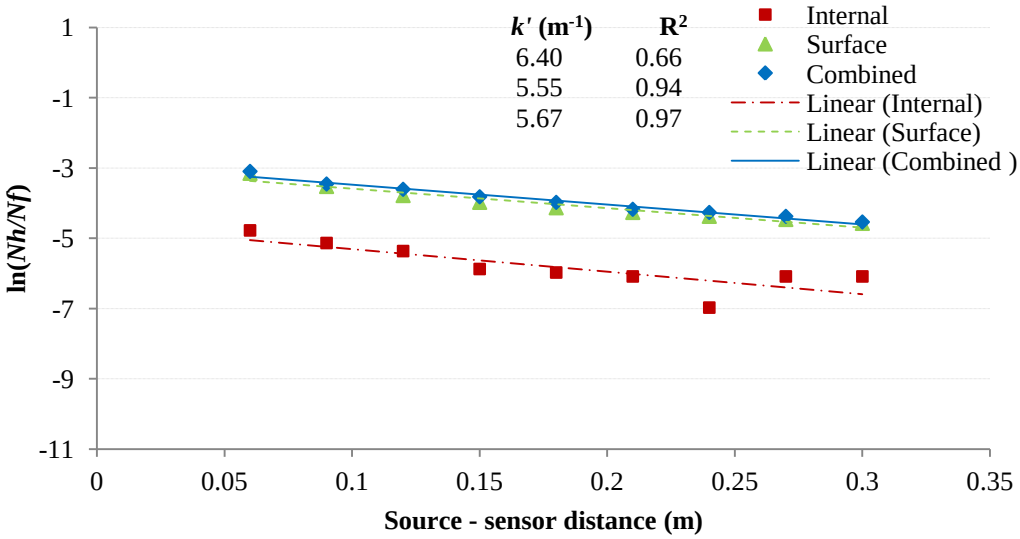

Figure C.16: Simulated internal, surface and combined ray attenuation on laminated glass plate, source at the centre, at 15625, 7500 and 23125 fired rays and 900 µsec

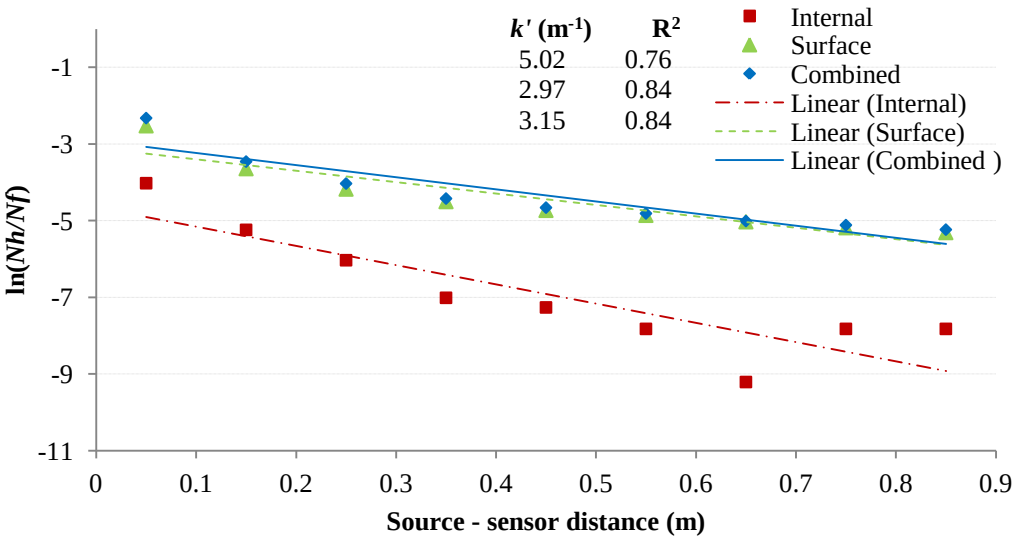

Figure C.17: Simulated internal, surface and combined ray attenuation on laminated glass plate, source at the edge, at 15625, 7500 and 23125 fired rays and 900 µsec

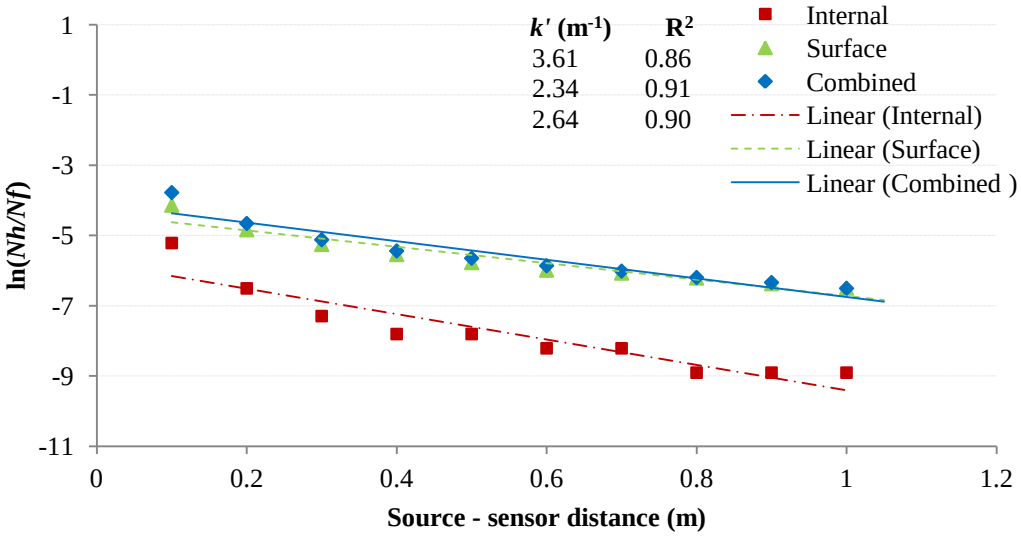

Figure C.18: Predicted internal, surface and combined rays attenuation on a laminated glass plate, source at the corner, at 15625, 7500 and 23125 fired rays and 900 µsec

D.2 Experiment results

Figures from D.1 to D.24 show the measurement attenuation on solid shapes, after averaging the data for three repeated tests, where the source was at different positions for the four different surrounding environments; air, dray sand, wet sand and water.

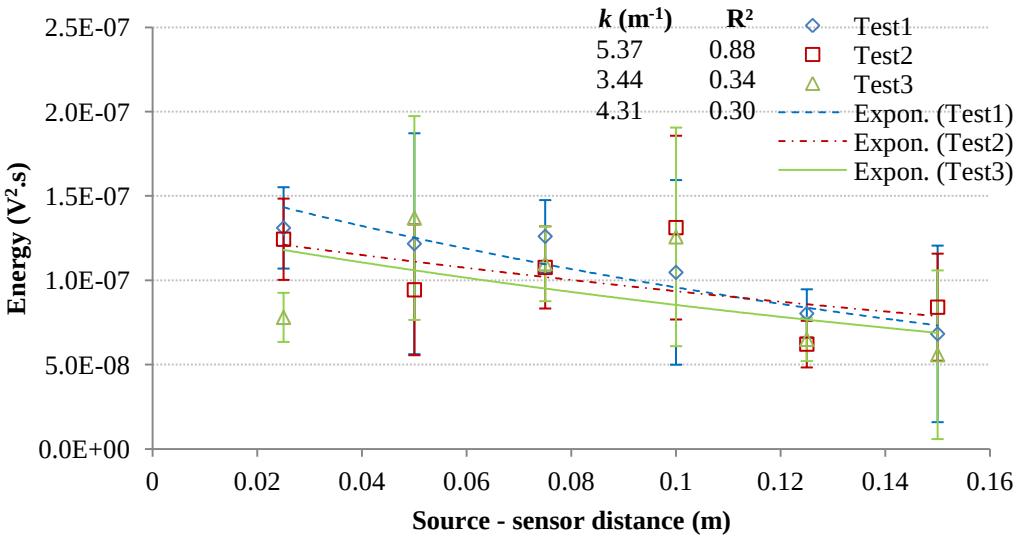

Figure D.1: Experimental AE attenuation on steel block, air, source at the centre.

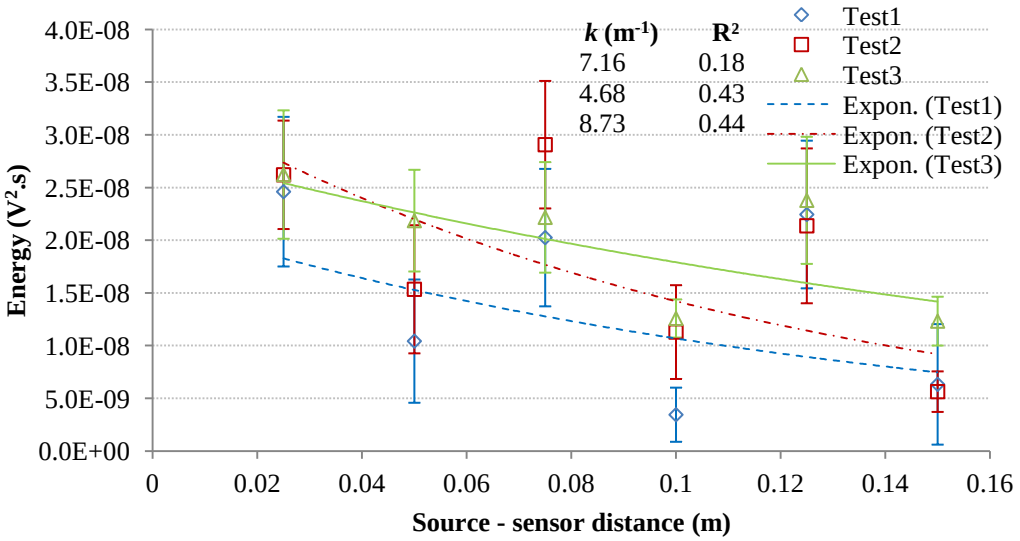

Figure D.2: Experimental AE attenuation on steel block, dry sand, source at the centre

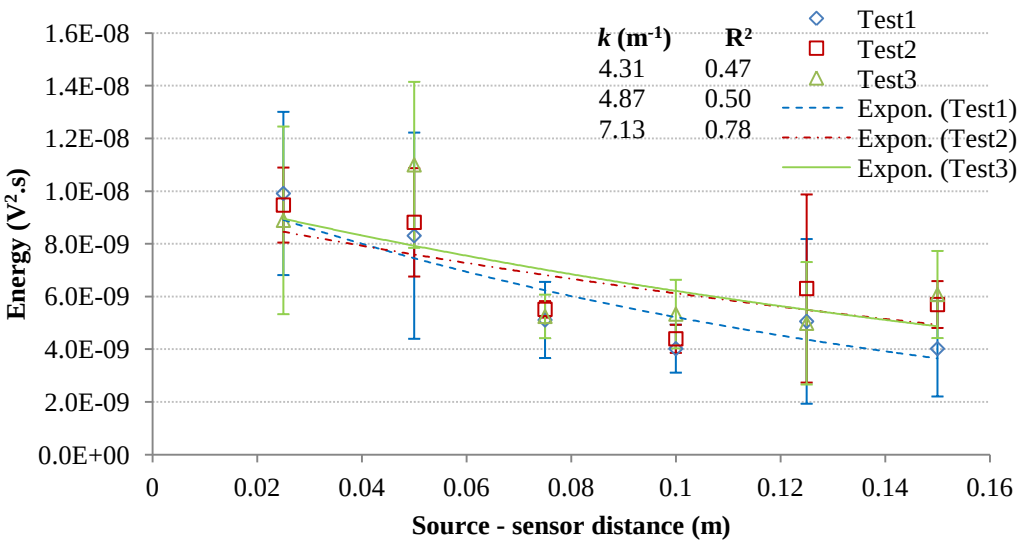

Figure D.3: Experimental AE attenuation on steel block, wet sand, source at the centre

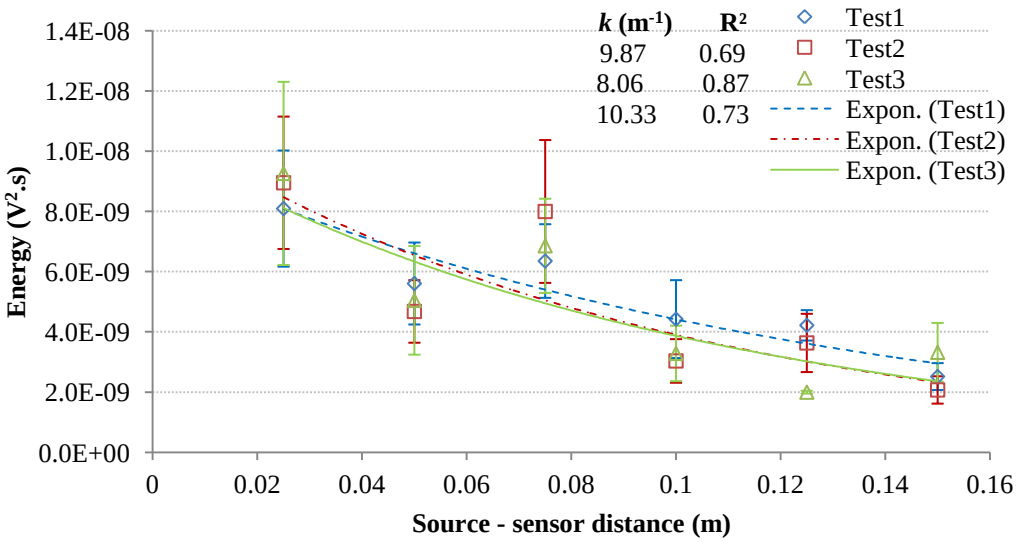

Figure D.4: Experimental AE attenuation on steel block, water, source at the centre

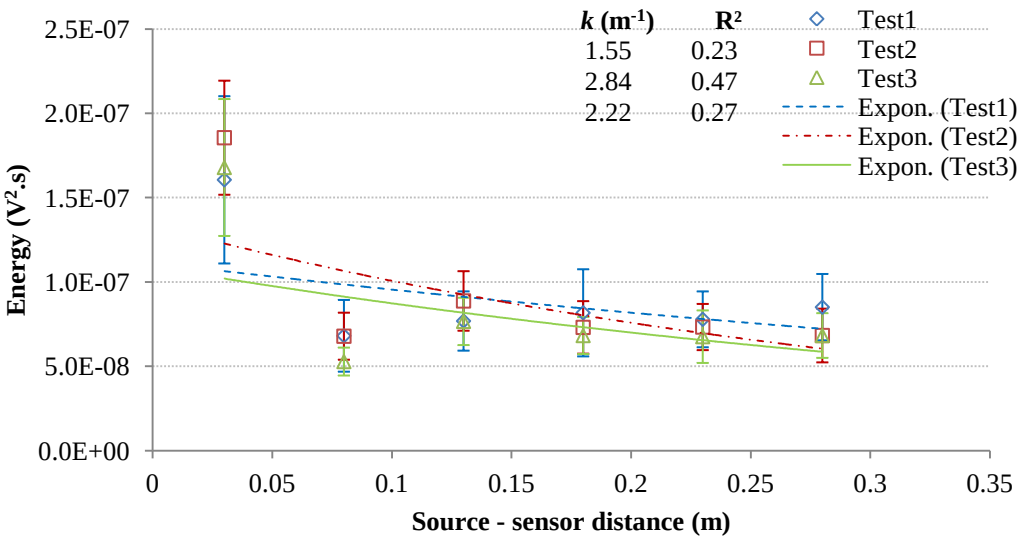

Figure D.5: Experimental AE attenuation on steel block, air, source at the edge

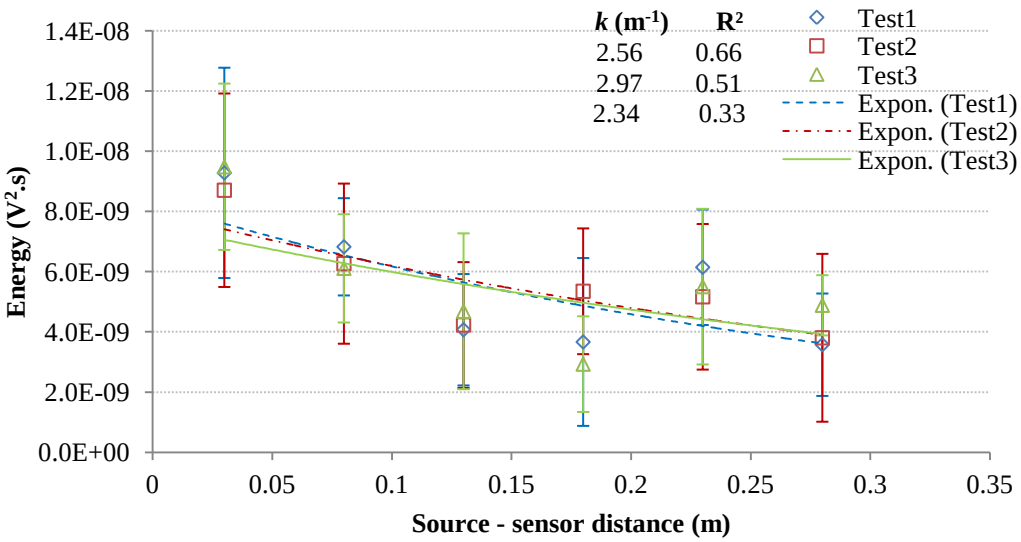

Figure D.6: Experimental AE attenuation on steel block, dry sand, source at the edge

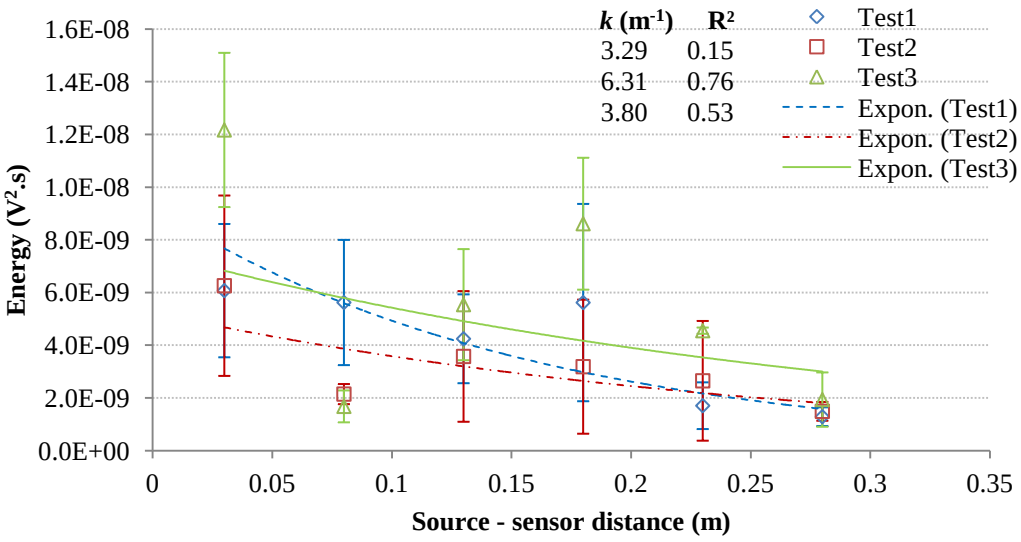

Figure D.7: Experimental AE attenuation on steel block, wet sand, source at the edge

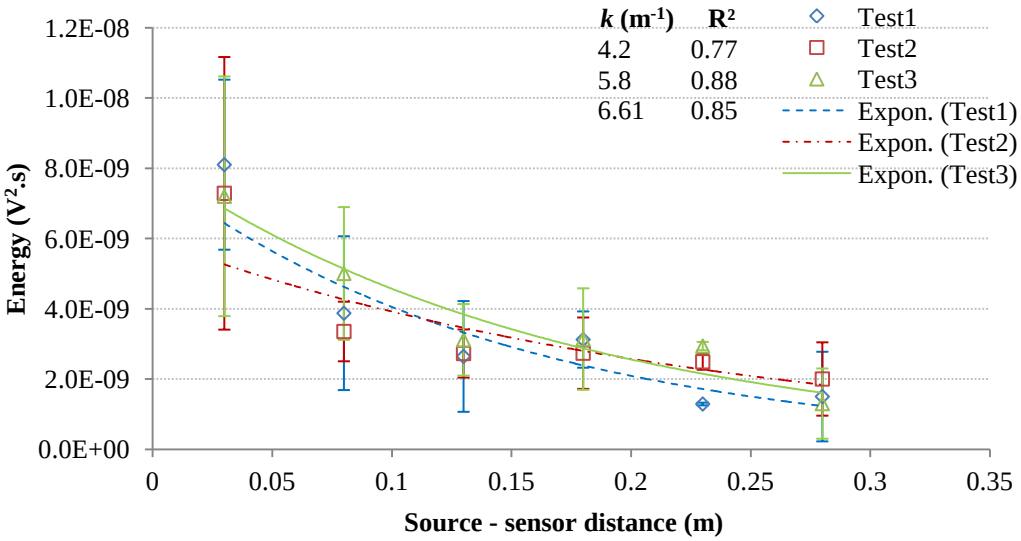

Figure D.8: Experimental AE attenuation on steel block, water, source at the edge

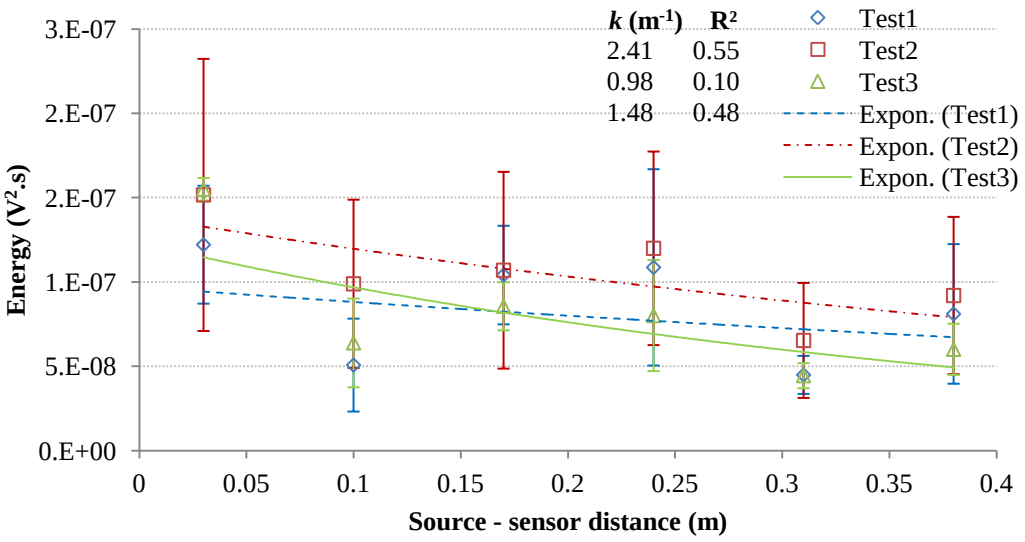

Figure D.9: Experimental AE attenuation on steel block, air, source at the corner

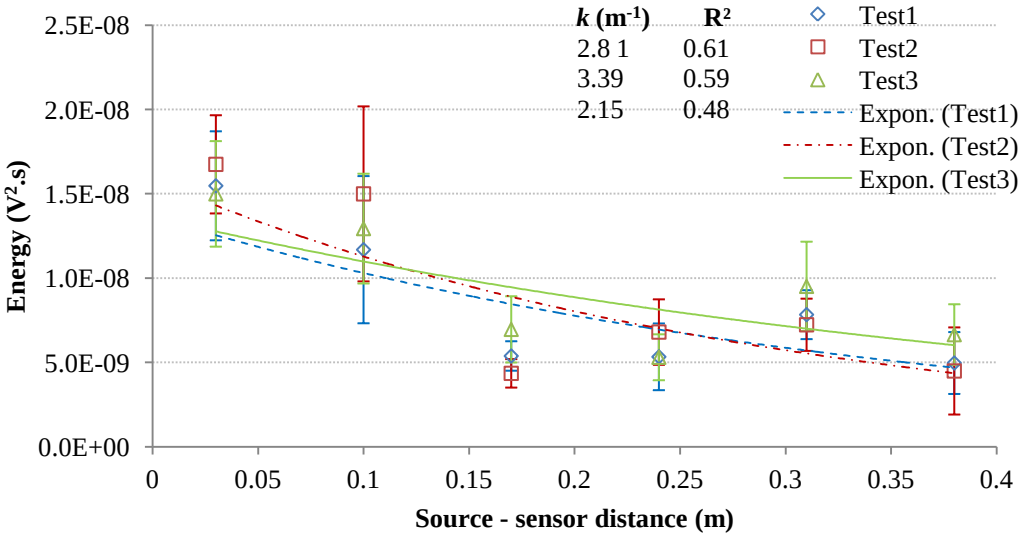

Figure D.10: Experimental AE attenuation on steel block, dry sand, source at the corner

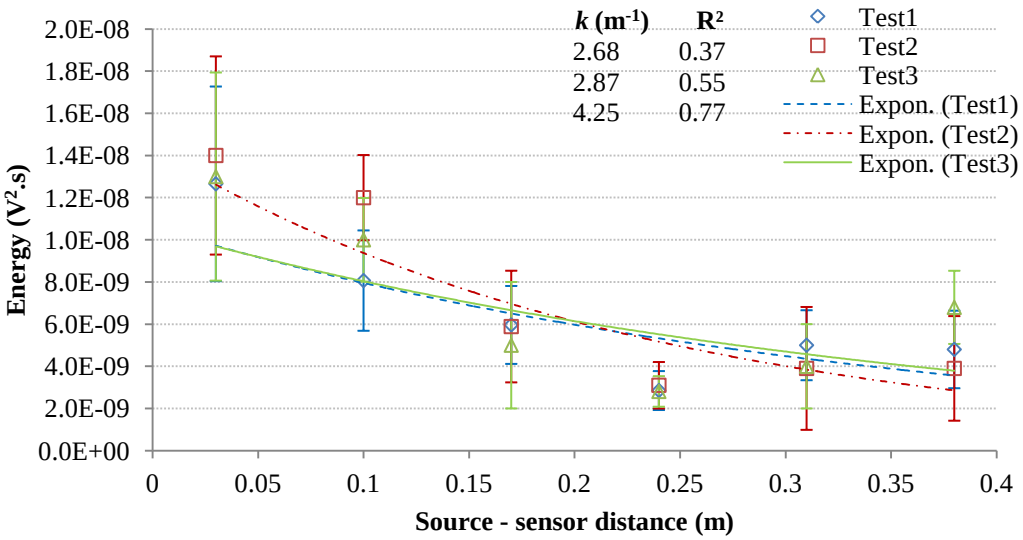

Figure D.11: Experimental AE attenuation on steel block, wet sand, source at the corner

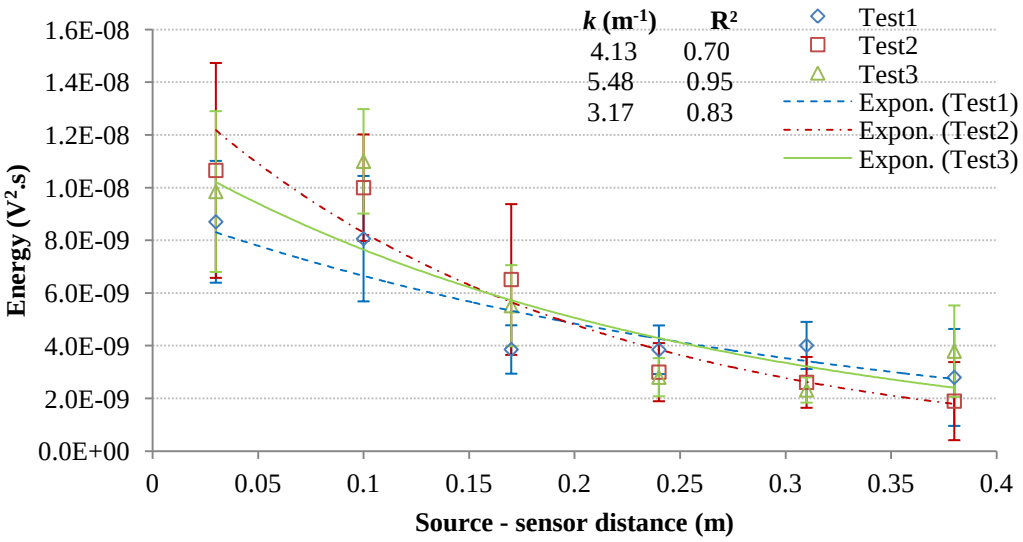

Figure D.12: Experimental AE attenuation on steel block, water, source at the corner

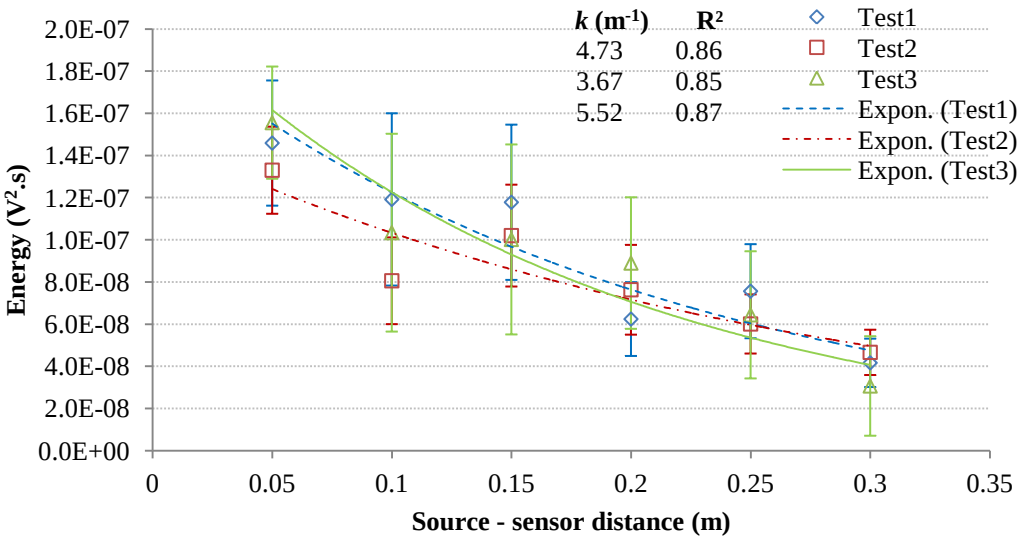

Figure D.13: Experimental AE attenuation on steel strip, air, source at the centre

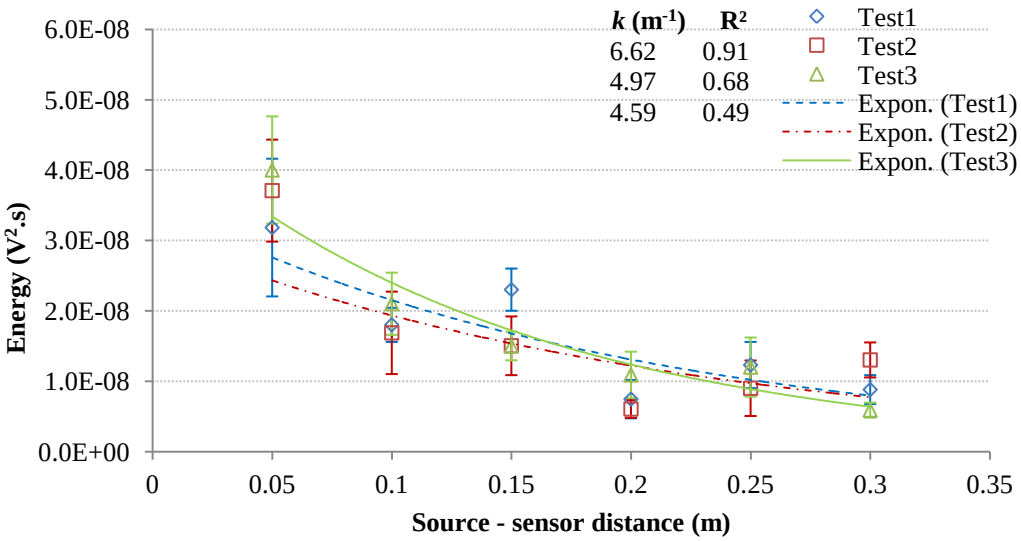

Figure D.14: Experimental AE attenuation on steel strip, dry sand, source at the centre

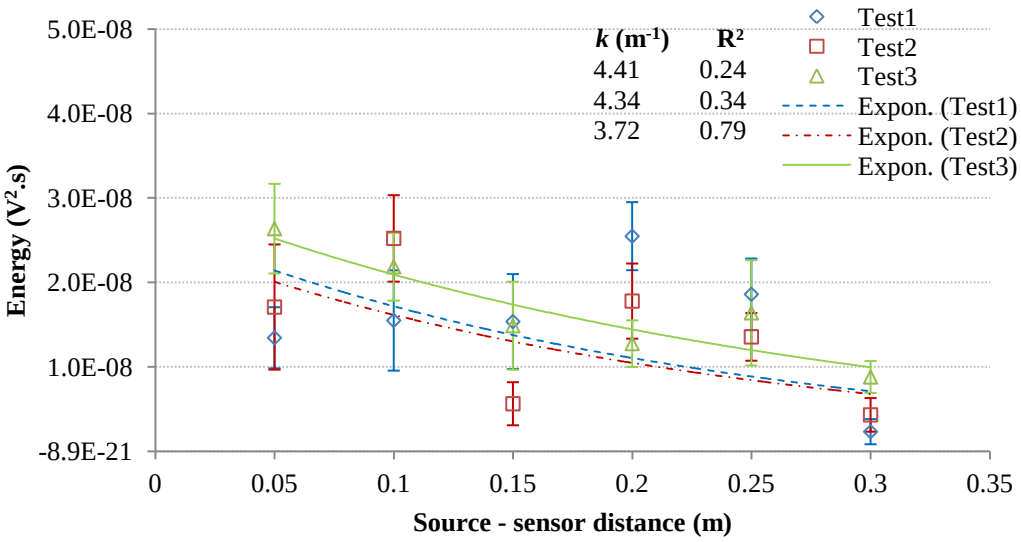

Figure D.15: Experimental AE attenuation on steel strip, wet sand, source at the centre

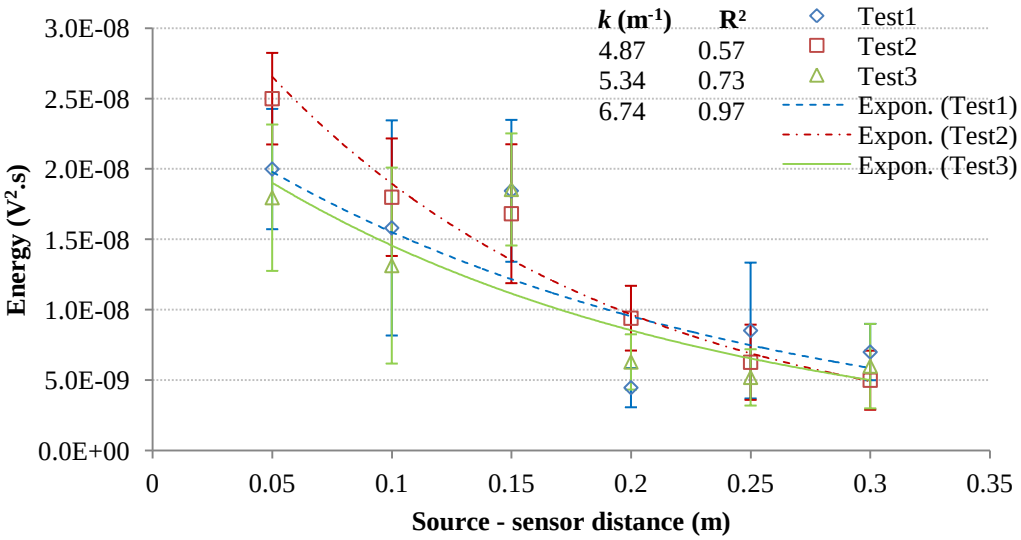

Figure D.16: Experimental AE attenuation on steel strip, water, source at the centre

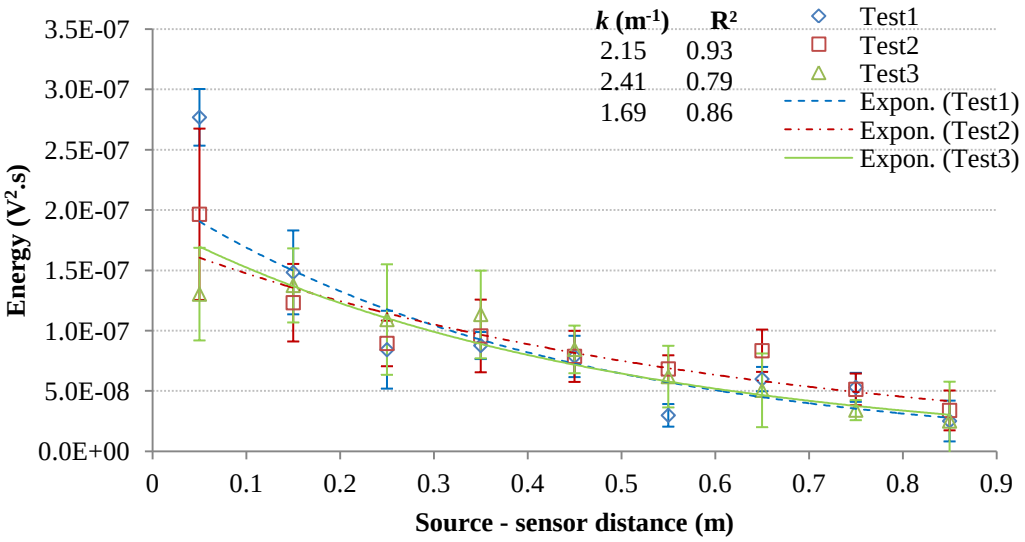

Figure D.17: Experimental AE attenuation on steel strip, air, source at the edge

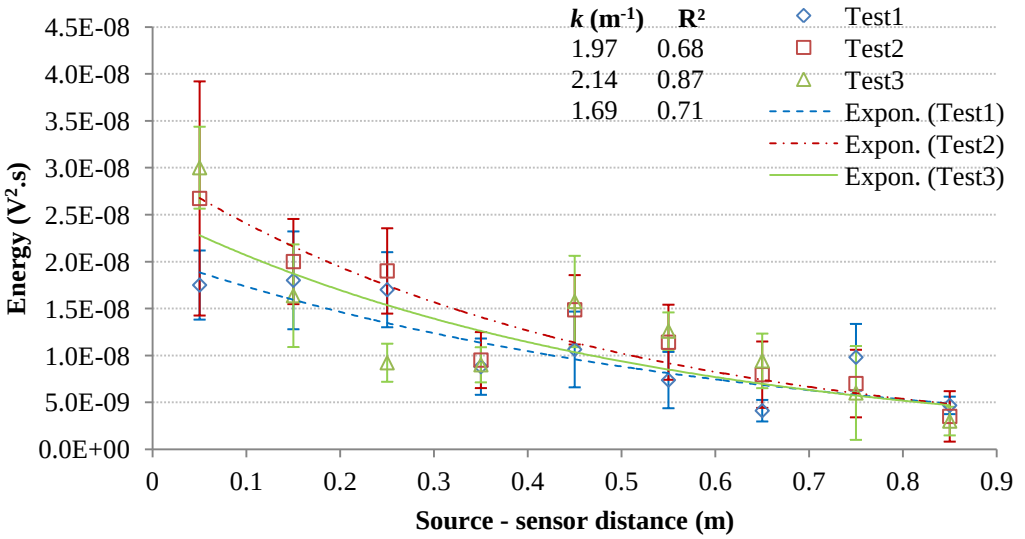

Figure D.18: Experimental AE attenuation on steel strip, dry sand, source at the edge

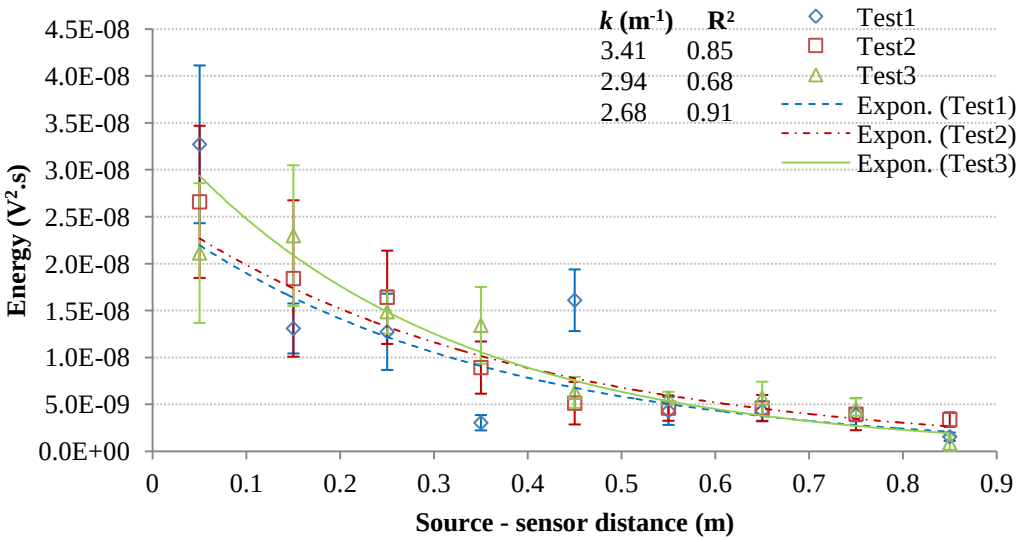

Figure D.19: Experimental AE attenuation on steel strip, wet sand, source at the edge

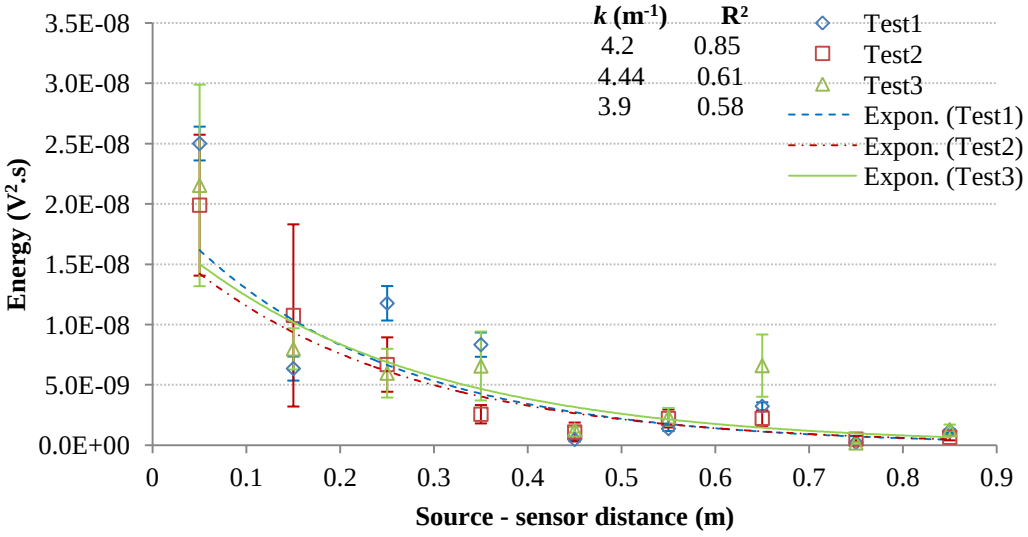

Figure D.20: Experimental AE attenuation on steel strip, water, source at the edge

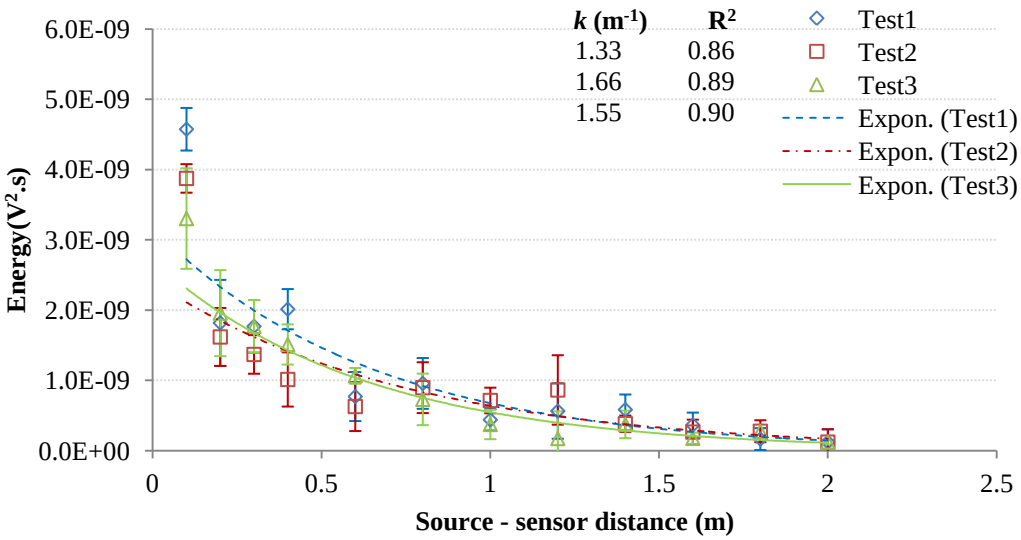

Figure D.21: Measured attenuation at longitudinal sensor array in large vessel, empty

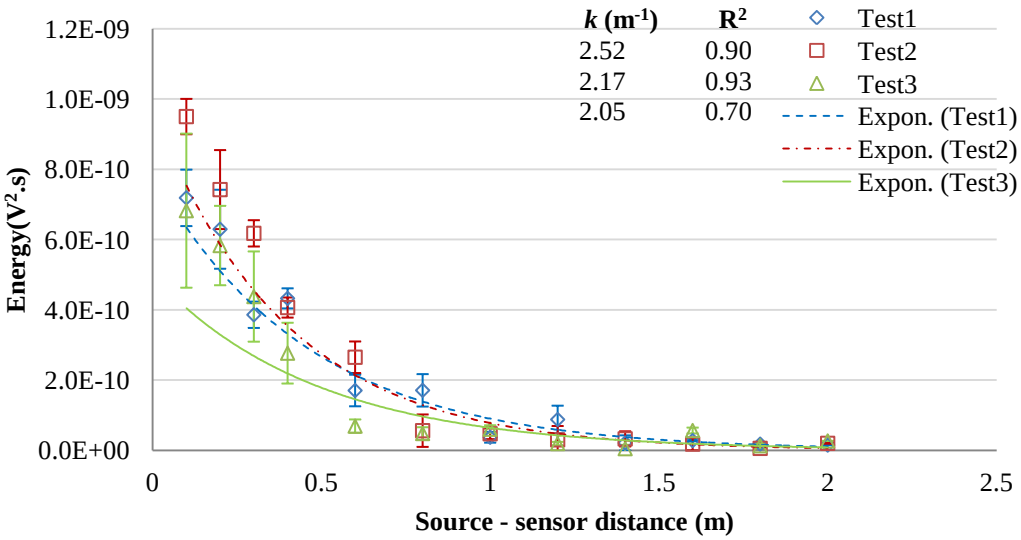

Figure D.22: Measured attenuation at longitudinal sensor array in large vessel, full of water

D.2 Simulation results

Figures from D.25 to D.39 shows the ray tracing prediction of the AE attenuation at four different reflections coefficient, 0.99, 0.97, 0.93 and 0.87 which can represent the effect of different environments, air, dry-sand, wet-sand and water respectively.

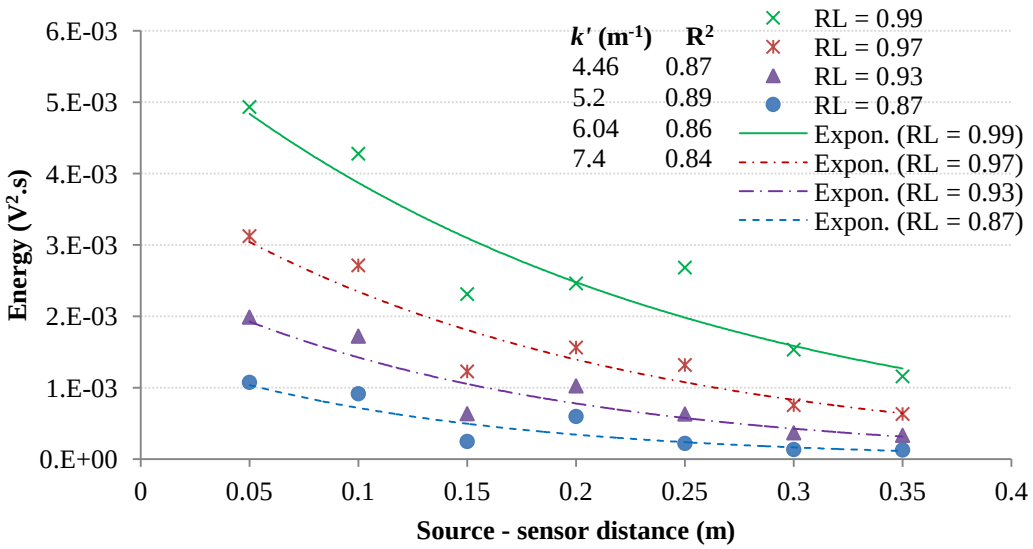

Figure D.23: Effect of reflection coefficient of simulated attenuation of internal rays on steel plate, source at the centre

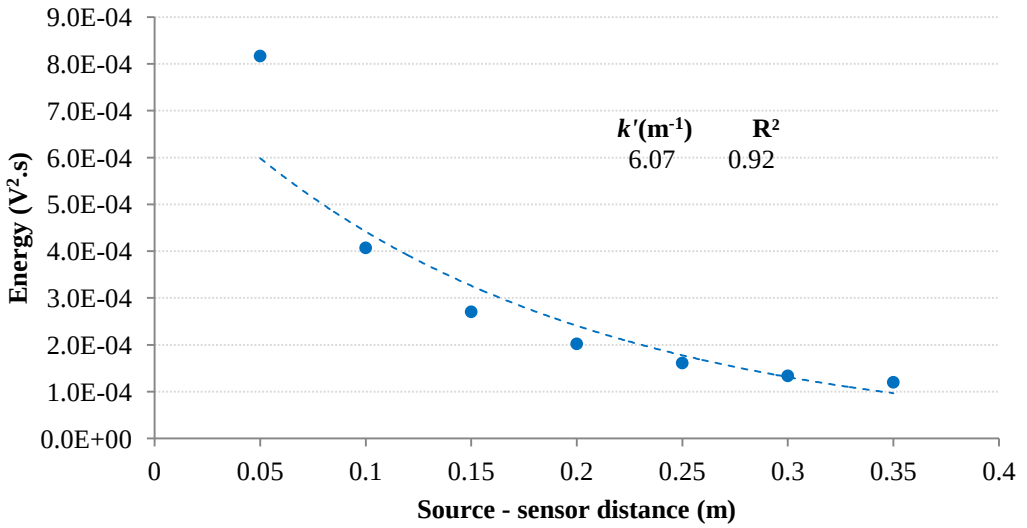

Figure D.24: Effect of reflection coefficient of simulated attenuation of surface rays on steel plate, source at the centre

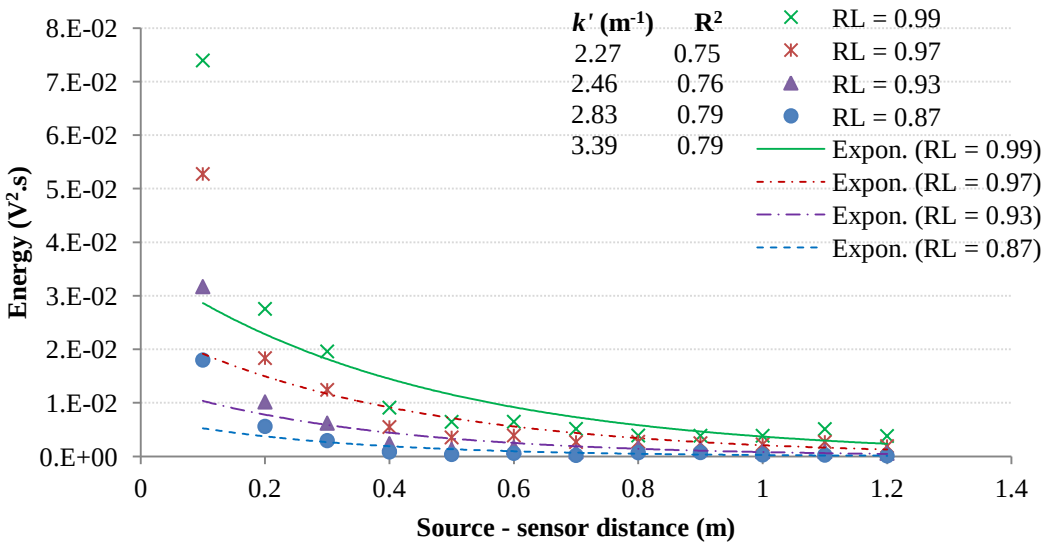

Figure D.25: Effect of reflection coefficient of simulated attenuation of internal rays on steel plate, source at the corner

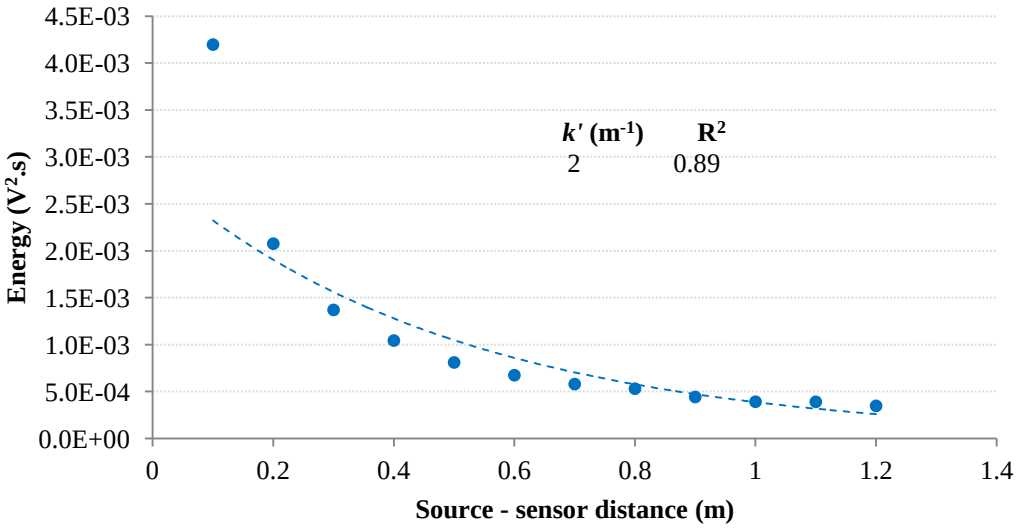

Figure D.26: Effect of reflection coefficient of simulated attenuation of surface rays on steel plate, source at the corner

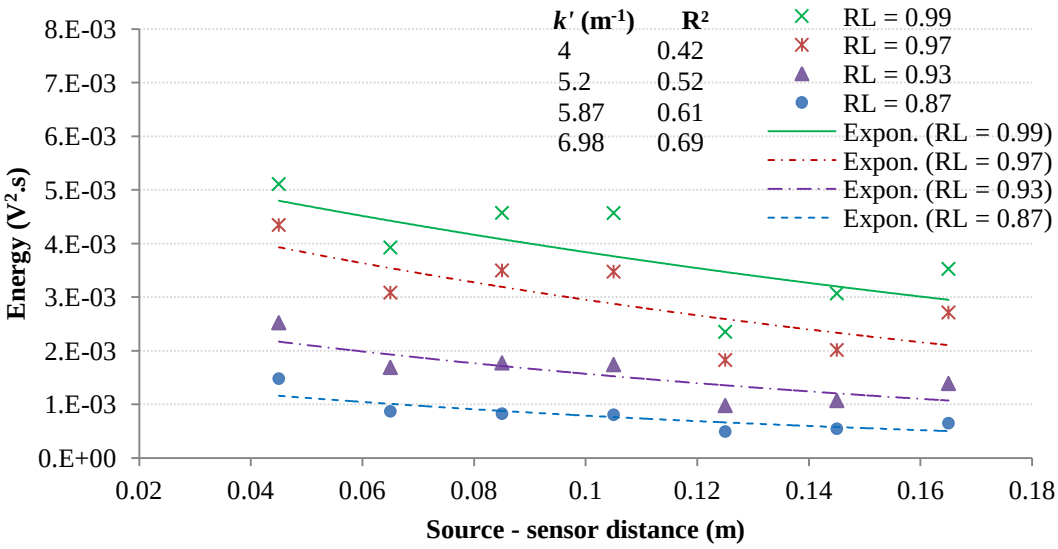

Figure D.27: Effect of reflection coefficient of simulated attenuation of internal rays on steel block, source at the centre

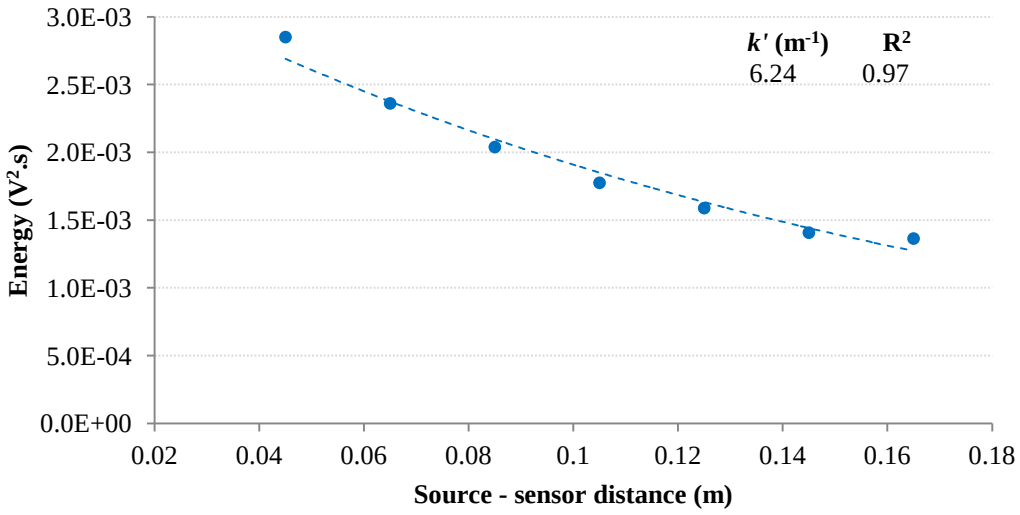

Figure D.28: Effect of reflection coefficient of simulated attenuation of surface rays on steel block, source at the centre

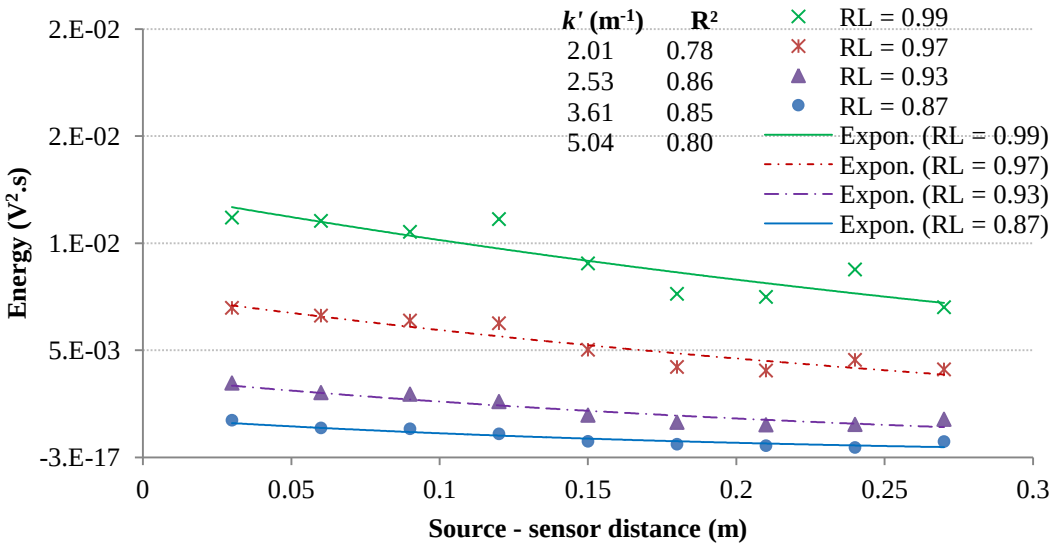

Figure D.29: Effect of reflection coefficient of simulated attenuation of internal rays on steel block, source at the edge

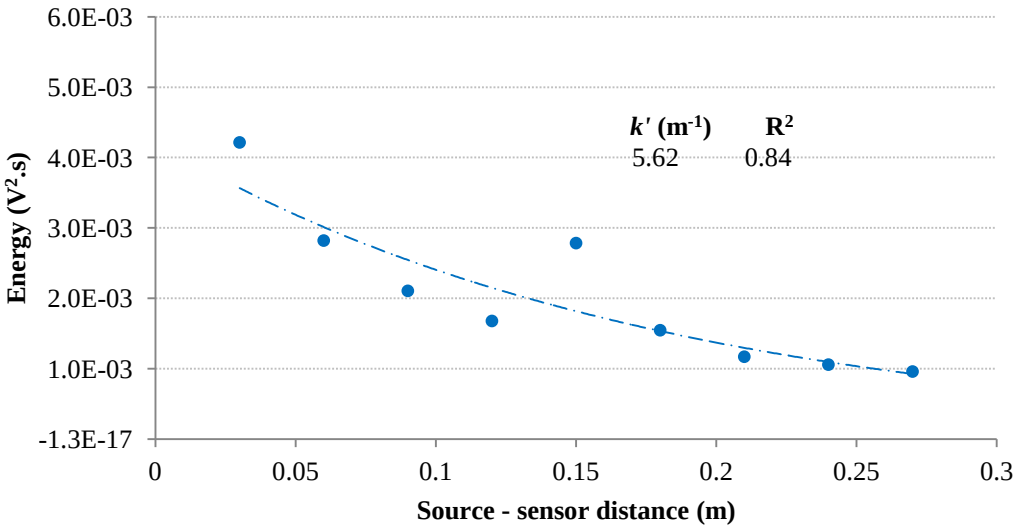

Figure D.30: Effect of reflection coefficient of simulated attenuation of surface rays on steel block, source at the edge

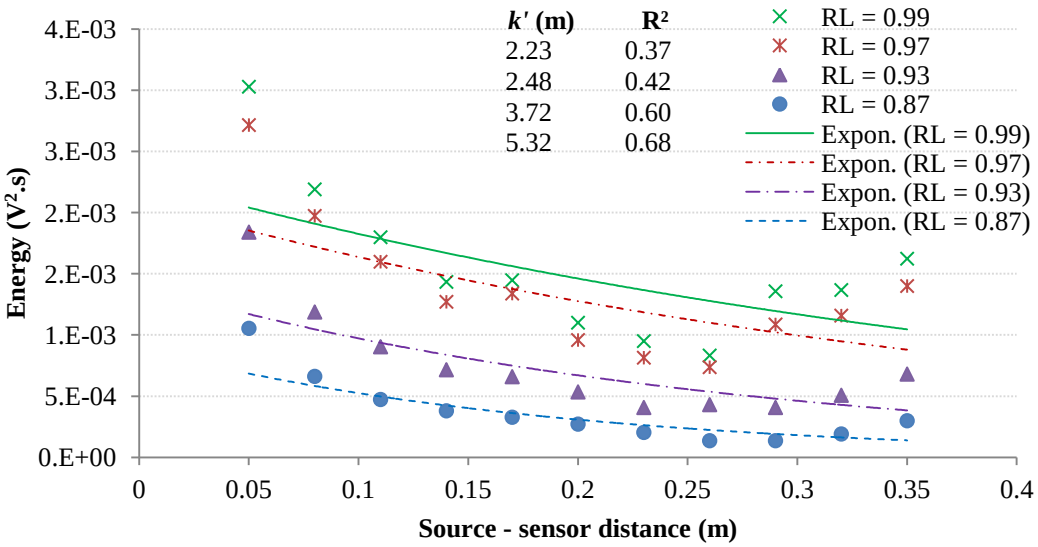

Figure D.31: Effect of reflection coefficient of simulated attenuation of internal rays on steel block, source at the corner

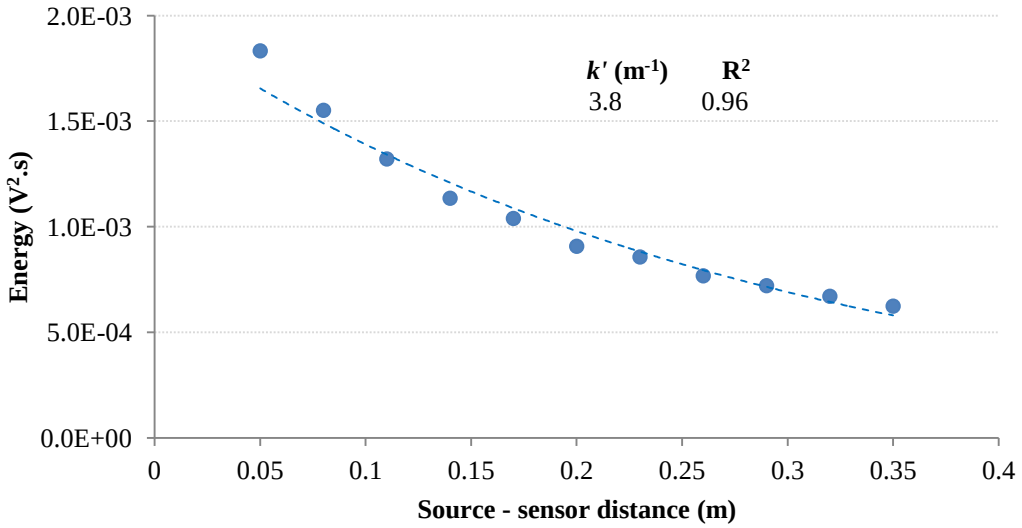

Figure D.32: Effect of reflection coefficient of simulated attenuation of surface rays on steel block, source at the corner

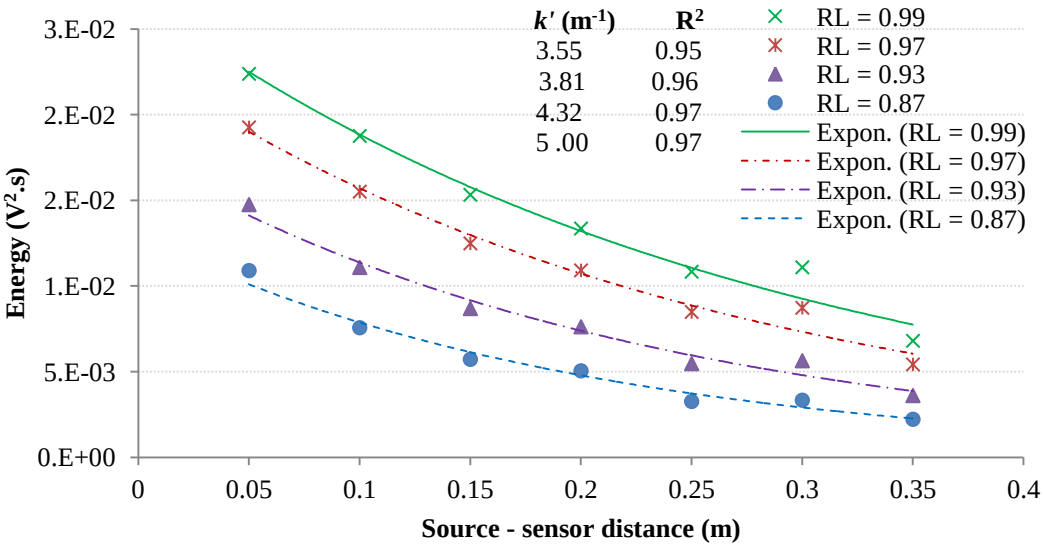

Figure D.33: Effect of reflection coefficient of simulated attenuation of internal rays on steel strip, source at the centre

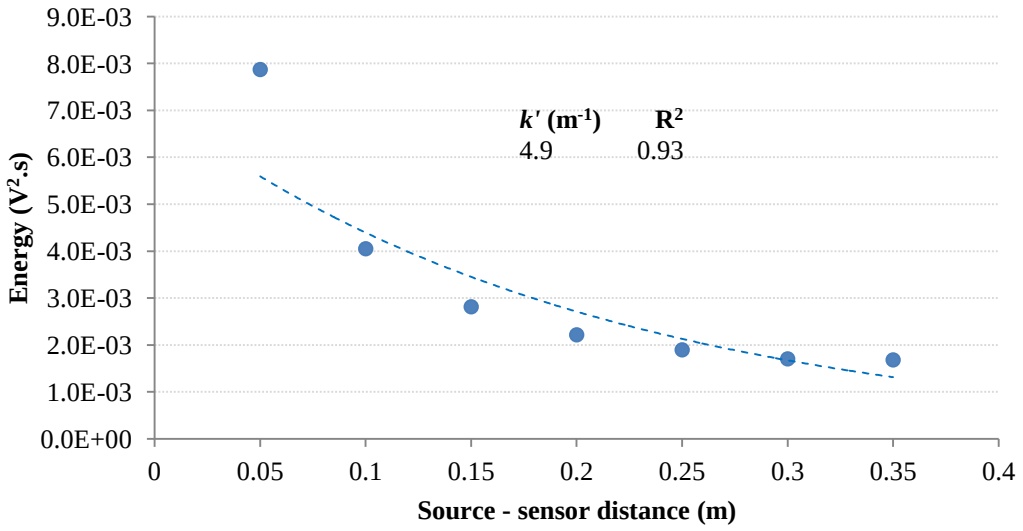

Figure D.34: Effect of reflection coefficient of simulated attenuation of surface rays on steel strip, source at the centre

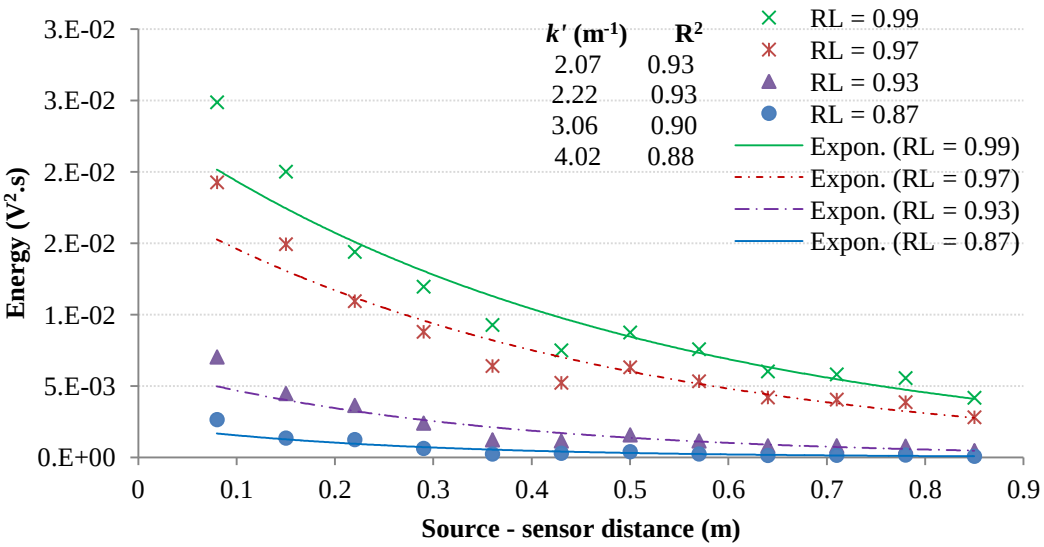

Figure D.35: Effect of reflection coefficient of simulated attenuation of internal rays on steel strip, source at the edge

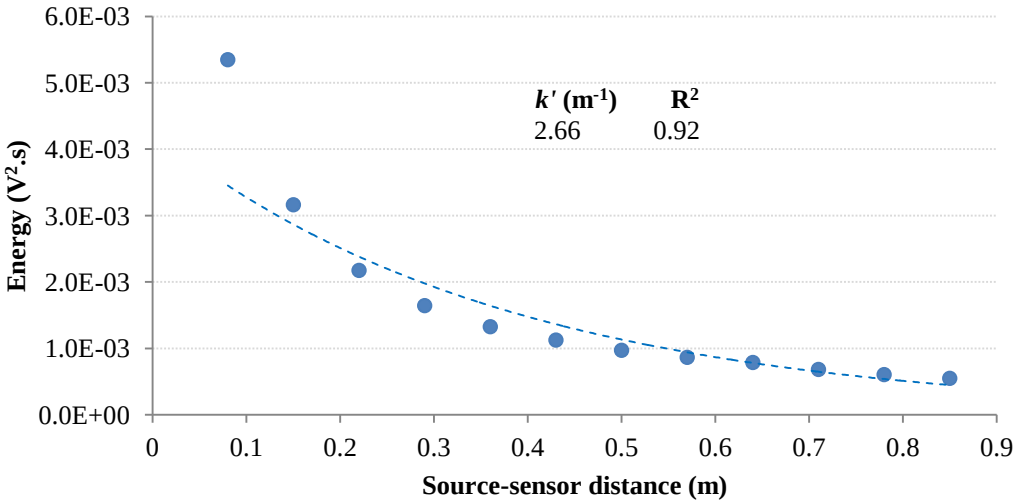

Figure D.36: Effect of reflection coefficient of simulated attenuation of surface rays on steel strip, source at the edge

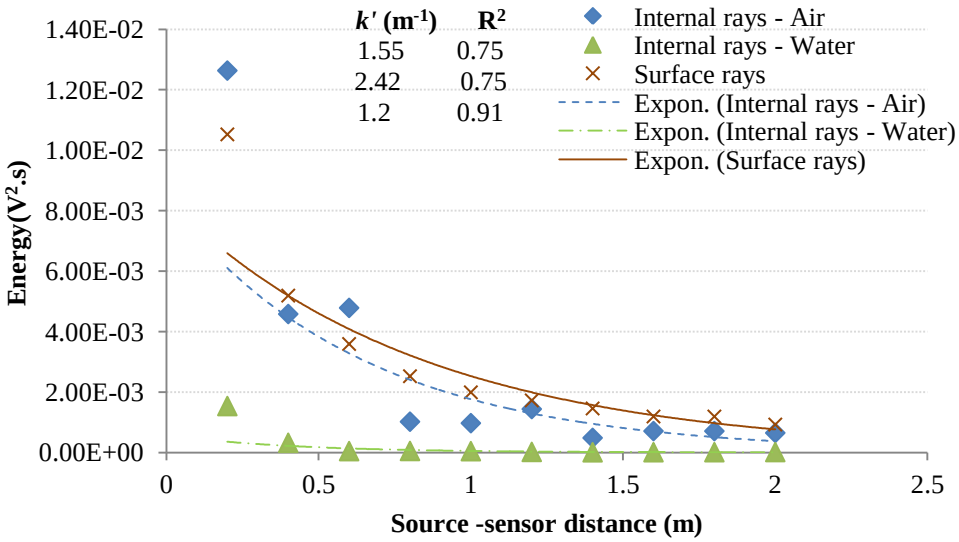

Figure D.37 : Effect of reflection coefficient of simulated attenuation of surface rays on stainless steel vessel for longitudinal sensor array